Title
Chiral Molecular Spintronics: Electron Dichroism in Biomolecular Assemblies

Author
Abendroth, John

Publication Date
2018

Peer reviewed|Thesis/dissertation

UNIVERSITY OF CALIFORNIA

Los Angeles

Chiral Molecular Spintronics: Electron Dichroism in Biomolecular Assemblies

A dissertation submitted in partial satisfaction of the

requirements for the degree of Doctor of Philosophy

in Chemistry

by

John Michael Abendroth

2018

ABSTRACT OF THE DISSERTATION

Chiral Molecular Spintronics: Electron Dichroism in Biomolecular Assemblies

by

John Michael Abendroth

Doctor of Philosophy in Chemistry

University of California, Los Angeles, 2018

Professor Paul S. Weiss, Chair

Recent observations of spin-dependent and enantioselective interactions between electrons and chiral biomolecules (*e.g.*, DNA, α-helical peptides, and proteins) at room temperature have inspired studies to elucidate the roles of spin and chirality in biology and in charge transfer at metal-molecule interfaces. Electrons of a certain spin orientation are transmitted through chiral molecules more easily in one direction *vs* the other, a phenomenon described as the chiral-induced spin selectivity effect.

However, identifying the preferred spin-velocity relationship for electrons confined to move along helical potentials has proven to be difficult, with conflicting experimental results regarding preferred polarization orientation. Thus, to elucidate the preferred spin polarization direction in DNA-mediated charge transport, I applied our group's expertise in molecular self-assembly, large-scale molecular patterning, and data processing and analysis from information-rich images, to investigate the effect *via* fluorescence microscopy.

Fluorescent perylenediimide derivatives were precisely incorporated within hydrophobic pockets in double-stranded DNA helices. The DNA/dye complexes were subsequently patterned on ferromagnetic substrates that could be magnetized parallel or antiparallel to the nominally vertically aligned DNA strands. There are two relaxation pathways following photoexcitation. The dye molecules either fluoresce, or when well-coupled to the DNA, display competitive quenching due to charge transfer to the underlying ferromagnetic surface. Because charge injection into ferromagnetic materials is spin dependent, a dependence of the fluorescence intensity on substrate magnetization direction is indicative of spin filtering; lower fluorescence intensities in this system correspond to higher degrees of charge quenching and transfer from the dye to the substrate. My results suggest that electron helicity, or spin projection along the helical axis of DNA, is preferentially aligned parallel to its velocity direction within this charge transport regime.

Yet, while I and others have demonstrated that chiral molecules can polarize transmitted electrons, unifying mechanisms that account for the magnitude of spin polarization, and that can predict the strength of the relativistic effects due to helix-induced spin-orbit coupling, remain elusive. Development of accurate models has been impeded, in part, by the lack of quantitative, experimental analyses on the relative energy barriers to spin-dependent scattering of electrons within chiral electrostatic fields with precise orientation control.

To tackle this challenge, I developed experiments to test spin selectivity in a second charge transport regime: photoelectron transmission through adsorbed chiral molecule assemblies. Ultraviolet photoelectron spectroscopy was used to measure the ionization energy and work function of these systems, and therefore the spin-selective energy barriers

to photoemission from chiral molecule films. I hypothesize that photoelectrons emitted by ionization of chiral molecular films using unpolarized ultraviolet radiation leave behind spin-polarized holes. Underlying ferromagnetic substrates provide a source of replenishing spin-polarized electrons, thus, effective ionization energies depend on substrate magnetization orientation. I measured significant differences in the ionization energies and work function values of ferromagnetic substrates coated with chiral films of *ca.* 100 and 80 meV, respectively, that depended on substrate magnetization orientation, relative saturation of the substrate magnetization, and molecular handedness.

Having shown that the chiral-induced spin selectivity effect is subtle in the context of charge-transport through self-assembled monolayers of chiral molecules, I internalized the necessity of repeated measurements, unbiased statistical analysis of large data sets, and careful design of control experiments. Continuing these practices, my measurements have enabled the unprecedented determination of the relative spin-dependent energy barriers to transmission through chiral molecules, which will be critical in the development and evolution of theoretical models necessary for foundational understanding of this phenomenon.

Moving forward, elucidating the mechanistic contributions to spin filtering from the adsorbed chiral species, underlying ferromagnetic materials, and metal-molecule interfaces will enable us to critically assess the practicality of chiral organic materials for spintronics applications. Devices that utilize stable organic layers may facilitate the design, development, and implementation of next-generation electronic device architectures that exploit spin injection and detection at metal/semiconductor, chiral-molecule interfaces for information storage, memory technology, sensors, optics, and energy-efficient electronics.

The dissertation of John Michael Abendroth is approved.

James K. Gimzewski

Jacob J. Schmidt

Paul S. Weiss, Committee Chair

University of California, Los Angeles

2018

For my parents,

who have always supported me.

Table of Contents

Chapter II

Chapter III

Chapter IV

Appendix

List of Abbreviations

Acronyms and Symbols

0dS DNA	zero deoxyribose spacer-containing DNA
1dS DNA	one deoxyribose spacer-containing DNA
A (Chapter 2)	adenine
A (Chapter 3)	alanine
A	transmission asymmetry
AFM	atomic force microscopy
Ag/AgCl	silver/silver chloride
Aib	2-aminoisobutyric acid
AlGaN	aluminum gallium nitride
Al_2O_3	aluminum oxide
Alq_3	aluminum *tris*(8-hydroxyquinone)
Au	gold
AUT	11-amino-1-undecanethiol
bp	base pair
BSA	bovine serum albumin
C (Chapter 2)	cytosine
C (Chapter 3)	cysteine
CD	circular dichroism
$CdCl_2$	cadmium(II) chloride
CdSe	cadmium selenide

CdTe	cadmium telluride
CISS	chiral-induced spin selectivity
CLL	chemical lift-off lithography
Co	cobalt
Cy3	cyanine 3
dBSA	thermally denatured bovine serum albumin
DNA	deoxyribonucleic acid
DRAM	dynamic random access memory
dsDNA	double-stranded DNA
dSp	deoxyribose spacer
E_B^{max}	maximum binding energy (secondary electron cutoff)
$E_B^{min;\,organic}$	minimum binding energy (valence band/Fermi edge)
E_F	Fermi level
EDTA	ethylenediaminetetraacetic acid
FM	ferromagnetic
G	guanine
GaAs	gallium arsenide
GaN	gallium nitride
h	Planck's constant
HCl	hydrochloric acid
hfc	hydrofluorocarbon
H_2O_2	hydrogen peroxide
HOMO	highest occupied molecular orbital

HOPG	highly ordered pyrolytic graphite
^{1}H NMR	proton nuclear magnetic resonance
I	ionization energy
InGaAs	indium gallium arsenide
K	lysine
k_B	Boltzmann's constant
k_{CR}	rate of charge recombination
k_{CS}	rate of charge separation
k_{CT}	rate of charge transfer
k_{SE}	rate of stimulated emission
LB	leucomethylene blue
LED	light-emitting diode
LUMO	lowest unoccupied molecular orbital
MB^+	methylene blue
MCU	11-mercapto-1-undecanol
MHA	6-mercaptohexanoic acid
$MgCl_2$	magnesium chloride
Mg^{2+}	divalent magnesium ion
MPA	mercaptopropionic acid
N_2	dinitrogen (gas)
NaCl	sodium chloride
NaOH	sodium hydroxide
Ni	nickel

NM	normal metal
O_2	molecular oxygen
OLED	organic light-emitting diode
p	electron momentum
P	spin polarization
PBS	phosphate buffered saline
PDI	*N*,*N*′-bis[3,3′-(dimethylamino)propylamine]-3,4,9,10-perylenetetracarboxylic diimide
PDMS	polydimethylsiloxane
PMA	perpendicular magnetic anisotropy
Pt	platinum
QD	quantum dot
SAM	self-assembled monolayer
S	sulfur
S	electron spin angular momentum
SCE	saturated calomel electrode
Si	silicon
SiO_2	silicon dioxide
spin-OLED	spin-polarized organic light-emitting diode
SQUID	superconducting quantum interference device
ssDNA	single-stranded DNA
STT	spin-transfer torque
STT-MRAM	spin-transfer torque magnetoresistive random-access memory

T	thymine
Ta	tantalum
TiO_2	titanium dioxide
TBO	toluidine blue O
EDTA	ethylenediaminetetraacetic acid
Θ	molar ellipticity
ϕ	work function
μ	electron magnetic dipole moment
UPS	ultraviolet photoelectron spectroscopy
UV	ultraviolet
UV-vis	ultraviolet-visible
XPS	X-ray photoelectron spectroscopy
$\bar{x}_{patterned}$	mean pixel intensity from patterned regions of fluorescence microscopy images
$\bar{x}_{unpatterned}$	mean pixel intensity from unpatterned regions of fluorescence microscopy images
Z	atomic number

Units

Å	Ångström
C	Celsius
cm	centimeter
cm^{-1}	wavenumber

eV	electronvolt
g	gram
GHz	gigahertz
h	hour
Hz	hertz
kJ	kilojoule
kOe	kilo-Oersted
M	molar
meV	millielectron volt
min	minute
mg	milligram
mL	milliliter
mM	millimolar
mol	mole
mW	milliwatt
nA	nanoampere
nm	nanometer
nM	nanomolar
Oe	Oersted
psi	pound-force per square inch
RFU	relative fluorescence units
s	second
T	Tesla

Torr	torr
μV	microvolt
V	volt

Acknowledgments

I thank first, Professor Paul S. Weiss, my advisor, for his continuous support and encouragement to push the boundaries of physical chemistry research in new and exciting fields, and for giving me the chance to develop the skills and expertise necessary to grow as an independent researcher. I would also like to acknowledge my thesis committee members, Professor Kendall N. Houk, Professor James K. Gimzewski, and Professor Jacob J. Schmidt, for their thoughtful feedback and encouragement as I progressed through my graduate career.

I thank the other academic mentors with whom I had the opportunity to collaborate and to share scientific ideas over the past six years as well. Professor Anne M. Andrews has been an inspiration as a scientist, by the way she approaches research questions in a systematic and rigorous manner, and I appreciate her thoughtful contributions to my research. During my graduate career, I also grew close with two of our group's sabbatical visitors, Professor Christopher J. Barrett and Professor Mary Elizabeth Anderson. Both Chris and Beth expressed some of the most positive attitudes and outlook towards pursuing a future in academia, and have always been supportive as friends and colleagues.

In addition, I thank our close collaborators with whom I have worked to design and to carry out my experiments. Professor Jacqueline K. Barton and her former student, Dr. Theodore J. Zwang, were immensely helpful as we started pursuing research in an unfamiliar area to probe DNA-mediated charge transfer by electrochemical methods. I also appreciate Professor Eric E. Fullerton, and his former and current postdoctoral researchers, Dr. Dokyun Kim and Dr. Mohammed S. El Hadri, who were responsible for the design and

fabrication of substrates we used for our experiments. They were always willing to provide materials according to our evolving experimental requirements.

I thank Professor Ron Naaman, and members of his group, Dr. Eyal Capua, Dr. Anup Kumar, and Dr. Vaibhav Varade for their warm hospitality and inspiring discussions when Professor Naaman hosted me in September 2017 at the Weizmann Institute of Science in Rehovot, Israel. In addition, I am grateful for the Feinberg Graduate School Visiting Fellowship for providing this opportunity to visit and to study abroad at the Weizmann Institute.

I am also appreciative of my fellow Weiss group members at UCLA, with whom I have had the pleasure of working with and sharing ideas over the past six years. In particular, I would like to acknowledge Kevin M. Cheung and Chuanzhen Zhao, whose hard work, dedication, and passion for science were reflected in the experiments we planned and carried out toward the end of my graduate career. Further, as a senior member of the Weiss group, I also had the chance to mentor Dominik M. Stemer and Matthew Ye in the area of chiral molecular spintronics. Both Dominik and Matthew show tremendous promise, and I am excited to see how their drive and creativity shapes the evolvement of new projects I was able to help start in this nascent field.

The research that I conducted at UCLA would not have been possible without the funding and support from the National Science Foundation ECCS (grant no. 1509794). I also gratefully acknowledge the UCLA Dissertation Year Fellowship for funding during the last year of my graduate work and the Graduate Dean's Fellowship that supported my first two years of studies.

I am also grateful to my family for their unconditional love and support to help me to reach this milestone in my life. I thank my mother, Maryann, my father, John, my sister, Jennifer, and her husband, Zachary, and even my little niece, Gemma, who I hope grows up to be a scientist just like her uncle.

The friends that I met along the way throughout graduate school shaped the person that I am today. I shared many highs and lows with my best friend, Colin, who I met merely days after moving to Los Angeles. Colin is one of the most genuine people I have ever met, and graduate school would not have been nearly as fun or crazy without him. I would also like to recognize Adam, Josh, Steve, Heidi, John, Miles, Renee, Maureen, Tim, Alex, Nick, Kelly, Brian, Natcha, and Andrew. It has been my pleasure to have met them and shared their friendship, and I wish them all the best in their future endeavors.

Finally, I want to thank Nako, my best friend, colleague, and partner. She has always selflessly brought out the best in me, and I cannot imagine graduate school without her. My success, I owe to her support, and I am excited to share the next stages of our lives together.

Vita

I started pursuing physical chemistry research with Professor W. David Wei at the University of Florida as an undergraduate student in the Department of Chemistry in 2009. My research focused on synthesizing anisotropic silver and gold nanostructures with tunable optical properties. I received several academic awards including the Chemical Physics Scholarship and the Colonel Allen R. and Margaret G. Crow Chemistry Scholarship. I graduated *summa cum laude* with my Bachelor of Science degree in Chemistry in 2011.

I began my graduate studies at the University of California, Los Angeles in 2012 under the mentorship of Professor Paul S. Weiss in the Department of Chemistry and Biochemistry. I independently designed and developed experimental techniques to measure room-temperature electron spin filtering in charge transmission through chiral molecules. In 2014, with the support of Professor Weiss, I authored an original, standard grant proposal to the National Science Foundation on investigating electron spin selectivity in DNA-mediated charge transport, and secured three years of funding to lead research in our group in the exciting and expanding field of chiral molecular spintronics. In a parallel project, I led a team to investigate the influence of thiolated self-assembled monolayers on Rashba spin-orbit coupling in gold at the Advanced Light Source at Lawrence Berkeley National Laboratory, an ongoing study. In 2017, I was awarded a Feinberg Graduate School Visiting Fellowship through the Weizmann Institute of Science in Rehovot, Israel, and spent time working abroad in the laboratory of our collaborator, Professor Ron Naaman, a pioneer in the field of molecular spintronics, in the Department of Chemical and Biological Physics. In 2018, I won the George Gregory Award and Physical Chemistry Award at the University of California,

Los Angeles, annual departmental awards recognizing outstanding research in the area of physical chemistry.

List of Publications

1. **Abendroth, J. M.**; Cheung, K. M.; Stemer, D. S.; El Hadri, M. S.; Zhao, C.; Fullerton, E. E.; Weiss, P. S. Spin-Polarized Photoemission by Ionization of Chiral Molecular Films, *in preparation* (2018).

2. Mondal, P. C.; **Abendroth, J.M.**; Stemer, D. M.; Roy, P.; Weiss, P. S.; Naaman, R. Spin-Dependent Photoluminescence in Chiral Molecular Films, *in preparation* (2018).

3. Nakatsuka, N.; Yang K. A.; **Abendroth, J. M.**; Cheung, K. M.; Xu, X.; Yang, H.; Zhao, C.; Zhu, B.; Rim, Y. S.; Yang Y.; Weiss, P. S.; Stojanovic, M. N.; Andrews, A. M. Aptamer Field-Effect Transistors Overcome Debye Length Limitations and Enable Small-Molecule Sensing, *under review for Science* (2018).

4. Cao, H. H.; Nakatsuka, N.; Deshayes, S.; **Abendroth, J. M.**; Yang, H.; Weiss, P. S.; Kasko, A. M.; Andrews, A. M.; Multiplexed Small-Molecule Patterning *via* Pre-Functionalized Alkanethiols. *Chemistry of Materials,* DOI: 10.1021/acs.chemmater.8b00377 (2018).

5. **Abendroth, J. M.**; Nakatsuka, N.; Ye, M.; Kim, D.; Fullerton, E. E.; Andrews, A. M.; Weiss, P. S. Analyzing Spin Selectivity in DNA-Mediated Charge Transfer *via* Fluorescence Microscopy. *ACS Nano*, **11**, 7516 (2017).

6. Xu, X.; Yang, Q.; Cheung, K. M.; Zhao, C.; Wattanatorn, N.; Belling, J. N.; **Abendroth, J. M.**; Slaughter, L. S.; Mirkin, C. A.; Andrews, A. M.; Weiss, P. S. Polymer-Pen Chemical Lift-Off Lithography. *Nano Letters* **17**, 3302 (2017).

7. Guttentag, A. I.; Wächter, T.; Barr, K. K.; **Abendroth, J. M.**; Song, T.-B.; Sullivan, N. F.; Yang, Y.; Allara, D. L.; Zarnikov, M.; Weiss, P. S. Surface Structure and Electron Transfer Dynamics of Cyanide on Au{111}. *The Journal of Physical Chemistry C* **120**, 26736 (2016).

8. **Abendroth, J. M.**;* Bushuyev, O. S.;* Weiss, P. S.; Barrett, C. J. Controlling Motion at the Nanoscale: Rise of the Molecular Machines. *ACS Nano* **9**, 7746 (2015) **equal contribution*.

Chapter I

The Chiral-Induced Spin Selectivity Effect

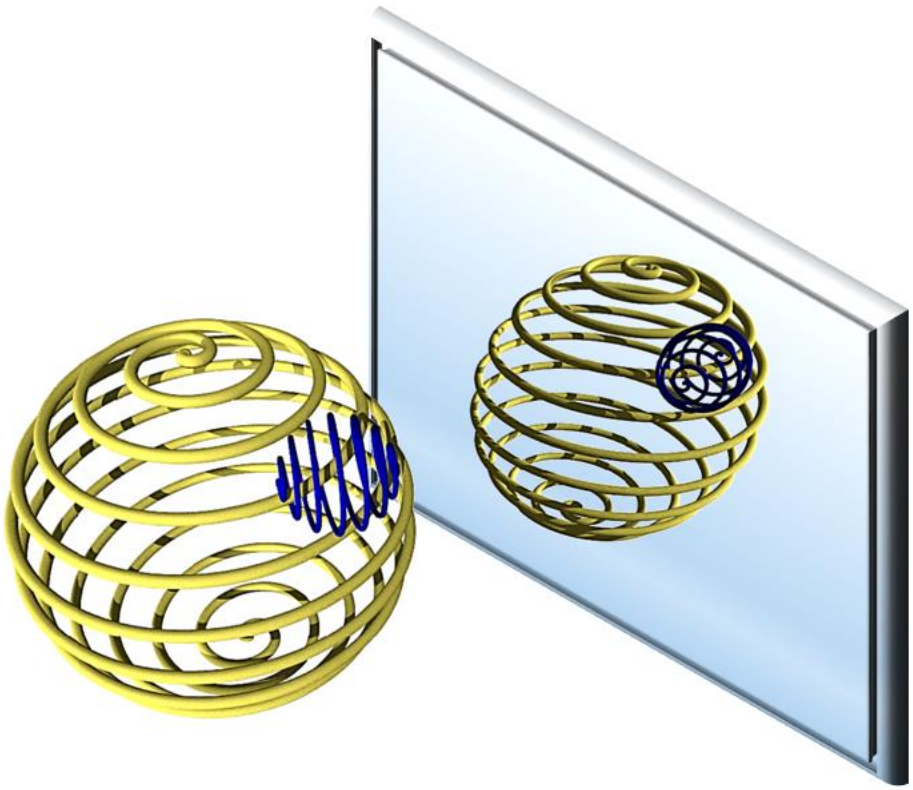

The information in this chapter is adapted from work in preparation for submission for publication, and is reproduced here.

Authors: Prakash C. Mondal, John M. Abendroth, Dominik M. Stemer, Partha Roy, Paul S. Weiss, and Ron Naaman

I.A. Discovering Enantioselective Chemical and Physical Properties of Chiral Systems

Chirality is ubiquitous in Nature, from the handedness of elementary particles and arrangements of atoms in molecules and crystals, to the macroscale. Chiral molecules are non-superimposable mirror images of one another with otherwise identical compositions (Figure I.1), yet the spatial dissymmetry gives rise to a myriad of fascinating physical and chemical properties that are unique to specific enantiomers.

From the beginning of the 19th century, early studies of light-matter interactions led to Pasteur's discover of molecular handedness *via* observation of the optical activity of natural tartaric acid.[1,2] The prevalence of molecules in biology that lack structural inversion symmetry was brought to light by Pasteur's subsequent discovery of enantioselectivity in 1857 by observing different rates of metabolism of tartaric acid enantiomers by microorganisms.[3-5] This finding was followed by Piutti's observation of stereoselectivity of biological receptors in 1886, that arose from perceiving that *D*-asparagine tastes sweet while *L*-asparagine is tasteless.[6,7] The first use of the term *chiral*, however, has been attributed to Kelvin who used it in 1893 to describe a material's lack of parity symmetry.[8]

While the dissymmetric optical properties of chiral molecules and the nature of enantioselective intermolecular interactions between chiral species are comparatively well understood,[8-10] explanations for varying electronic and magnetic properties of molecules and assemblies attributed to broken inversion symmetry remain elusive. Despite a history of contradictory investigations into spin-dependent electron – chiral molecule interactions that began *ca*. 1960,[11] Mayer and Kessler confirmed in 1995 that randomly oriented chiral species in the gas phase display asymmetric scattering of spin-polarized electrons, validating theoretical predictions.[12] However, such asymmetry could only be observed when the

molecules were engineered to incorporate heavy atoms with measurable spin-orbit coupling.[13,14]

More recently, room-temperature spin polarization of electrons transmitted through organized chiral molecular assemblies on surfaces has been observed with scattering asymmetries 10^3-10^4 times larger than those of gas-phase molecules.[15-17] These results have catalyzed a new wave of investigations into the fundamental roles of spin in biology and for the prospective use of chiral molecules for organic spintronics.[18-21] These spin-dependent and enantioselective interactions between electrons and chiral molecules are described by the chiral-induced spin selectivity (CISS) effect (Figure I.2).[22]

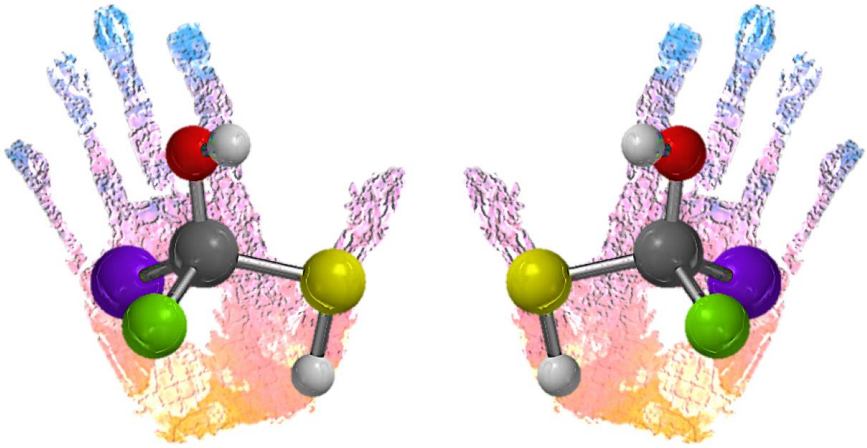

Figure I.1. Illustration of chirality, or lack of mirror symmetry, between two asymmetric chemical structures. Like our hands, the two mirror image molecules, or enantiomers, cannot be superimposed on one another.

Many theoretical models have been developed to explain this phenomenon, including spin-dependent scattering by helical electrostatic potentials and tight-binding models to describe band motion along helical paths.[23-38] Many models attribute the observed effects to unconventional Rashba-like (momentum-dependent) spin-orbit coupling,[39] and conclude that chirality is essential to observe spin polarization due to inversion asymmetry. Spin filtration is thus hypothesized to arise from coupling between the magnetic moment of an electron and effective magnetic fields due to relativistic effects in electron propagation through chiral electrostatic potentials.

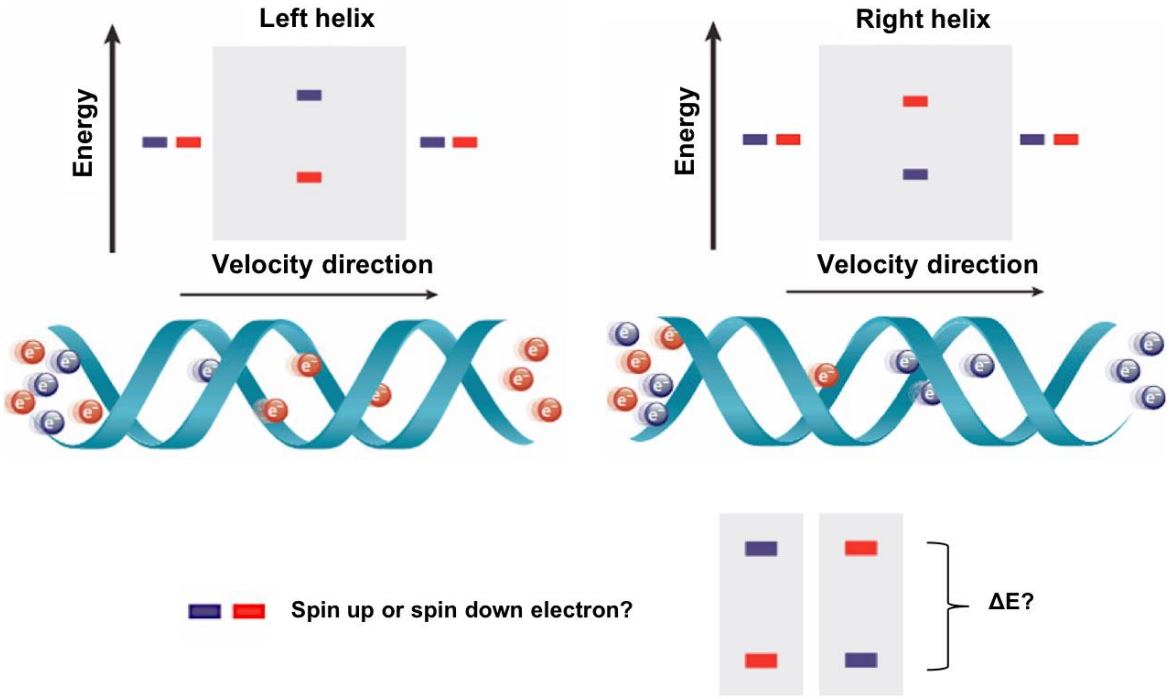

Figure I.2. Schematic of the chiral-induced spin selectivity effect. Electrons of opposite spin states (red and blue) are transmitted through chiral molecules (*e.g.* double-stranded DNA, shown above) more easily in one direction *vs* the other depending on molecular handedness. My research aims to elucidate two important aspects of this phenomenon: identifying the preferred spin state in electron-chiral molecule interactions, and measuring the relative spin-dependent energy barriers to transmission through chiral molecules. Adapted with permission from ref 22. Copyright 2015 Annual Reviews.

This effective magnetic field induces energy splitting between the two otherwise degenerate spin states, preferentially aligning electron spin parallel or antiparallel to its linear momentum. Even when an external magnetic field is applied, no spin polarization is expected in the absence of spin-orbit interactions.[40] When the handedness of a molecule is reversed, the sign of the spin-orbit interaction changes, and the preferred longitudinal spin orientation of an electron transmitted through a chiral molecule should be reversed.

Still, the models that suggest filtering is a consequence of an intramolecular magnetic field from helix-induced spin-orbit coupling solely fail to explain many observations. For example, to account for the large photoelectron polarization consistent with experiments, the effective magnetic field must exceed a few hundred Tesla – over three orders of magnitude larger than any possible intramolecular field based on typical spin-orbit interactions in organic molecules.

Two important questions remain unanswered due, in part, to the lack of systematic investigations of parameters that may influence and enhance spin filtration by chiral molecules, as well as conflicting experimental results (Figure I.2, and Table I.1 in Section I.D.). First, given molecule handedness and electron propagation direction, which spin is preferentially transmitted? Second, what are the relative energy barriers to transmission of electrons with opposite spin through a chiral molecule? My thesis research aimed to answer both of these questions.

In this chapter, I provide a brief history of the discovery of the spin angular momentum of the electron during the advent of quantum mechanics, and define electron helicity, which is pertinent within the context of the work described herein. I provide an overview of how investigations of the CISS effect evolved into a fascinating and emergent

field of its own within the scope of organic spintronics. Finally, I conclude by describing the state of the field, and suggest ways in which experiments to study the CISS effect may evolve beyond mere observation of spin selectivity to understanding the mechanisms of polarization.

I.B. Electron Dichroism

I.B.1. The Spin of an Electron

In addition to their negative charge, electrons possess an intrinsic angular momentum attributed to a property known as spin, which gives rise to a magnetic dipole moment (μ) aligned opposite to the spin angular momentum vector (*S*). This value is quantized, and upon measurement, one of two possible spin states for a particular laboratory-defined axis is observed: spin up or spin down.

What is now known as the Stern-Gerlach experiment, envisioned in 1921[41] and conducted in 1922,[42,43] represents the first observation of quantization of magnetic moment associated with the electron spin, although it was not conceived for this purpose. This experiment was designed originally to test classical *vs* (old) quantum mechanical interpretations of the behavior of particles with *orbital* angular momentum, and resulting magnetic moment, within a magnetic field.[44] The observations, described below, resulted in a radical departure from the use of classical mechanics to describe magnetic phenomena at the atomic scale. Uhlenbeck and Goudsmit's postulate of the idea of an intrinsic *spin* angular momentum of an electron in 1925[45] (originally put forth by Compton in 1921,[46] but applied to line spectra fine structure interpretation by Uhlenbeck and Goudsmit[47]), led to the unintentional rejection of the old quantum theory as well.

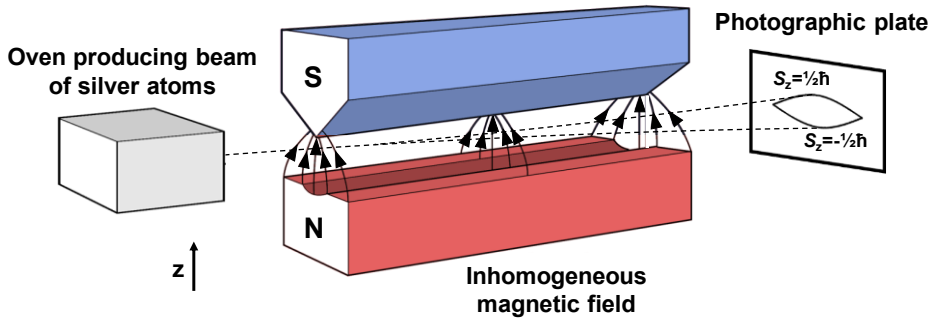

Figure I.3. Schematic of the Stern-Gerlach experiment.

In the Stern-Gerlach experiment, silver was heated in an oven with a small hole that allowed some gas-phase silver atoms to escape. The resulting beam of silver atoms passed through a collimator and was subjected to a perpendicularly oriented, inhomogeneous magnetic field in the z-direction (Figure I.3). Silver atoms are composed of a nucleus and 47 electrons; 46 electrons have paired spins and may be envisioned as a spherically symmetrical electron cloud with zero net orbital angular momentum, whereas the 47th (5s) electron has an intrinsic and uncompensated spin angular momentum (and as we know now, zero orbital angular momentum). Ignoring nuclear spin, each atom as a whole possesses a value of μ proportional to the spin of a single electron, S.

Atoms with the z-component of μ aligned parallel to the magnetic field ($\mu_z>0$, and therefore $S_z<0$) experienced a downward force while atoms with $\mu_z<0$ ($S_z>0$) experienced an upward force. Despite the atoms (and μ) being randomly oriented, the deflected atoms were split into two distinct components rather than a continuous dispersion (which is what would be expected from classical mechanics), indicating that only two possible values of S_z were possible: S_z up and S_z down.

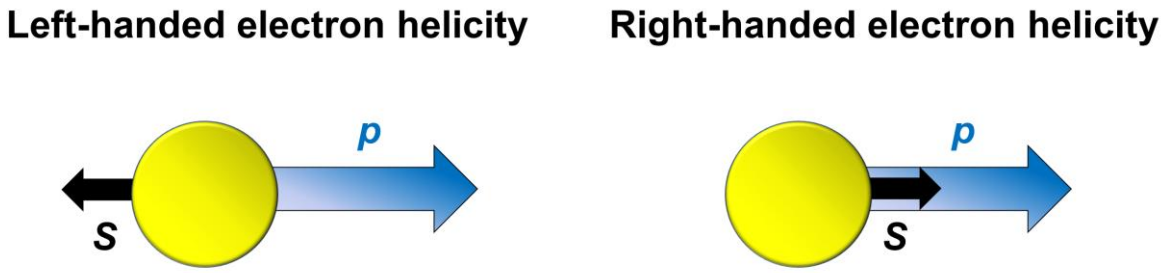

Figure I.4. Illustration of electron helicity. An electron is characterized as having left-(right-) handed helicity if the projection of the spin angular momentum, *S*, is aligned antiparallel (parallel) to the electron's momentum, *p*.

Within the context of the works described in this thesis, the spin of an electron may be used to define its handedness, or helicity, in relation to its motion. The helicity of an electron is the projection of the spin vector onto the momentum vector, *p*; an electron with right-handed helicity has the component of *S* along *p* oriented parallel to momentum direction, while for an electron with left-handed helicity, *S* and *p* point in opposite directions (Figure I.4). While not yet fully understood, it is now clear that the helicity of an electron and the handedness of a chiral molecule may dictate the transmission probabilities or tunneling efficiencies (depending on the charge transport regime) of electrons through chiral molecules.

I.B.2. Spin-Dependent Scattering of Polarized Electron Beams by Chiral Molecules

Analogous to the dissymmetric nature in which chiral molecules that possess optical activity absorb left- or right-handed circularly polarized light preferentially, that is, *circular dichroism*, it is thought that chiral molecules of opposite handedness would interact with electrons differently depending on the electron helicity. These ideas stemmed as a byproduct

from experimental investigations of enantioselective syntheses or decompositions of optical isomers using circularly polarized light to explain the origin of molecular asymmetry in living organisms. The experimental sources of circularly polarized radiation, chosen to reflect possible sources of circularly polarized light in Nature, were radioactive isotopes that undergo β-decay. This radioactive β^-- (β^+-)decay process where a neutron (proton) is converted to a proton (neutron) results in the emission of an electron (positron) and an antineutrino (electron neutrino), and sometimes bremsstrahlung, which is circularly polarized "secondary radiation".

Despite previous reports of insignificant differences in decay rates of one enantiomer *vs* another,[48-50] in 1968, Garay reported the positive observation of enantioselective destruction of *D*- or *L*-tyrosine in basic solutions by β-particles from strontium-90, and suggested that there may be a spin dependence in the interaction between polarized electrons and chiral species.[11] However, subsequent experiments that were designed to test this hypothesis were inconclusive.[51,52] In 1980, Farago extended this thinking to a generalized theoretical formalism to predict that electron scattering from optically active molecules should be accompanied by (albeit small) spin polarization, an observation that would not be observed with achiral species. This phenomenon was called *electron dichroism*.[53]

While previous attempts were unsuccessful,[54] in 1985, Campbell and Farago reported spin-dependent electron scattering from randomly-oriented gaseous *D*- and *L*-camphor molecules.[55,56] These experiments were designed to measure the attenuation and polarization of beams of longitudinally-polarized photoelectrons from a gallium arsenide (GaAs) source through vapor of the optically active molecules. This asymmetric scattering

was expected due to different elastic forward scattering amplitudes that may depend on the handedness of the target molecules. Transmission asymmetry, A, was defined as:

$$A = \frac{I(P) - I(-P)}{I(P) + I(-P)} \quad (1)$$

where $I(P)$ and $I(-P)$ represent the intensities of transmitted electrons with spin polarization aligned parallel (right-handed electron helicity) or antiparallel (left-handed electron helicity) to the beam axis. Using electrons with kinetic energies of 5 eV, transmission asymmetries of $A(D)$ = 23 ± 11 × 10^{-4} and $A(L)$ = -50 ± 17 × 10^{-4} were calculated for *D*- and *L*-camphor molecules, respectively.

Still, these results could not be reproduced. In 1995, Mayer and Kessler reported, using a similar experimental setup, with smaller measurement uncertainties, and for multiple electron kinetic energies between 0.5 and 10 eV, *no* transmission asymmetry that differed from zero (by >3×10^{-5}) nor chirality-induced spin polarization (irrespective of electron energy or handedness of camphor isomers).[12] However, the incorporation of high atomic number (Z) atoms in camphor-lanthanoid complexes (Figure I.5) and in bromo- and dibromocamphor resulted in the positive experimental verification of electron dichroism.[12-14] These results were in agreement with theoretical predictions that scattering asymmetries from randomly oriented chiral molecules should only be observed for species that contain high-Z atoms.[57]

Surprisingly, spin-dependent interactions between electrons and common biological molecules composed of low-Z atoms have since been confirmed with electron transmission asymmetries that are 10,000 times larger than those observed for optically active molecules in the gas phase.[15-17] Such large electron polarization has been achieved by adsorbing

molecules on surfaces, thereby imparting orientation to enhance and to focus asymmetry in scattering of low kinetic energy electrons through chiral molecule assemblies. In the following section, I highlight the experiments that led to the discovery and verification of electron dichroism by surface-bound chiral molecule species, a phenomenon that has evolved into what is now referred to as the CISS effect.[44]

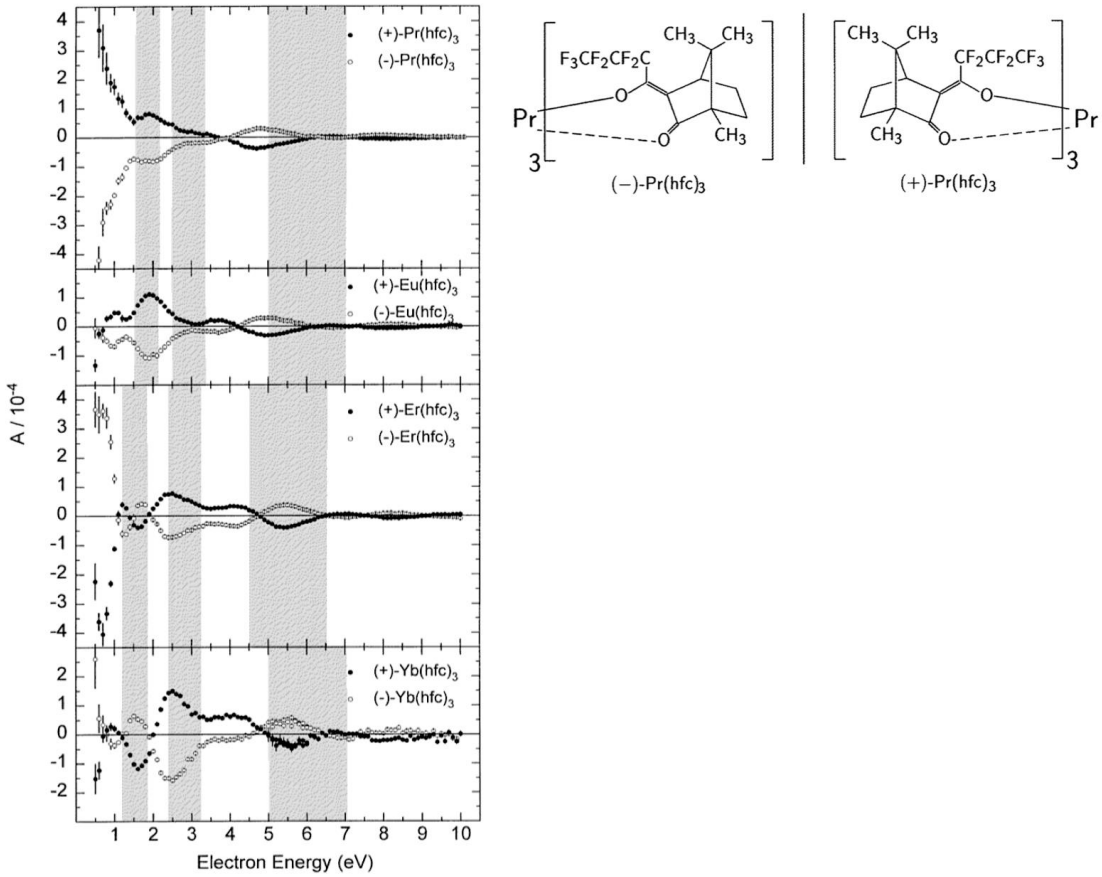

Figure I.5. Transmission asymmetry, *A*, in the transmission of spin-polarized electron beams through vapor of (+)- (black circles) and (-)- (white circles) camphor-lanthanoid complexes as a function of electron kinetic energies. Representative chemical structures of metallo-organic hydrofluorocarbon (hfc) derivatives of camphor with praseodymium are shown on the right. Reproduced with permission from ref 14. Copyright 1997 IOP Publishing Ltd.

I.C. Experimental Demonstrations of Chiral-Induced Spin Selectivity by Chiral-Molecule Assemblies

I.C.1. Photoelectron Spin Filtering by Organized Films of Chiral Molecules

While dissymmetric scattering of spin-polarized electron beams by enantiomers in the gas phase could only be confirmed using camphor derivatives functionalized with heavy atoms, theoretical investigations predicted that larger asymmetry in scattering could be obtained from oriented molecules composed of atoms with low atomic spin-orbit coupling strengths.[59,60] Work led by Naaman and Waldeck demonstrated this effect for the first time by measuring asymmetric scattering of polarized electrons through Langmuir-Blodgett films of either *L*- or *D*-stearoyl lysine on gold (Au) substrates (Figure I.6a).[15] Photoelectron transmission was tested through enantiomerically pure multilayers (5*L* or 5*D*) films, mixed layers (*i.e.*, 3*L*2*D* or 3*D*2*L* and 1*L*2*D*2*L* or 1*D*2*L*2*D*), and 5*L* films where each layer was doped with 1% *D*-stearoyl lysine. Spin-polarized photoelectrons were ejected from Au surfaces using left- or right-handed circularly polarized light[61,62] from a 247 nm ultraviolet (UV) light source and the intensities of collected photoelectrons were compared for each of the above conditions.

The electron energy distributions that were measured showed increased yields of photoelectrons collected through 5*L* films when surfaces were irradiated with right-handed circularly polarized light *vs* left-handed circularly polarized light (Figure I.6b); the opposite trend was observed using 5*D* films.[15] Films containing mixed layers of *D*- and *L*-stearoyl lysine were similar to one another and showed lower electron transmission probability than films of pure multilayers. Interestingly, in 5*L* films doped with 1% *D*-stearoyl lysine impurities, the effect disappeared, and no dependence of the photoelectron transmission

yield on light polarization could be measured (Figure I.6c). This observation, and the overall enhancement of spin selectivity in electron transmission probabilities through organized films of chiral molecules *vs* dilute molecule vapors, is hypothesized to be attributed to the interaction of the wavefunctions of transmitted electrons with multiple molecules simultaneously.

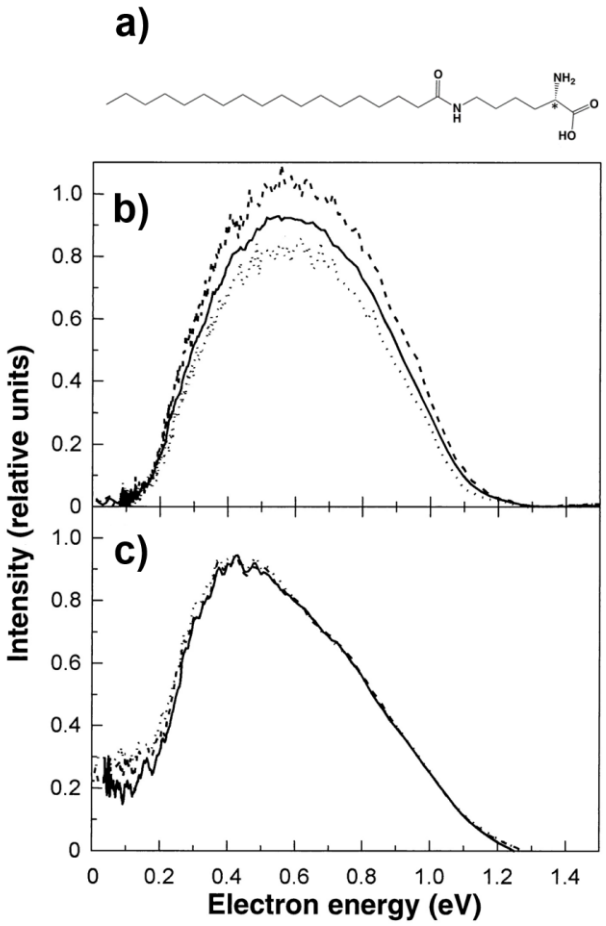

Figure I.6. (**a**) Chemical structure of *L*-stearoyl lysine. (**b**) Electron energy distribution of photoelectrons from Au surfaces coated with 5 Langmuir-Blodgett layers (5*L*) of *L*-stearoyl lysine and (**c**) 5*L* films of *L*-stearoyl lysine where each layer was doped with 1% *D*-stearoyl lysine. Photoelectrons were ejected using right-handed (clockwise) circularly polarized light (dashed lines), left-handed (counter-clockwise) circularly polarized light (dotted lines), or linearly polarized light (solid line). Reproduced with permission from ref 15. Copyright 1999 American Association for the Advancement of Science.

Naaman and coworkers subsequently performed analogous experiments with self-assembled monolayers (SAMs) of single-stranded or double-stranded deoxyribonucleic acid (DNA) attached to Au surfaces *via* thiolated tethers due to the formation of robust gold-sulfur (S) bonds.[16] Single-stranded DNA (ssDNA) molecules are chiral due to the deoxyribose sugars (*D*-form) within the phosphodiester backbone, while the hierarchically more complex structures of double-stranded DNA (dsDNA) duplexes exhibit higher order chirality due to the double-helical nature of the hybridized forms. No dependence of the polarization of light was observed in the electron energy distribution from photoelectrons transmitted through SAMs of ssDNA. To explain these observations, the authors suggest that while chiral, the ssDNA molecules lack a rigid helical structure and films are much less organized resulting in no measureable spin selectivity.

However, in the case of dsDNA SAMs, a higher transmission efficiency of photoelectrons was detected by irradiation *via* left-handed circularly polarized light *vs* right-handed circularly polarized light. Naaman and coworkers later measured explicitly the spin polarization of photoelectrons emitted from Au surfaces coated with SAMs of dsDNA molecules using a Mott polarimeter (Figure I.7a).[17] The spin polarization was measured parallel to the surface normal for each substrate; that is, the electron spin angular momentum vector of photoelectrons was measured to be parallel (S_z up, right-handed helicity) or antiparallel (S_z down, left-handed helicity) to the axes of nominally vertically aligned dsDNA helices in the SAMs.

Using linearly polarized light, which results in initially unpolarized photoelectron populations, increasingly negative spin polarization of collected photoelectrons was measured with increasing lengths of the DNA helices, with polarization of *ca*. -60% for SAMs

of double-stranded DNA composed of 78 base pairs (*ca*. eight helical turns) (Figure I.7b). Spin polarization (P) is defined as:

$$P = \frac{N_{\uparrow} - N_{\downarrow}}{N_{\uparrow} + N_{\downarrow}} \tag{2}$$

where $N_{\uparrow}$ and $N_{\downarrow}$ represent the number of spin up and spin down electrons within a population, respectively. The negative sign of the polarization observed by Naaman and coworkers indicates that the preferred spin of transmitted electrons was aligned antiparallel to the initial velocity direction (left-handed helicity).

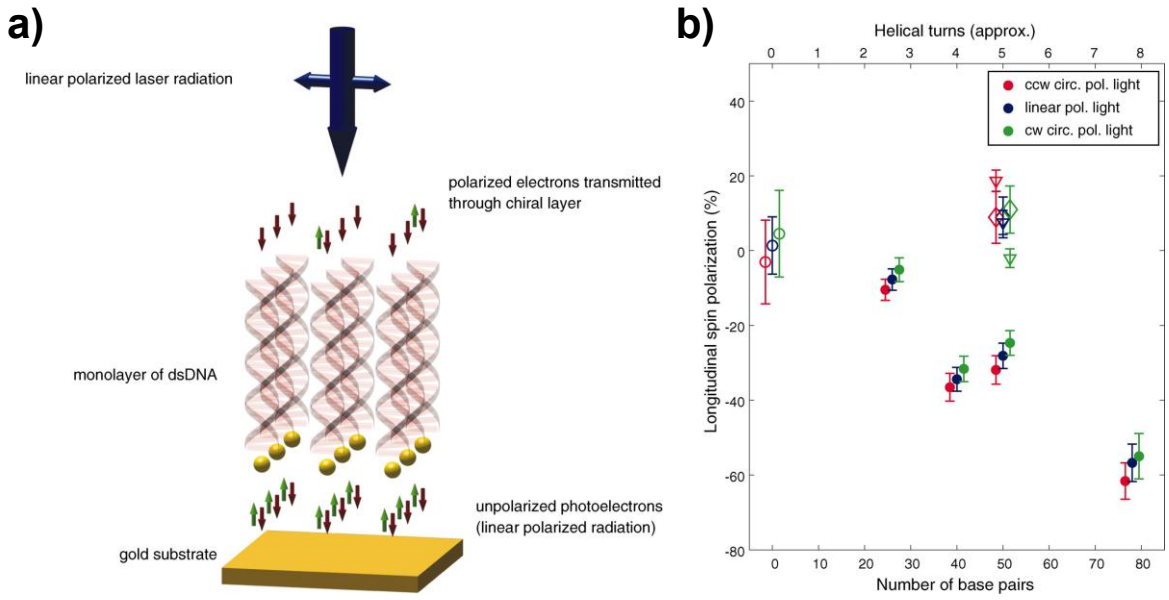

Figure I.7. (**a**) Schematic illustrating double-stranded DNA (dsDNA) self-assembled monolayers (SAMs) as a photoelectron spin filter. (**b**) Longitudinal spin polarization of photoelectrons as a function of DNA length. Open circles represent bare Au surfaces. Closed circles represent Au surfaces functionalized with dsDNA SAMs. Open diamonds represent Au surfaces functionalized with single-stranded DNA SAMs. Open triangles represent Au surfaces functionalized with dsDNA SAMs damaged with ultraviolet radiation. Photoelectrons were ejected using left-handed (counter-clockwise) circularly polarized light (red), linearly polarized light (blue), or right-handed (clockwise) circularly polarized light (green). Reproduced with permission from ref 17. Copyright 2011 American Association for the Advancement of Science.

Importantly, these measurements, and those described below, were all performed at *room temperature*. The generation and manipulation of spin-polarized electrons are typically associated with inorganic materials with large spin-orbit coupling strengths and cryogenic conditions, yet the observed spin polarization by double-stranded DNA SAMs was comparable to the magnitude of polarization obtained *via* photoemission from InGaAs using circularly polarized light (*ca*. 70-80%).[63] Similar experiments to measure the spin polarization of photoelectrons transmitted through chiral molecule assemblies have since been performed using films of proteins such as bacteriorhodopsin embedded within lipid bilayers,[64] monolayers of α-helical peptides,[65] and most recently, helicenes.[66] Together, these results suggest that chiral molecule films may be applied as efficient room-temperature electron spin filters and serve as sources of polarized electrons for either spintronics applications or to facilitate enantioselective chemistries.[67,68]

I.C.2. Spin-Dependent Conduction and Charge Transfer through Chiral Molecules

Compared to over-the-barrier electron transmission in photoemission studies, when electrons are confined to move within helical electrostatic potentials in hopping or tunneling, the supposed mechanisms of spin filtration appear to be different as indicated by more efficient conduction by electrons of opposite helicity. As an example, using conductive atomic force microscopy (AFM), the conductance through isolated DNA molecules assembled on nickel (Ni) was measured (Figure I.8a).[69] The magnitude of the current was shown to depend on the magnetization direction of the underlying Ni, dictated by a permanent magnet placed underneath the substrates with poles oriented parallel or antiparallel to the surface normal. While the DNA acts as a spin filter, invariant of an external magnetic field, charge injection

into or out of ferromagnetic (FM) materials such as Ni is spin dependent, resulting in different conductances when the substrates were magnetized up *vs* down. In these experiments, larger currents through right-handed double-stranded DNA helices were observed when the magnetization of the substrate was oriented down (Figure I.8b), an effect that increased with the length of DNA. Thus, the spin angular momentum of electrons within the majority (minority) spin subbands of the Ni substrates were oriented up (down) under this condition, indicating that the right-handed DNA molecules preferentially transmitted electrons with right-handed helicity, compared to left-handed helicity as measured in photoemission experiments.

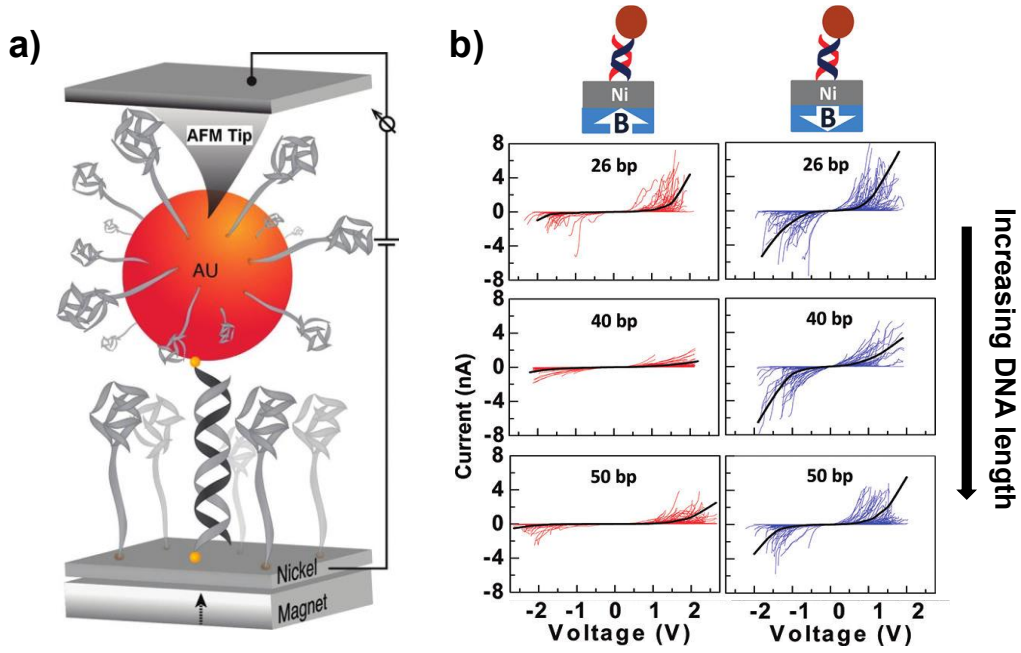

Figure I.8. (**a**) Experimental setup in which current through double-stranded DNA junctions is measured by applying a bias between a conductive atomic force microscopy (AFM) tip and a ferromagnetic substrate. Metallic Au nanoparticles were used to make electrical contact to the DNA molecules. (**b**) Current as a function of applied bias when substrates were magnetized up *vs* down with an externally applied magnetic field when functionalized with double-stranded DNA with increasing numbers of base pairs (bp). Reproduced with permission from ref 69. Copyright 2011 American Chemical Society.

While measurements of current through chiral molecules in which one electrode or contact is a FM material provides direct verification of suppression or enhancement of charge transfer through the molecular junctions,[70-74] many creative experimental designs have demonstrated ways to observe the CISS effect *via* indirect techniques. Mondal *et al*. demonstrated the capability of using emission from quantum dots (QDs) tethered to FM substrates *via* chiral linkers as an indirect method to probe spin selectivity in competitive charge transfer to the substrates upon photoexcitation (Figure I.9a).[75] Molecular assemblies of α-helical oligopeptides were prepared on top of FM substrates composed of multilayer stacks of cobalt (Co) and platinum (Pt) and capped with a thin layer of Au to minimize oxidation and to facilitate binding of the oligopeptides to the surface *via* Au-sulfur (S) bonds. Cadmium selenide (CdSe) QDs were chemically attached to the free terminal amines on the *N*-termini of bound oligopeptides. Spin-dependent photoluminescence measurements were performed by placing a permanent magnet directly underneath the functionalized substrates. Again, the magnetic field direction was changed between "up" or "down" orientations by rotating the underlying magnet by 180°.

Upon photoexcitation, CdSe QD holes were selectively transferred to the FM substrates (electrons from the surfaces to the CdSe QDs) *via* the chiral oligopeptide tethers. As a result, the photoluminescence intensity, which depends on the probability of radiative electron-hole recombination, was dependent on the direction of the injected spin from the FM substrates (Figure I.9b). The oligopeptides acted as spin filters, and exhibited spin dependence in the charge transfer process, preferentially transmitting spin-down electrons injected from the FM substrate. Under "field up" conditions, charge transfer and radiative recombination are suppressed, and photoluminescence intensities are partially quenched.

In contrast, when CdSe QDs were attached to the FM substrates by achiral SAMs of 4-aminophenol, biphenyl-4,4'-dithiol, or 1,16-hexadecanedithiol molecules, there was no dependence of the photoluminescence on the external magnetic field direction (Figure I.9c-e).

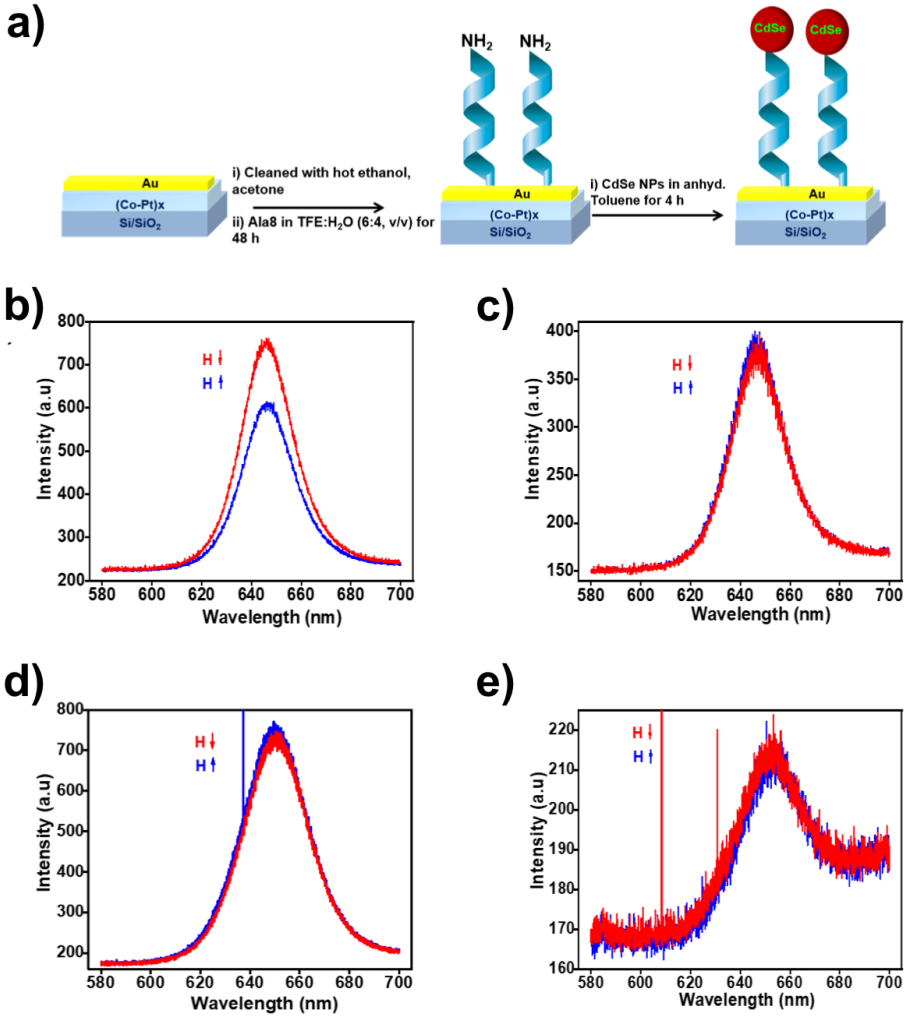

Figure I.9. (**a**) Surface functionalization strategy to tether sequentially α-helical oligopeptides (Ala8) and cadmium selenide (CdSe) quantum dots (QDs) to Au-coated ferromagnetic (FM) multilayer stacks of cobalt (Co) and platinum (Pt) on Si/SiO_2 substrates. (**b**) Photoluminescence intensity from CdSe QDs bound to FM films by Ala8 when substrates were magnetized up *vs* down with an external magnetic field (H) using a green laser at 514 nm. (**c**) Identical measurements in which CdSe QDs were tethered to FM films by achiral self-assembled monolayers of 1,16-hexadecanedithiol, (**d**) biphenyl-4,4'-dithiol, and (**e**) 4-aminophenol. Reproduced from ref 75. Copyright 2016 American Chemical Society.

In a second example of investigating the CISS effect indirectly through photoluminescence measurements, Roy *et al*. demonstrated that films of wild-type bacteriorhodopsin-CdSe assemblies bound within lipid membranes were formed on FM Ni substrates (Figure I.10a).[76] Using experiments analogous to those described above, spin-dependent electron transfer was observed from the Ni substrates to holes within the photoexcited CdSe NPs *via* a retinal in the purple membrane wild-type bacteriorhodopsin protein (Figure I.10b). The photoluminescence intensity was affected by the orientation of an external magnetic field used to magnetize the Ni substrates up or down, which was hypothesized to be due to spin-filtering by the protein that contains multiple, parallel α-helical subunits.

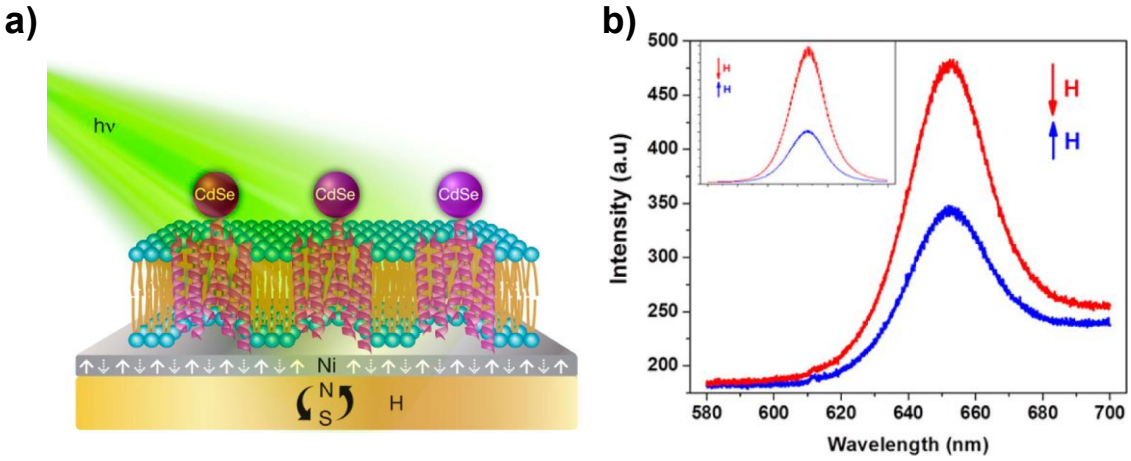

Figure I.10. (**a**) Schematic of an experimental setup to measure photoluminescence intensity from cadmium selenide (CdSe) quantum dots (QDs) tethered to bacteriorhodopsin assemblies bound within lipid membranes on ferromagnetic (FM) nickel substrates. (**b**) Photoluminescence intensity from CdSe QDs in which the FM substrates were magnetized up *vs* down with an external magnetic field (H) using a green laser at 514 nm. The inset displays the maximum difference in photoluminescence observed between magnetic field orientations. Reproduced from ref 76. Copyright 2016 American Chemical Society.

These and other observations of spin-dependent charge transfer through proteins are particularly exciting because of the possible biological implications that relate spin and chirality in electron transfer processes in Nature.[64,77,78] Still, additional measurements and new experimental designs are necessary to investigate spin selectivity in charge transfer through proteins within native environments as opposed to being adsorbed on planar substrates.

Indeed, all of the aforementioned experimental frameworks used external magnetic fields and FM materials to probe spin-dependent charge transfer and conductance due to the spin-valve-like combinations of chiral molecule spin filters and preferential spin alignment in charge injection (ejection) into (from) FM surfaces. However, recent work by Waldeck and co-workers demonstrated chiral-dependent fluorescent lifetimes in QD dyad assemblies through the use of circularly polarized light in an experimental design that circumvented the need for both FM surfaces and external magnetic fields.[66]

In these experiments, CdSe QDs were coated with the chiral ligands *D*- and *L*-cysteine, which imprinted them with a chiral signature (Figure I.11a,b). Chiral CdSe QDs were covalently tethered to achiral donor cadmium telluride (CdTe) donor QDs to form a QD charge-transfer dyad with a chiral bridge. These QD dyads were then electrostatically adsorbed on positively charged SiO_2 microbeads. Microbeads with slower rates of rotational averaging due to their significantly larger size oriented the QDs with respect to the incident light, such that QDs on the front side of the microbeads were illuminated more strongly than QDs on the back side. This asymmetric irradiation enabled the photoexcited charge carrier population to be spin polarized within a laboratory-defined axis.

Alternatively exciting the system with circularly polarized incident radiation, the achiral CdTe donor QDs generated unequal populations of spin-up and spin-down excited state electrons due to conservation of angular momentum. Fluorescence lifetime measurements were conducted to monitor the duration of the CdTe excited state generated upon light absorption, which is dependent on the energy barrier to charge transfer from the donor to the acceptor QD through the chiral bridge. A lower barrier to charge transfer leads to increased fluorescence quenching and a lowered lifetime, and *vice versa*. Due to the chiral nature of the linker, the charge transfer barrier is spin selective.

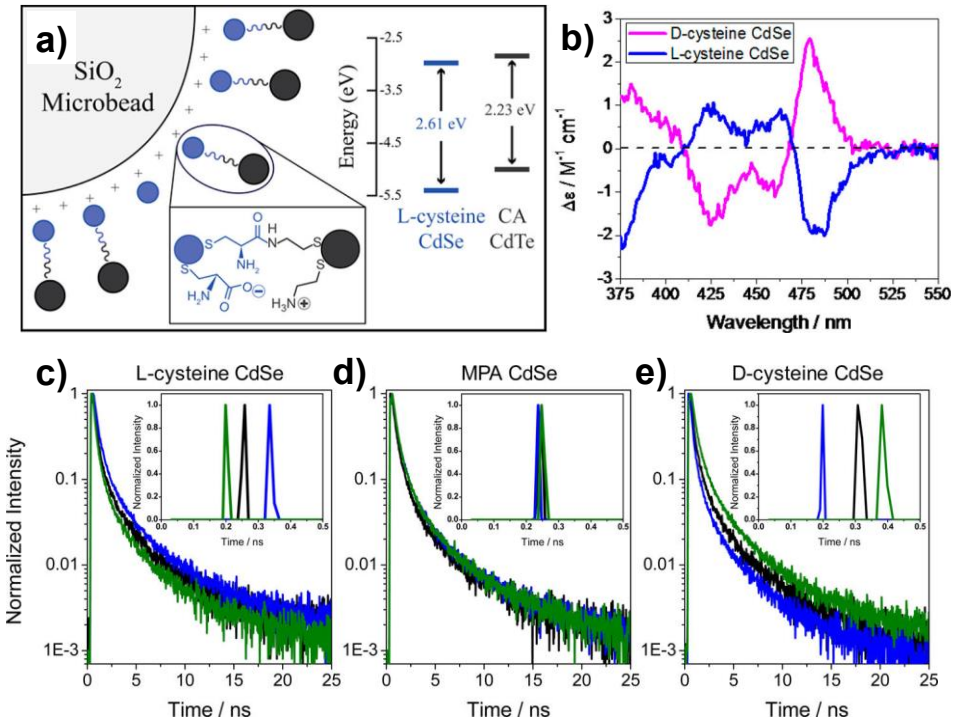

Figure I.11. (**a**) Schematic depicting the electrostatic adsorption of cadmium selenide (CdSe) – cadmium telluride (CdTe) quantum dot (QD) charge-transfer dyad assemblies on SiO_2 microbeads. (**b**) Circular dichroism spectra demonstrating the chiral imprinting of CdSe QDs with *D*- and *L*-cysteine capping ligands. (**c-e**) Representative photoluminescence decays of chiral and achiral (using mercaptopropionic acid, MPA) QD assemblies excited using right-handed (clockwise) circularly polarized light (blue), left-handed (counter-clockwise) circularly polarized light (green), or linearly polarized light (black). Insets show lifetime distributions. Reproduced with permission from ref 79. Copyright 2017 American Chemical Society.

Using this methodology, Bloom *et al.* were able to measure dissymmetric charge transfer lifetimes that depended on both the chirality of the linker and the polarization of the incident light. Using *L*-cysteine linkers, the fluorescent lifetimes of the dyads were enhanced when illuminated with clockwise circularly polarized light, and suppressed when illuminated with counterclockwise circularly polarized light (*vs* lifetimes measured upon illumination with linearly polarized light) (Figure I.11c). No dependence was observed using achiral mercaptopropionic acid linkers (Figure I.11d), and the opposite trend was observed if the acceptor QD was instead capped with *D*-cysteine (Figure I.11e). The experiments demonstrate the sensitivity of fluorescence lifetime measurements in elucidating spin-selective charge transport in chiral fluorescent assemblies, which may provide more detailed information on the unexplored relative energy barriers to spin-flip transitions in chiral electrostatic potentials.

I.C.3. Spin Dependence in Electrochemical Reactions

Magnetic field effects in electrochemistry have been investigated for decades.[80-82] However, many of these observations have been attributed to Lorentz or Kelvin forces. The Lorentz force describes the force from magnetic fields acting on a freely moving point charge (such as an electron or ions), which has been used to explain the interactions between the external fields and local electric current density.[83] The Kelvin force due to magnetic field gradients acts directly on paramagnetic species in electrolyte solutions to influence local concentration gradients near electrode surfaces.[84] Additional magnetic field effects on electrochemical reaction rates and on the kinetics of electron transfer of radical pairs have been reported and are well studied.[85,86]

Electrodes with enantioselectivity toward chiral targets have also been developed that show different reaction rates between isomers in redox processes, which demonstrate promising avenues toward green enantioselective chemical syntheses and determination of enantiopurity.[87,88] Typically, this selectivity is accomplished by the use of magnetic fields to tune the morphology of electrodeposited films,[89] by adsorbing chiral molecules directly on electrode surfaces,[90] or by imprinting polymer coatings with chiral molecules[91] resulting in larger steric hindrance of left- or right-handed analytes for binding to electrode surfaces. However, until recently, the spin polarization of Faradaic currents, which may result from chiral molecule-modified electrodes, has not been considered.[92]

Importantly, compared to aforementioned studies of the CISS effect in photoemission and conduction with molecules under dry and ultrahigh vacuum conditions, investigating spin selectivity in charge transfer reactions that occur in solution or under physiological conditions will be critical to assess possible biological significance of the CISS effect. Electrochemical techniques present convenient methods to study these effects and enable the investigation of redox reactions that occur between free or tethered analytes and hydrated chiral biomolecules assembled on FM electrodes.

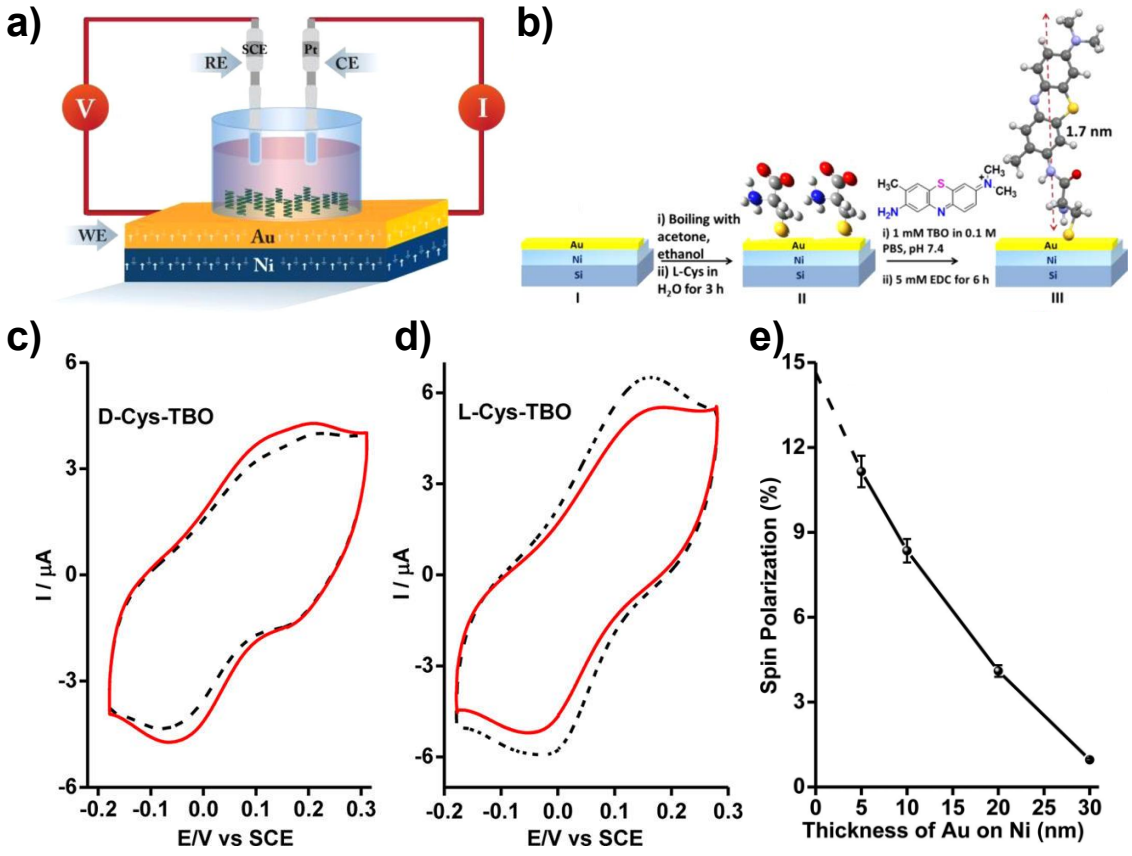

Figure I.12. (**a**) Schematic of electrochemical cell using a saturated calomel electrode (SCE) as a reference electrode (RE), a Pt wire as a counter electrode (CE), and a Au-coated Ni substrate as a working electrode (WE). Current (I) between the WE and CE is measured while the potential (V) between the WE and RE is varied. (**b**) Surface functionalization strategy to tether subsequently *L*- or *D*-cysteine and the redox-active dye, toluidine blue O (TBO) to WE surfaces. (**c**) Representative cyclic voltammograms of TBO reduction and oxidation when an underlying magnetic field is oriented up (dashed black cure) or down (solid red curve) to magnetize the Au/Ni functionalized with *L*- or (**d**) *D*-cysteine tethers. (**e**) Spin polarization by *L*-cysteine, calculated as the difference between peak currents measured when substrates are magnetized up *vs* down, divided by their sum, as a function of the thickness of the Au capping layer. Reproduced from ref 93. Copyright 2015 American Chemical Society.

Naaman and coworkers reported that redox reactions are sensitive to electron spin orientation in experiments that used ferromagnetic Ni electrodes coated with varying thicknesses of Au.[93] The Au capping layers are necessary due to facile oxidation of the underlying FM materials in electrolyte solutions and to enable the formation of robust SAMs

of thiolated molecules. In one experiment, Au surfaces were functionalized with the achiral redox active dye toluidine blue O *via* chiral cysteine tethers (Figure I.12a,b). The magnitude of the cathodic and anodic currents were used to compare charge transfer efficiencies dependent on the handedness of the cysteine tether and the magnetization orientation of the Ni electrode modulated parallel or antiparallel to the surface normal with a permanent magnet underneath the substrates (Figure I.12c,d). In the same work, cytochrome *c*, a globular protein with well-known redox chemistry, was electrostatically adsorbed on Au-coated Ni electrodes functionalized with achiral SAMs of alkanethiols.[93] Surprisingly, despite the random orientation of proteins within the adsorbed layer, spin polarization effects were observed to be larger than 30% compared to substrates functionalized with chiral cysteine tethers bound directly on the Au surfaces.

An important experiment that the authors performed was measuring the dependence of the spin polarization effect on the thickness of the Au capping layer ranging from 5-30 nm (Figure I.12e). The difference in current measured when the Ni substrates were magnetized up *vs* down was found to decrease as the thickness of the Au layer increased. This result is attributed to the large spin-orbit coupling of the Au which depolarizes the injected charge at the Ni/Au interface, and confirms the necessity for ultrathin Au capping layers to immobilize molecular films on easily oxidized FM substrates.

Using similar experimental setups, Barton and coworkers demonstrated helix-dependent spin filtering through hydrated DNA duplexes using Ni working electrodes capped with a 10 nm layer of Au, and functionalized with double-stranded DNA SAMs (Figure I.13a).[94] The efficiency of reduction of a redox probe, methylene blue (MB^+, which intercalates within the duplexes, and is therefore well-coupled to the base stacks – a

necessity for DNA-mediated charge transfer), and thus the efficiency of DNA-mediated charge transfer, was found to be higher when substrates were magnetized up (magnetization parallel to the surface normal) *vs* down for right-handed, B-form DNA (Figure I.13b). When the helicity of the DNA within the SAMs was reversed to the left-handed, Z-form, with the addition of magnesium chloride to the electrolyte solutions, the spin selectivity was reversed. This reversal led to higher cathodic currents attributed to MB^+ reduction when the substrates were magnetized down (Figure I.13c).

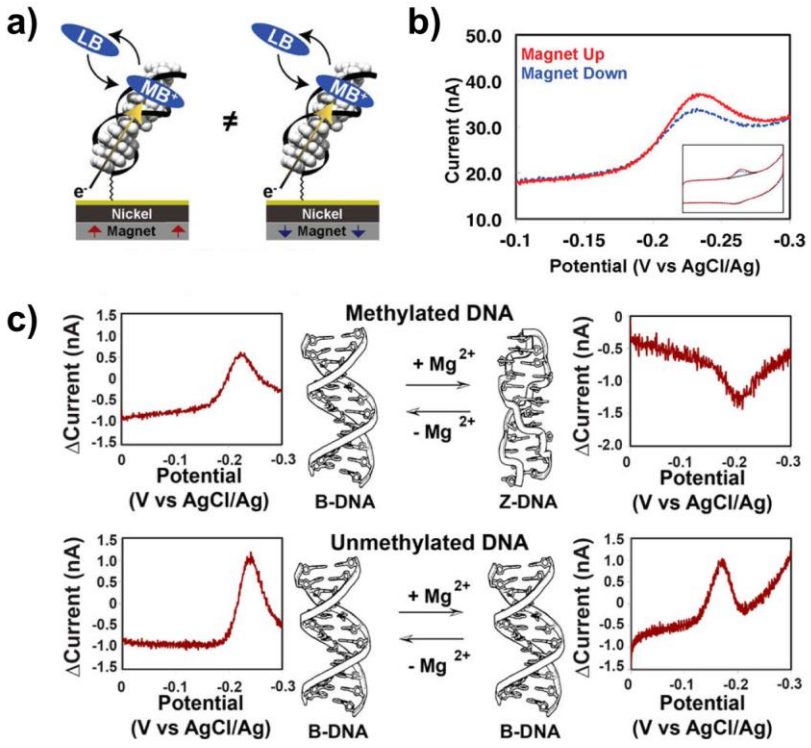

Figure I.13. (**a**) Schematic of reversible reduction of methylene blue (MB^+) to leucomethylene blue (LB) noncovalently bound to double-stranded DNA assembled on Au-capped nickel working electrodes used in electrochemical experiments. (**b**) Represenative cathodic peak region of a cyclic voltammogram of MB^+ reduction when an external magnetic field is applied up (red) *vs* down (blue) to magnetize the underlying nickel substrate. Inset shows the full voltammogram. (**c**) Differences in current obtained by subtracting cathodic scans obtained for substrates magnetized down from up conditions when working electrode surfaces are functionalized with double-stranded DNA containing methylated cysteine. High salt conditions in the electrolyte obtained by the addition of magnesium (Mg^{2+}) induced conformational change from right-handed B-DNA to left-handed Z-DNA, resulting in a reversal of spin selectivity in the measured current. Reproduced with permission from ref 94. Copyright 2016 American Chemical Society.

Thus, the supramolecular organization of the DNA duplexes was found to dictate the spin polarization in charges that propagate along the π-stack, as opposed to the handedness of the individual monomeric sugars within the phosphodiester backbone that remain unchanged in the conformational rearrangement from B-form to Z-form. This observation is interesting because similar deliberation of results must be considered in other systems, namely, right- (left-) handed α-helical peptides that are composed of "left- (right-) handed" amino acid monomers. Competing mechanisms may exist in different charge transport regimes in which the wavefunction of transmitted electrons interacts with individual chiral centers *vs* the helical secondary or tertiary structure of molecules.

I.D. Challenges and State of the Field

In addition to molecular handedness and electron helicity, system-dependent factors may influence experimental observations. These factors include the relative density of states of majority and minority electrons within FM materials, as well as externally applied bias[37] and/or intrinsic electric dipole orientations within molecules.[95]

Definitive observations of the CISS effect can be impeded by measurement variability under ambient pressure and temperature conditions. These challenges confound the fundamental understanding of enhanced *vs* suppressed charge transfer, for instance, at molecule-FM metal interfaces. Thus, identifying the preferred helicity for electrons confined to move along chiral potentials, such as hopping or tunneling along a helical molecule, has proven to be difficult, with conflicting experimental studies regarding the preferred polarization orientation.

Preferred electron helicities reported in transmission through various chiral molecule systems are listed in Table I.1. Where spin polarization of transmitted electrons is not explicitly measured, I assume that majority (minority) spin electrons are preferentially ejected (injected) from (into) FM substrates or probe tips. Experimental reports that agree or disagree with theoretical predictions of preferred electron helicity are highlighted in blue and orange, respectively; that is, that for right-handed helical molecules, right-handed electron helicity is selected for in bound-electron transfer, while left-handed electron helicity is preferred in over-the-barrier transmission (and *vice versa* for left-handed molecules).[31,36,38]

The preferred spin polarization determined from theoretical models has also been inconsistent.[24] Adoption of the aforementioned predictions as the "correct" relationship between molecule and electron helicity in charge transport was chosen based on the agreement with my own experimental results, but otherwise picked simply to enable discrimination of experimental works that report opposite trends. Furthermore, no established theoretical models have been made for spin selectivity in transmission through molecules of *D*-/*L*- without hierarchical helical structure or *M*-/*P*- convention, so, I group *D*- and *P*-enantiomers with right-handed helices; and *L*- and *M*-enantiomers with left-handed helices.

Table I.1: Preferred electron helicity in charge transport determined from various experimental systems.

Chiral Molecule	Enantiomer	Experimental System	Charge Transport Regime	Preferred Electron Helicity	Ref.
Single-stranded DNA	*D*-form (deoxyribose in nucleotides)	SAMs on Au	Photoemission	None	16,17
	D-form (deoxyribose in nucleotides)	SAMs on Au/Ni	Electrochemical charge transfer	None	94
Double-stranded DNA	Right-handed double helix	SAMs on Au	Photoemission	None	96
	Right-handed double helix	SAMs on Au	Photoemission	Left	16,17
	Right-handed double helix	SAMs on Ni, NM tip	Conduction (AFM)	Right	69
	Right-handed double helix	SAMs on Ag/AlO_x/Ni	Photoexcited charge transfer	Right	97
	Right-handed double helix	SAMs on Au/Ni	Electrochemical charge transfer	Left	94
	Right-handed double helix	SAMs on Au/(Co/Pt)	Photoexcited charge transfer	Right	98
α-helical oligopeptide	Right-handed helix (*L*-form amino acids)	SAMs on Au	Photoemission	Left	65
	Right-handed helix (*L*-form amino acids)	SAMs on Ni	Electrochemical charge transfer	Left	65
	Right-handed helix (*L*-form amino acids)	SAMs on Ni	Conduction (AFM)	Right	65,74
	Right-handed helix (*L*-form amino acids)	SAMs on Au, FM tip	Conduction (STM)	Right	73
	Left-handed helix (*D*-from amino acids)	SAMs on Au, FM tip	Conduction (STM)	Left	73
	Right-handed helix (*L*-form amino acids)	SAMs on Au/(Co/Pt)	Electrochemical charge transfer	Right	75
	Right-handed helix (*L*-form amino acids)	SAMs on Au/(Co/Pt)	Photoexcited charge transfer	Left	75
	Right-handed helix (*L*-form amino acids)	SAMs on Au/(Co/Pt)	Photoemission	Left	99
	Left-handed helix (*D*-from amino acids)	SAMs on Au/(Co/Pt)	Photoemission	None	99
Cysteine	*D*-form	SAMs on Au/Ni	Electrochemical charge transfer	Right	93
	L-form	SAMs on Au/Ni	Electrochemical charge transfer	Left	93
	D-form	Functionalized QDs on HOPG, FM tip	Conduction (AFM)	Left	71
	L-form	Functionalized QDs on HOPG, FM tip	Conduction (AFM)	Right	71
Stearyol lysine	*L*-form	LB films on Au	Photoemission	Right	15
	D-form	LB films on Au	Photoemission	Left	15
Helicene	*M*-form (left-handed helix advancement)	SAMs on HOPG, FM tip	Conduction (AFM)	Right	72
	P-form (right-handed helix advancement)	SAMs on HOPG, FM tip	Conduction (AFM)	Left	72
	M-form (left-handed helix advancement)	SAMs on Cu, Ag, Au	Photoemission	Left	66
	P-form (right-handed helix advancement)	SAMs on Cu, Ag, Au	Photoemission	Right	66

SAM: self-assembled monolayer; FM: ferromagnetic; NM: non-ferromagnetic material; AFM: atomic force microscopy; STM: scanning tunneling microscopy; LB: Langmuir-Blodgett; HOPG: highly-ordered pyrolytic graphite; QD: quantum dot.

With few exceptions, nearly all experimental investigations of the CISS effect to date have relied on molecular self-assembly on planar metal or semiconducting surfaces, which do not mimic biological environments and complicates deconvolution of the role of the substrates in spin polarization.[31,66] In addition, the formation of SAMs on readily oxidized FM materials yield less well-packed and stable monolayers which presents challenges compared to functionalization of noble metal surfaces.[100] However, lack of experimental capabilities to measure absolute spin orientation of electrons explicitly under ambient conditions in typical experimental setups described above necessitates a laboratory-defined axis to assemble and to orient chiral molecules. Measurement and analysis of spin polarization effects attributed to the CISS effect without tethering molecules on planar substrates will circumvent these experimental difficulties and will bring us closer to understanding the role of electron spin in biologically-relevant systems, *e.g.* in charge transfer processes within membrane-embedded proteins and peptides.

There are some agreements between experimental results and theoretical predictions. First, the approximately linear dependence of the degree of spin polarization on the length of molecular helices including DNA and α-helical peptides that have been observed in many experimental systems is supported by theoretical models. Indeed, this behavior has been identified in both over-the-barrier photoelectron transmission and within conduction regimes.[17,65,69,74,94]

Second, the inverse relationship between radius to pitch ratio of a molecular helix and spin polarization has been demonstrated by magnetic conductive probe AFM with α-helical peptides, in agreement with theory. In these experiments, a FM AFM probe tip was used to apply increasing force to compress α-helical peptides assembled on Au substrates and the

current was measured as a function of bias between the tip and sample (Figure I.15a).[74] While the current increased with applied force, the spin polarization (the difference in current measured with the tip magnetized up *vs* down divided by the sum of these values) decreased. To test the interpretation of these results, additional experiments should be conducted. Electrochemical measurements to study spin dependence in DNA-mediated charge transport with right-handed A-DNA *vs* B-DNA, which contain different pitches, radii, and rise distances between bases, may provide additional insight into the relationship between molecular geometry and spin polarization.

However, while significant effort has been directed toward developing theoretical frameworks, these models also fail to explain many observations. These observations include the varying quantitative values of electron polarization, the spin-dependent charge polarization and magnetization effects due to proximity of chiral species,[101] and the inconsistencies in polarization direction for electrons transmitted through chiral molecules across various experimental systems.

Many other mechanistic questions remain unanswered. In photoelectron transmission through films of chiral molecules, what is the kinetic energy dependence of spin selectivity? Rosenberg *et al*. demonstrated using X-ray photoelectron spectroscopy from synchrotron radiation sources that photoelectrons ejected from Au core levels in dsDNA monolayer-functionalized Au with kinetic energies between 30 and 760 eV showed no dichroism upon excitation with left- *vs* right-handed circularly polarized light.[96] That is, the DNA films were unable to attenuate the transmission of electrons selectively with one spin *vs* another that were preferentially ejected using circularly polarized light.

Yet, Rosenberg *et al.* subsequently reported a higher quantum yield of dissociation for (*S*)- *vs* (*R*)-epichlorohydrin adsorbed on double-stranded DNA SAMs on gold substrates using photoelectrons produced using photon energies of 950 eV an 740 eV.[68] The enantioselective dissociations suggest the production of spin-polarized electrons due to spin filtering by the DNA films. However, the kinetic energy distribution of electrons with positive or negative helicity remains unclear.

In addition, while the parameters that influence DNA conductivity have been elucidated (without considering electron helicity),[102,103] the role of base sequence, guanine (G) and cytosine (C) content, DNA conformation and rigidity, and solvent on spin-dependent charge transfer through DNA duplexes have yet to be investigated experimentally. Further investigation into these molecular and environmental factors may provide insight into the experimental discrepancies observed; the modularity of DNA makes it an ideal system by which to test such parameters.

In particular, an interesting direction to pursue would be the comparison of the magnitude and polarization direction of spin-dependent DNA-mediated charge transport between duplexes containing alternating d(-GCGC-)$_n$ *vs* stacked d(-GGGG-)$_n$ base sequences.[104] Charge transport within DNA helices composed of these two sequences are characterized by incoherent hopping and coherent tunneling, respectively. Understanding how the efficiency of spin filtering affects charge transmission through chiral electrostatic potentials in these different regimes may be pertinent to the design and synthesis of organic molecule candidates for next generation spintronics devices.[19-21]

Ultimately, with the help of advanced theoretical models, elucidating these phenomena would benefit from systematically designed experiments in which the

characterization of spin selectivity for a particular system includes an assessment of the efficiency and reproducibility, and thus the viability, of a chiral molecule or assembly as a spin filter. Including data using both enantiomers is also desirable where applicable. Objectively evaluating these criteria, and subjecting measurements to proper statistical analyses to compare an experiment's figure of merit between measurement conditions (*i.e.*, magnetic field orientations when magnetizing FM substrates functionalized with chiral molecules) is essential.

I.E. Thesis Organization

In Chapter II, I describe our group's first published research in this field: the investigation of spin selectivity in DNA-mediated charge transfer using fluorescence microscopy to visualize indirectly spin-dependent charge transfer between organic dyes incorporated within double-stranded DNA and underlying FM substrates.[98] A hallmark of this work is the use of surface-patterned DNA microarrays that provide background measurements in every fluorescence image, enabling accurate determination of substrate magnetization-dependent emission. Moreover, the use of mathematical image segmentation algorithms developed by our group maximizes the quantity of data used in calculating relative fluorescence intensities and eliminates user bias when extracting quantitative information from images. Our robust analytical framework enables us to distinguish small, yet statistically significant, differences in relative fluorescence intensities. Thus, our methods are expected to also be of particular interest across disciplines in the discernment of minute differences in image processing and analysis.

In Chapter III, I detail the results of experiments to measure spin-dependent energy barriers to photoemission through chiral molecular films of left- and right-handed α-helical peptides, and of the protein, bovine serum albumin, which is composed of multiple α-helical subunits, assembled on FM substrates.[99] Calculated substrate magnetization-dependent differences in the work function (ionization energy) of the surfaces functionalized with chiral molecules, and therefore the energy barriers to photoemission, are of reasonable orders of magnitude considering the core atomic electric field strengths thought to influence spin-selectivity through spin-orbit coupling interactions. Further, while the spin polarization of photoelectrons transmitted through chiral molecule assemblies may be explicitly measured using specialized experimental methods (*i.e.*, the use of a Mott polarimeter), these experiments establish figures of merit to measure spin selectivity that can be assessed more easily by other research groups and compared with varying molecular systems.

In Chapter IV, I conclude and provide an outlook on possible biological implications and future applications of the spin-filtering capability of chiral molecules for next-generation spintronics applications. In addition, I describe how discoveries in this emerging field will lead to broader impacts across disciplines. These advances include understanding the roles of spin in enantioselective interactions between molecules which will enable the development of more efficient enantioselective separation strategies, chiral-selective electrochemical syntheses, and electrochemical reactions such as photo-catalytic water splitting for energy storage.

Finally, prior to immersing myself in the field of organic spintronics, my initial graduate studies expanded on work previously established by our group on the role of intermolecular and molecule-substrate interactions on photoswitching efficiencies of

azobenzene and dihydroazulene molecules tethered to Au surfaces.[105-108] I probed the isomerization of these molecules at the single-molecule and ensemble levels *via* scanning tunneling microscopy and surface-enhanced Raman spectroscopy, respectively. In the Appendix, I included a literature review on the state of the field (as of 2015) of molecular switches, rotors, motors, and machines.[109] I elaborate on the need for hierarchical organization of these molecules in one-, two-, and three-dimensions to perform work at the macroscale. This Review was my contribution to the fascinating and creative field of molecular machines prior to beginning the research that has become the subject of my dissertation.

References

1. Pasteur, M. L. Recherches sur les Relations qui Peuvent Exister entre la Forme Crystalline, la Composition Chimique et le Sens de la Polarisation Rotatoire. *Ann. Chim. Phys.* **1848**, 24, 442–459.

2. Gal, J. Molecular Chirality in Chemistry and Biology: Historical Milestones. *Helv. Chim. Acta* **2013**, 96, 1617–1657.

3. Pasteur, M. L. Mémoire sur la Fermentation Alcoolique, *C. R. Séances Acad. Sci.* **1857**, 45, 1032–1036.

4. Pasteur, M. L. Mémoire sur la Fermentation de l'Acide Tartrique. *C. R. Séances Acad. Sci.* **1858**, 46, 615–618.

5. Gal, J. The Discovery of Biological Enantioselectivity: Louis Pasteur and the Fermentation of Tartaric Acid, 1857 – A Review and Analysis 150 Yr Later. *Chirality* **2008**, 20, 5–19.

6. Piutti, A. Ein Neues Asparagin. *Ber. Dtsch. Chem. Ges.* **1886**, 19, 1691–1695.

7. Gal, J. The Discovery of Stereoselectivity at Biological Receptors: Arnaldo Piutti and the Taste of the Asparagine Enantiomers – History and Analysis on the 125th Anniversary. *Chirality* **2012**, 24, 959–976.

8. Bentley, R. From Optical Activity in Quartz to Chiral Drugs: Molecular Handedness in Biology and Medicine. *Perspect. Biol. Med.* **1995**, 38, 188–229.

9. Schellman, J. A. Circular Dichroism and Optical Rotation. *Chem. Rev.* **1975**, 75, 323–331.

10. Hutt, A. J. Drug Chirality and its Pharmacological Consequences, Ch. 5. *Introduction to the Principles of Drug Design and Action*. CRC Press, *e*. Smith, H. J. Taylor & Francis, **2006**.

11. Garay, A. S. Origin and Role of Optical Isomery in Life. *Nature* **1968**, 219, 338–340.

12. Mayer, S.; Kessler, J. Experimental Verification of Electron Optic Dichroism. *Phys. Rev. Lett.* **1995**, 74, 4803–4806.

13. Mayer, S.; Nolting, C.; Kessler, J. Electron Scattering from Chiral Molecules. *J. Phys. B: At. Mol. Opt. Phys.* **1996**, 29, 3497–3511.

14. Nolting, C.; Mayer, S.; Kessler, J. Electron Dichroism – New Data and an Experimental Cross-Check. *J. Phys. B: At. Mol. Opt. Phys.* **1997**, 30, 5491–5499.

15. Ray, K.; Ananthavel, S. P.; Waldeck, D. H.; Naaman, R. Asymmetric Scattering of

Polarized Electrons by Organized Organic Films of Chiral Molecules. *Science* **1999**, 283, 814–816.

16. Ray, S. G.; Daube, S. S.; Leitus, G.; Vager, Z.; Naaman, R. Chirality-Induced Spin-Selective Properties of Self-Assembled Monolayers of DNA on Gold. *Phys. Rev. Lett*. **2006**, 96, 036101.

17. Göhler, B.; Hamelbeck, V.; Markus, T. Z.; Kettner, M.; Hanne, G. F.; Vager, Z.; Naaman, R.; Zacharias, H. Spin Selectivity in Electron Transmission through Self-Assembled Monolayers of Double-Stranded DNA. *Science* **2011**, 331, 894–897.

18. Michaeli, K.; Kantor-Uriel, N.; Naaman, R.; Waldeck, D. H. The Electron's Spin and Molecular Chirality – How are They Related and How Do They Affect Life Processes? *Chem. Soc. Rev*. **2016**, 45, 6478–6487.

19. Sanvito, S. Molecular Spintronics: The Rise of Spinterface. *Nat. Phys*. **2010** 6, 562–564.

20. Cinchetti, M.; Dediu, V. A.; and Hueso, L. E. Activating the Molecular Spinterface. *Nat. Mater.* **2017**, 16, 507–515.

21. Michaeli, K.; Varade, V.; Naaman, R.; Waldeck, D. H. A New Approach towards Spintronics-Spintronics with No Magnets. *J. Phys. Condens. Matter* **2017**, 29, 103002.

22. Naaman, R.; Waldeck, D. H. Spintronics and Chirality: Spin Selectivity in Electron Transport through Chiral Molecules. *Ann. Rev. Phys. Chem.* **2015**, 66, 263–281.

23. Krstić, V.; Rikken, G. L. J. A. Magneto-Chiral Anisotropy of the Free Electron in a Helix. *Chem. Phys. Lett.* **2002**, 364, 51–56.

24. Yeganah, S.; Ratner, M. A.; Medina, E.; Mujica, V. Chiral Electron Transport: Scattering through Helical Potentials. *J. Chem. Phys.* **2009**, 131, 014707.

25. Koretsune, T.; Arita, R.; Aoki, H. Magneto-Orbital Effect without Spin-Orbit Interactions in a Noncentrosymmetric Zeolite-Templated Carbon Structure. *Phys. Rev. B* **2012**, 86, 125207.

26. Medina, E.; Lopez, F.; Ratner, M. A. Mujica, V. Chiral Molecular Films as Electron Polarizers and Polarization Modulators. *Europhys. Lett.* **2012**, 99, 17006.

27. Gutierrez R.; Díaz, E.; Naaman, R.; Cuniberti, G. Spin Selective Transport through Helical Molecular Systems. *Phys. Rev. B* **2012**, 85, 081404.

28. Guo, A. M.; Sun, Q. F. Spin-Selective Transport of Electrons in DNA Double Helix. *Phys. Rev. Lett.* **2012**, 108, 218102.

29. Guo, A. M.; Sun, Q. F. Sequence-Dependent Spin-Selective Tunneling along Double-Stranded DNA. *Phys. Rev. B* **2012**, 86, 115441.

30. Vager, D.; Vager, Z. Spin Order without Magnetism: A New Phase of Spontaneously Broken Symmetry in Condensed Matter. *Phys. Lett. A* **2012**, 376, 1895–1897.

31. Gersten, J.; Kaasbjerg, K.; Nitzan, A. Induced Spin Filtering in Electron Transmission through Chiral Molecule Layers Adsorbed on Metals with Strong Spin-Orbit Coupling. *J. Chem. Phys.* **2013**, 139, 114111.

32. Gutierrez, R.; Díaz, E.; Gaul, C.; Brumme, T.; Domínguez-Adame, F.; Cuniberti, G. Modeling Spin Transport in Helical Fields: Derivation of an Effective Low-Dimensional Hamiltonian. *J. Phys. Chem. C* **2013**, 117, 22276–22284.

33. Eremko, A. A.; Loktev, V. M. Spin Sensitive Electron Transmission through Helical Potentials. *Phys. Rev. B* **2013**, 88, 165409.

34. Rai, D.; Galperin, M. Electrically Driven Spin Currents in DNA. *J. Phys. Chem.* **2013**, 117, 13730–13737.

35. Guo, A. M.; Sun, Q. F. Spin-Dependent Electron Transport in Protein-like Single-Helical Molecules. *Proc. Natl. Acad. Sci. USA* **2014**, 111, 11658–11662.

36. Medina, E.; González-Arraga, L. A.; Finkelstein-Shapiro, D.; Berche, B.; Mujica, V. Continuum Model for Chiral Induced Spin Selectivity in Helical Molecules. *J. Chem. Phys.* **2015**, 142, 194308–194313.

37. Michaeli, K.; Naaman, R. Origin of Spin Dependent Tunneling through Chiral Molecules. arXiv 1512.03435v2, **2016**.

38. Varela, S.; Mujica, V.; Medina, E. Effective Spin-Orbit Couplings in an Analytical Tight-Binding Model of DNA: Spin Filtering and Chiral Spin Transport. *Phys. Rev. B: Condens. Matter Mater. Phys*. **2016**, 93, 155436.

39. Manchon, A.; Koo, H. C.; Nitta, J.; Frolov, S M.; Duine, R. A. New Perspectives for Rashba Spin-Orbit Coupling. *Nat. Mater.* **2015**, 14, 871–882.

40. Simchi, H.; Esmaeilzadeh, M.; Mazidabadi, H. The Effect of a Magnetic Field on the Spin-Selective Transport in Double-Stranded DNA. *J. App. Phys.* **2014**, 115, 204701.

41. Gerlach, W.; Stern, O. Der Experimentelle Nachweis des Magnetischen Moments des Silveratoms. *Z. Phys.* **1921**, 8, 110–111.

42. Gerlach, W.; Stern, O. Der Experimentelle Nachweis der Richtungsquantelung im Magnetfeld. *Z. Phys.* **1922**, 9, 349–352.

43. Gerlach, W.; Stern, O. Das Magnetische Moment des Silberatoms, *Z. Phys.* **1922**, 9,

353–355.

44. Weinert, F. Wrong Theory – Right Experiment: The Significance of the Stern-Gerlach Experiments. *Stud. Hist. Phil. Mod. Phys.* **1995**, 26, 75–86.

45. Uhlenbeck, G. E.; Goudsmit, S. Ersetzung der Hypothese vom Unmechanischen Zwang durch eine Forderung Bezüglich des Inneren Verhaltens jedes Einzelnen Elektrons. *Naturwissenschaften* **1925**, 13, 953–954.

46. Compton, A. K. The Magnetic Electron. *Journ. Frankl. Inst.* **1921**, 192, 145–155.

47. Uhlenbeck, G. E.; Goudsmit, S. Spinning Electrons and the Structure of Spectra. *Nature* **1926**, 117, 264–265.

48. Vester, F.; Ulbricht, T. L. V.; Krauch, H. Optische Aktivität und die Paritätsverletzung im β-Zerfall **1959**, 46, 68.

49. Ulbricht, T. L. V. Asymmetry: The Non-Conservation of Parity and Optical Activity. *Quart. Revs.* **1959**, 13, 48–60.

50. Ulbricht, T. L. V.; Vester, F. Attempts to Induce Optical Activity with Polarized *β*-Radiation. *Tetrahedron* **1962**, 18, 629–637.

51. Keszthelyi, L. Origin of the Asymmetry of Biomolecules and Weak Interaction. *Orig. Life* **1977**, 8, 299–340.

52. Hodge, L. A.; Dunning, F. B.; Walters, G. K.; White, R. H.; Schroepfer G. J. Jr. Degradation of *DL*-Leucine with Longitudinally Polarized Electrons. *Nature* **1979**, 280, 250–252.

53. Farago, P. S. Spin-Dependent Features of Electron Scattering from Optically Active Molecules. *J. Phys. B: At. Mol. Phys.* **1980**, 13, L567–L571.

54. Beerlage, M. J. M.; Farago, P. S.; Van der Weil, M. J. A Search for Spin Effects in Low-Energy Electron Scattering from Optically Active Camphor. *J. Phys. B: At. Mol. Phys.* **1981**, 14, 3245–3253.

55. Campbell, D. M.; Farago, P. S. Spin-Dependent Scattering from Optically Active Molecules. *Nature* **1985**, 318, 52–53.

56. Campbell, D. M.; Farago, P. S. Electron Optic Dichroism in Camphor. *J. Phys. B: At. Mol. Phys.* **1987**, 20, 5133–5143.

57. Randreyer, R.; Thompson, D.; Blum, K. Attenuation of Longitudinally Polarized Electron Beams by Chiral Molecules. *J. Phys. B: At. Mol. Opt. Phys.* **1990**, 23, 3031–3040.

58. Naaman, R.; Waldeck, D. H. Chiral-Induced Spin Selectivity Effect. *J. Phys. Chem. Lett.* **2012**, 3, 2178–2187.

59. Blum, K.; Thompson, D. G. Chiral Effects in Electron Scattering by Molecules. *Adv. At. Mol. Opt. Phys.* **1997**, 38, 39–86.

60. Smith, I. M.; Thompson, D. G.; Blum, K. Chiral Effects in Electron Scattering by Molecules using a Continuum Multiple Scattering Method. *J. Phys. B: At. Mol. Opt. Phys.* **1998**, 31, 4029–4058.

61. Meier, F.; Pescia, D. Band-Structure Investigation of Gold by Spin-Polarized Photoemission. *Phys. Rev. Lett.* **1981**, 47, 374–377.

62. Borstel, G.; and Wöhlecke, M. Spin Polarization of Photoelectrons Emitted from Nonmagnetic Solids. *Phys. Rev. B* **1982**, 26, 1148–1155.

63. Maruyama, T.; Garwin, E. L.; Prepost, R.; Zapalac, G. H.; Smith, J. S.; Walker, J. D. Observation of Strain-Enhanced Electron-Spin Polarization in Photoemission from InGaAs. *Phys. Rev. Lett.* **1991**, 66, 2376–2379.

64. Mishra, D.; Markus, T. Z.; Naaman, R.; Kettner, M.; Göhler, B.; Zacharias, H.; Friedman, N.; Sheves, M.; Fontanesi, C. Spin-Dependent Electron Transmission through Bacteriorhodopsin Embedded in Purple Membrane. *Proc. Natl. Acad. Sci. U. S. A*. **2013**, 110, 14872–14876.

65. Kettner, M.; Göhler, B.; Zacharias, H.; Mishra, D.; Kiran, V.; Naaman, R.; Fontanesi, C.; Waldeck, D. H.; Sęk, S.; Pawłowski, J.; Juhaniewicz, J. Spin Filtering in Electron Transport through Chiral Oligopeptides. *J. Phys. Chem. C* **2015**, 119, 14542–14547.

66. Kettner, M.; Maslyuk, V. V.; Nürenberg, D.; Seibel, J.; Gutierrez, R.; Cuniberti, G.; Ernst, K. –H.; Zacharias, H. Chirality-Dependent Electron Spin Filtering by Molecular Monolayers of Helicenes. *J. Phys. Chem. Lett.* **2018**, 9, 2025–2030.

67. Rosenberg, R. A.; Haija, M. A.; Ryan, P. J. Chiral-Selective Chemistry Induced by Spin-Polarized Secondary Electrons from a Magnetic Substrate. *Phys. Rev. Lett.* **2008**, 101, 178301.

68. Rosenberg, R. A.; Mishra, D.; Naaman, R. Chiral Selective Chemistry Induced by Natural Selection of Spin-Polarized Electrons. *Angew. Chem., Int. Ed*. **2015**, 54, 7295–7298.

69. Xie, Z.; Markus, T. Z.; Cohen, S. R.; Vager, Z.; Gutierrez, R.; Naaman, R. Spin Specific Electron Conduction through DNA Oligomers. *Nano Lett.* **2011**, 11, 4652–4655.

70. Mondal, P. C.; Kantor-Uriel, N.; Mathew, S. P.; Tassinari, F.; Fontanesi, C.; Naaman, R. Chiral Conductive Polymers as Spin Filters. *Adv. Mater.* **2015**, 27, 1924–1927.

71. Bloom, B. P.; Kiran, V.; Varade, V.; Naaman, R.; Waldeck, D. H. Spin Selective Charge Transport through Cysteine Capped CdSe Quantum Dots. *Nano Lett*. **2016**, 16, 4583–4589.

72. Kiran, V.; Mathew, S. P.; Cohen, S. R.; Delgado, I. H.; Lacour, J.; Naaman, R. Helicenes – A New Class of Organic Spin Filter. *Adv. Mater.* **2016**, 28, 1957–1962.

73. Aragonès, A. C.; Medina, E.; Ferrer-Huerta, M.; Gimeno, N.; Teixidó, M.; Palma, J. L.; Tao, N.; Ugalde, J. M.; Giralt, E.; Díez-Pérez, I.; Mujica, V. Measuring the Spin-Polarization Power of a Single Chiral Molecule. *Small* **2017**, 13, 1602519.

74. Kiran, V.; Cohen, S. R.; Naaman, R. Structure Dependent Spin Selectivity in Electron Transport through Oligopeptides. *J. Chem. Phys*. **2017**, 146, 092302.

75. Mondal, P. C.; Roy, P.; Kim, D.; Fullerton, E. E.; Cohen, H.; Naaman, R. Photospintronics: Magnetic Field-Controlled Photoemission and Light-Controlled Spin Transport in Hybrid Chiral Oligopeptide-Nanoparticle Structures. *Nano Lett*. **2016**, 16, 2806–2811.

76. Roy, P.; Kantor-Uriel, N.; Mishra, D.; Dutta, S.; Friedman, N.; Sheves, M.; Naaman, R. Spin-Controlled Photoluminescence in Hybrid Nanoparticles Purple Membrane System. *ACS Nano* **2016**, 10, 4525–4531.

77. Carmeli, I.; Senthil Kumar, K.; Heifler, O.; Carmeli, C.; Naaman, R. Spin Selectivity in Electron Transfer in Photosystem I. *Angew. Chem., Int. Ed.* **2014**, 18, 8953–8958.

78. Einati, H.; Mishra, D.; Friedman, N.; Sheves, M.; Naaman, R. Light-Controlled Spin Filtering in Bacteriorhodopsin. *Nano Lett.* **2015**, 11, 1052–1056.

79. Bloom, B. P.; Graff, B. M; Ghosh, S.; Beratan, D. N.; Waldeck, D. H. Chirality Control of Electron Transfer in Quantum Dot Assemblies. *J. Am. Chem. Soc.* **2017**, 139, 9038–9043.

80. Fahidy, T. Z. Magnetoelectrolysis. *J. Appl. Electrochem.* **1983**, 13, 553–563.

81. Mogi, I. *New Challenges in Organic Electrochemistry*; Gordon and Breach Science Publishers: Amsterdam, The Netherlands **1998**; Chapter 1.

82. Alemany, A.; Chopart, J. -P. *Magnetohydrodynamics*; Springer: Dordrecht, The Netherlands, **2007**; Part IV.

83. Monzon, L. M. A.; Coey, J. M. D. Magnetic Fields in Electrochemistry: The Lorentz Force. A Mini-Review. *Electrochem. Commun.* **2014**, 42, 38–41.

84. Monzon, L. M. A.; Coey, J. M. D. Magnetic Fields in Electrochemistry: The Kelvin Force. A Mini-Review. *Electrochem. Commun.* **2014**, 42, 42–45.

85. Saravanan, G.; Ozeki, S. Magnetic Field Control of Electron Tunneling Pathways in the Monolayer of (Ferrocenylmethyl)dodecyldimethylammonium Bromide on a Gold Electrode. *J. Phys. Chem. B* **2008**, 112, 3–6.

86. Lee, C. -C.; Chou, T. -C. Effects of Magnetic Field on the Reaction Kinetics of Electroless Nickel Deposition. *Electrochim. Acta* **1995**, 40, 965–970.

87. Mandler, D. Chiral Self-Assembled Monolayers in Electrochemistry. *Curr. Op. Electrochem.* **2018**, 7, 42–47.

88. Wattanakit, C. Chiral Metals as Electrodes. *Curr. Op. Electrochem*. **2018**, 7, 544–60.

89. Mogi, I.; Watanabe, K. Enantioselective Recognition of Tartaric Acid on Magneto-Electrodeposited Copper Film Electrodes. *Chem. Lett.* **2012**, 41, 1439–1441.

90. Nakanishi, T.; Matsunaga, M.; Nagasaka, M.; Asahi, T.; Osaka, T. Enantioselectivity of Redox Reaction of DOPA at the Gold Electrode Modified with a Self-Assembled Monolayer of Homocysteine. *J. Am. Chem. Soc.* **2006**, 128, 13322–13323.

91. Challier, L.; Mavré, F.; Moreau, J.; Fave, C.; Schöllhorn, B.; Marchal, D.; Peyrin, E.; Noël, V.; Limoges, B. Simple and Highly Enantioselective Electrochemical Aptamer-Based Binding Assay for Trace Detection of Chiral Compounds. *Anal. Chem.* **2012**, 84, 5415–5420.

92. Mondal, P. C.; Fontanesi, C.; Waldeck, D. H.; Naaman, R. Spin-Dependent Transport through Chiral Molecules Studied by Spin-Dependent Electrochemistry. *Acc. Chem. Res.* **2016**, 49, 2560–2568.

93. Mondal, P. C.; Fontanesi, C.; Waldeck, D. H.; Naaman, R. Field and Chirality Effects on Electrochemical Charge Transfer Rates: Spin Dependent Electrochemistry. *ACS Nano* **2015**, 9, 3377–3384.

94. Zwang, T. J.; Hürlimann, S.; Hill, M. G.; Barton, J. K. Helix-Dependent Spin Filtering through the DNA Duplex. *J. Am. Chem. Soc*. **2016**, 138, 15551–15554.

95. Eckshtain-Levi, M.; Capua, E.; Refaely-Abramson, S.; Sarkar, S.; Gavrilov, Y.; Mathew, S. P.; Paltiel, Y.; Levy, Y.; Kronik, L.; Naaman, R. Cold Denaturation Induces Inversion of Dipole and Spin Transfer in Chiral Peptide Monolayers. *Nat. Commun*. **2016**, 7, 10744.

96. Rosenberg, R. A.; Symonds, J. M.; Kalyanaraman, V.; Markus, T.; Orlando, T. M.; Naaman, R.; Medina, E. A.; López, F. A.; Mujica, V. Kinetic Energy Dependence of

Spin Filtering of Electrons Transmitted through Organized Layers of DNA. *J. Phys. Chem. C* **2013**, 117, 22307–22313.

97. Kumar, K. S.; Kantor-Uriel, N.; Mathew, S. P.; Guliamov, R.; Naaman, R. A Device for Measuring Spin Selectivity in Electron Transfer. *Phys. Chem. Chem. Phys*. **2013**, 15, 18357–18362.

98. Abendroth, J. M.; Nakatsuka, N.; Ye, M.; Kim, D.; Fullerton, E. E.; Andrews, A. M.; Weiss, P. S. Analyzing Spin Selectivity in DNA-Mediated Charge Transfer *via* Fluorescence Microscopy. *ACS Nano* **2017**, 11, 7516–7526.

99. Abendroth, J. M.; Cheung, K. C.; Stemer, D. M.; El Hadri, M. S.; Zhao, C.; Fullerton, E. E.; Weiss, P. S. Spin-Polarized Photoemission by Ionization of Chiral Molecular Films. *In preparation*, *see Chapter III.*

100. Hoertz, P. G.; Niskala, J. R.; Dai, P.; Black, H. T.; You, W. Comprehensive Investigation of Self-Assembled Monolayer Formation on Ferromagnetic Thin Film Surfaces. *J. Am. Chem. Soc.* **2008**, 130, 9763–9772.

101. Dor, O. B.; Yochelis, S.; Radko, A.; Vankayala, K.; Capua, E.; Capua, A.; Yang, S. -H.; Baczewski, L. T.; Parkin, S. S. P.; Naaman, R.; Paltiel, Y. Magnetization Switching in Ferromagnets by Adsorbed Chiral Molecules without Current or External Magnetic Field. *Nat. Commun.* **2017**, 8, 14567.

102. Gorodetsky, A. A.; Green, O.; Yavin, E.; Barton, J. K. Coupling into the Base Pair Stack Is Necessary for DNA-Mediated Electrochemistry. *Bioconjugate Chem.* **2007**, 18, 1434– 1441.

103. Genereux, J. C.; Barton, J. K. Mechanisms for DNA Charge Transport. *Chem. Rev.* **2010**, 110, 1642–1662.

104. Xiang, L.; Palma, J. L.; Bruot, C.; Mujica, V.; Ratner, M. A.; Tao, N. Intermediate Tunneling-Hopping Regime in DNA Charge Transport. *Nat. Chem.* **2015**, 7, 221–226.

105. Kumar, A. S.; Ye, T.; Takami, T.; Yu, B. -C.; Flatt, A. K.; Tour, J. M.; Weiss, P. S. Reversible Photo-Switching of Single Azobenzene Molecules in Controlled Nanoscale Environments. *Nano Lett.* **2008**, 8, 1644–1648.

106. Zheng, Y. B.; Payton, J. L.; Chung, C. -H.; Liu, R.; Cheunkar, S.; Pathem, B. K.; Yang, Y.; Jensen, L.; Weiss, P. S. Surface-Enhanced Raman Spectroscopy to Probe Reversibly Photoswitchable Azobenzene in Controlled Nanoscale Environments. *Nano Lett.* **2011**, 11, 3447–3452.

107. Pathem, B. K.; Zheng, Y. B.; Payton, J. L.; Song, T. -B.; Yu, B. -C.; Tour, J. M.; Yang, Y.; Jensen, L.; Weiss, P. S. Effect of Tether Conductivity on the Efficiency of

Photoisomerization of Azobenzene-Functionalized Molecules on Au{111}. *J. Phys. Chem. Lett.* **2012**, 3, 2388–2394.

108. Pathem, B. K.; Zheng, Y. B.; Morton, S.; Petersen, M. Å.; Zhao, Y.; Chung, C. -H.; Yang, Y.; Jensen, L.; Nielsen, M. B.; Weiss, P. S. Photoreaction of Matrix-Isolated Dihydroazulene-Functionalized Molecules on Au{111}. *Nano Lett.* **2013**, 13, 337–343.

109. Abendroth, J. M.; Bushuyev, O. S.; Weiss, P. S.; Barrett, C. J. Controlling Motion at the Nanoscale: Rise of the Molecular Machines. *ACS Nano* **2015**, 9, 7746–7768.

Chapter II

Analyzing Spin Selectivity in DNA-Mediated Charge Transfer *via* Fluorescence Microscopy

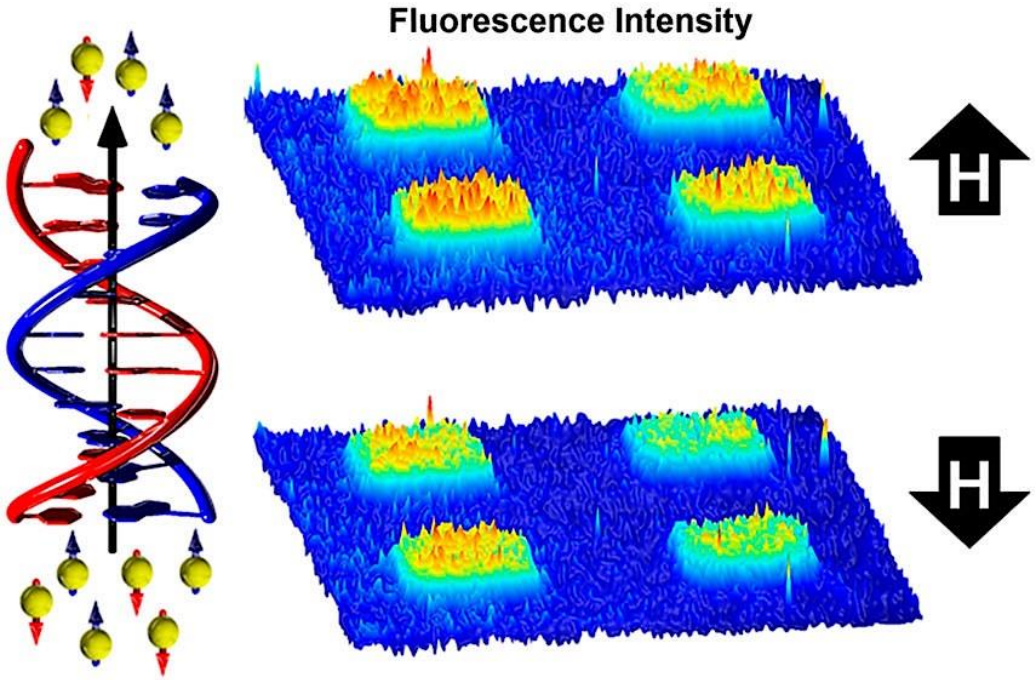

The information in this chapter was published in
ACS Nano 2017, 11, 7516–7526, and is reproduced with permission here.

Authors: John M. Abendroth, Nako Nakatsuka, Matthew Ye, Dokyun Kim, Eric E. Fullerton, Anne M. Andrews, and Paul S. Weiss

II.A. Introduction

Understanding how interfacial parameters beyond molecule chirality affect electron transmission and the strength of the CISS effect at chiral molecule–metal interfaces is critical for interpreting results from experiments designed to study this phenomenon. As discussed in Chapter I, in many experimental methods, chiral molecules have been assembled on FM surfaces or probed in conductive AFM measurements with FM tips to study the external magnetic field dependence of charge-transfer processes based on substrate or tip magnetization orientation. While this effect has been measured in diverse systems, the preferred substrate or tip magnetization direction (field up or field down) for more efficient charge transfer through dsDNA or α-helical peptides with the same handedness has *not* been consistently reported.

For example, using conductive AFM, Xie *et al*. investigated conduction through dsDNA molecules assembled on Ni substrates.[1] Thiolated, ssDNA monolayers were first assembled and then incubated with complementary sequences tethered to gold nanoparticles to form a top electrode contact. Higher conductance through the Ni-DNA-Au nanoparticle-(nonferromagnetic) tip junctions was measured when an external magnetic field and the substrate magnetization were oriented *antiparallel* to the surface normal. By contrast, Zwang *et al*. designed electrochemical experiments using intercalating redox reporters within dsDNA assembled on Au-capped Ni substrates to measure the effects of an external magnetic field on charge transfer through duplexes.[2] Using cyclic voltammetry, more efficient DNA-mediated charge transfer was measured in right-handed DNA duplexes when the underlying substrate was magnetized *parallel* to the surface normal.

Differences in the findings of these and other studies[3,4] may be attributed to system-dependent factors. For example, variable barriers to charge transport across metal–molecule interfaces favor transmission of majority *vs* minority spin electrons in FM metal tips or thin films.[5] Strong dipole electric fields can also influence the affinity of helices for particular electron spin orientations.[6,7] Moreover, tip or substrate magnetization-dependent differences in charge injection at interfaces due to the CISS effect may be fairly small compared to measurement variability under ambient temperature and pressure conditions, presenting a challenge to determining conclusively whether charge transmission is enhanced or suppressed.

To address the latter, we designed experiments with precisely patterned microenvironments to validate each sample preparation step and the measurements and to quantify large amounts of data using a robust mathematical framework. We used DNA SAMs modified with fluorescent dyes that were precisely patterned at the microscale onto FM multilayer substrates. Substrates were specifically designed to possess perpendicular magnetic anisotropy, ensuring saturation of spin-polarized electrons aligned parallel or antiparallel to the axis of nominally vertically oriented DNA molecules using modest external magnetic fields. Patterned arrays enabled quantification of relative fluorescence intensities providing an internal control for each measurement when conducting fluorescence microscopy as an indirect method to monitor the spin-filtering phenomenon. On FM substrates, fluorescence quenching of photoexcited dye molecules was controlled with an external magnetic field to polarize spins within the metal due to competitive relaxation of chromophores leading to charge transfer to the surface. While tethered dsDNA is expected to act as an electron spin filter invariant with respect to the presence or orientation of an

external magnetic field, the efficiency of charge injection into a FM material is dependent on the populations of electrons and spin orientations within the majority and minority spin subbands.

II.B. Perylenediimide Dyes Assemble Noncovalently within Double-Stranded DNA Containing Hydrophobic Pockets

Electron or hole donors must be well-coupled to DNA base stacks for efficient charge injection because charge transport within DNA is mediated by π-stacking of the nucleic acid bases.[8,9] We synthesized a water-soluble, photooxidizing perylenediimide derivative, *N*,*N*′-bis[3,3′-(dimethylamino)propylamine]-3,4,9,10-perylenetetracarboxylic diimide (PDI), which π-stacks with nitrogenous base pairs above and below the conjugated plane of the dye molecules. The PDI molecules assemble specifically within hydrophobic pockets created by matching abasic sites in duplex DNA molecules using noncovalent host–guest chemistry (Figure II.1a).[10] Compared to intercalating dyes that bind indiscriminately within base stacks, using PDI enabled precise control over the number of base pairs between dye molecules and metal surfaces without covalently tethering dye molecules to sugar-phosphate backbones of DNA. By ensuring that PDI binds in the same location in each DNA molecule, we avoided the need to consider length dependence in spin-selective charge transmission through DNA as a variable.[1,2,11]

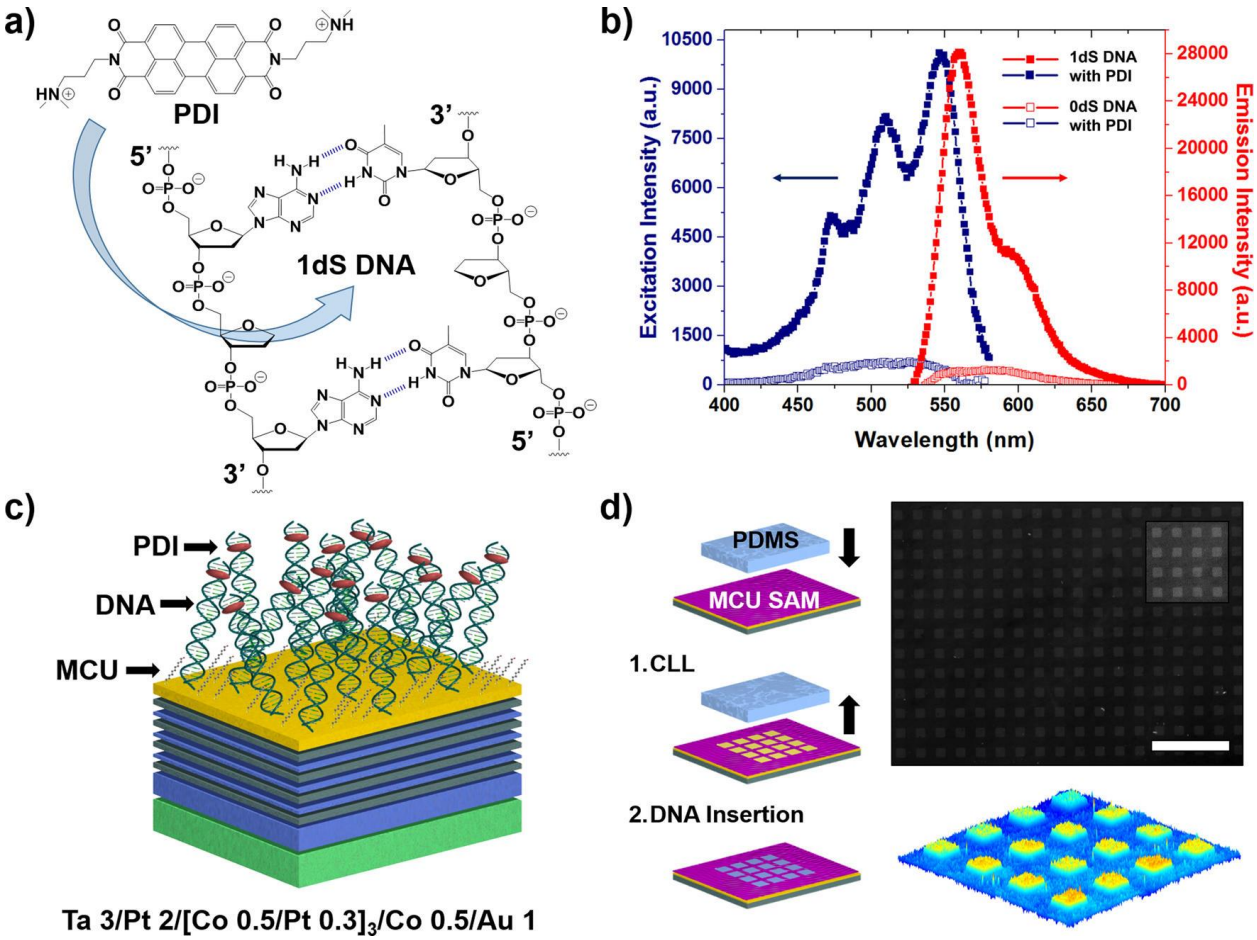

Figure II.1. (**a**) Chemical structures of the DNA-assembling dye *N*,*N*′-bis[3,3′-(dimethylamino)propylamine]-3,4,9,10-perylenetetracarboxylic diimide (PDI) and the hydrophobic pocket created in double-stranded DNA upon annealing complementary oligonucleotide strands each containing a deoxyribose spacer, *i.e.*, abasic site. (**b**) Representative excitation and emission spectra of PDI in a 1:1 ratio (30 μM) with double- stranded DNA with (1dS) or without (0dS) deoxyribose spacers. Excitation was at 475 nm, and emission was at 620 nm. (**c**) Schematic of a mixed monolayer of 11-mercapto-1-undecanol (MCU) and double-stranded DNA with associated PDI self-assembled on a gold-capped multilayer ferromagnetic substrate having perpendicular magnetic anisotropy. Layers and thicknesses are indicated in the figure (in nm). (**d**) Schematic of DNA patterning on gold-capped ferromagnetic substrates and a representative microscopy image showing the fluorescent pattern due to emission from PDI molecules associated with DNA (excitation wavelength: 550 ± 25 nm; emission wavelength: 605 ± 70 nm; exposure time: 8 s). Scale bar: 200 μm. A three-dimensional representation of fluorescence intensities from a 200 μm × 200 μm region of the surface is displayed below corresponding to the contrast-enhanced region shown in the top right corner of the black and white image. PDMS: polydimethylsiloxane, SAM: self-assembled monolayer, CLL: chemical lift-off lithography.

Photooxidation by perylenediimides has been exploited to study charge-transfer processes through DNA by tuning the base sequences surrounding the dye molecules.[12-15] However, fluorescence quenching, when incorporated within DNA, suggests that this class of molecules is ill-suited as emissive probes without substitution of electron-donating groups at bay positions in the perylene core.[16-20] The low emission yields of perylenediimide derivatives in DNA conjugates are a direct result of strong coupling of photooxidizing dyes with nucleobases due to π-stacking of the aromatic perylene core with bases above and below the plane of the molecule. Consequently, the perylenediimide derivatives synthesized here are excellent candidates for probing spin-selective charge transmission through DNA by monitoring their (albeit low) fluorescence indirectly as a figure of merit. The DNA sequences were carefully selected to minimize nonradiative charge recombination pathways, while still enabling competitive charge injection into the base stack upon photoexcitation (*vide infra*).

Excitation and emission spectra of PDI in phosphate-buffered saline (PBS) solutions in a 1:1 ratio with dsDNA molecules containing a single hydrophobic pocket (1dS) are shown in Figure II.1b. The maxima in both spectra are red-shifted by *ca.* 12 nm from the excitation and emission spectra of PDI alone in PBS (Figure SII.1), which is indicative of electronic coupling due to π-stacking with adjacent bases within DNA abasic sites. In contrast, PDI mixed with a 1:1 ratio of dsDNA of the same length and sequence but lacking hydrophobic pockets (0dS) displayed minimal excitation and emission intensities due to aggregation-induced quenching, which supports the necessity for abasic sites in DNA for specific dye-molecule binding (Figure II.1b).[21]

Complementary 36-mer oligonucleotide strands containing matching abasic sites (deoxyribose spacers, dSp) were annealed in a 5:1 molar ratio with PDI prior to surface assembly. Because dye molecules are not covalently attached to DNA, using an excess of DNA minimizes the presence of free and nonspecifically bound PDI, which might convolute fluorescence signals from PDI specifically bound within DNA hydrophobic pockets. Complementary sequences were (1) 5′-CGC TTC GCT TCG CTT CGC TTC GCT TCG CTT TT/dSp/TTT T-3′ and (2) 5′-AAA A/dSp/A AAA GCG AAG CGA AGC GAA GCG AAG CGA AGC G-3′. Sequence (1) was functionalized with a thiol separated from the 5′-end of the sugar phosphate backbone by six methylene units to enable DNA self-assembly on metal surfaces. Adoption of the right-handed B-form of the annealed DNA/PDI complexes prior to surface assembly was confirmed by circular dichroism spectroscopy (Figure SII.2).

II.C. Spin Selectivity in DNA-Mediated Charge Transfer Is Measured Indirectly *via* Fluorescence Microscopy

Substrates were soft FM multilayer thin-films composed of Ta 3/Pt 2/[Co 0.5/Pt 0.3]$_3$/Co 0.5/Au 1 layers (in nm) sputter-deposited on Si/SiO_2 (Figure II.1c). These substrates possess perpendicular magnetic anisotropy. Their design, fabrication, and use in investigating the CISS effect in oligopeptide SAMs have been described previously.[22] Briefly, Co and Pt orbital hybridization in [Co/Pt] multilayers is one of the most common sources to realize perpendicular magnetic anisotropy.[23] Here, substrates were optimized to reduce Pt layer thicknesses to minimize depolarization of electron currents due to strong spin–orbit coupling in Pt. The thin capping layer of Au maintains the spin polarization from the Co layer

and enables the assembly of SAMs of thiolated molecules due to strong Au–S bond formation, while protecting the underlying substrate from corrosion and oxidation in PBS solutions.

Patterning SAMs of DNA/PDI complexes on FM substrates ensures background reference regions for every observation. We previously developed and investigated insertion-directed chemistries within alkanethiol and related SAMs,[24-29] and demonstrated the use of chemical patterning with fluorophore-labeled targets to quantify emission intensities, relative to background reference regions, *via* fluorescence microscopy.[30] We developed chemical lift-off lithography (CLL),[31-34] a subtractive patterning method, which has been shown to improve DNA hybridization efficiencies, while optimizing DNA surface coverage.[35] Briefly, in CLL, high-resolution patterned features are fabricated *via* silicone rubber stamps activated by oxygen plasma to remove hydroxyl-terminated alkanethiols from SAMs on Au surfaces within the contact regions.[36]

There are two key advantages of CLL when patterning DNA on substrates. First, in the stamp-contact areas that are lifted off, not all alkanethiolate molecules are removed.[35] The remaining molecules serve as a dilute matrix to space out and to orient subsequently inserted molecules, which reduces the probability of DNA molecules laying down on surfaces. Compared to methods that require assembling DNA first and subsequently backfilling with short, water-soluble alkanethiols, CLL enables longer background molecules, such as 11-mercapto-1-undecanol (MCU), to be used as matrix molecules further enabling upright DNA orientations at surfaces while minimizing nonspecific DNA–substrate interactions. Second, sharper pattern boundaries are possible with CLL compared to alternative patterning strategies,[37] which is advantageous for image analysis due to the low fluorescence yield of PDI molecules specifically bound within DNA. In this work, we

patterned preannealed DNA/PDI complexes in 25 μm × 25 μm arrays on FM substrates (Figure II.1d). The regions of contrast provided by chemical patterning differentiating areas where DNA/PDI complexes are assembled *vs* background (unpatterned) regions enabled validation of self-assembly on each surface and differentiation of fluorescent signals specifically from PDI molecules incorporated in DNA *vs* PDI nonspecifically associated with the background matrix.

We conducted multiple experiments to confirm assembly of DNA/PDI complexes on substrates and to ensure that fluorescence was attributable to PDI molecules bound within the hydrophobic pockets of DNA. When DNA molecules containing abasic sites were annealed and assembled on substrates in the absence of PDI, neither patterns nor contrast were observed in fluorescence images (Figure SII.3). We similarly observed no fluorescence when complementary DNA strands lacking abasic sites or thiolated ssDNA molecules (sequence 1, above) were incubated with PDI molecules and assembled on surfaces (Figure SII.3).

For spin-selective measurements, an external magnetic field was applied by placing an axially polarized permanent magnet directly beneath substrates. A magnetic field of *ca.* 0.3 T in each direction normal to the sample substrate layers was measured at sample surfaces, which was sufficient to saturate the perpendicular magnetization of the FM substrates. Figure II.2a shows representative fluorescence images from the same region of a sample patterned with DNA/PDI complexes obtained with the external magnetic field oriented either parallel to (field up) or antiparallel to (field down) the surface normal. Fluorescence microscopy images were obtained for both external magnetic field orientations under two additional experimental conditions. In the first, patterned DNA monolayers were

formed in an identical manner on non-ferromagnetic, 100-nm-thick Au films deposited on Si substrates to test the influence of the external magnetic field (Figure II.2b). In the second, identical dsDNA sequences *sans* abasic sites but modified with cyanine fluorescent probes (Cy3) were assembled on FM substrates to test the necessity for charge transfer to the underlying substrate for observing the CISS effect as well as the significance of dye coupling to the DNA base stack for efficient charge transfer (Figure II.2c). The Cy3 probes were covalently attached to the 5′ ends of the DNA sugar phosphate backbones of the nonthiolated complementary DNA strands *via* three methylene units.

Relative fluorescence was quantified in the patterned (DNA/dye complexes) *vs* unpatterned regions (MCU only) for multiple images taken from all substrates in the three experimental conditions illustrated in Figure II.2a–c. Images were analyzed using a region-based segmentation algorithm based on the Chan–Vese model.[38,39] This method partitions images into foreground (patterned) and background (unpatterned) regions, while detecting and excluding artifacts and illumination bias that skew segmentation. Image analysis by this method maximizes the quantity of data used in calculating pixel intensities for each image and removes bias in drawing line profiles (regions of interest) to extract quantitative information.

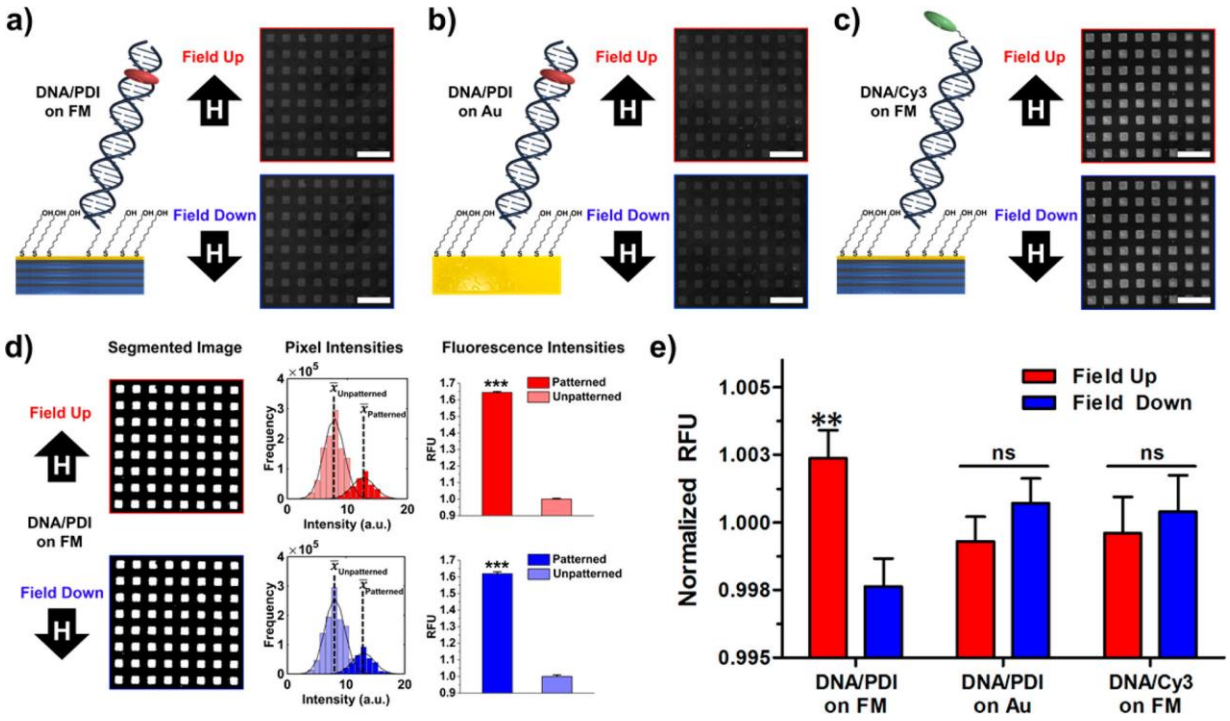

Figure II.2. Analyzing spin selectivity in DNA-mediated charge transport using fluorescence microscopy. (**a**) Schematic and representative fluorescence microscopy images of DNA/*N*,*N*′-bis[3,3′-(dimethylamino)propylamine]-3,4,9,10-perylenetetracarboxylic diimide (PDI) complexes assembled on ferromagnetic (FM) substrates with an external magnetic field applied parallel to (up) or antiparallel to (down) the surface normal. Schematics and representative fluorescence microscopy images of (**b**) DNA/PDI complexes assembled on nonferromagnetic Au substrates and (**c**) DNA/Cy3 complexes assembled on ferromagnetic substrates. (**d**) Segmented images of the fluorescence images shown in (**a**) illustrating patterned (white) and unpatterned (black) regions. Histograms of pixel intensities of the patterned and unpatterned regions from the segmented images with Gaussian fitting (mean values indicated by $\bar{x}$) Mean fluorescence intensities relative to the unpatterned regions from the representative DNA/PDI on FM sample (N = 9 images field up, N = 9 images field down, ***$P < 0.001$). (**e**) Normalized relative fluorescence intensities for each of the three experimental conditions illustrated in (**a**–**c**) (N = 22 samples for each condition, **$P < 0.01$ *vs* field down, ns is not significant). Error bars represent standard errors of the means. The fluorescence microscopy images in (**a**–**c**) are contrast-enhanced for display purposes. In all images, scale bars are 100 μm, excitation wavelength: 550 ± 25 nm, emission wavelength: 605 ± 70 nm, and exposure time: 5 s.

An example of segmentation and quantification of relative fluorescence intensities of the images in Figure II.2a is shown in Figure II.2d. Histograms of pixel intensities from the patterned and unpatterned regions of the segmented images were created, and the data were fit to Gaussian distributions to obtain the mean values, $\bar{x}_{patterned}$ and $\bar{x}_{unpatterned}$. Each substrate was repeatedly imaged under field-up *vs* field-down conditions. Mean relative fluorescence intensities of the patterned and unpatterned regions (obtained by normalizing $\bar{x}_{patterned}$ and $\bar{x}_{unpatterned}$ to $\bar{x}_{unpatterned}$ and reported in relative fluorescence units, RFU) for each substrate were then calculated (Figure II.2d, bar graphs). Mean intensities of the patterned regions were significantly greater than those in the unpatterned regions for both field orientations for all samples for DNA/PDI complexes on FM substrates (***$P < 0.001$).

Relative fluorescence intensities of the patterned regions ($\bar{x}_{patterned}/\bar{x}_{unpatterned}$) for field-up *vs* field-down measurements from each substrate were further normalized to the overall average value due to large differences in relative fluorescence intensities across substrates relative to between magnetic field orientations from identical substrates (Figure II.2e and Figure SII.4). Two-way analysis of variance showed a significant interaction between field orientation and dye/substrate condition for normalized relative fluorescence intensities [$F(2,126) = 4.64$, $P < 0.05$]. This finding indicates that the ability of field orientation to influence fluorescence intensities depended on the dye/substrate condition, *i.e.*, with *vs* without FM layers (Figure II.2a,b), and PDI *vs* Cy3 (Figure II.2a,c). *Post hoc* analysis revealed that relative fluorescence intensities were significantly higher when the external magnetic field and substrate magnetization were oriented parallel to the surface normal compared to the opposite orientation only for PDI molecules assembled within DNA on ferromagnetic substrates (Figure II.2e, **$P < 0.01$).

No significant differences in relative fluorescence intensities were observed between field-up and field-down orientations for DNA/PDI complexes assembled on nonferromagnetic Au substrates (Figure II.2e), consistent with other reports on the CISS effect using analogously designed experiments.[1,2] These results support the idea that the spin-valve-like combination of a chiral SAM, which mediates charge transfer to a surface, and perpendicularly magnetized substrates are responsible for the magnetic-field dependence of the fluorescence generated by PDI molecules—not simply the external magnetic field. Furthermore, no significant differences in magnetic field-dependent relative fluorescence intensities were observed when DNA/Cy3 complexes were assembled on FM substrates (Figure II.2e). Cyanine dyes tethered to the ends of double-stranded DNA can adopt planar configurations that cap the base stack due to π-stacking with DNA bases.[40] However, unlike the strong coupling of the highly electron-deficient, unsubstituted perylene core of PDI to adjacent adenine bases, which facilitates rapid charge separation upon photoexcitation (*vide infra*), charge transfer in cyanine dyes is not thermodynamically favorable.[41,42] Thus, the DNA/Cy3 complexes exhibited enhanced fluorescence intensities but no significant magnetic field dependence of fluorescence intensity due to the reduced efficiency of charge injection into the π-stack.

II.D. Photoelectrochemical Measurements Confirm DNA-Mediated Charge Transfer Between PDI Molecules and Metal Substrates

Photoelectrochemical experiments were carried out to validate the assumption that charge transfer between the PDI molecules associated with DNA and metal substrates occurs upon photoexcitation and to determine the direction of electron or hole transfer based on the

generation of positive or negative photovoltages. Previous studies on charge separation and recombination following photoexcitation of perylenediimide derivatives associated with DNA duplexes or hairpins using transient absorption spectroscopy demonstrated that the rates of different relaxation pathways are dependent on DNA sequences.[12-14,43,44] Here, PDI molecules were separated from the nearest G by four adenine (A) bases, thereby preventing hole trapping at guanines and subsequent regeneration of the ground state *via* superexchange, which reduces the possibility of radiative relaxation.[12] Following photoexcitation to the singlet excited state, $(A)_4$-^{1*}PDI-$(A)_4$-G, rapid charge separation *via* hole injection from the dye into the adjacent 5′ (k_{CS1}) or 3′ (k_{CS2}) adenine tracts of sequence (2) results in the formation of a polaron delocalized over 3–4 adenine bases, represented in Figure II.3a as $(A)_4^{+\bullet}$-PDI$^{-\bullet}$-$(A)_4$-G or $(A)_4$-PDI$^{-\bullet}$-$(A)_4^{+\bullet}$-G, respectively.[45] Repopulation of the ground state $(A)_4$-PDI-$(A)_4$-G occurs through nonradiative charge recombination (CR) (k_{CR3} and k_{CR4}) of the radical ion pairs or by regeneration of $(A)_4$-^{1*}PDI-$(A)_4$-G (k_{CR1} and k_{CR2}) followed by stimulated emission (k_{SE}).[12] Competing relaxation pathways are illustrated in Figure II.3a.

When DNA/PDI complexes are coupled to a metal substrate, the long-lived charge-separated states allow electron–hole pair migration to the metal surfaces (k_{CT1}) *via* DNA-mediated charge transfer through the π-stack.[43,44] Photoelectrochemical measurements provided evidence for charge transfer between PDI and the underlying metal surface in pure DNA/PDI SAMs on FM and nonferromagnetic Au substrates (Figure II.3b). A negative, steady-state photovoltage was detected upon illumination for either type of substrate at 532 nm under open-circuit voltage conditions. The anodic photovoltage is indicative of increasing the electron potential due to electron transfer from DNA to the substrates. These

experiments were performed in deoxygenated PBS in the absence of electron or hole scavengers. Therefore, we attribute the buildup of negative charge at substrates to lower back-transfer rates of electrons (k_{CT2}) to neutralize PDI molecules.

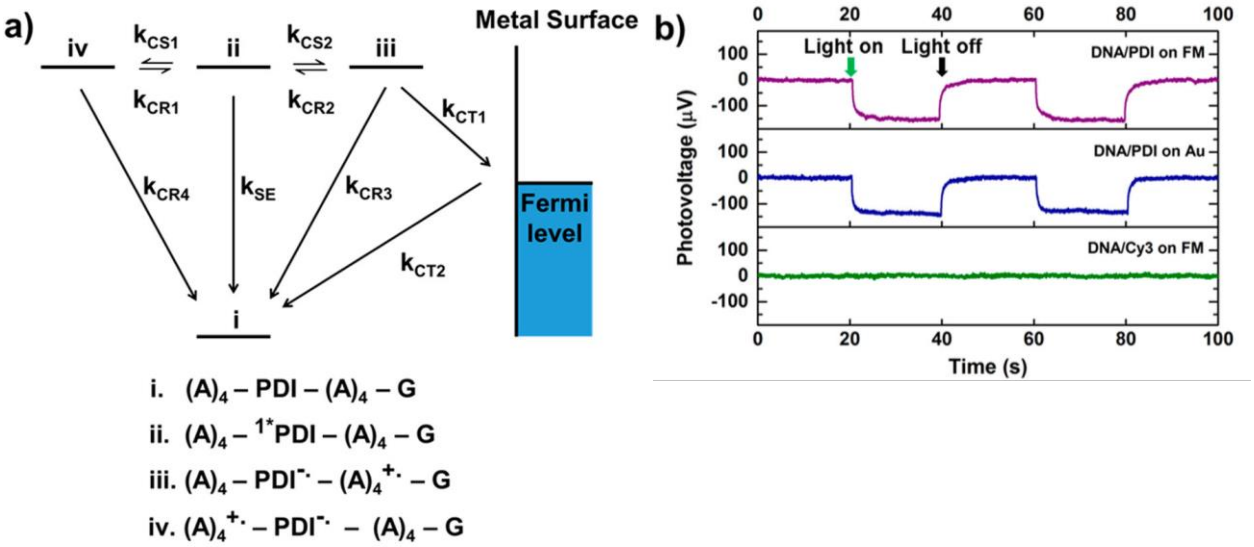

Figure II.3. (**a**) Schematic of relaxation pathways following photo- excitation of *N*,*N*′-bis[3,3′-(dimethylamino)propylamine] 3,4,9,10-perylenetetracarboxylic diimide (PDI) associated within abasic sites in DNA, where k_{CSn}, k_{CRn}, and k_{CTn} describe the rates of charge separation, recombination, and transfer to/from the underlying nonferromagnetic Au or ferromagnetic Au substrates, respectively. The rate of stimulated emission is described by k_{SE}. Roman numerals represent the ground and excited states of DNA/PDI complexes and are described further in the text. (**b**) Representative baseline-subtracted photovoltage measurements under open-circuit conditions in deoxygenated PBS obtained by irradiating DNA/PDI complexes assembled on ferromagnetic substrates (top), DNA/PDI complexes on nonferromagnetic Au substrates (middle), and DNA/ Cy3 complexes on ferromagnetic substrates (bottom) with 532 nm illumination at 20 s intervals.

On FM or nonferromagnetic Au substrates, negligible changes in photovoltages were measured when DNA molecules that contain abasic sites were annealed and assembled on substrates in the absence of PDI, when complementary DNA strands lacking abasic sites were annealed and assembled in the presence of PDI, or when thiolated ssDNA molecules incubated with PDI were assembled on FM or nonferromagnetic Au substrates (Figure SII.5).

The photoelectrochemical findings for pure DNA/PDI SAMs agree with the positive, anodic photocurrents generated in experiments by Yamana and co-workers with PDI molecules associated with dsDNA containing abasic sites on Au substrates.[43,44] In our experiments, negligible changes in photovoltages were generated on FM substrates functionalized with pure DNA/Cy3 SAMs (Figure II.3b). These results are consistent with our hypothesis that Cy3 chromophores do not facilitate efficient charge injection into the π-stacks of DNA duplexes (Figure II.2e).

Based on the magnetic field dependence of fluorescence contrast on FM substrates, we hypothesized that a substrate magnetization dependence would also occur in photoelectrochemical measurements. However, we did not definitively observe the CISS effect based on relative photocurrent/voltage magnitudes under opposite magnetic field conditions due to the high variability across substrates. Detectable differences in relative fluorescence intensities under opposite substrate magnetization orientations for DNA/PDI complexes on FM substrates (Figure II.2d,e) were enabled by background subtraction using the unpatterned SAM regions for each substrate and the large amounts of information gathered for each fluorescence image using segmented image analysis.

II.E. Discussion

Within polarized substrates, there are unequal distributions of electrons having magnetic dipole moments aligned parallel or antiparallel to the external magnetic field; electronic bands are split into majority and minority subbands, respectively. Because magnetic dipole moments lie *opposite* to the spin angular momentum of each electron, the spin direction lies

antiparallel to the external magnetic field direction for electrons in the majority subband and parallel to the field for electrons in the minority subband (Figure II.4).

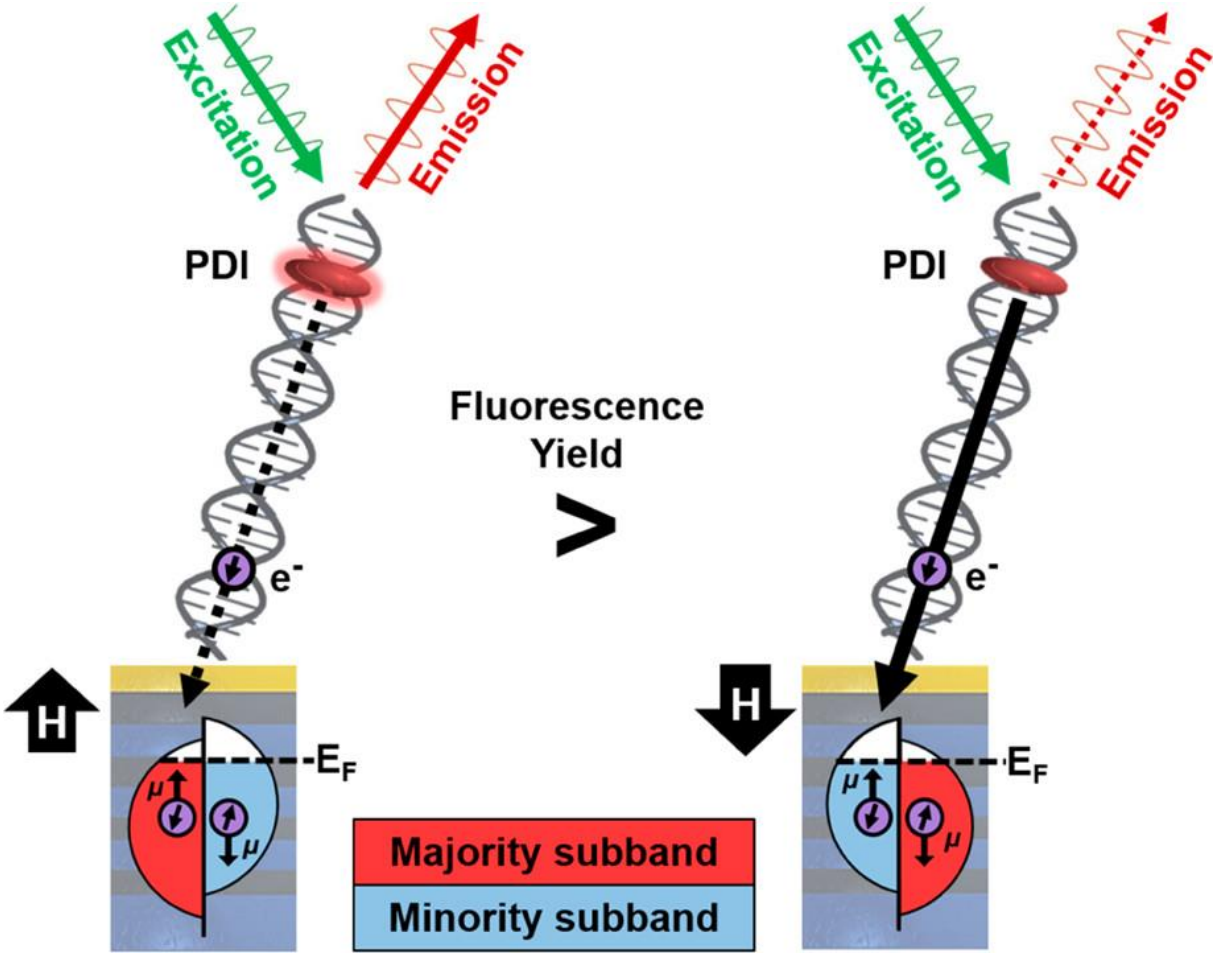

Figure II.4. Schematic depicting external magnetic field-dependent fluorescence of intercalated *N*,*N*′-bis[3,3′-(dimethylamino)-propylamine]-3,4,9,10-perylenetetracarboxylic diimide (PDI) molecules due to chiral-induced spin selectivity by helical DNA molecules. Fluorescence quenching as a result of DNA-mediated charge transfer to the underlying substrate is suppressed or enhanced when the ferromagnetic substrate is magnetized parallel (left) or antiparallel (right) to the surface normal, respectively. Purple arrows represent electron-spin orientation, μ represents the direction of the magnetic dipole moment of electrons, and E_F indicates the Fermi level of the metal substrate.

The observation of an increase in emission quenching and lower fluorescence intensity when the magnetic field is down suggests that DNA-mediated charge transfer and

injection into metal substrates is more efficient under this field orientation, *i.e.*, $(k_{CT1}, k_{CT2})_{\downarrow} > (k_{CT1}, k_{CT2})_{\uparrow}$. In Co/Pt multilayer substrates, the minority subbands are expected to have higher densities of unoccupied states above the Fermi level than the majority subband,[46] which makes the population of electrons transferred to the substrate more favorable when the spin of injected electrons is aligned with carriers in the minority subbands. Therefore, while the absolute spin orientation in the laboratory-defined axis cannot be directly measured, we infer that bound electrons, with their helicity or spin projections on the DNA helical axis aligned parallel to their motion, are preferentially transmitted through right-handed DNA duplexes in the charge-transport regime, consistent with theoretical predictions.[47]

While the relative fluorescence intensities of DNA/PDI complexes on FM substrates were significantly different between opposite substrate magnetization orientations, the absolute magnitude of the difference in our figure of merit was notably smaller than differences reported in other investigations of the CISS effect in double-stranded DNA. Göhler *et al*. reported spin polarizations as high as *ca.* −60% by dehydrated 78-mer dsDNA SAMs on Au substrates by measuring the spin of transmitted photoelectrons using a Mott polarimeter.[11] However, these results may not be directly comparable to our measurements due to possibly different mechanisms responsible for negative and positive spin polarization that result from multiple scattering events in photoemission *vs* hopping or tunneling along the extended π-stack of the DNA interior.[48-54] In the charge-transport regime of bound electrons confined to the helical molecules, the magnitudes of the relative barriers to transmission of electrons with helicity parallel *vs* antiparallel to velocity within dsDNA may depend on the effective potential difference across the molecules.[7] Indeed, in the conductive

AFM measurements performed by Xie *et al*., the differences in average current measured when the underlying Ni substrates were magnetized up *vs* down increased as the electric potential between the tip and substrate was increased from 0 V to ±3 V.[1] In those measurements, minimal differences in the average current measured through individual Ni-DNA-Au nanoparticle-(nonferromagnetic) tip junctions were observed below ~1 nA (at *ca.* ± 0.5 V). For comparison, in our work, substantially lower photocurrent densities of ~3–4 nA/cm^2 for pure SAMs of DNA/PDI complexes on FM substrates were measured under open-circuit conditions (Figure SII.6). Moreover, the differences in the magnitude of the spin filtering effect observed between our work and that of Xie *et al*. may also arise from structural differences in the equilibrium conformation of dsDNA and variation in possible conduction mechanisms along the duplex that accompany dehydration.[9]

Using electrochemical techniques to probe spin selectivity in DNA-mediated charge transfer in hydrated DNA SAMs, Zwang et al. reported changes in the integrated reduction peaks of 15 ± 1% for MB^+ and 12 ± 2% for Nile blue using ferromagnetic electrodes modified with 30-mer and 29-mer double-stranded DNA, respectively.[2] Comparatively, it is possible that observation of the CISS effect using the photoelectrochemical system described herein is hindered by the high relative rates of charge recombination within DNA/PDI complexes *vs* the rate of charge transfer to the metal surface. While the rate constants for charge separation and recombination within DNA/PDI complexes ($k_{CS1,2}$ and $k_{CR1,2,3,4}$, Figure II.3a) are on the order of 10^{10} s^{-1}, the electron transfer rates between redox reporters within DNA assembled *via* thiolated tethers on Au substrates are orders of magnitude smaller.[12,55] The latter rates decrease exponentially with increasing numbers of methylene units that commonly comprise the thiolated tethers attached to DNA sugar-phosphate backbones,

which demonstrates limitations of charge-transfer rates on tunneling through alkanethiol bridges.[24,55-57] Alternative tethering strategies resulting in stronger coupling between DNA π-stacks and underlying substrates, such as by direct covalent substrate attachment to nucleic acid bases, may be beneficial in probing additional parameters influencing spin-selective transport through DNA.

In summary, we have demonstrated and applied a technique to investigate and to quantify the chiral-induced spin selectivity effect in patterned DNA SAMs that contain noncovalently tethered perylenediimide chromophores. Emission was observed to depend on external magnetic field orientation only when DNA/dye complexes were assembled on FM substrates and photooxidizing chromophores were well coupled to the DNA base stack to enable charge injection and subsequent transfer to surfaces. Under these conditions, fluorescence intensities associated with opposite magnetic field orientations were significantly different. Importantly, our results suggest that differences in DNA-mediated charge transport associated with field orientation are modest compared to substrate-to-substrate variations. Thus, investigating large numbers of substrates, conducting statistically relevant numbers of measurements, and using patterned image analysis are necessary to determine which substrate magnetization direction favors polarized charge injection at molecule–metal interfaces.

II.F. Materials and Methods

II.F.1. Materials

Perylene-3,4,9,10-tetracarboxylic dianhydride, 3-(dimethylamino)propylamine, 11-mercapto-1-undecanol (MCU), magnesium chloride, sodium chloride, potassium chloride, 0.01 M phosphate-buffered saline, (PBS, [NaCl] = 138 mM, [KCl] = 2.7 mM, pH 7.4), tris-EDTA buffer (with 50 mM NaCl, pH 8.0), *DL*-dithiothreitol, and illustra NAP-5 size-exclusion gravity columns were purchased from Sigma-Aldrich (St. Louis, MO, USA). Absolute ethanol was from Decon Laboratories, Inc. (King of Prussia, PA, USA). Deionized water (~18 MΩ) was obtained from a Millipore water purifier (Billerica, MA, USA). Hydrochloric acid, sodium hydroxide, and 1-butanol were purchased from Thermo Fisher Scientific (Waltham, MA, USA). The SYLGARD 184 silicone elastomer base and curing agent were purchased from Ellsworth Adhesives (Germantown, WI, USA). All DNA sequences (shown below) were purchased from Integrated DNA Technologies (IDT, HPLC-purified with a certificate of analysis *via* mass spectroscopy, Coralville, IA, USA).

The following DNA sequences were used (5′ → 3′):

(1) /5ThioMC6-D/CG CTT CGC TTC GCT TCG CTT CGC TTC GCT TTT/dSp/TT TT

(2) AAA A/idSp/A AAA GCG AAG CGA AGC GAA GCG AAG CGA AGC G

(3) /5ThioMC6-D/CG CTT CGC TTC GCT TCG CTT CGC TTC GCT TTT TTT T

(4) AAA AAA AAG CGA AGC GAA GCG AAG CGA AGC GAA GCG

(5) /5Cy3/AA AAA AAA GCG AAG CGA AGC GAA GCG AAG CGA AGC G

II.F.2. Substrate Fabrication and Surface Preparation

Perpendicular magnetic thin films were fabricated on Si substrates with thermally oxidized SiO_2 using a multicathode magnetron sputtering system with a base pressure of $<3 \times 10^{-8}$ Torr. The stacking structure of samples was Si/SiO_2 substrate/Ta 3/Pt 2/[Co 0.5/Pt 0.3]$_3$/Co 0.5/Au 1 (layers in nm). The deposition temperature was fixed at room temperature in an Ar gas atmosphere. Vibrating sample magnetometry and SQUID magnetometry were used to characterize the films (Figure SII.7). Nonferromagnetic Au substrates were prepared by electron-beam evaporation (CHA Industries, SOLUTION, Fremont, CA, USA) onto Si wafers. Titanium was deposited as an adhesion layer (10 nm, 1 Å/s), followed by Au evaporation (100 nm, 2 Å/s) at a base pressure of 1.5×10^{-6} Torr. Before functionalizing substrates, both FM and nonferromagnetic Au substrates were cleaned by sonicating for 10 min in ethanol and 10 min in water before being rinsed with water and blown dry.

II.F.3. Synthesis of *N*,*N*′-Bis[3,3′-(dimethylamino)propylamine]-3,4,9,10-perylenetetracarboxylic diimide (PDI)

The synthetic procedure was modified from the literature (Figure SII.8).[58] In a typical synthesis, 1.25 g of perylene-3,4,9,10-tetracarboxylic dianhydride and 3 mL of 3-(dimethylamino)propylamine were combined in 100 mL of 1-butanol at room temperature in a 500 mL round-bottom flask. While stirring, the solution was heated to 90 °C for 12 h under reflux. The insoluble, crude product was isolated by vacuum filtration and washed thoroughly with water and ethanol. The washed product was then dissolved in 1 M HCl. The solution was vacuum filtered to remove insoluble impurities. The pH of the filtered aqueous solution was adjusted to ~10 with 5% NaOH to precipitate the product, which was

isolated by filtration and washed thoroughly with water before vacuum drying. The purified product was characterized by mass spectrometry and ^{1}H NMR (Figures SII.9 and SII.10). The isolated compound was stored in a sealed container at ambient temperature and pressure.

II.F.4. DNA and DNA/*N*,*N*′-bis[3,3′-(dimethylamino)-propylamine]-3,4,9,10-perylene-tetracarboxylic diimide (PDI) Complex Preparation and Annealing

Desalted and lyophilized single-stranded oligonucleotides, as received from IDT, that contained disulfide tethers attached to 5′ ends were dispersed in 50 μL tris-EDTA buffer, pH 8.0, and mixed with ∼30 mg of *DL*-dithiothreitol for at least 1 h to reduce the disulfide moieties to thiols. Oligonucleotides were then purified *via* gravity-flow size-exclusion chromatography using illustra NAP-5 columns. The eluent DNA concentrations were determined using UV absorption signatures (Thermo Scientific NanoDrop 2000 spectrophotometer). Desalted and lyophilized single-stranded oligonucleotides, as received from IDT, that did not contain disulfide modifications were simply dispersed in tris-EDTA buffer, pH 8.0, without further purification and were diluted to specific concentrations as needed.

Fresh stock solutions of 10 μM PDI in PBS were prepared before each experiment due to aggregation and irreversible precipitation of PDI in aqueous solutions after a few days. To promote dispersion in aqueous solution from the as-synthesized powder, ∼2 mg of PDI was first dissolved in a few milliliters of 10× PBS, pH 6.8, and subsequently diluted with water because the slightly acidic conditions favored protonation of terminal tertiary amines. To anneal oligonucleotides and to create double-stranded DNA/PDI complexes for surface assembly, complementary strands of stock DNA dispersed in tris-EDTA buffer, pH 8.0, were

combined in a 5:1 ratio for a final 5 μM DNA concentration and 1 μM of PDI in 1× PBS buffer. Solutions were bubbled with N_2 and annealed using the following protocol: 95 °C for 10 min, 85 °C for 10 min, 75 °C for 10 min, and 65 °C for 10 min, followed by slow cooling to room temperature using a programmable dry bath (ThermoFisher Scientific). The annealed and assembled DNA/PDI complexes were characterized *via* UV−vis spectroscopy (Figures SII.11, SII.12, and SII.13).

An appropriate volume of 1 M $MgCl_2$ was added before incubation on surfaces for a final 100 mM $MgCl_2$ to minimize electrostatic repulsion between negatively charged backbones of oligonucleotides and to form denser DNA assemblies on surfaces.

II.F.5. Polydimethylsiloxane (PDMS) Stamp Preparation and Chemical Patterning

The SYLGARD 184 silicone elastomer base and curing agent were mixed thoroughly in a 10:1 mass ratio, degassed under vacuum, and subsequently cast onto master substrates containing protruding square (25 μm × 25 μm) pillars (images not shown) or holes (Figures II.1d and II.2a–d). The masters were previously fabricated using standard photolithography and situated in plastic Petri dishes. The PDMS was cured overnight at 70 °C. Polymerized stamps were then removed from the master, cut to appropriate sizes, and cleaned by 4.5 h soaking in hexanes. The stamps were once more heated at 70 °C overnight, sonicated in 1:1 water/ethanol solution for 15 min, rinsed briefly with ethanol, and stored under ambient conditions until used.

For fluorescence microscopy measurements, surfaces were patterned to provide regions of contrast between patterned areas containing inserted DNA and those devoid of DNA (except where DNA inserts into native SAM defects).[35] Patterning was carried out using

CLL from substrates with 100% 11-mercapto-1-undecanol (MCU) SAMs. Monolayers of MCU were formed on ferromagnetic or Au substrates by immersing clean substrates in a 1 mM ethanolic solution of MCU for 18 h. Substrates were then rinsed thoroughly with ethanol and dried with nitrogen gas. Patterned PDMS stamps were exposed to oxygen plasma (Harrick Plasma, 18 W, 10 psi O_2) for 40 s to create reactive surfaces. Activated stamps were brought into contact with surfaces functionalized with MCU for 4 h prior to stamp removal. After lift-off, substrates were rinsed thoroughly with water and ethanol before incubation with preannealed DNA/PDI (5:1) solutions containing 100 mM $MgCl_2$ in a humid environment for 24–48 h.

II.F.6. Fluorescence Microscopy and Image Analysis

Deionized water and PBS were used to rinse substrates thoroughly before imaging the hydrated surfaces using an inverted fluorescence microscope and a 10× objective lens (Axio Observer.D1, Carl Zeiss MicroImaging, Inc., Thornwood, NY, USA) with a fluorescence filter set (43 HE/high efficiency) having excitation and emission wavelengths of 550 ± 25 nm and 605 ± 70 nm, respectively. The DNA-functionalized surfaces were kept hydrated to prevent dehybridization or structural changes that accompany loss of water molecules associated with DNA duplexes.[9] For spin-selective measurements, a cylindrical neodymium-iron-boron magnet (K&J Magnetics, Pipersville, PA, USA) was placed directly beneath substrates. Under field-up (down) conditions, the north (south) pole of the magnet was flush with the backside of the substrates.

Grayscale images contained 1040 × 1388 pixels with fluorescence intensity values assigned integer values between 0 and 255. Images were subjected to a region-based

segmentation algorithm. Details of the analysis with links to the MATLAB code are found elsewhere.[38] All fluorescence microscopy images obtained under an external magnetic field that were used for image analysis to quantify fluorescence were obtained using 5 s exposures and subjected to identical operations for image segmentation, including the number of iterations, weight of bias field smoothness, and artifact thresholds. If image pixel intensities were too low for pattern identification and segmentation failed, image contrast was uniformly adjusted as necessary for all images (field up and field down) from a sample/field of view.

Substrates bearing DNA/PDI complexes assembled on ferromagnetic (FM) substrates, DNA/PDI complexes on nonferromagnetic Au substrates, and DNA/Cy3 complexes on FM substrates were imaged (N = 22 substrates per experimental condition). A total of 18 images (nine for field-up and nine for field-down conditions) were obtained for each substrate from the same field of view. The magnetic field orientation was reversed after acquisition of each three images. Following image segmentation, histograms of pixel intensities were created and fit to Gaussian distributions. Relative fluorescence intensities for each image were calculated using mean pixel intensities acquired from the Gaussian fits ($\bar{x}_{patterned}$ and $\bar{x}_{unpatterned}$) and then by normalizing $\bar{x}_{patterned}$ and $\bar{x}_{unpatterned}$ to the average $\bar{x}_{unpatterned}$ value calculated from every three sequential captured images (Figure II.2d). To account for substrate-to-substrate variability, the 18 $\bar{x}_{patterned}/\bar{x}_{unpatterned}$ values from each substrate were normalized to the overall fluorescence intensity average value from all field-up and field-down images. These normalized mean fluorescence intensities are reported in Figure II.2e.

II.F.7. Statistics

Two-tailed paired t tests were used to compare $\bar{x}_{patterned}$ and $\bar{x}_{unpatterned}$ to test statistical significance in fluorescence intensity in patterned *vs* unpatterned regions for both external magnetic field orientation for every sample. Normalized mean fluorescence intensities were evaluated by two-way analysis of variance followed by Bonferroni *post hoc* tests. The notation [$F(2,126) = 4.64$, $P < 0.05$] in the main text that describes the results of the two-way analysis of variance indicates that there are 2 degrees of freedom for the interaction between both factors (calculated from the product of 2 – 1 = 1 degree of freedom for magnetic field orientation and 3 – 1 = 2 degrees of freedom for dye/substrate condition). The value of 126 represents residual variation that results from differences among replicates that are not related to systematic alterations between measurements and is calculated from N – (a × b) where N = 132 is the number of average normalized relative fluorescence intensity values used in the statistical analysis (22 field-up values and 22 field-down values from each dye/substrate condition), and a and b represent the number of levels for each factor (2 different magnetic field orientations and 3 different dye/substrate conditions). The *F* statistic of 4.64 describes the interaction effect that one factor has over the other and is used to calculate a *P* value by comparing against the sampling distribution for the null hypothesis. Statistical analyses were carried out using GraphPad Prism (GraphPad Software Inc., San Diego, CA, USA). Data are reported as means ± standard errors of the means with probabilities $P < 0.05$ considered statistically significant.

II.F.8. Photoelectrochemical Measurements

These measurements were conducted on a Reference 600 Potentiostat/Galvanostat/ZRA (Gamry Instruments, Warminster, PA, USA). A custom-made (polytetrafluoroethylene) electrochemical cell and a three-electrode setup were used with a Ag/AgCl reference electrode and Pt-wire counter electrode. Ferromagnetic multilayer thin films and nonferromagnetic Au films deposited on Si or Si/SiO_2 substrates and functionalized with pure SAMs of DNA or DNA/dye complexes were used as the working electrodes. Top electrical contact was made with the substrates using a custom-made gold ring. A rubber O-ring on the interior of the gold contact made a leak-proof seal. The electrolyte solution, 1× PBS, was bubbled with N_2 for 20 min prior to measurements. Substrates were kept hydrated during cell assembly. Chronoamperometric measurements were performed using PHE200 Physical Electrochemistry Software (Gamry Instruments, Warminster, PA, USA) and open-circuit voltages. Working electrode surfaces were irradiated with 532 nm light (4.5 mW, Thorlabs, Newton, NJ, USA) in 20 s intervals. Working electrode areas were 0.08 cm^2.

Supplementary Material

Analyzing Spin Selectivity in DNA-Mediated Charge Transfer *via* Fluorescence Microscopy

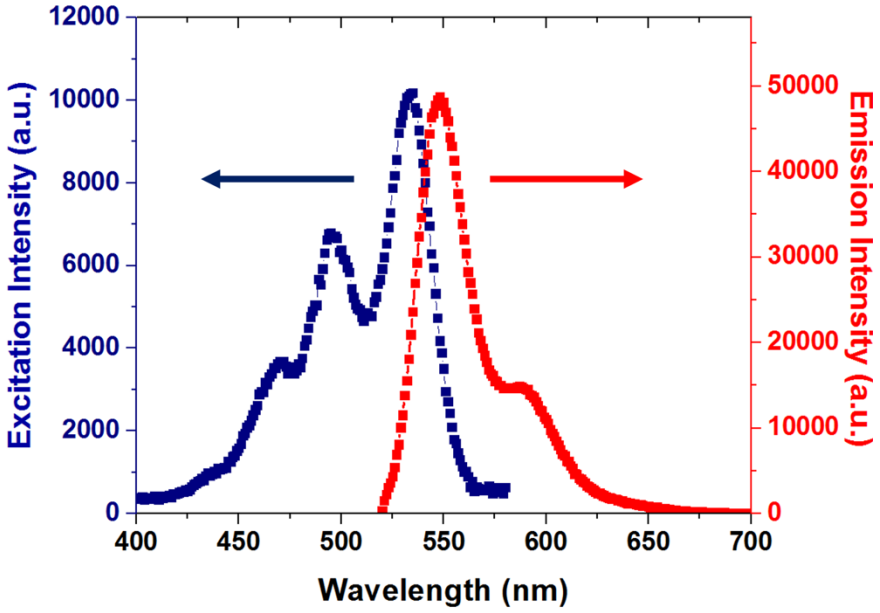

Figure SII.1. Representative excitation and emission spectra of *N*,*N*'-bis[3,3'-(dimethylamino)propylamine]-3,4,9,10-perylenetetracarboxylic diimide (PDI, 30 μM) in phosphate-buffered saline *sans* DNA. Excitation scans were collected by monitoring emission at 620 nm. Emission spectra were collected using excitation at 475 nm. All excitation and emission spectra were collected on a QuantaMaster spectrofluorometer (Photon Technology International).

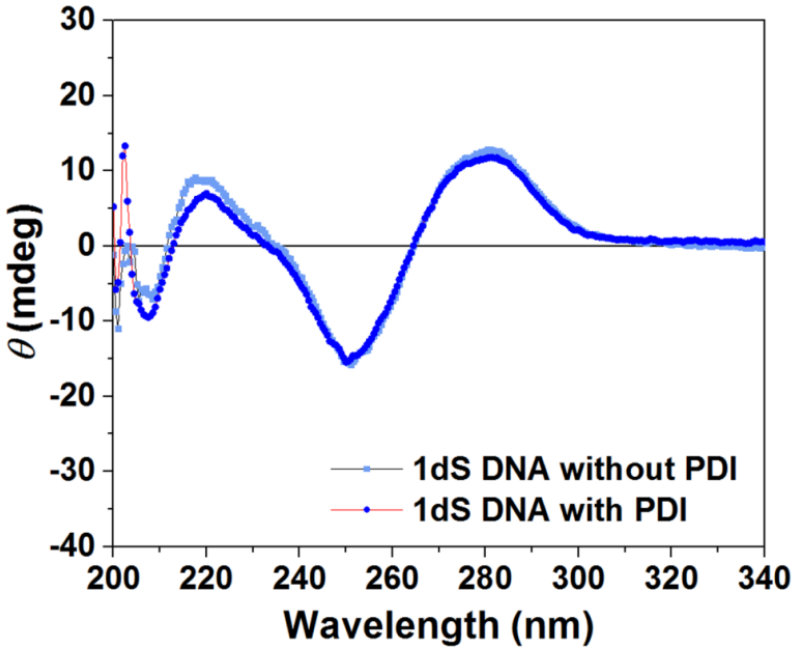

Figure SII.2. Representative circular dichroism spectra of double-stranded DNA containing abasic sites (1dS) in the absence and presence of *N*,*N*'-bis[3,3'-(dimethylamino)propylamine]-3,4,9,10-perylenetetracarboxylic diimide (PDI) in a 1:1 ratio in phosphate-buffered saline (PBS) containing 100 mM $MgCl_2$.The DNA concentrations were 2 μM. Solutions of pre-annealed DNA without or with PDI were prepared as described in the main text Methods section. The right-handed B-form of DNA duplexes are confirmed in the two spectra by positive bands near 285 nm and negative bands near 250 nm. The two spectra are nearly superimposable indicating that the binding of PDI molecules within the hydrophobic pockets of 1dS DNA do not significantly disrupt the right-handed helical structure of double-stranded 1dS DNA. Measurements were taken on a JASCO J-715 circular dichroism spectrophotometer at room temperature with six scans per sample. Average scans are shown after baseline subtraction of spectra taken in PBS. The resolution was 0.5 nm, the bandwidth was 1.0 nm; the response time was 4 s, and the collection speed was 20 nm/min.

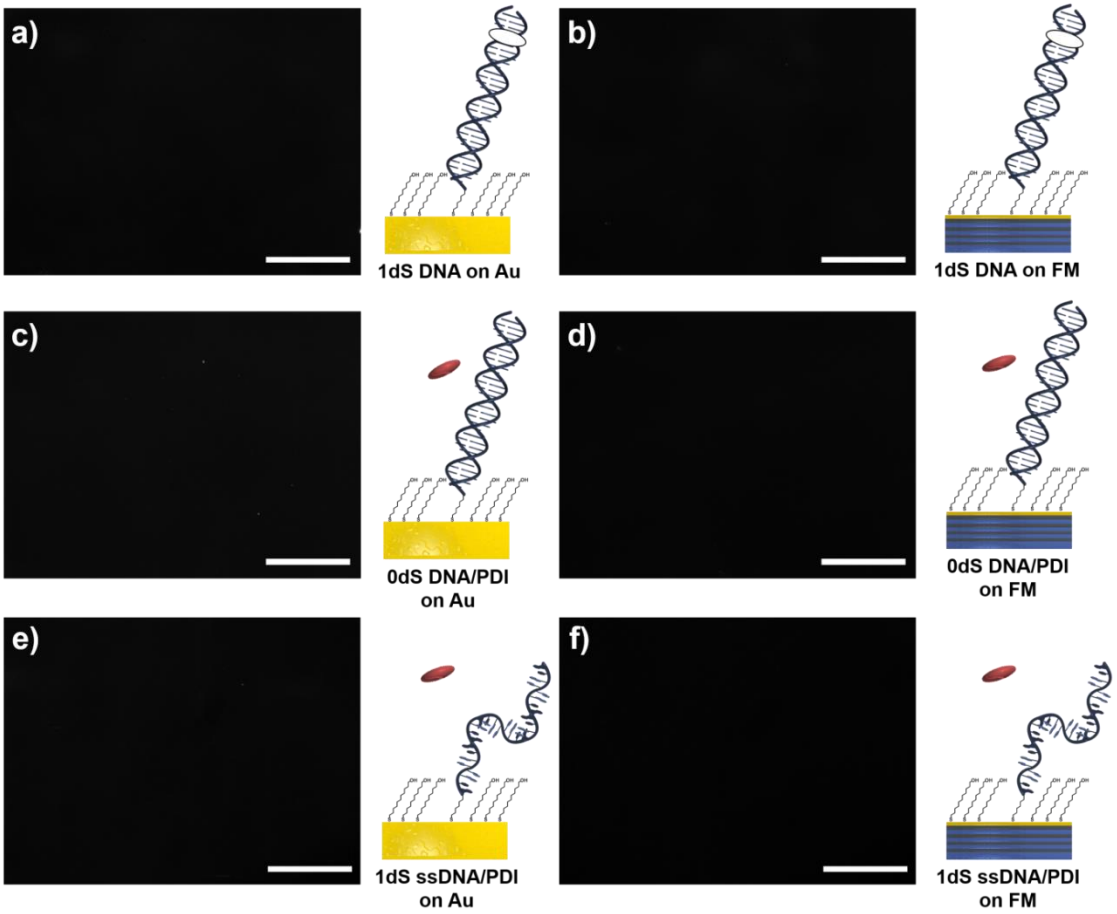

Figure SII.3. Fluorescence microscopy images and schematics of photoelectrochemical control experiments. No fluorescent patterns (contrast) was observed for any condition. The excitation wavelength was 550 nm. The exposure time was 7 s (scale bars are 200 μm.) The following samples were prepared on 11-mercapto-1-undecanol SAMs patterned *via* chemical lift-off lithography: (**a**) duplex DNA with abasic sites (1dS) without *N*,*N*'-bis[3,3'-(dimethylamino)propylamine]-3,4,9,10-perylenetetracarboxylic diimide (PDI) assembled on non-ferromagnetic (Au) substrates, (**b**) 1dS DNA without PDI on ferromagnetic (FM) substrates, (**c**) duplex DNA without abasic sites (0dS) annealed in the presence of PDI assembled on Au or (**d**) FM substrates, and (**e**) 1dS single-stranded thiolated DNA incubated with PDI molecules on Au or (**f**) FM substrates.

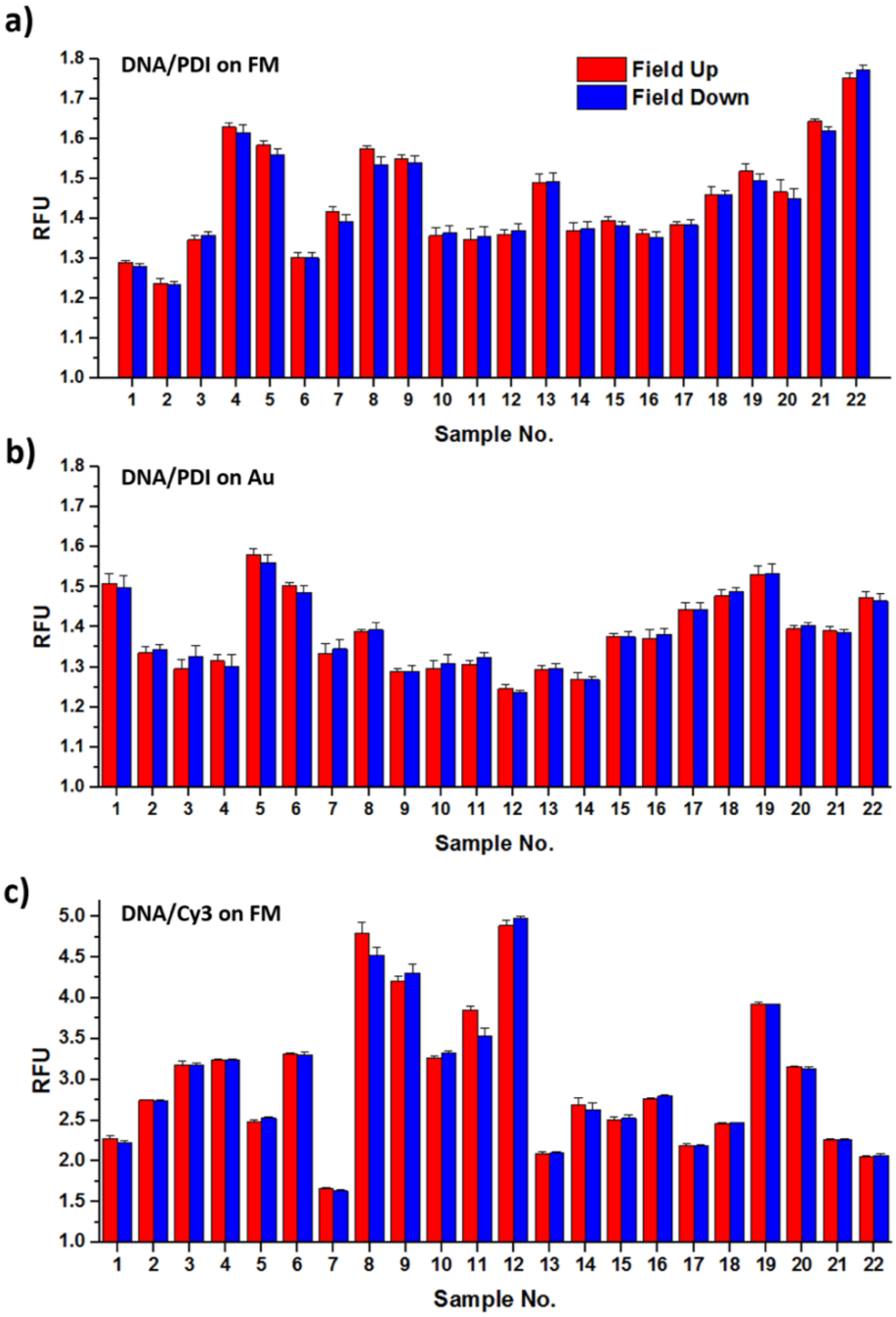

Figure SII.4. Mean fluorescence intensities (reported as relative fluorescence units, RFU) of patterned regions relative to the unpatterned regions from DNA/*N*,*N*'-bis[3,3'-(dimethylamino)propylamine]-3,4,9,10-perylenetetracarboxylic diimide (PDI) complexes assembled on (**a**) ferromagnetic (FM) substrates, (**b**) DNA/PDI on non-ferromagnetic Au substrates, and (**c**) DNA/Cy3 complexes on FM substrates. For each sample, *N*=9 images field up, *N*=9 images field down. Error bars represent standard errors of the means.

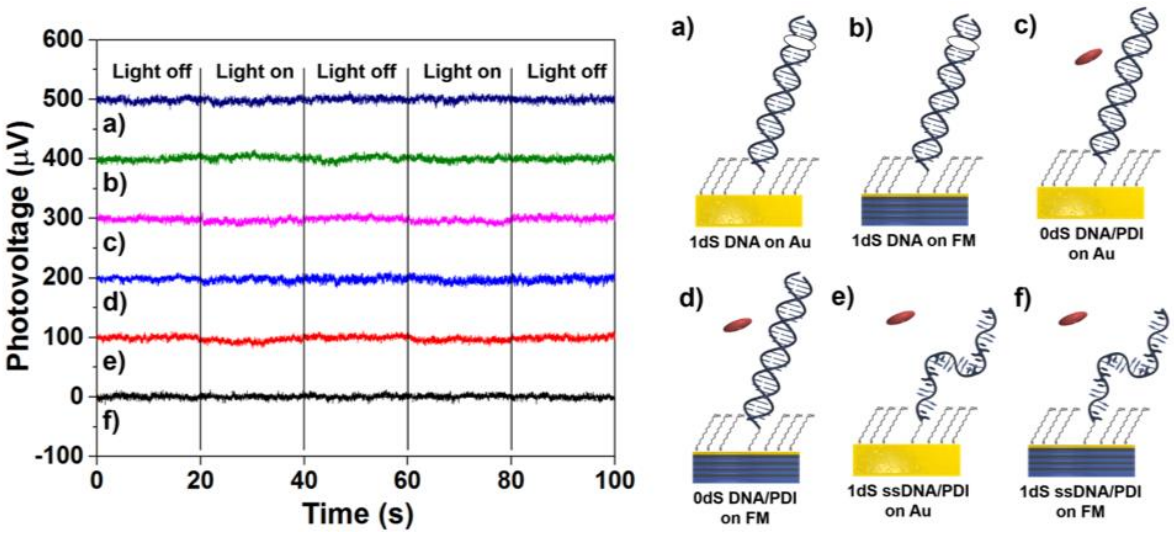

Figure SII.5. Representative control baseline-subtracted photovoltage measurements under open-circuit voltage conditions in phosphate-buffered saline obtained by irradiating the following samples of pure DNA self-assembled monolayers with 532 nm light at 20 s intervals: (**a**) duplex DNA with abasic sites (1dS) without *N*,*N*'-bis[3,3'-(dimethylamino)propylamine]-3,4,9,10-perylenetetracarboxylic diimide (PDI) assembled on non-ferromagnetic (Au) substrates, (**b**) 1dS DNA without PDI on ferromagnetic (FM) substrates, (**c**) duplex DNA without abasic sites (0dS) annealed in the presence of PDI assembled on Au or (**d**) FM substrates, and (**e**) 1dS single-stranded thiolated DNA incubated with PDI molecules on Au or f) FM substrates.

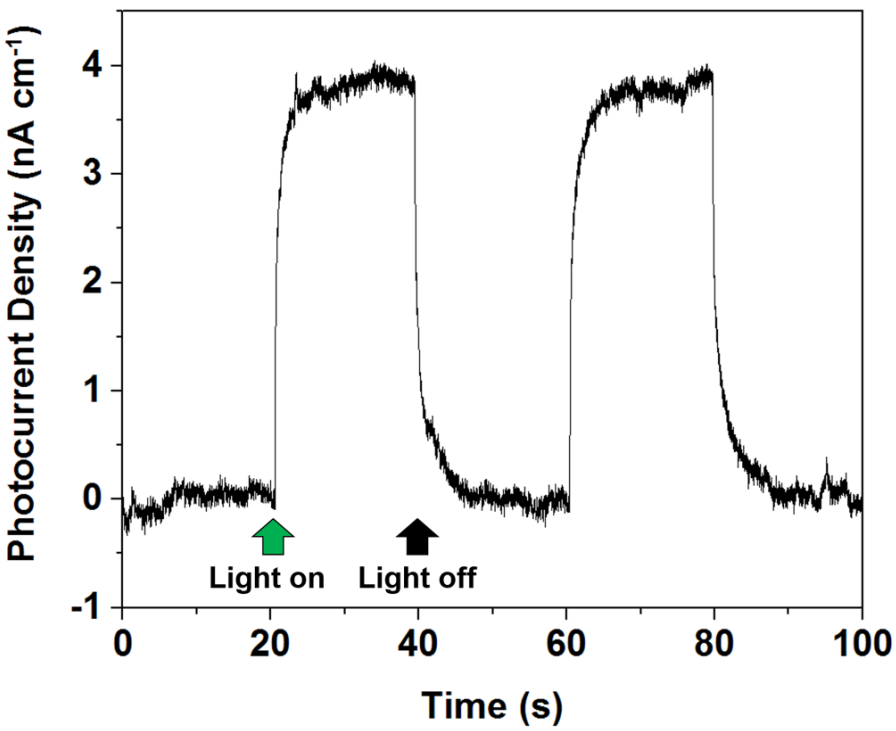

Figure SII.6. Representative baseline-subtracted photocurrent density measurements under open-circuit conditions in deoxygenated phosphate-buffered saline obtained by irradiating DNA/PDI complexes assembled on ferromagnetic substrates with 532 nm illumination in 20 s intervals.

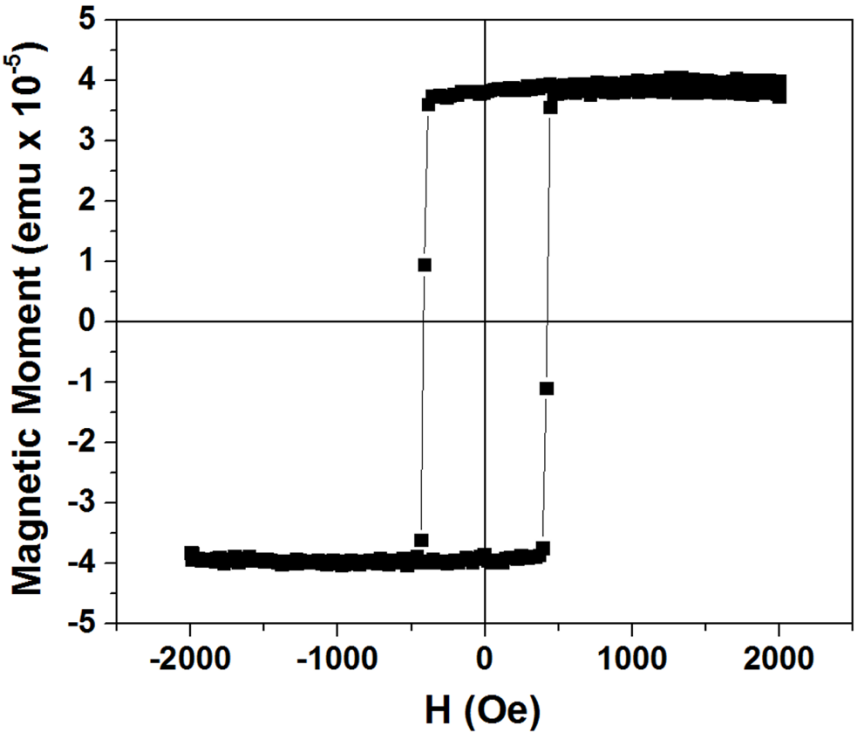

Figure SII.7. Characterization of ferromagnetic substrates with perpendicular magnetic anisotropy. Representative hysteresis of bare, perpendicularly magnetized ferromagnetic multilayer substrates composed of Ta 3/Pt 2/[Co 0.5/Pt 0.3]$_3$/Co 0.5/Au 1 (layers in nm) on Si/SiO_2. Measurements were performed at room temperature on a Quantum Design, Inc. instrument (VersaLab, San Diego, CA, USA).

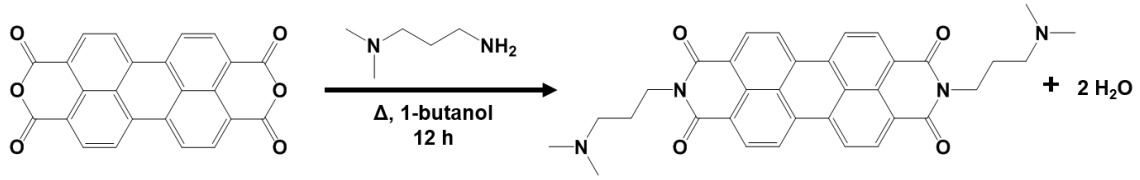

Figure SII.8. Synthesis scheme of *N*,*N*'-bis[3,3'-(dimethylamino)propylamine]-3,4,9,10-perylenetetracarboxylic diimide (PDI).

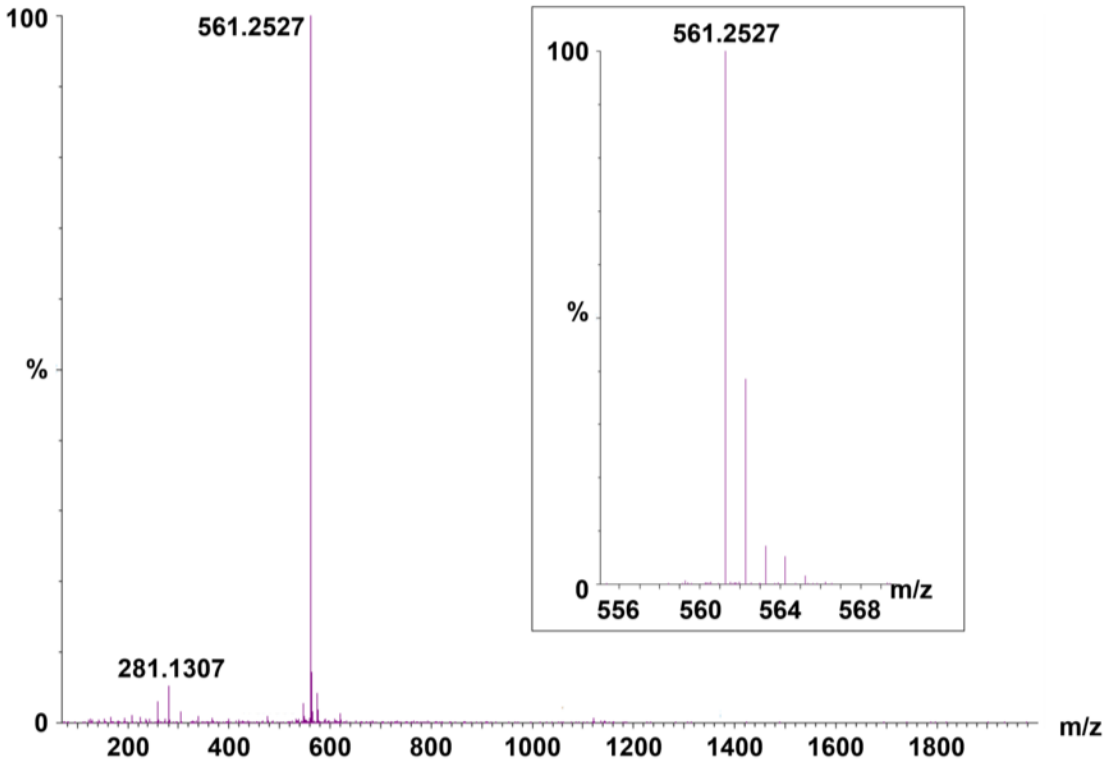

Figure SII.9. Time-of-flight electrospray ionization mass spectrum of *N*,*N*' -bis[3,3'-(dimethylamino)propylamine]-3,4,9,10-perylenetetracarboxylic diimide (PDI) in chloroform. Calculated mass for $C_{34}N_4O_4H_{32}$ H=561.2502 Da. Mass deviation=0.0025 Da or 4.6 ppm. Peaks at mass-to-charge ratios (m/z) 561.2527 and 281.1307 correspond to singly and doubly ionized forms of PDI, respectively. Inset displays a high-resolution spectrum of isotope effects near the molecular ion peak at m/z=561.2527. Data were taken on a Waters Micromass LCT Premier mass spectrometer equipped with a Waters ACQUITY UPLC System.

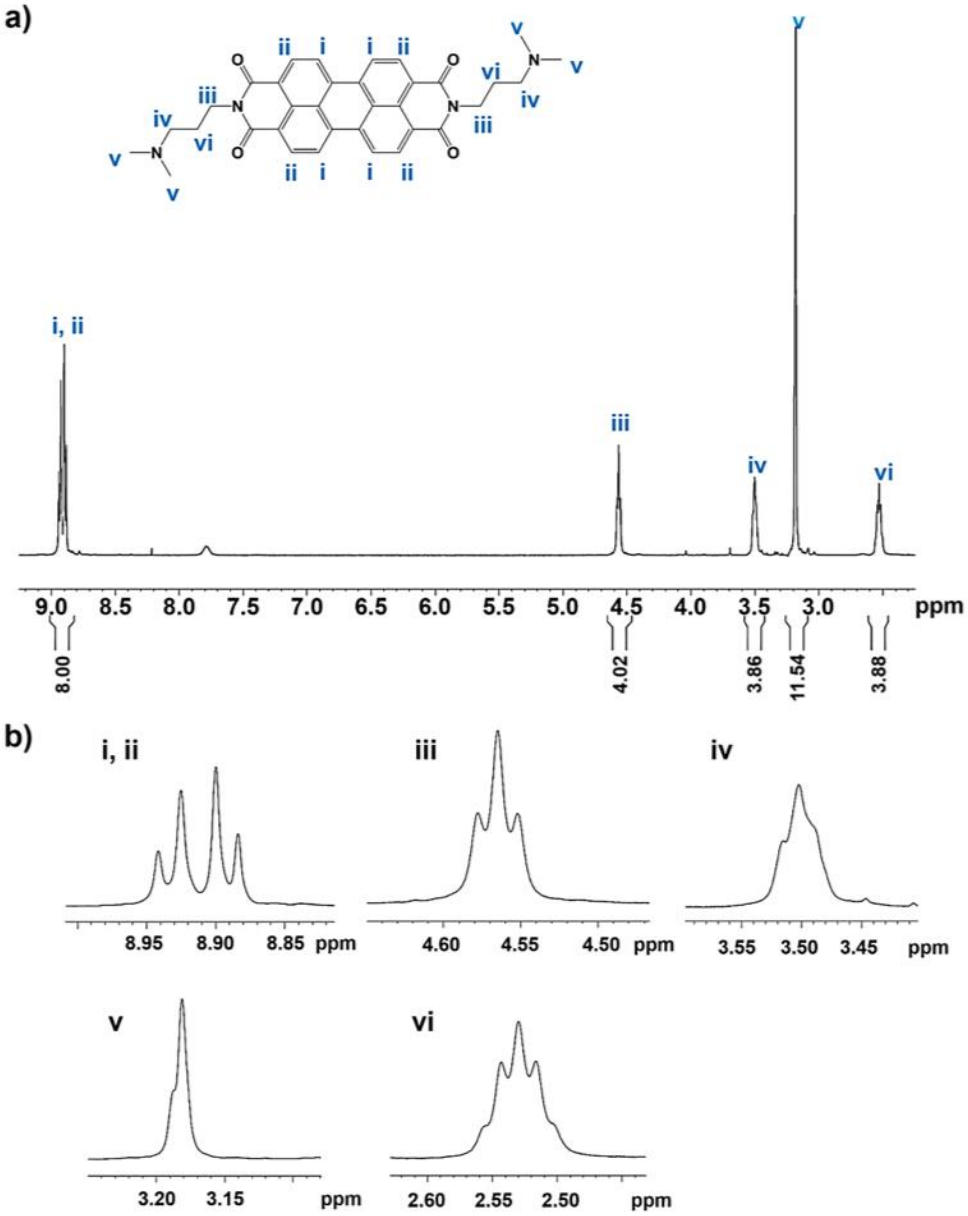

Figure SII.10. (**a**) A ^{1}H NMR (500 MHz, deuterated trifluoroacetic acid) spectrum of *N*,*N*'-bis[3,3'-(dimethylamino)propylamine]-3,4,9,10-perylenetetracarboxylic diimide. Spectra were recorded at 25 °C on a Bruker AV500 spectrometer. (**b**) High resolution spectra of each series of equivalent hydrogens. Positions of equivalent hydrogens are indicated by Roman numerals. (i, ii) δ 8.91 (dd; J = 8.1, 22.5 Hz; 8H; CH), (iii) δ 4.56 (t; J = 6.4 Hz; 4H; CH_2), (iv) δ 3.50 (t; J = 6.6, ~6.2 Hz; 4H; CH_2), (v) δ 3.18 (d; ~3.3 Hz; 12H, CH_3), (vi) δ 2.58 (quin; J = 6.6 Hz; 4H; CH_2). The apparent and skewed doublet of doublets in (i, ii) that appears for the unresolved, non-equivalent aryl hydrogens is a result of higher order coupling. We attribute the skewed triplet in (iv) and the doublet in (v) to hindered internal rotation of the terminal nitrogen atoms bearing lone pairs resulting in non-equivalent environments for hydrogen atoms on the adjacent methylene and methyl groups.

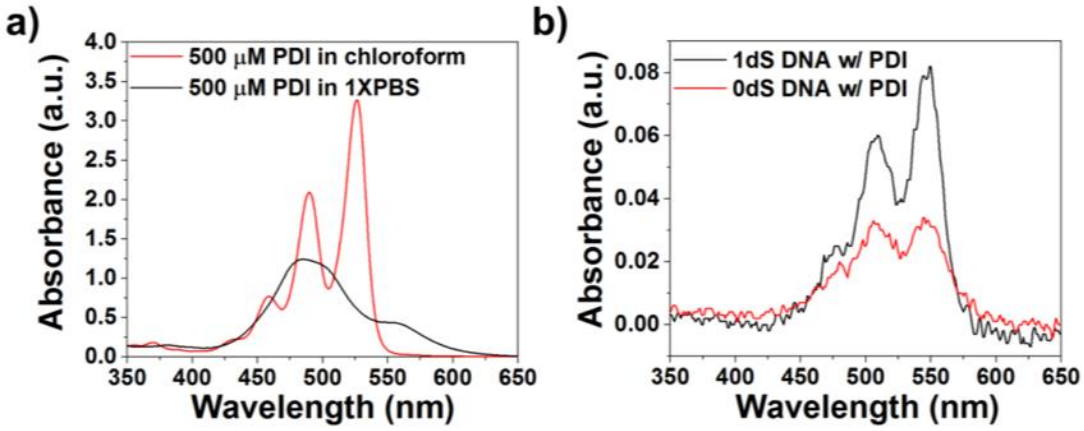

Figure SII.11. Characterization of the optical properties of perylenediimide derivatives. (**a**) Representative ultraviolet-visible spectra of *N*,*N*'-bis[3,3'-(dimethylamino)propylamine]-3,4,9,10-perylenetetracarboxylic diimide (PDI) dispersed in chloroform (red) or phosphate-buffered saline (PBS). In aqueous solutions, the diminished and broadened absorption spectrum is attributed to aggregation of the dye molecules. (**b**) Representative ultraviolet-visible spectra of PDI in a 1:1 ratio with double-stranded DNA containing abasic sites (1dS) or lacking abasic sites (0dS). The DNA and PDI concentrations are 20 μM. Solutions of pre-annealed DNA with or without PDI were prepared as described in the main text Methods section. In the presence of DNA containing abasic hydrophobic pockets, the absorption spectrum of PDI resembles that of free, non-aggregated PDI dispersed in chloroform. By contrast, the diminished absorption peaks in the presence of 0dS DNA indicate self-aggregation or nonspecific binding with the negatively charged backbone of the DNA duplex. Measurements in a) and b) were taken using a Thermo Scientific Evolution 600 UV-Vis and a Thermo Scientific NanoDrop 2000 spectrophotometer, respectively.

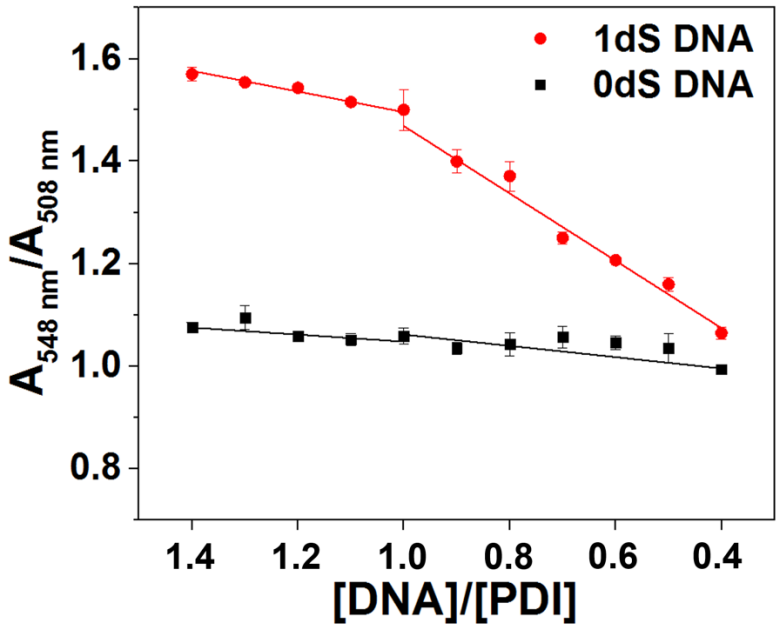

Figure SII.12. Evidence for noncovalent binding of PDI at abasic sites in DNA in a 1:1 ratio. Absorbance ratios (548 nm/508 nm) from ultraviolet-visible spectra of *N*,*N*'-bis[3,3'-(dimethylamino)propylamine]-3,4,9,10-perylenetetracarboxylic diimide (PDI) in varying concentration ratios with double-stranded DNA with abasic sites (1dS) (red) or without abasic sites (0dS) (black) in in phosphate-buffered saline (PBS). Solutions of pre-annealed DNA with PDI were prepared as described in the main text Methods section. Lines are biphasic linear fits to regions of [DNA]/[PDI] ratios from 1.4 to 1.0 and 1.0 to 0.4 for 1dS DNA and 0dS DNA. The (lack of) change in slope at [DNA]/[PDI]=1.0 for 1dS (0dS) DNA is indicative of a 1:1 binding ratio of PDI molecules to hydrophobic pockets created by matching abasic sites in duplex DNA. Similar analyses have been performed by others to determine non-covalent binding of PDI molecules within abasic sites in duplex DNA. Error bars represent standard deviations for *N*=3 samples per data point. Measurements were taken using a Thermo Scientific NanoDrop 2000 spectrophotometer.

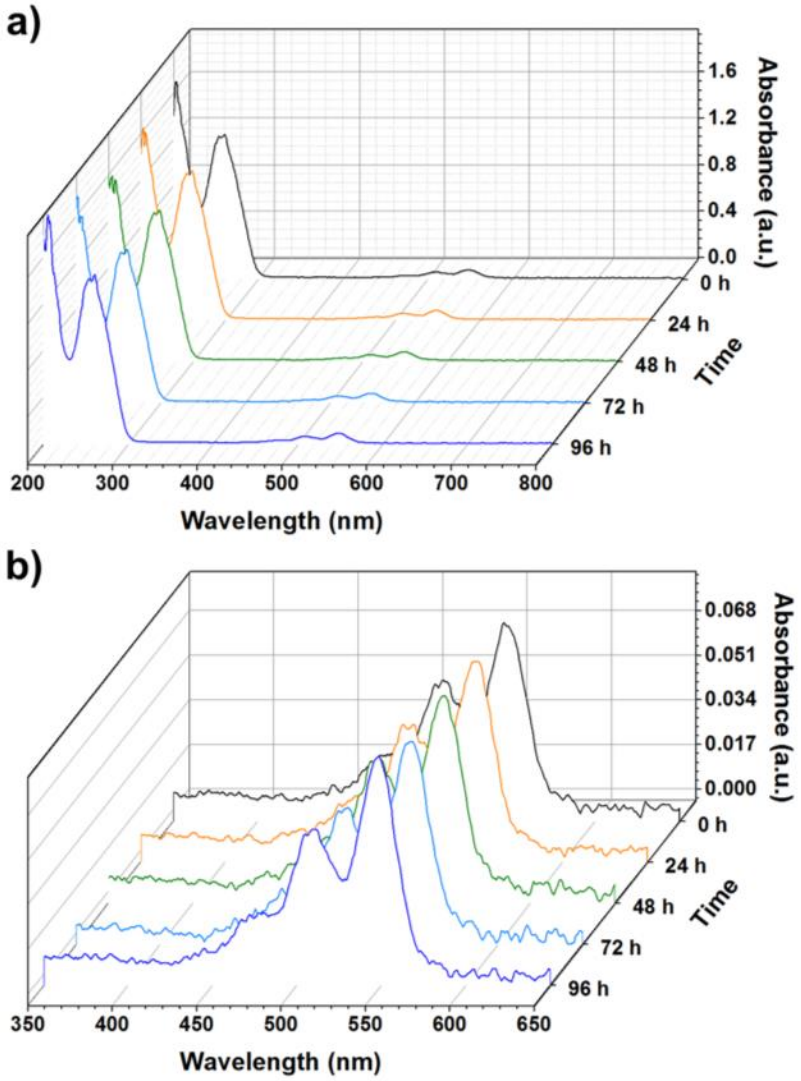

Figure SII.13. Stability of DNA/PDI complexes in phosphate-buffered saline. (**a**) Ultraviolet-visible spectra of *N*,*N*'-bis[3,3'-(dimethylamino)propylamine]-3,4,9,10-perylenetetracarboxylic diimide (PDI) in a 1:1 ratio with double-stranded DNA containing abasic sites acquired over 96 h under ambient conditions. The DNA and PDI concentrations were 20 μM. Solutions of pre-annealed DNA with PDI were prepared as described in the main text Methods section. (**b**) Ultraviolet-visible spectra from (**a**) within the wavelength window of 350 to 650 nm to highlight absorbance by PDI. Spectra are averages of 3 scans. Measurements were taken using a Thermo Scientific NanoDrop 2000 spectrophotometer.

References

1. Xie, Z.; Markus, T. Z.; Cohen, S. R.; Vager, Z.; Gutierrez, R.; Naaman, R. Spin Specific Electron Conduction through DNA Oligomers. *Nano Lett.* **2011**, 11, 4652–4655.

2. Zwang, T. J.; Hürlimann, S.; Hill, M. G.; Barton, J. K. Helix-Dependent Spin Filtering through the DNA Duplex. *J. Am. Chem. Soc*. **2016**, 138, 15551–15554.

3. Kumar, K. S.; Kantor-Uriel, N.; Mathew, S. P.; Guliamov, R.; Naaman, R. A Device for Measuring Spin Selectivity in Electron Transfer. *Phys. Chem. Chem. Phys*. **2013**, 15, 18357–18362.

4. Kettner, M.; Göhler, B.; Zacharias, H.; Mishra, D.; Kiran, V.; Naaman, R.; Fontanesi, C.; Waldeck, D. H.; Sęk, S.; Pawłowski, J.; Juhaniewicz, J. Spin Filtering in Electron Transport through Chiral Oligopeptides. *J. Phys. Chem. C* **2015**, 119, 14542–14547.

5. Aragonès, A. C.; Medina, E.; Ferrer-Huerta, M.; Gimeno, N.; Teixidó, M.; Palma, J. L.; Tao, N.; Ugalde, J. M.; Giralt, E.; Díez-Pérez, I.; Mujica, V. Measuring the Spin-Polarization Power of a Single Chiral Molecule. *Small* **2017**, 13, 1602519.

6. Eckshtain-Levi, M.; Capua, E.; Refaely-Abramson, S.; Sarkar, S.; Gavrilov, Y.; Mathew, S. P.; Paltiel, Y.; Levy, Y.; Kronik, L.; Naaman, R. Cold Denaturation Induces Inversion of Dipole and Spin Transfer in Chiral Peptide Monolayers. *Nat. Commun.* **2016**, 7, 10744.

7. Michaeli, K.; Naaman, R. Origin of Spin Dependent Tunneling through Chiral Molecules. arXiv 1512.03435v2, **2016**.

8. Gorodetsky, A. A.; Green, O.; Yavin, E.; Barton, J. K. Coupling into the Base Pair Stack Is Necessary for DNA-Mediated Electrochemistry. *Bioconjugate Chem.* **2007**, 18, 1434– 1441.

9. Genereux, J. C.; Barton, J. K. Mechanisms for DNA Charge Transport. *Chem. Rev.* **2010**, 110, 1642–1662.

10. Takada, T.; Otsuka, Y.; Nakamura, M.; Yamana, K. Molecular Arrangement and Assembly Guided by Hydrophobic Cavities inside DNA. *Chem. - Eur. J.* **2012**, 18, 9300–9304.

11. Göhler, B.; Hamelbeck, V.; Markus, T. Z.; Kettner, M.; Hanne, G. F.; Vager, Z.; Naaman, R.; Zacharias, H. Spin Selectivity in Electron Transmission through Self-Assembled Monolayers of Double-Stranded DNA. *Science* **2011**, 331, 894–897.

12. Zeidan, T. A.; Carmieli, R.; Kelley, R. F.; Wilson, T. M.; Lewis, F. D.; Wasielewski, M. R. Charge-Transfer and Spin Dynamics in DNA Hairpin Conjugates with

Perylenediimide as a Base-Pair Surrogate. *J. Am. Chem. Soc.* **2008**, 130, 13945–13955.

13. Carmieli, R.; Zeidan, T. A.; Kelley, R. F.; Mi, Q.; Lewis, F. D.; Wasielewski, M. R. Excited State, Charge Transfer, and Spin Dynamics in DNA Hairpin Conjugates with Perylenediimide Hairpin Linkers. *J. Phys. Chem. A* **2009**, 113, 4691–4700.

14. Carmieli, R.; Thazhathveetil, A. K.; Lewis, F. D.; Wasielewski, M. R. Photoselective DNA Hairpin Spin Switches. *J. Am. Chem. Soc.* **2013**, 135, 10970–10973.

15. Würthner, F.; Saha-Möller, C. R.; Fimmel, B.; Ogi, S.; Leowanawat, P.; Schmidt, D. Perylene Bisimide Dye Assemblies as Archetype Functional Supramolecular Materials. *Chem. Rev.* **2016**, 116, 962–1052.

16. Bevers, S.; O'Dea, T. P.; McLaughlin, L. W. Perylene- and Naphthalene-Based Linkers for Duplex and Triplex Stabilization. *J. Am. Chem. Soc.* **1998**, 120, 11004–11005.

17. Wagner, C.; Wagenknecht, H.-A. Perylene-3,4:9,10-Tetracarboxylic Acid Bisimide Dye as an Artificial DNA Base Surrogate. *Org. Lett.* **2006**, 8, 4191–4194.

18. Baumstark, D.; Wagenknecht, H.-A. Fluorescent Hydrophobic Zippers inside Duplex DNA: Interstrand Stacking of Perylene-3,4:9,10-Tetracarboxylic Acid Bisimides as Artificial DNA Base Dyes. *Chem. - Eur. J.* **2008**, 14, 6640–6645.

19. Huang, C.; Barlow, S.; Marder, S. R. Perylene-3,4,9,10-Tetracarboxylic Acid Diimides: Synthesis, Physical Properties, and Use in Organic Electronics. *J. Org. Chem.* **2011**, 76, 2386–2407.

20. Takada, T.; Yamaguchi, K.; Tsukamoto, S.; Nakamura, M.; Yamana, K. Light-Up Fluorescent Probes Utilizing Binding Behavior of Perylenediimide Derivatives to a Hydrophobic Pocket within DNA. *Analyst* **2014**, 139, 4016–4021.

21. Takada, T.; Yamaguchi, K.; Tsukamoto, S.; Nakamura, M.; Yamana, K. Light-Up Fluorescent Probes Utilizing Binding Behavior of Perylenediimide Derivatives to a Hydrophobic Pocket within DNA. *Analyst* **2014**, 139, 4016–4021.

22. Mondal, P. C.; Roy, P.; Kim, D.; Fullerton, E. E.; Cohen, H.; Naaman, R. Photospintronics: Magnetic Field-Controlled Photoemission and Light-Controlled Spin Transport in Hybrid Chiral Oligopeptide-Nanoparticle Structures. *Nano Lett*. **2016**, 16, 2806–2811.

23. Johnson, M. T.; Bloemen, P. J. H.; den Broeder, F. J. A.; de Vries, J. J. Magnetic Anisotropy in Metallic Multilayers. *Rep. Prog. Phys.* **1996**, 59, 1409–1458.

24. Bumm, L. A.; Arnold, J. J.; Cygan, M. T.; Dunbar, T. D.; Burgin, T. P.; Jones, L., II; Allara, D. L.; Tour, J. M.; Weiss, P. S. Are Single Molecular Wires Conducting? *Science* **1996**, 271, 1705–1707.

25. Cygan, M. T.; Dunbar, T. D.; Arnold, J. J.; Bumm, L. A.; Shedlock, N. F.; Burgin, T. P.; Jones, L., II; Allara, D. L.; Tour, J. M.; Weiss, P. S. Insertion, Conductivity, and Structures of Conjugated Organic Oligomers in Self-Assembled Alkanethiol Monolayers on Au{111}. *J. Am. Chem. Soc.* **1998**, 120, 2721–2732.

26. Lewis, P. A.; Inman, C. E.; Maya, F.; Tour, J. M.; Hutchison, J. E.; Weiss, P. S. Molecular Engineering of the Polarity and Interactions of Molecular Electronic Switches. *J. Am. Chem. Soc.* **2005**, 127, 17421–17426.

27. Vaish, A.; Shuster, M. J.; Cheunkar, S.; Singh, Y. S.; Weiss, P. S.; Andrews, A. M. Native Serotonin Membrane Receptors Recognize 5-Hydroxytryptophan-Functionalized Substrates: Enabling Small-Molecule Recognition. *ACS Chem. Neurosci.* **2010**, 1, 495–504.

28. Kim, M.; Hohman, J. N.; Cao, Y.; Houk, K. N.; Ma, H.; Jen, A. K.-Y.; Weiss, P. S. Creating Favorable Geometries for Directing Organic Photoreactions in Alkanethiolate Monolayers. *Science* **2011**, 331, 1312–1315.

29. Shuster, M. J.; Vaish, A.; Gilbert, M. L.; Martinez-Rivera, M.; Nezarati, R. M.; Weiss, P. S.; Andrews, A. M. Comparison of Oligo(ethyleneglycol)alkanethiols versus n-Alkanethiols: Self-Assembly, Insertion, and Functionalization. *J. Phys. Chem. C* **2011**, 115, 24778–24787.

30. Liao, W.-S.; Cao, H. H.; Cheunkar, S.; Shuster, M. J.; Altieri, S. C.; Weiss, P. S.; Andrews, A. M. Small-Molecule Arrays for Sorting G-Protein-Coupled Receptors. *J. Phys. Chem. C* **2013**, 117, 22362–22368.

31. Liao, W.-S.; Cheunkar, S.; Cao, H. H.; Bednar, H. R.; Weiss, P. S.; Andrews, A. M. Subtractive Patterning *via* Chemical Lift-Off Lithography. *Science* **2012**, 337, 1517–1521.

32. Andrews, A. M.; Liao, W.-S.; Weiss, P. S. Double-Sided Opportunities Using Chemical Lift-Off Lithography. *Acc. Chem. Res.* **2016**, 49, 1449–1457.

33. Kim, J.; Rim, Y. S.; Chen, H.; Cao, H. H.; Nakatsuka, N.; Hinton, H. L.; Zhao, C.; Andrews, A. M.; Yang, Y.; Weiss, P. S. Fabrication of High-Performance Ultrathin In_2O_3 Film Field-Effect Transistors and Biosensors Using Chemical Lift-Off Lithography. *ACS Nano* **2015**, 9, 4572–4582.

34. Xu, X.; Yang, Q.; Cheung, K. M.; Zhao, C.; Wattanatorn, N.; Belling, J. N.; Abendroth, J. M.; Slaughter, L. S.; Mirkin, C. A.; Andrews, A. M.; Weiss, P. S. Polymer-Pen Chemical Lift-Off Lithography. *Nano Lett.* **2017**, 17, 3302–3311.

35. Cao, H. H.; Nakatsuka, N.; Serino, A. C.; Liao, W.-S.; Cheunkar, S.; Yang, H.; Weiss, P. S.; Andrews, A. M. Controlled DNA Patterning by Chemical Lift-Off Lithography: Matrix Matters. *ACS Nano* **2015**, 9, 11439–11454.

36. Kim, E.; Park, K.; Hwang, S. Electrochemical Investigation of Chemical Lift-Off Lithography on Au and ITO. *Electrochim. Acta* **2017**, 246, 165–172.

37. Claridge, S. A.; Liao, W.-S.; Thomas, J. C.; Zhao, Y.; Cao, H. H.; Cheunkar, S.; Serino, A. C.; Andrews, A. M.; Weiss, P. S. From the Bottom Up: Dimensional Control and Characterization in Molecular Monolayers. *Chem. Soc. Rev*. **2013**, 42, 2725–2745.

38. Zosso, D.; An, J.; Stevick, J.; Takaki, N.; Weiss, M.; Slaughter, L. S.; Cao, H. H.; Weiss, P. S.; Bertozzi, A. L. Image Segmentation with Dynamic Artifacts Detection and Bias Correction. *Inverse Probl. Imaging* **2017**, 11, 577–600.

39. Chan, T. F.; Vese, L. A. Active Contours without Edges. *IEEE Trans. Image Process*. **2001**, 10, 266– 277.

40. Norman, D. G.; Grainger, R. J.; Uhrín, D.; Lilley, D. M. J. Location of Cyanine-3 on Double-Stranded DNA: Importance for Fluorescence Resonance Energy Transfer Studies. *Biochemistry* **2000**, 39, 6317–6324.

41. Torimura, M.; Kurata, S.; Yamada, K.; Yokomaku, T.; Kamagata, Y.; Kanagawa, T.; Kurane, R. Fluorescence-Quenching Phenomenon by Photoinduced Electron Transfer Between a Fluorescent Dye and a Nucleotide Base. *Anal. Sci.* **2001**, 17, 155–160.

42. Heinlein, T.; Knemeyer, J.-P.; Piestert, O.; Sauer, M. Photoinduced Electron Transfer between Fluorescent Dyes and Guanosine Residues in DNA-Hairpins. *J. Phys. Chem. B* **2003**, 107, 7957–7964.

43. Takada, T.; Ashida, A.; Nakamura, M.; Fujitsuka, M.; Majima, T.; Yamana, K. Photocurrent Generation Enhanced by Charge Delocalization over Stacked Perylenediimide Chromophores Assembled within DNA. *J. Am. Chem. Soc.* **2014**, 136, 6814–6817.

44. Takada, T.; Ido, M.; Ashida, A.; Nakamura, M.; Fujitsuka, M.; Kawai, K.; Majima, T.; Yamana, K. Photocurrent Generation through Charge-Transfer Processes in

Noncovalent Perylenediimide/DNA Complexes. *Chem. - Eur. J.* **2015**, 21, 6846–6851.

45. Kucherov, V. M.; Kinz-Thompson, C. D.; Conwell, E. M. Polarons in DNA Oligomers. *J. Phys. Chem. C* **2010**, 114, 1663–1666.

46. Uba, S.; Uba, L.; Yaresko, A. N.; Perlov, A. Ya.; Antonov, V. N.; Gontarz, R. Optical and Magneto-Optical Properties of Co/Pt Multilayers. *Phys. Rev. B: Condens. Matter Mater. Phys.* **1996**, 53, 6526.

47. Varela, S.; Mujica, V.; Medina, E. Effective Spin-Orbit Couplings in an Analytical Tight-Binding Model of DNA: Spin Filtering and Chiral Spin Transport. *Phys. Rev. B: Condens. Matter Mater. Phys.* **2016**, 93, 155436.

48. Yeganeh, S.; Ratner, M. A.; Medina, E.; Mujica, V. Chiral Electron Transport: Scattering through Helical Potentials. *J. Chem. Phys.* **2009**, 131, 014707.

49. Guo, A.-M.; Sun, Q.-F. Spin-Selective Transport of Electrons in DNA Double Helix. *Phys. Rev. Lett.* **2012**, 108, 218102.

50. Gutierrez, R.; Díaz, E.; Naaman, R.; Cuniberti, G. Spin-Selective Transport through Helical Molecular Systems. *Phys. Rev. B: Condens. Matter Mater. Phys.* **2012**, 85, 081404.

51. Gutierrez, R.; Díaz, E.; Gaul, C.; Brumme, T.; Domínguez-Adame, F.; Cuniberti, G. Modeling Spin Transport in Helical Fields: Derivation of an Effective Low-Dimensional Hamiltonian. *J. Phys. Chem. C* **2013**, 117, 22276–22284.

52. Guo, A.-M.; Sun, Q.-F. Spin-Dependent Electron Transport in Protein-Like Single-Helical Molecules. *Proc. Natl. Acad. Sci. U. S. A.* **2014**, 111, 11658–11662.

53. Gersten, J.; Kaasbjerg, K.; Nitzan, A. Induced Spin Filtering in Electron Transmission through Chiral Molecular Layers Adsorbed on Metals with Strong Spin-Orbit Coupling. *J. Chem. Phys.* **2013**, 139, 114111.

54. Medina, E.; González-Arraga, L. A.; Finkelstein-Shapiro, D.; Berche, B.; Mujica, V. Continuum Model for Chiral Induced Spin Selectivity in Helical Molecules. *J. Chem. Phys.* **2015**, 142, 194308–194313.

55. Drummond, T. G.; Hill, M. G.; Barton, J. K. Electron Transfer Rates in DNA Films as a Function of Tether Length. *J. Am. Chem. Soc.* **2004**, 126, 15010–15011.

56. Bumm, L. A.; Arnold, J. J.; Dunbar, T. D.; Allara, D. L.; Weiss, P. S. Electron Transfer through Organic Molecules. *J. Phys. Chem. B* **1999**, 103, 8122–8127.

57. Monnell, J. D.; Stapleton, J. J.; Dirk, S. M.; Reinerth, W. A.; Tour, J. M.; Allara, D. L.; Weiss, P. S. Relative Conductances Alkaneselenolate and Alkanethiolate Monolayers on Au{111}. *J. Phys. Chem. B* **2005**, 109, 20343–20349.

58. Liu, Z. R.; Rill, R. L. *N*,*N*′-bis[3,3′-(dimethylamino)propylamine]-3,4,9,10-Perylenetetracarboxylic Diimide, a Dicationic Perylene Dye for Rapid Precipitation and Quantitation of Trace Amounts of DNA. *Anal. Biochem.* **1996**, 236, 139–145.

Chapter III

Spin-Polarized Photoemission by Ionization of Chiral Molecular Films

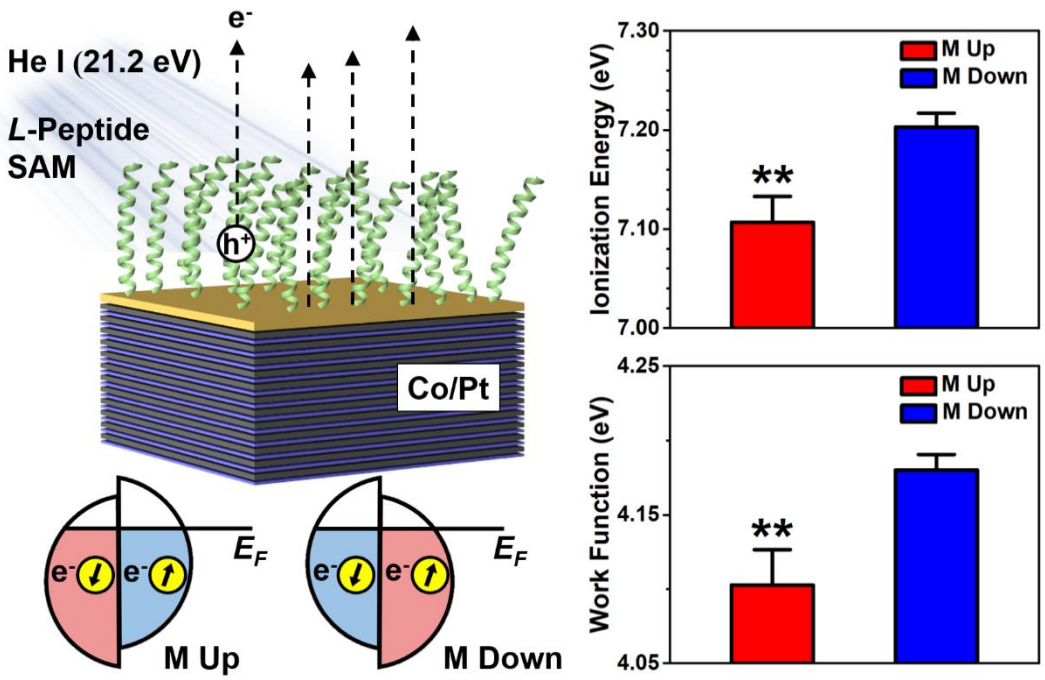

The information in this chapter is in preparation for submission for publication, and is reproduced here.

Authors: John M. Abendroth, Kevin M. Cheung, Dominik M. Stemer, Mohammed S. El Hadri, Chuanzhen Zhao, Eric E. Fullerton, and Paul S. Weiss

III.A. Introduction

Enantioselective interactions between chiral molecules and electrons that depend on electron helicity, that is, the projection of an electron's spin angular momentum on its linear momentum, enable the generation and manipulation of spin polarized electrons at room temperature.[1,2] This spin-filtering phenomenon is attributed to the CISS effect, also known as electron dichroism, and has been observed in a wide range of dissymmetric molecular systems.[3-5] Spin polarization in photoelectron transmission through chiral organic monolayers has been measured explicitly, using both linearly and circularly polarized radiation to emit unpolarized or longitudinally polarized photoelectrons, respectively, from noble metal substrates.[6-9] In these studies, photon energies lower than the ionization potentials of the adsorbed organic films were used to excite photoelectrons solely from the underlying metal surfaces. However, little is known about the relative energetic barriers to transmission of spin-up *vs* spin-down electrons through chiral organic films within this charge transport regime, and whether spin-polarized photoelectrons may be emitted from chiral molecular films using ionizing radiation.

Herein, using ultraviolet photoelectron spectroscopy (UPS), we characterized the valence electronic structure of FM surfaces with adsorbed chiral molecules as a function of molecular handedness and secondary structure, substrate magnetization orientation, and substrate polarization. Using unpolarized ionizing radiation from a helium-ion ultraviolet light source (He I emission line), we collected primary and secondary valence photoelectrons that originated from both the FM substrates and adsorbed chiral molecule films. Our experiments were designed to deconvolute potential mechanisms of spin filtering in photoemission by ionizing radiation, and to measure the relative energy barriers to

transmission of spin-up *vs* spin-down electrons through chiral molecular assemblies.

The experimental schematic for the UPS measurements is illustrated in Figure III.1. Spin selectivity in photoemission from FM substrates functionalized with chiral organic films may be attributed to three possible mechanisms. Nominally, the spin polarization of photoelectrons from FM substrates reflects the polarization within the material itself; an incident photon excites an electron below the Fermi level to a final state with identical spin.[10] However, when FM substrates are functionalized with chiral organic monolayers or films, the spin polarization of photoelectrons emitted from the metal depends on the chirality of the adsorbed molecules that act as spin filters due to the asymmetric scattering probabilities of electrons with opposite helicity and spatial structure of unoccupied high-lying states.[6-9,11] Thus, the work function (ϕ), defined as the difference between the photon energy, $h\nu$ (21.2 eV), and the binding energy of the secondary electron cutoff (*i.e.*, maximum binding energy), $E_B^{max;\,organic}$:

$$\phi = h\nu - E_B^{max;\,organic} \quad (1)$$

of FM surfaces should depend on both the magnetization orientation of the FM substrate, and on the molecular handedness. This value represents the energy barrier to remove an electron from the solid surface to a point in the vacuum just outside the surface. Thus, when the spin state of majority-spin electrons match the preferred spin orientation of electrons transmitted through chiral monolayers, a lower ϕ is expected.

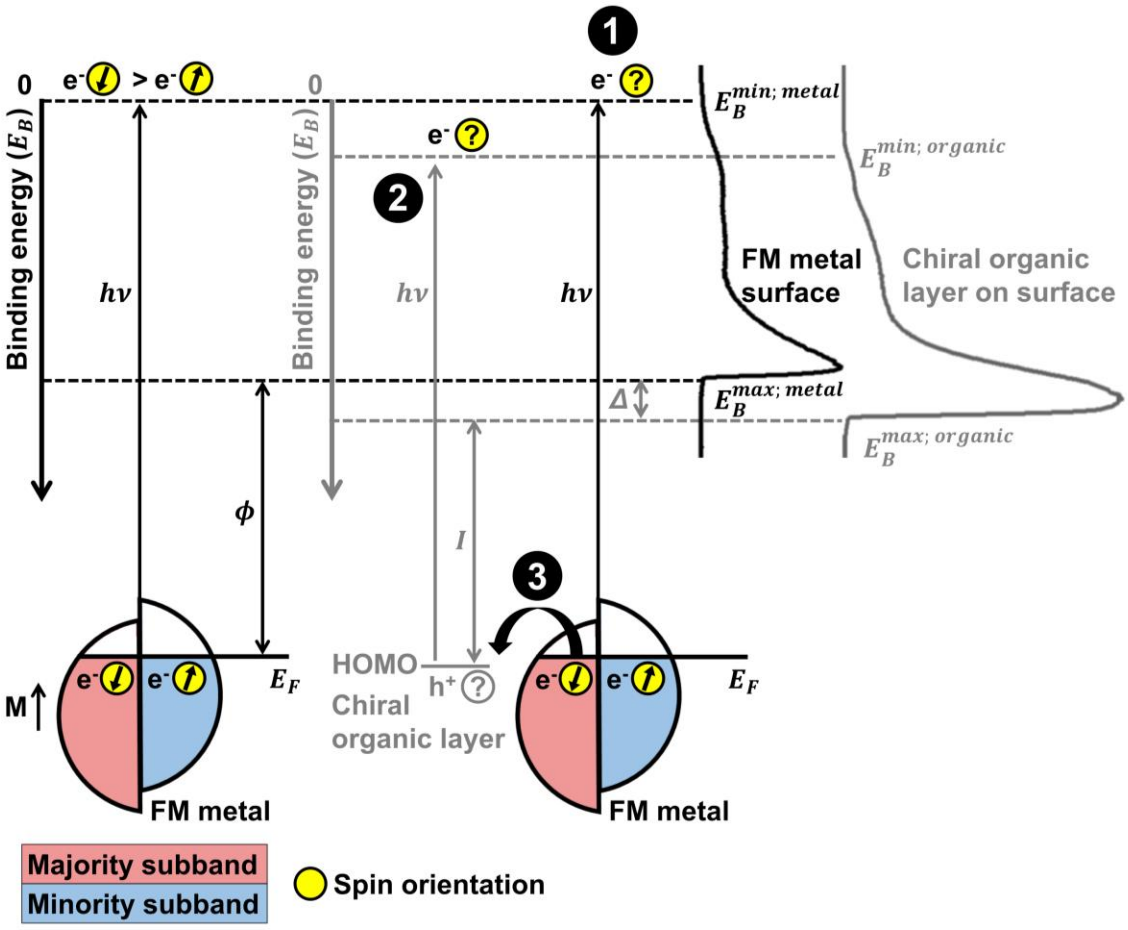

Figure III.1. Experimental schematic of ultraviolet photoelectron spectroscopy (UPS). Spin-selective processes due to the chiral-induced spin selectivity effect include filtering of photoelectrons originating from the metal by adsorbed chiral species (1), spin-polarized photoemission by ionization of chiral films (2), or filtering of conduction electrons supplied by the metal to fill holes left in the highest-occupied molecular orbitals (HOMO) of the organic films (3). The right side of the image depicts representative ultraviolet photoelectron spectra from bare ferromagnetic (FM) surfaces and surfaces coated with chiral organic films. The large peaks at high binding energies correspond to the collection of secondary electrons that scatter one or more times, losing energy. The spin polarization of photoelectrons emitted from bare FM surfaces by photons with energy *hv* reflects the polarization within the metal dictated by the magnetization orientation, M. The minimum energy required to remove an electron from the metal is the work function, ϕ. The Fermi edge and minimum binding energy, $E_B^{min;\,metal}$, is at 0 eV, and the secondary electron cutoff of electrons with lowest kinetic energy is $E_B^{max;\,metal}$. When functionalized with organic chiral layers, photoelectrons are collected from both the metal surface as well as the organic material due to ionization. The valence band edge of the spectra, $E_B^{min;\,organic}$ and the secondary electron cutoff, $E_B^{max;\,organic}$, represent the highest and lowest kinetic energies of collected photoelectrons, respectively. The work function shift, Δ, reflects the change in the minimum energy to remove an electron from the surface.

If the photon energy is higher than the ionization potential of the organic film, such as in UPS measurements, electrons are also collected from occupied electronic states within the organic films by ionizing the adsorbed molecules. Spin-polarized photoemission by ionization of surface adsorbates has been detected using circularly polarized light, which is solely a result of spin-orbit interactions that depends on the helicity of the incident photons, and are therefore more prominent in high-Z systems.[12] Photoemission using unpolarized or linearly polarized radiation, however, is not expected to yield spin-polarized photoelectrons except within particular non-coplanar observation geometries.[13] Still, scattering of secondary electrons originating from the organic material within a chiral film may lead to spin polarization. This process is analogous to mechanisms related to filtering photoelectrons emitted from underlying metal surfaces,[6-9,11] leaving behind an excess of holes of a particular spin state dictated by the handedness of the organic material due to inversion-symmetry breaking. Compared to randomly dispersed molecules in the gas phase, the surface assembly imparts orientation and alignment that enhances and focuses asymmetry in scattering of low-kinetic-energy electrons within chiral molecular assemblies.

The ionization potential of the organic film (I) is defined as the energy difference between the photon energy and the width of the photoelectron spectra:

$$I = h\nu - \left(E_B^{max;\,organic} - E_B^{min;\,organic}\right) \quad (2)$$

where $E_B^{min;\,organic}$ represents the valence band edge (*i.e.*, minimum binding energy). If the holes within the chiral organic films are spin polarized, they must be filled by electrons with a matching spin state supplied from the grounded FM substrate. Therefore, holes are more efficiently filled when substrates are in the preferred magnetization orientation (based on the chirality of the molecular films and spin polarization of holes), corresponding to a

lower *I*. In the opposite magnetization condition, an accumulation of positive charge within the chiral organic layer results in a higher *I*.

Finally, spin polarization may occur *via* electron transfer by conduction from the underlying metal to neutralize the positively-charged organic films with a dependence on the handedness of the organic layer. The CISS effect has been demonstrated within this charge-transport regime, and the spin-valve-like architecture between FM layers and chiral molecules as spin filters show high- or low-resistance states dictated by the substrate magnetization orientation and molecule chirality.[8,14-16] Thus, if the holes left by secondary electrons originating from the organic films are *not* spin polarized, differences in *I* between substrate magnetization orientations may still result from spin-dependent charge transfer through the chiral organic molecules.

III.B. Results

III.B.1. Ferromagnetic Substrate Characterization

Ferromagnetic films with perpendicular magnetic anisotropy were grown on glass substrates with a composition of Ta 3/Pt 2/$[Co\ 0.6/Pt\ 0.3]_{69}$/Co 0.6/Au 1 (layers in nm) and used for UPS measurements. While the thin layer of Au is insufficient to prevent partial oxidation of the underlying Co layers (Figure SIII.1), it enables the formation of stable molecular films of thiolated molecules due to the formation of robust Au-S bonds.

The magnetic hysteresis of this substrate material is shown in Figure III.2a. The substrates retain their magnetization out of the plane of the films upon removal of external magnetic fields. Substrates were designed with large coercivities (~3 kOe) to prevent loss of initial magnetization within the instrument chamber due to magnetic fields used to focus

photoelectrons to the detector. As indicated by the slanted shape of the hysteresis curves, the large substrate coercivity also made it possible to magnetize substrates reproducibly to sub-saturation conditions. We investigated conditions when the substrates were magnetized with a saturating field of ± 12 kOe and sub-saturating field of ± 7 kOe to probe different spin polarizations (*i.e.*, ratio of spin-up to spin-down electrons) within the FM substrate.

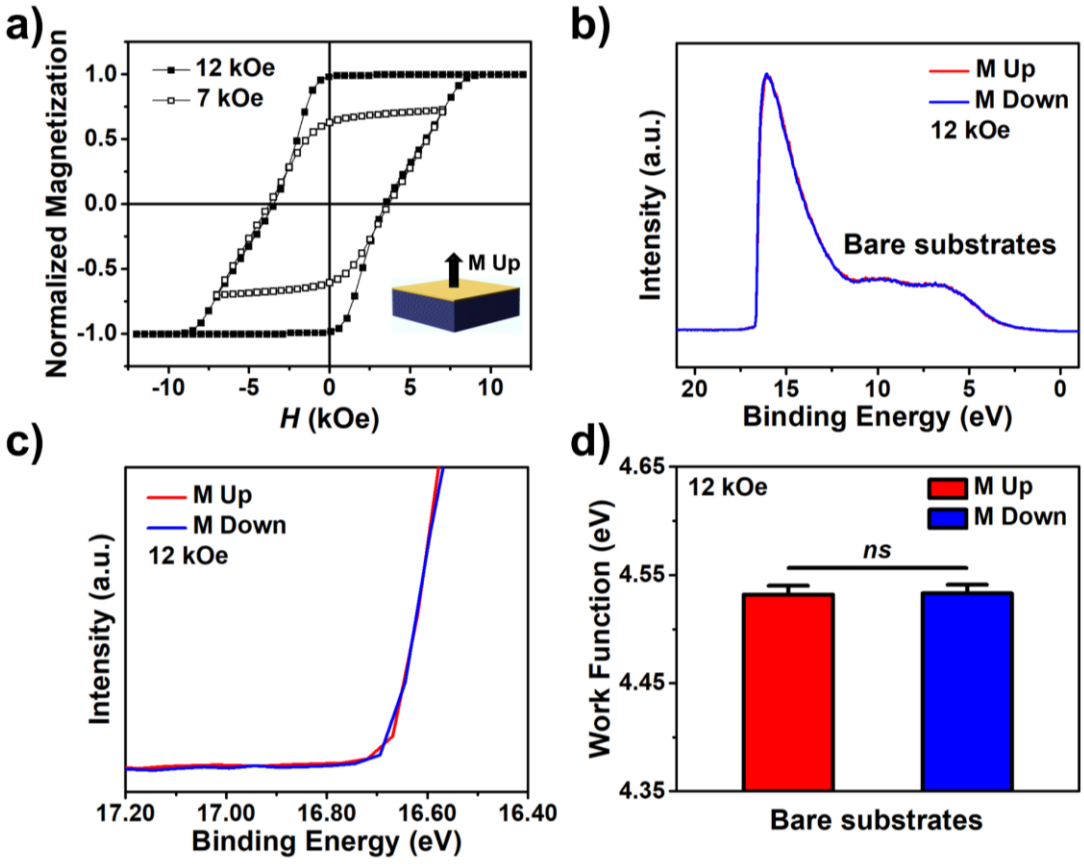

Figure III.2. Characterization of bare ferromagnetic (FM) films with composition: glass substrate/Ta 3/Pt 2/[Co 0.6/Pt 0.3]$_{69}$/Co 0.6/Au 1 (layers in nm). (**a**) Hysteresis loops of FM substrates with ± 12 kOe and ± 7 kOe saturating magnetic fields (H). (**b**) Representative full ultraviolet photoelectron spectra of bare substrates magnetized up (red) or down (blue) at full saturation using a helium-ion ultraviolet light source (He I). **c**) Magnification of the secondary electron cutoff region of the spectra in (**b**). (**d**) Work function values of the surfaces magnetized up (red) or down (blue) at full saturation calculated from the ultraviolet photoelectron spectra. Error bars represent standard errors of the mean; *ns* is not significant ($P > 0.05$).

Representative ultraviolet photoelectron spectra and secondary electron cutoff regions for bare substrates are shown in Figure III.2b,c at full saturation. No differences in ϕ were measured between opposite magnetization conditions when the substrates were not functionalized with organic films (Figure III.2d). Importantly, these results show that the influence of magnetic fields at the surface of the perpendicularly-magnetized substrates due to remnant magnetization on emitted photoelectrons is negligible. Additionally, no significant differences were found in the secondary electron peak intensities nor total integrated areas of the spectra between substrate magnetization conditions (Table SIII.1). The energies of the secondary electron cutoffs, Fermi edges, and ϕ can be found in Table SIII.2.

III.B.2. Spin-Selective Photoemission from *L*- and *D*-Peptide Monolayers

Monolayers of left- and right-handed α-helical peptides (henceforth *D*- and *L*-peptides, respectively) composed of (N terminus → C terminus) $[K(Aib)A(Aib)A]_6KC$ were formed on FM substrates by binding of the thiol functional group of cysteine residues on the C-termini of the oligopeptides to the Au layers (Figure III.3a). All lysine (K), alanine (A), and cysteine (C) residues were *L*-form in the *L*-peptides and *D*-form in *D*-peptides. The achiral 2-aminoisobutyric acid (Aib) residues were used to stabilize the α-helical secondary structure of peptides of both handedness,[15] which was confirmed in solution by circular dichroism spectroscopy (Figure SIII.2). Peptide assembly on FM surfaces was confirmed by the presence of amide I and II stretching bands observed *via* infrared reflection-absorption spectroscopy (Figure SIII.3).

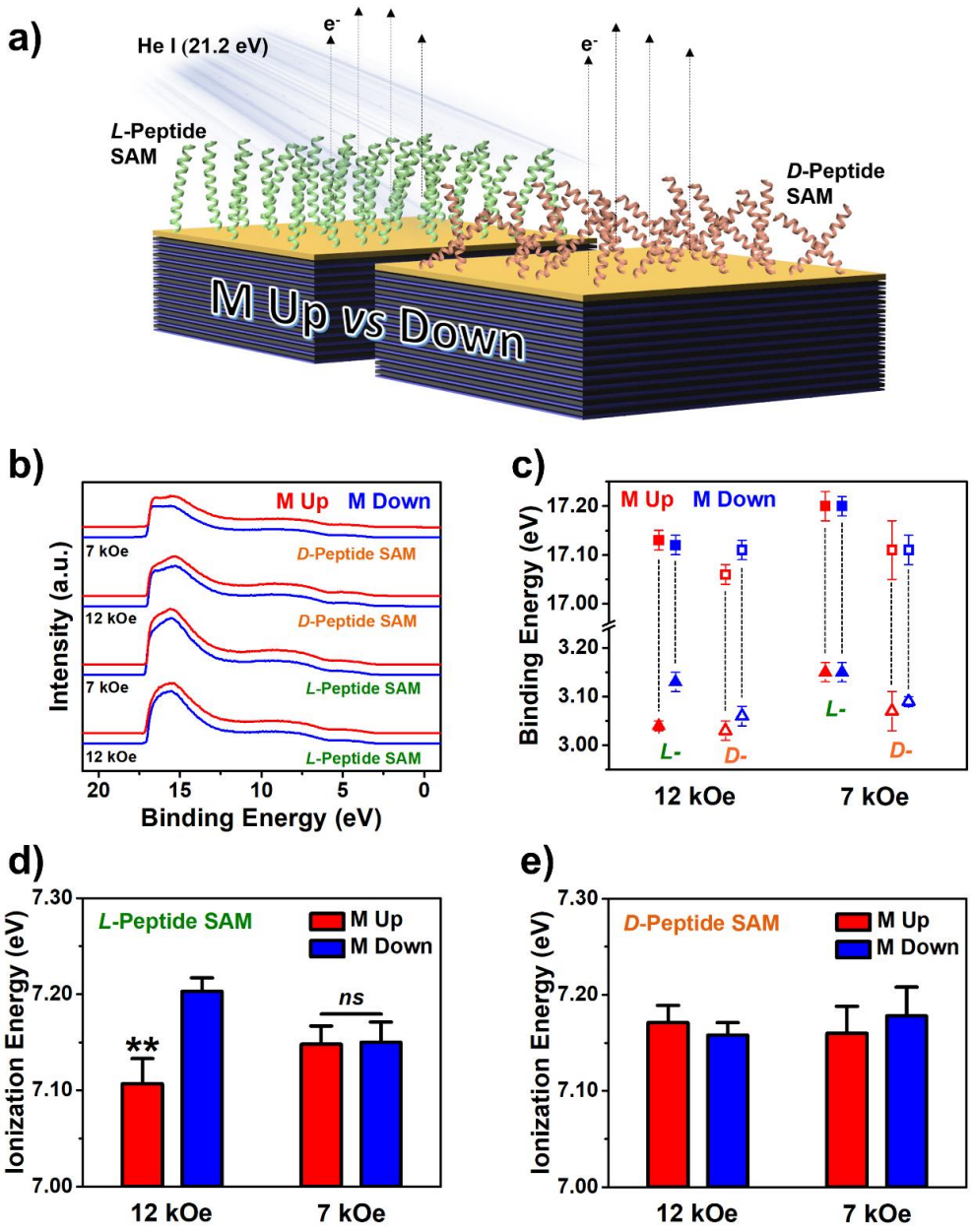

Figure III.3. Characterization of ferromagnetic (FM) substrates functionalized with self-assembled monolayers (SAMs) of *L*- or *D*-peptides by ultraviolet photoelectron spectroscopy using a helium-ion ultraviolet light source (He I). (**a**) Experimental schematic for two opposite (up *vs* downrientations (M). (**b**) Full, representative photoelectron spectra for *L*- and *D*-peptide SAMs on FM substrates magnetized with +/- 12 or +/- 7 kOe. Spectra obtained from substrates magnetized up *vs* down are offset for clarity. (**c**) Secondary electron cutoffs (squares) and valence band edges (triangles) for *L*- (solid symbols) and *D*- (open symbols) peptide SAMs on substrates magnetized to full- *vs* sub-saturation magnetization. (**d**) Ionization energies of FM substrates magnetized up *vs* down at full- and sub-saturation magnetization for *L*-peptide SAMs and (**e**) *D*-peptide SAMs. Error bars represent standard error of the means; $^{**}P < 0.01$ *vs* M down; *ns* is not significant ($P > 0.05$).

Representative ultraviolet photoelectron spectra and the energies of the secondary electron cutoffs and valence band edges of the spectra obtained from FM substrates functionalized with *L*- or *D*-peptides at full- and sub-saturation magnetization conditions are shown in Figures III.3b and c, respectively. The negative shift in the work function of the substrates upon both *L*- and *D*-peptide functionalization indicates covalent binding of the thiolated cysteine residues to the metal surface due to the positive dipole (C terminus → N terminus) of the α-helices pointing away from the surfaces (Table SIII.2).[17-19] No significant differences in secondary electron peak intensities, total integrated area of the spectra, or ϕ were determined in all four conditions between substrate magnetization orientations.

Two-way analysis of variance showed a significant interaction between substrate magnetization orientation and saturation condition for I when FM substrates were functionalized with *L*-peptide SAMs. *Post hoc* analysis revealed that ionization energies were significantly *lower* when the magnetization of substrates were oriented up *vs* down only when FM substrates were fully magnetized (Figure III.3d, $^{**}P < 0.01$). When the spin polarization of the substrate was lowered by magnetizing the samples with a sub-saturating field, no significant differences between magnetization orientations were found. The results indicate that the magnitude of spin polarization of the substrate determines whether spin selectivity in photoemission can be experimentally determined in our measurements.

Based on results observed with *L*-peptide SAMs, we hypothesized that surfaces functionalized with *D*-peptide SAMs with opposite chirality would show instead *higher I* when the magnetization of substrates were oriented parallel to the surface normal. However, two-way analysis of variance showed no significant interaction between substrate

magnetization orientation and saturation condition, nor significance in the main effects for I when FM substrates were functionalized with *D*-peptide SAMs (Figure III.3e).

The absence of any dependence of I on the substrate magnetization may be due to poorer SAM quality of *D*-peptides *vs L*-peptides. This hypothesis is based on the measured thicknesses of *L*- and *D*-peptide SAMs on FM surfaces by ellipsometry (Table SIII.3). The average thickness of *L*-peptide SAMs was 3.7 ± 0.5 nm. Assuming a rise of 0.15 nm per amino acid residue, the length of a peptide of 32 resides would be 4.8 nm. Thus, the measured thickness may be a result of off-normal orientation of the *L*-peptide molecules within the SAMs, or incomplete surface coverage. The average thickness of *D*-peptide SAMs was 1.9 ± 0.3 nm, suggesting an even poorer surface coverage compared to that of *L*-peptide SAMs, which reflects the lower signal intensity measured in infrared reflection-absorption measurements (Figure SIII.3). Because our laboratory axis of electron spin polarization within the FM substrates is defined as the surface normal (up *vs* down), and because spin polarization by the CISS effect is expected to be along the axis of helical molecules,[20-32] deviation of molecules from vertical alignment would result in lower spin filtering efficiency. Further, higher densities of chiral molecules are expected to yield a larger spin polarization in electron transmission due to wavefunction overlap with multiple molecules.[11,33] Thus, we attribute the absence of substrate magnetization dependence of the ionization potential of *D*-peptide SAMs to low surface coverage.

We also tested mixed SAMs composed of *L*- and *D*-peptides formed from racemic mixtures. Because each photoelectron spectra represent an ensemble characterization of the surfaces, dilution of *L*-peptide SAMs with molecules of the opposite chirality in this manner was hypothesized to result in no net measureable spin selectivity in photoemission. Indeed,

no differences in *I* between substrate magnetization orientations were observed when fully saturated (Figure SIII.4). These results agree qualitatively with the seminal work done by Ray *et al*., who observed that enantioselectivity in the transmission of spin-polarized photoelectrons emitted from Au using left- *vs* right-handed circularly polarized light through films of *L*-stearoyl lysine films disappeared when films were formed with impurities of *D*-stearoyl lysine.[11]

III.B.3. Spin-Selective Photoemission from Protein Films

To investigate the influence of structure and orientation on spin-selective photoemission, ultraviolet photoelectron spectra were also compared between FM substrate magnetization conditions when surfaces were functionalized with adsorbed films of the protein, bovine serum albumin (BSA), in unmodified *vs* thermally denatured (dBSA) conditions (Figure III.4a). Adsorption of BSA on various surfaces has been widely investigated, and generally, higher densities are achieved using charged substrates compared to hydrophobic surfaces.[34,35] Thus, positively charged SAMs of achiral 11-amino-1-undecanethiolate (AUT) monolayers were formed first on FM substrates to facilitate the electrostatic binding of BSA molecules with net negative charge at pH 7.4 in PBS solutions by association with negatively charged residues.[36]

In its native conformation, the globular protein, BSA, is composed of multiple right-handed α-helical subunits with *ca.* 60% structural helicity. However, upon adsorption on surfaces and dehydration, conditions necessary for the experiments performed herein, pristine secondary structure is lost, with a decrease in structural helicity and slight increase in β-sheet content.[37,38] When irreversibly denatured due to heating prior to surface

assembly, a greater loss of structural helicity and conversion to a conformation with higher composition of β-sheets is evident by circular dichroism spectroscopy (Figure SIII.5).[39] Infrared reflection-absorption spectroscopy confirms the greater β-sheet content of dBSA when dried on FM substrates based on analysis of the amide I band with reduction of absorbance in the range 1655-1650 cm^{-1}, attributed to α-helical composition, and increase in absorbance in the range 1685-1633 cm^{-1}, due to β-sheets (Figure SIII.6).[40] Still, the chemical nature of the protein is not lost by thermal denaturation as evidenced by comparison of the nearly identical C 1s, N 1s, and O 1s regions of high-resolution X-ray photoelectron spectra for BSA and dBSA films on AUT SAMs (Figure SIII.7). Thus, films composed of dBSA have reduced α-helicity, but maintain chirality due to the *L*-amino acid subunits.

Representative ultraviolet photoelectron spectra and the energies of the secondary electron cutoffs and valence band edges of the spectra obtained from FM substrates functionalized with AUT SAMs and BSA or dBSA films at full- and sub-saturation magnetization conditions are shown in Figures III.4b and c, respectively. Similar to the measurements of *L*- and *D*-peptide SAMs, no significant differences in secondary electron peak intensities, total integrated area of the spectra, or ϕ were determined in all four conditions between substrate magnetization orientations (Tables SIII.1,2).

Two-way analysis of variance showed no significant interaction between substrate magnetization orientation and saturation condition, nor significance in the main effects for *I* when FM substrates were functionalized with BSA films (Figure III.4d). The absence of the dependence of spectral widths on magnetization condition may be attributed to the random orientation of disordered α-helical subunits and overall lower α-helical content that occurs

upon surface adsorption as indicated by infrared reflection-absorbance spectroscopy compared to that of well-aligned *L*-peptide SAMs (Figure SIII.6).

Alternatively, two-way analysis of variance showed a significant interaction between substrate magnetization orientation and saturation condition for I when FM substrates were functionalized with AUT SAMs and dBSA films. *Post hoc* analysis showed that values of I were significantly *higher* when the magnetization of substrates were oriented up *vs* down only when FM substrates were fully magnetized (Figure III.4e, $^*P < 0.05$). Again, when the spin polarization of the substrate was lowered by magnetizing the samples with a sub-saturating field, no significant differences between magnetization orientations were found.

No differences in I were measured between opposite magnetization orientations of FM substrates at full saturation when functionalized with achiral AUT SAMs (Figure SIII.8). These results are expected, as no dependence of transmission on electron helicity should occur if the molecular films lack inversion asymmetry, and provide additional evidence that the observations for *L*-peptide SAMs and AUT SAMs with dBSA films are not artifacts attributed to magnetic fields at the metal surfaces of the FM substrates due to remnant magnetization of the substrates.

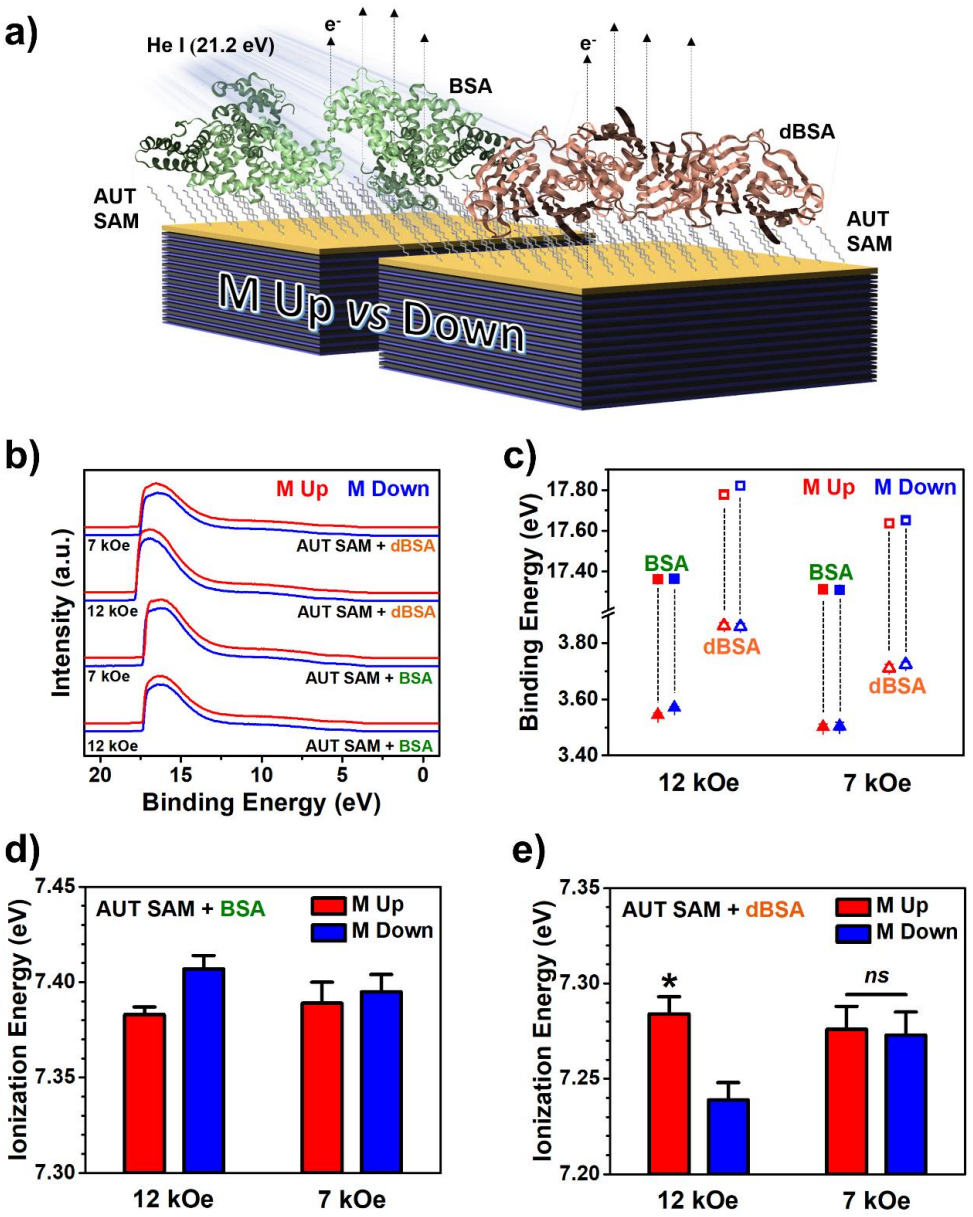

Figure III.4. Characterization of ferromagnetic (FM) substrates functionalized with self-assembled monolayers (SAMs) of 11-amino-1-undecanethiol and films of bovine serum albumin (BSA) or thermally denatured bovine serum albumin (dBSA) by ultraviolet photoelectron spectroscopy using a helium-ion ultraviolet light source (He I). (**a**) Experimental schematic. (**b**) Full, representative photoelectron spectra for AUT SAMs with BSA or dBSA films on FM substrates magnetized with +/- 12 or +/- 7 kOe. Spectra obtained from substrates magnetized up *vs* down are offset for clarity. (**c**) Secondary electron cutoffs (squares) and valence band edges (triangles) for AUT SAMs with BSA (solid symbols) or dBSA films (open symbols) on substrates magnetized to full- *vs* sub-saturation magnetization. (**d**) Ionization energies of FM substrates magnetized up *vs* down at full- and sub-saturation magnetization for AUT SAMs with BSA and (**e**) dBSA. Error bars represent standard error of the means; $*P < 0.05$ *vs* M down; *ns* is not significant ($P > 0.05$).

III.B.4. Photoemission Measurements with Charge Neutralization

Positive charging of the surfaces under all conditions was evident by a shift in ultraviolet photoelectron spectra to higher binding energies upon multiple scans on the same substrates (Figure SIII.9). To test if differences in the photoelectron spectral features on fully saturated FM substrates were due to differences in positive charging and nonuniform surface potentials within the films upon ionization (Figure III.5a), conventional charge neutralization methods were employed.

A uniform flood of low-energy electrons (~0.1 eV) from a coaxial (normal to the surface) source was delivered using a combined magnetic/electrostatic lens during spectral acquisition. While the conductive FM substrates provide a source of spin-polarized electrons to fill holes within the ionized chiral films, the additional unpolarized electrons contribute to charge neutralization independent of the magnetization orientation of substrates and minimize charging effects.

For FM substrates functionalized with *L*-peptide SAMs, *I* decreased for both magnetization orientation conditions under charge neutralization conditions when compared to the aforementioned measurements without use of the electron flood gun, indicative of a reduction in the positive charging of the organic films. No significant differences in *I* as a function of magnetization orientation were determined upon charge neutralization conditions (Figure III.5b). These results confirm that positive charging and thus ionization energies of *L*-peptide SAMs upon photoionization depend on substrate magnetization orientation.

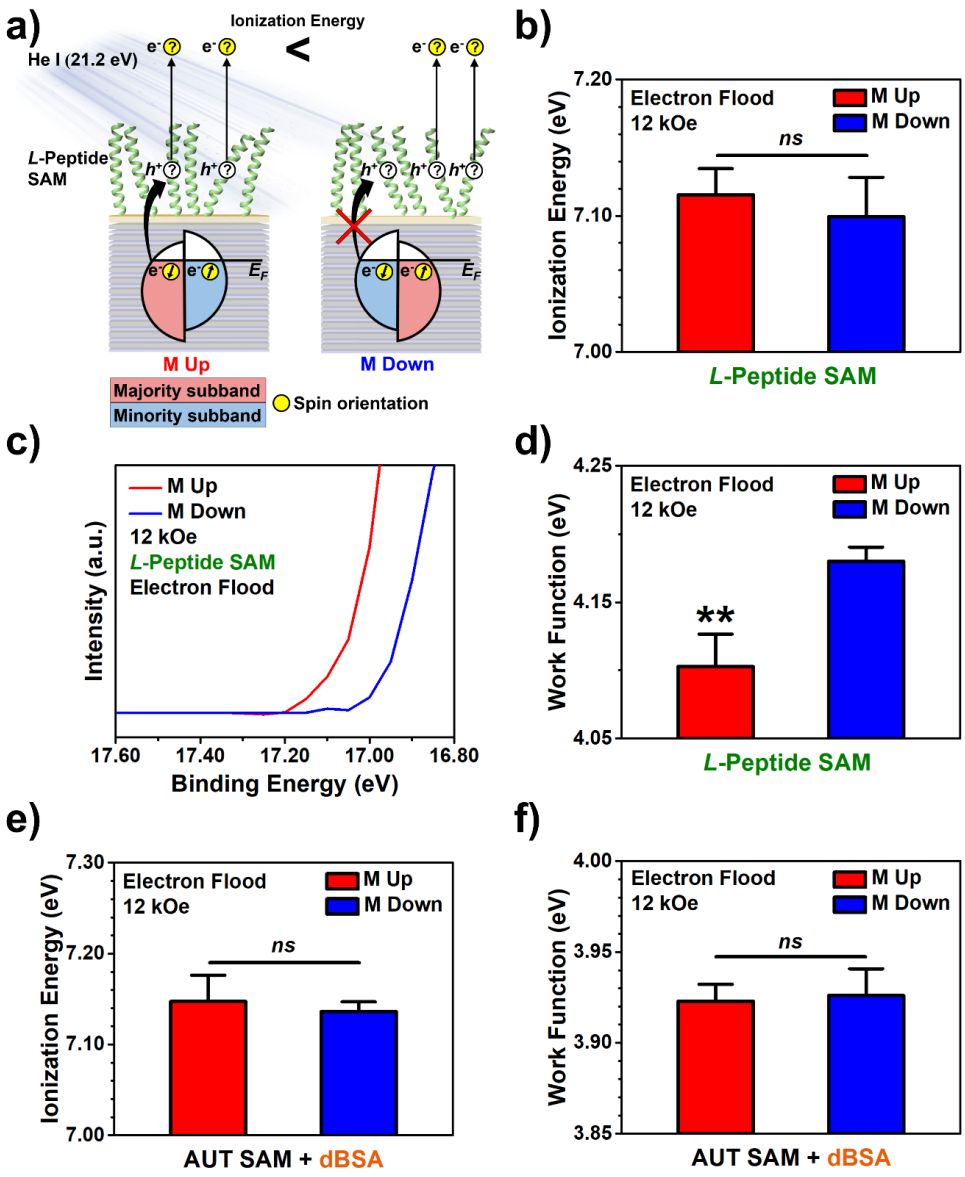

Figure III.5. Characterization of ferromagnetic (FM) substrates functionalized with *L*-peptide self-assembled monolayers (SAMs) and SAMs of 11-amino-1-undecanethiol with films of thermally denatured bovine serum albumin (dBSA) by ultraviolet photoelectron spectroscopy using a helium-ion ultraviolet light source (He I) under charge neutralization conditions. (**a**) Experimental schematic. For clarity, depiction of photoelectrons emitted from the metal substrates is omitted. (**b**) Ionization energy of FM substrates magnetized up *vs* down at full saturation magnetization for *L*-peptide SAMs. (**c**) Magnified region of the secondary electron cutoff of representative photoelectron spectra from FM substrates functionalized with *L*-peptide SAMs magnetized up *vs* down. (**d**) Work function values of FM substrates magnetized up *vs* down at full saturation magnetization for *L*-peptide SAMs. (**e**) Ionization energy and (**f**) work function values of FM substrates magnetized up *vs* down at full saturation magnetization for AUT SAMs + dBSA. Error bars represent standard error of the means; $^{**}P < 0.01$ *vs* M down; *ns* is not significant ($P > 0.05$).

In addition, differences in ϕ were determined under charge neutralization between magnetization orientations as indicated by different shifts in the secondary electron cutoff positions (Figure III.5c). A lower ϕ was measured for FM surfaces functionalized with *L*-peptide SAMs when substrates were magnetized up (Figure III.5d). Shifts in ϕ became apparent by deconvoluting the influence of substrate magnetization-dependent charging of the ionized chiral organic films on the photoelectron spectra.

We also tested the influence of charge neutralization on I and ϕ for AUT SAMs with dBSA films on fully saturated FM substrates between substrate magnetization orientations. Again, a decrease in I was observed for both magnetization orientation conditions compared to measurements without use of the electron flood gun, and no differences between magnetization up *vs* down conditions were determined (Figure III.5e), analogous to measurements with *L*-peptide SAMs. However, no substrate magnetization-dependent differences in ϕ were observed under charge neutralization conditions for AUT SAMs with dBSA films. These results may be attributed to the larger thickness of AUT SAMs with dBSA films (9.4 ± 0.4 nm) compared to *L*-peptide SAMs as indicated by ellipsometry measurements (Table SIII.3). The thicker organic layers may attenuate transmission of photoelectrons originating from the FM substrate sufficiently to prevent resolution of ϕ differences in our measurements. Further, characterization of AUT SAMs with adsorbed BSA and dBSA films by AFM indicate greater inhomogeneity of surfaces compared to bare FM substrates and AUT SAMs only (Figure SIII.10) which may also mask subtle differences in ϕ.

III.B.5. Testing Spin-Dependent Conduction through Protein Films

Ultraviolet photoelectron spectroscopy measurements indicated that the charging of chiral organic films on FM substrates due to the buildup of holes is dependent upon the substrate magnetization orientation. These differences in I may be due to spin-polarized holes left by secondary electrons upon ionization of the chiral molecule films, or, if spin-polarized photoemission by ionization of the organic films does not occur, to filtering of spin-polarized conduction electrons supplied by the underlying metal surface to neutralize the chiral layers.

Electron-helicity-dependent charge transfer through *L*- and *D*-peptides has been reported previously, and are not tested here.[8,14,41] To test if BSA or dBSA films can effectively filter electrons transferred in the tunneling/hopping regime as well, solid-state spin-valve devices were fabricated to measure spin selectivity in conduction. Non-ferromagnetic Au electrodes, functionalized with AUT SAMs and BSA or dBSA films, were capped with Ni or Au electrodes with a thin aluminum oxide (Al_2O_3) tunneling barrier (Figure III.6a). Due to spin-polarized electron injection into the minority spin subband and out of the majority spin subband within FM materials, dependence of the current on the magnetization orientation of the Ni electrode would indicate that the protein layers could polarize electron transport through the films. If Au rather than Ni capping electrodes are used, no significant difference of the current on an external magnetic field is expected.

The current between top and bottom electrodes was measured while sweeping the voltage when an external magnetic field was applied underneath the devices to magnetize the top Ni electrodes up or down as shown in Figure III.6a at room temperature. Sixty devices per magnetic field orientation were tested on each of three independently prepared substrates (inset, Figure III.6b), and the average current values for the three substrates are

shown in Figure III.6b. In each case, no significant differences in current were determined between field up *vs* field down conditions within the error of our measurements.

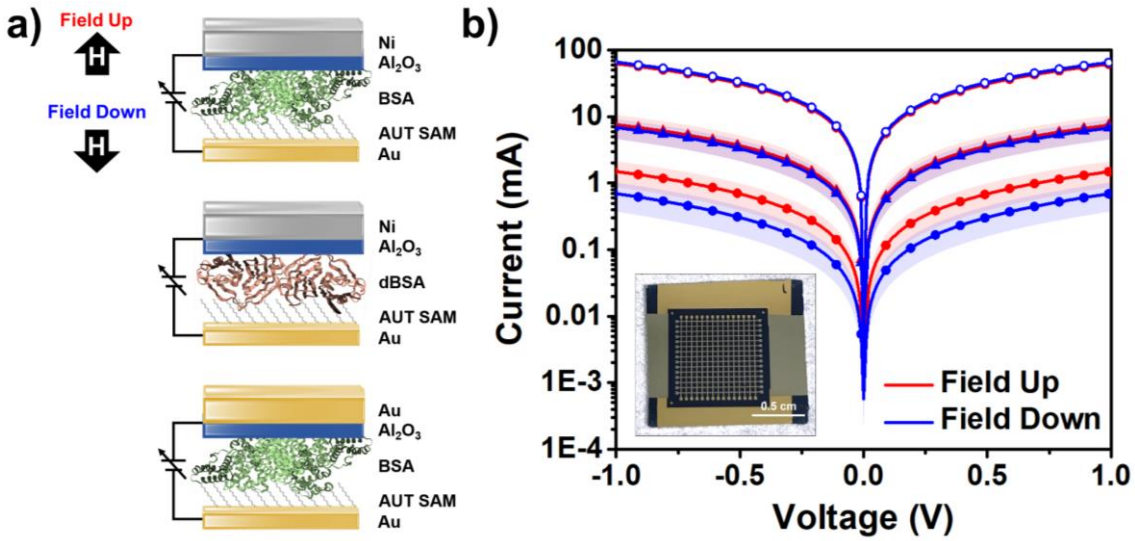

Figure III.6. (**a**) Schematic of spin-valve device architectures composed of self-assembled monolayers (SAMs) of 11-amino-1-undecanethiol (AUT) and electrostatically adsorbed films of bovine serum albumin (BSA) or thermally denatured bovine serum albumin (dBSA) sandwiched between non-ferromagnetic Au and ferromagnetic Ni electrodes. An external magnetic field is used to magnetize the Ni electrodes parallel or antiparallel to the normal axis of the devices. (**b**) Average current-voltage measurements for Au/BSA/Ni (solid circles), Au/dBSA/Ni (solid triangles), and Au/BSA/Au (open circles) junctions from three substrates (photograph in inset). Shaded areas represent standard error of the mean from *N*=3 substrates for each condition (*N*=60 panels tested per magnetic field orientation per substrate).

The characterization of similar device architectures was recently reported by Varade *et al*. in which the magnetoresistance of solid-state bacteriorhodopsin spin valves was measured.[42] While the native secondary structure of both bacteriorhodopsin and BSA contains multiple α-helical subunits, unlike in BSA, the helices are well-aligned in bacteriorhodopsin, which likely enhances its ability to polarize transmitted electrons.

Furthermore, the performance of the devices was enhanced when bacteriorhodopsin was treated with the non-ionic detergent *n*-octyl-thioglucoside. Optimization of film deposition and device fabrication may enable the use of proteins within next-generation solid-state electrical components or spin valves.[2,43,44] However, our results suggest that neither BSA nor dBSA films can efficiently filter electrons within the conduction regime under the film preparation conditions used for UPS measurements.

III.C. Discussion

We investigated substrate magnetization-dependent photoemission from FM substrates functionalized with chiral molecular assemblies and found that when functionalized with chiral molecules, I depended on the magnetization orientation and polarization of the underlying FM metal. We hypothesize that these results are due to the buildup of spin-polarized holes within the chiral organic films upon ionization. Three alternative explanations may be used to rationalize our results that do *not* require that ionization causes the formation of spin-polarized hole states.

First, asymmetric scattering angles of photoelectrons depending on the handedness of the adsorbed chiral molecules may be manifested in ultraviolet photoelectron spectra. Asymmetric forward and backwards scattering of photoelectrons emitted from chiral molecule vapors using circularly polarized ionizing radiation has been detected by circular dichroism in the angular distribution of photoelectrons.[45,46] This process is a result of a pure electronic dipole transition, and does not depend on spin-orbit coupling interactions. This phenomenon can be observed with achiral molecules as well, provided that they are oriented,[47] and the combined interaction between incident photons and molecular target

exhibit a defined handedness, which can be induced by precise experimental geometries.[12] However, because unpolarized radiation was used as an excitation source in our experiments, photoelectron circular dichroism is likely not responsible for the substrate magnetization-dependent effects described herein. Furthermore, the lack of dependence of I on substrate magnetization conditions for achiral, yet aligned, AUT SAMs on FM substrates also rules out this explanation.

Second, if the different surface charging, and thus I, that we measured between substrate magnetization orientations without charge neutralization were attributed to the capture of photoelectrons originating from the FM substrate with unfavorable helicity, then I and ϕ should show opposite trends. Right-handed *L*-peptides assembled on Au have been shown to polarize transmitted photoelectrons with their spin oriented antiparallel to the surface normal.[8] Our UPS results under charge neutralization conditions agree with these observations; a lower ϕ when the substrates were magnetized up corresponds to a lower energy barrier to remove electrons from the surface when the spins of electrons within the majority subband are oriented antiparallel to the surface. When the substrates are magnetized down, a higher percentage of photoelectrons with their spins oriented parallel to the surface normal are emitted upon irradiation. Under these conditions, if more electrons do not escape the surface organic layer due to spin filtering than from surfaces magnetized in the opposite direction, then less charging, and lower I would be expected when substrates were magnetized down. However, this prediction is not in agreement with our results, where lower I and ϕ were measured when substrates were magnetized up.

Third, spin polarization of electrons transferred from the metal surface to neutralize holes within the organic layers may cause a buildup of positive charge in the film when the

substrates are magnetized in the unfavorable orientation. When the majority electrons of the FM substrate do not match the preferred helicity in charge transfer, a higher resistance state results. In our experiments, differences in the *I* between substrate magnetization orientations were observed for *L*-peptide SAMs and for AUT SAMs with dBSA films. For *L*-peptide SAMs, the preferred helicity of electrons that tunnel through the molecules is positive, that is, with spin aligned parallel to its linear momentum direction.[41] In our experimental setup, substrates magnetized down would provide favorable spin alignment for electrons transferred from the FM substrates to the organic films based only on the chirality of the peptides, and would result in a lower buildup of charge, and thus a lower *I* when substrates are magnetized down. However, this prediction does not match our experimental results. Further, we found that dBSA films are not capable of filtering transferred electrons *via* conduction under the film conditions prepared for UPS measurements, eliminating this possible contribution to substrate magnetization-dependent surface charging in dBSA films.

Collectively, our results suggest that the holes remaining within photoionized films of chiral films adsorbed on FM substrates have polarized spin components along the normal axis of the organic layers, dictated by the chirality of the films. When the substrates are magnetized in the preferred orientation, that is, such that the spin of electrons supplied by the majority subband matches that of the holes within the organic film, more efficient electron-hole recombination occurs to regenerate the organic film (Figure III.a,d). However, when the substrates are magnetized in the opposite direction, the electrons within the majority subbands do not match the spin state of the holes left in the organic films (Figure III.b,c). Thus the surfaces build up a net positive charge effectively increasing *I*.

Therefore, we postulate that oriented films of chiral molecules are capable of emitting spin-polarized photoelectrons when excited with unpolarized ionizing radiation.

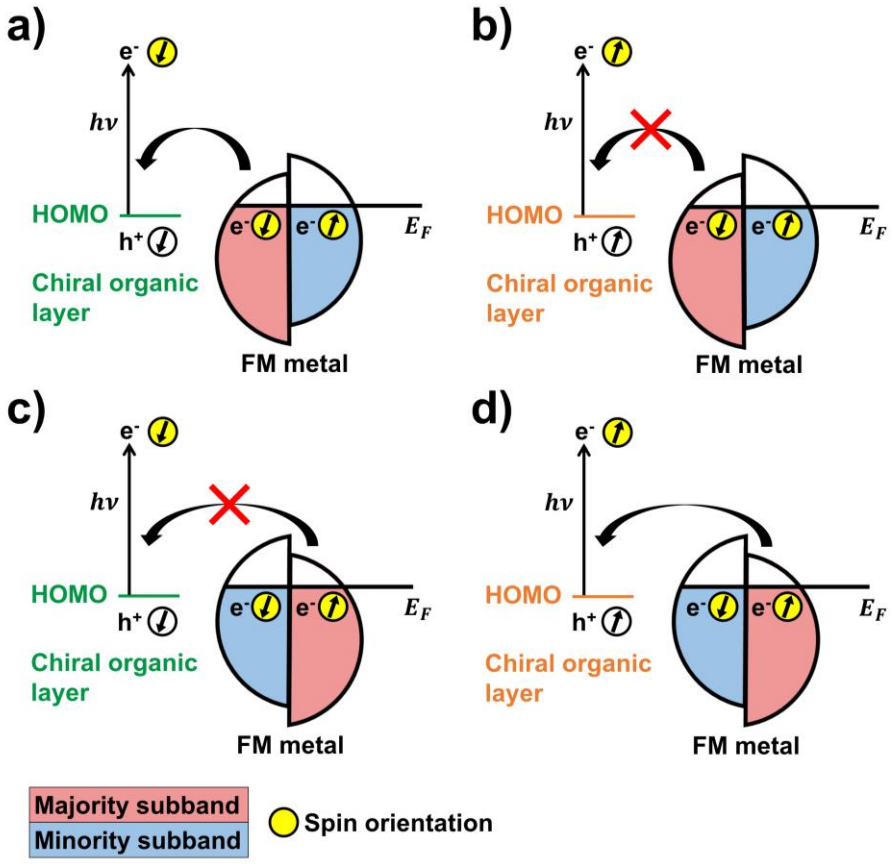

Figure III.7. (**a,b**) Schematics representing allowed *vs* suppressed electron transfer from ferromagnetic (FM) substrates magnetized up or (**c,d**) down to fill spin-polarized holes resulting from ionization of chiral molecule films of opposite handedness (green and orange).

Interestingly, the trend in substrate magnetization orientation-dependence of I was reversed between α-helical *L*-peptide SAMs and dBSA films with high β-sheet content. These results suggest that photoelectrons collected from *L*-peptide SAMs and dBSA films are spin polarized with negative and positive helicity, respectively. The structure of surface-adsorbed BSA molecules represents a disorganized intermediate between these two systems, which

may also explain the absence of the dependence of I on substrate magnetization conditions for BSA films on AUT SAMs. While both the peptides and proteins are composed of left-handed *L*-amino acid monomer subunits, we find that the secondary structure of the molecules dictate spin-selective interactions with transmitted electrons. These results corroborate studies on dsDNA.[48] While oligonucleotide strands of DNA contain *D*-deoxyribose sugars within the phosphodiester backbone, the handedness of the tertiary double-helix structure that results upon hybridization of complementary strands dictates the helicity preference in spin-selective interactions with electrons.[48]

Further, because of the disappearance of this effect when substrates were magnetized to sub-saturation conditions with ±7 kOe applied magnetic fields, I must depend on the polarization of electrons within the underlying FM material. At full saturation, the magnetization of the perpendicularly-magnetized Co/Pt substrates is still <100%. Therefore, the difference in ϕ of *ca.* 80 meV measured between opposite magnetization orientations under surface charge neutralization conditions represents a *lower limit* for the relative energy barrier to transmission of electrons with energies above the vacuum level with right- *vs* left-handed helicity through right-handed α-helical peptide SAMs of approximately ten helical turns. By comparison, spin-dependent energy barriers to transport through α-helical peptides in the conduction regime for electrons with energies below the vacuum level have been reported to be *ca.* 500 meV for peptides of approximately half the length of those used herein.[8] This value was determined by comparing the differences in the band gaps for the spin-density of states from dI/dV plots from conductive AFM measurements of peptides assembled on Ni surfaces magnetized up *vs* down. The lower, relative energy barrier that we obtain in over-the-barrier transmission of photoelectrons through α-helical peptides may be

attributed to the escape of electrons from regions devoid of SAM molecules due to inhomogeneous surface coverage, which would not depend on substrate magnetization condition.

Lastly, under every measurement condition, no significant differences in the intensity, or counts, of photoelectrons collected, nor in the total integrated area considering photoelectrons of all kinetic energies (between 0 eV and *ca*. 14-16 eV, depending on the width of the spectra) were determined between substrates magnetized up *vs* down. In contrast, higher or lower intensities in electron energy distributions within the kinetic energy range of ~0-2 eV have been reported when Au substrates functionalized chiral films are irradiated with left- *vs* right-handed circularly polarized light to emit spin polarized electrons of opposite helicity from the Au surface.[6,11] In our measurements, photon energies are substantially larger than I ($h\nu \gg I$) and are likely insensitive to small (<1%) differences in I. Thus, while UPS enables the determination of relative energy barriers for photoemission of electrons with opposite helicity from chiral organic films, a disadvantage of our measurement strategy is the inability to detect differences in photoelectron yield.

III.D. Conclusions and Prospects

In conclusion, we demonstrated that photoelectrons emitted by ionization of chiral molecular films using unpolarized ultraviolet radiation can be spin polarized by indirectly measuring the capability of FM substrates to neutralize spin-polarized holes remaining within the assemblies. Differences in ultraviolet photoelectron spectra that depended on substrate magnetization were measured from monolayers of α-helical peptides and films of thermally denatured proteins lacking α-helical secondary structures composed of *L*-amino

acid monomers. We hypothesize that these results are due to dissymmetric scattering probabilities of low-energy secondary electrons with opposite helicity originating from both underlying metal surfaces and chiral molecules due to the asymmetric arrangement of atoms within the films as described by the CISS effect. This hypothesis was tested using UPS and spin-valve device architectures to deconvolute I and ϕ attributed to the buildup of spin-polarized holes upon film ionization and the relative energy barriers to transmission of spin up *vs* spin down electrons through chiral molecules, respectively.

Furthermore, while the spin polarization of photoelectrons transmitted through chiral molecular assemblies may be measured using specialized experimental methods (*i.e.*, the use of a Mott polarimeter), this work establishes figures of merit to measure spin selectivity that can be assessed more readily by other research groups and compared with varying molecular systems. Our experimental protocol to measure the magnetization-dependent ϕ of chiral molecule assemblies on FM substrates is highly generalizable, and will provide new mechanistic insight into spin polarization by chiral molecules. Correlating experimental measurements of these barriers with new and evolving theoretical models will be critical to develop a foundational understanding of the CISS effect.

III.E. Materials and Methods

III.E.1. Materials

Bovine serum albumin (BSA), 11-mercapto-1-undecanethiol hydrochloride (AUT), acetone, and 0.01 M phosphate buffered saline, (PBS, [NaCl]=138 mM, [KCl]=2.7 mM, pH 7.4), and dimethyl sulfoxide (DMSO), were purchased from Sigma-Aldrich (St. Louis, MO, USA). Absolute ethanol was purchased from Decon Laboratories, Inc. (King of Prussia, PA, USA). Deionized water (~18 MΩ) was obtained from a Millipore water purifier (Billerica, MA, USA). Oligopeptides were purchased from Bio Synthesis, Inc. (Lewisville, TX, USA) with a sequence of (N → C) $[K(Aib)A(Aib)A]_6KC$, where K = lysine, Aib = α-aminoisobutyric acid, A = alanine, and C = cysteine. Left- and right-handed α-helical sequences, referred to as *D*- and *L*-peptides, respectively, were identical except that left-handed α-helical sequences (*D*-peptide) contained the *D* form of all K, A, and C residues, while right-handed α-helical sequences (*L*-peptide) contained the *L* form of all K, A, and C residues. Unless otherwise noted, the convention "left" and "right" refers to the helical handedness.

III.E.2. Ferromagnetic Multilayer Thin Film Growth and Surface Preparation

Thin films with perpendicular magnetic anisotropy were fabricated on glass substrates using a multi-cathode magnetron sputtering system with a base pressure of $< 3\times10^{-8}$ Torr. The stacking structure of samples was glass substrate/Ta 3/Pt 2/$[Co\ 0.6/Pt\ 0.3]_{69}$/Co 0.6/Au 1 (layers in nm). The deposition was performed in an Ar gas atmosphere and the temperature was fixed at room temperature. The Ar pressure during the sputtering was 10 mTorr for the Co and Pt layers and 2.7 mTorr for the Ta and Au layers. Prior to functionalizing the substrates, FM substrates were cleaned by thorough rinsing with acetone and ethanol before

being blown dry with N_2. The films were characterized using a MPMS 3 superconducting quantum interference device (SQUID) magnetometer (Quantum Design, Inc., San Diego, CA).

Prior to the functionalization of the FM thin film surfaces and photoelectron spectroscopy measurements, each sample (*ca.* 30 mm^2) was magnetized up or down within the SQUID magnetometer by applying a magnetic field perpendicular to the plane of the surface. For surfaces magnetized to saturation, a field of +12 kOe or -12 kOe was applied to magnetize the substrates up or down, respectively. For surfaces magnetized at approximately half of their saturation magnetization, a field of -12 kOe or +12 kOe was applied first, followed by application of a field of +7 kOe or -7 kOe to magnetize the substrates up or down, respectively.

III.E.3. Ferromagnetic Multilayer Thin Film Surface Functionalization

Pure monolayers of *L*- and *D*-peptides were prepared by immersing clean FM substrates in 0.5 mM solutions of the peptides (1:11 DMSO:PBS) for 48 h. Mixed monolayers of *L*- and *D*-peptides were formed from racemic (1:1 mole:mole) 0.5 mM solutions. Solid peptides were first dissolved in DMSO, and diluted to 0.5 mM with PBS. Both DMSO and PBS were degassed with N_2 for at least 1 h prior to solution preparation to minimize oxidation of the cysteine residues resulting in disulfide formation. Following monolayer formation, substrates were rinsed with deionized water and blown dry with N_2. Rinsing and drying steps were performed twice.

Preparation of BSA and denatured BSA (dBSA) films began with the formation of self-assembled monolayers of AUT formed on clean FM thin films by immersing substrates in a 1 mM ethanolic solution of AUT for 18 h. The substrates were then rinsed with ethanol and

blown dry with N_2 and immersed in 1 mg/mL solutions of BSA in PBS for 48 h to prepare BSA films electrostatically adsorbed to the AUT SAMs. To prepare sample surfaces functionalized with denatured BSA, stock solutions of 1 mg/mL BSA in PBS were first heated at 95 °C for 30 min and cooled slowly to room temperature before incubating with AUT-functionalized substrates. Following monolayer preparation, substrates were rinsed with deionized water and blown dry with N_2.

III.E.4. Circular Dichroism Spectroscopy

Measurements were carried out on a J-715 circular dichroism spectrophotometer (JASCO Inc., Easton, MD, USA) at room temperature with four scans per sample. The resolution was 0.5 nm, the bandwidth was 1.0 nm, the response time was 8 s, and the collection speed was 20 nm/min. Average scans are shown after baseline subtraction of spectra taken with just ethanol (for peptides) or PBS (for BSA and dBSA).

III.E.5. Ellipsometry

Measurements were carried out in ambient conditions using an LSE Stokes Ellipsometer (Gaertner Scientific Corporation, Skokie, IL, USA), utilizing a 632.8 nm HeNe laser measuring beam with a 70° angle of incidence. Optical constants for FM multilayers were referenced from the literature for similar material stacks.[49] The refractive indices and extinction coefficients of organic layers were set to 1.5 and 0 respectively, a standard approximation in the ellipsometric measurement of organic thin films using visible light.[50,51] Thicknesses were calculated from an average of 5 measurements per sample. All samples were prepared as outlined above.

III.E.6. Infrared Reflection-Absorption Spectroscopy

Measurements were performed using a Nicolet 6700 FT-IR (Thermo Electron Corporation, Madison, WI, USA) in reflectance mode with infrared light incident at *ca.* 70° relative to the surface normal. Spectra with 512 scans and a resolution of 4 cm^{-1} were collected for all cases. Samples of *L*- and *D*-peptide SAMs on FM substrates were prepared as described above. For sufficient signal to noise ratios, samples of BSA and dBSA were prepared by vacuum drying 50 mg/mL and 1 mg/mL solutions in PBS on AUT SAMs on FM substrates. The infrared reflection-absorption spectra therefore do not reflect the exact structure of the proteins on samples used for photoelectron spectroscopy measurements, but can be used to compare empirically structural differences between films of native BSA and its thermally denatured forms.

III.E.7. Atomic Force Microscopy

Bare and functionalized FM multilayer thin film surfaces were imaged by AFM using a Dimension Icon scanning probe microscope (Bruker, Billerica, MA). Surface topographies and mechanical properties were simultaneously measured using the PeakForce Quantitative Nanomechanical Property Mapping (PeakForce QNM) mode. ScanAsyst-Air cantilevers (Bruker, spring constant = 0.4 ± 0.1 N m^{-1}, resonant frequency = 70 kHz) were calibrated with a clean piece of silicon wafer before every measurement. A peak-force set-point of 400 pN and a scan rate of 1 Hz was maintained for all measurements. The Nanoscope Analysis software (Bruker) was used to analyze and to calculate root mean square (R_q) and average (R_a) roughnesses for all images. Average grain areas were determined *via* the watershed algorithm using Gwyddion.[52,53]

III.E.8. Surface Characterization by X-Ray Photoelectron Spectroscopy

X-ray photoelectron spectroscopy of FM multilayer thin film surfaces was done using an AXIS Ultra DLD photoelectron spectrometer (Kratos Analytical Inc., Chestnut Ridge, NY) and a monochromatic Al K_α X-ray source with a 200 μm circular spot size under ultrahigh vacuum (10^{-9} Torr). The heights of all samples were optimized prior to spectral acquisition to maximize the signal to noise. High-resolution spectra of C 1s, O 1s, N 1s, Co 2p, Pt 4f, and Au 4f were acquired at a pass energy of 20 eV using a 300 ms dwell time. For all scans, 15 kV was applied with an emission of 15 mA. An average of 15 scans were collected for each of the high-resolution spectra. X-Ray photoelectron spectra were fit with the CasaXPS Software Version 2.3.17PR1.1 using a Shirley background and Gaussian-Lorentzian peak shapes.

III.E.9. Surface Characterization by Ultraviolet Photoelectron Spectroscopy

Measurements of FM multilayer thin film surfaces (N = 6 to 10 substrates per experimental condition) were done using a Kratos Axis Ultra DLD photoelectron spectrometer (Kratos Analytical, Manchester, UK) and a He I excitation source (21.2 eV) under a -9 V bias between the samples and detector. The heights of all samples were optimized prior to spectral acquisition to maximize the signal to noise. Spectra were acquired at a pass energy of 5 eV with a 100 ms dwell time and aperture size of 100 μm. Three spectra were obtained per sample on different areas of each surface. Independent substrates with magnetization parallel (up) or antiparallel (down) to the surface normal were used to avoid organic film degradation due to UV light irradiation. The incident angle of UV irradiation was fixed at 35° relative to the plane of the surface for all measurements.

The energies of the secondary electron cutoffs and Fermi edges (onsets and offsets)

were measured at the x-intercept of the maximum slope of their rising edges using linear fits to the data of every spectrum using the OriginPro graphing software (OriginLab, Northampton, MA). Spectra were fit with a Shirley background to account for uneven baselines using CasaXPS Software Version 2.3.17PR1.1. Values of secondary electron peak intensities and total integrated areas were obtained using command features within this software. For all experimental conditions, the secondary electron peak intensities, integrated areas of the full spectra, binding energy values of the secondary electron cutoff, the binding energy values of the Fermi edges, spectrum widths, ϕ, and I are tabulated in Tables SIII.1 and SIII.2, below.

III.E.10. Spin Valve Fabrication and Testing

Prime quality 4″ Si{100} wafers (P/B, 0.001-0.005 Ω·cm, thickness 500 μm) were purchased from Silicon Valley Microelectronics, Inc. (Santa Clara, CA, USA), and were cut into pieces of 1.5 cm × 1.5 cm before fabrication of devices. Shadow masks were purchased from Photo Sciences, Inc. (Torrance, CA, USA). Titanium and gold of 10 and 50 nm thicknesses, respectively, were deposited sequentially using an electron-beam evaporator (CHA Industries, SOLUTION, Fremont, CA, USA) through shadow masks under high vacuum (base pressure of 10^{-8} Torr) with an evaporation rate of 1 Å s^{-1} to form the bottom electrodes (100 μm width).

Bottom Au electrodes were functionalized with AUT SAMs and thin films of electrostatically adsorbed BSA and dBSA as described above. Top electrodes consisting of an Al_2O_3 (7 nm) tunneling barrier and Ni (150 nm) were deposited sequentially by electron-beam evaporation through shadow masks rotated 90° to the original configuration under

high vacuum (base pressure of 10^{-6} Torr) at a rate of 1 Å s^{-1} and 2 Å s^{-1}, respectively.

Electronic measurements were performed on a manual analytical probe station (Signatone, Gilroy, CA) using a Keithley 4200A (Tektronix, Beaverton, OR) semiconductor parameter analyzer. Current-voltage (I-V) curves were obtained by measuring the current between top and bottom electrodes while sweeping the voltages from –2 V to 2 V with a step size of 10 mV. During measurements, a cylindrical neodymium-iron-boron magnet of *ca.* 0.3 T (K&J Magnetics, Pipersville, PA, USA) was placed directly beneath substrates. Under field-up (down) conditions, the north (south) pole of the magnet was flush with the backside of the substrates. For each external magnetic field condition, 180 separate junctions were tested across three individually prepared substrates.

III.E.11. Statistics

GraphPad Prism (GraphPad Software Inc., San Diego, CA, USA) was used to perform statistical analyses. Probabilities $P < 0.05$ were considered statistically significant, and throughout the main text and Supplementary Information file, data are reported as mean values ± standard errors of the mean. Two-tailed, unpaired *t*-tests were used to compare the secondary electron peak intensities and integrated areas of the full ultraviolet photoelectron spectra for substrates magnetized up vs down under every experimental condition, and to compare I calculated for *L*-peptide SAMs and dBSA films on AUT SAM-functionalized FM substrates under charge neutralization, ϕ under all conditions, I of FM substrates functionalized with AUT SAMs, and I of FM substrates functionalized with mixed monolayers of *L*- and *D*-peptides magnetized up *vs* down at full saturation (Table SIII.4).

Ionization energy values for FM substrates magnetized at full and sub-saturation and

modified with SAMs of *L*- and *D*-peptides, and with BSA and dBSA films electrostatically bound to AUT SAMs, were evaluated by two-way analysis of variance followed by Bonferroni *post hoc* tests if significance was determined in the interaction or in the main effect of substrate magnetization orientation (Table SIII.5).

Supplementary Material

Spin-Polarized Photoemission by Ionization of Chiral Molecule Films

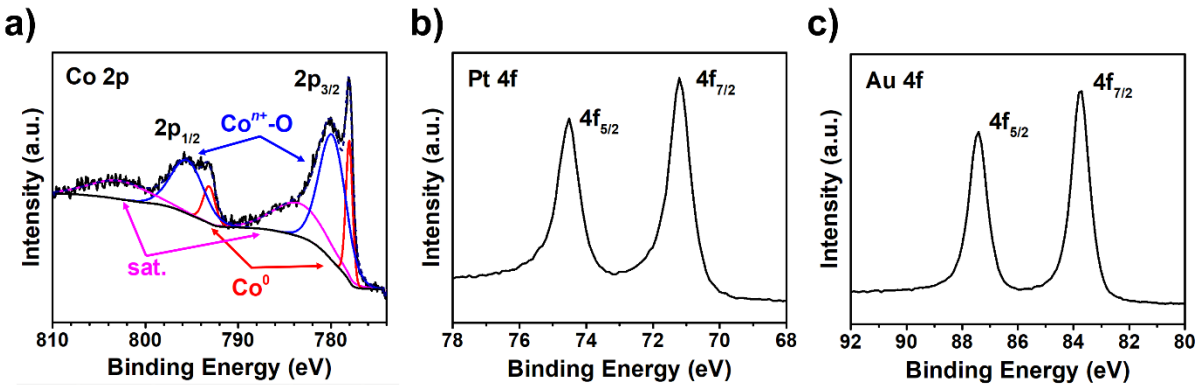

Figure SIII.1. Representative high-resolution X-ray photoelectron spectra of bare ferromagnetic substrates showing (**a**) Co 2p, (**b**) Pt 4f, and (**c**) Au 4f regions. Peaks in (**a**) were fit according to previous reports.[54]

Table SIII.1. Secondary electron peak intensities and integrated areas of entire spectra for bare ferromagnetic substrates, and substrates functionalized with organic films as indicated in the left-hand column when samples were magnetized up or down (↑ or ↓) and magnetized with ±12 kOe or ±7 kOe applied fields. The errors represent standard errors of the means. SAM: self-assembled monolayer; AUT: 11-amino-1-undecanethiol; BSA: bovine serum albumin; dBSA; thermally denatured bovine serum albumin.

Condition	Field (kOe)		Secondary Electron Peak Intensity (a.u.)	Integrated Area (a.u.*eV)	*N*
Bare substrates	12	↑	139980 ± 3660	576030 ± 14100	9
		↓	137880 ± 9560	477410 ± 28320	8
AUT SAM	12	↑	480170 ± 11110	1236220 ± 25100	9
		↓	476270 ± 11530	1232330 ± 24250	9
***L*- and *D*-Peptide Mixed SAM**	12	↑	95040 ± 3010	460730 ± 10540	8
		↓	97000 ± 3520	478590 ± 16600	8
***L*-Peptide SAM**	12	↑	127590 ± 7760	641490 ± 31340	10
		↓	111620 ± 7930	585400 ± 38360	10
	7	↑	162170 ± 7340	799080 ± 29380	8
		↓	150840 ± 5600	752250 ± 24420	8
***D*-Peptide SAM**	12	↑	128240 ± 7390	651210 ± 27310	10
		↓	132830 ± 10200	666430 ± 34210	10
	7	↑	83560 ± 9680	411960 ± 31040	7
		↓	94250 ± 4840	465520 ± 21270	8
AUT SAM + BSA	12	↑	320170 ± 5300	1236170 ± 21310	10
		↓	314530 ± 8340	1227050 ± 32940	9
	7	↑	322190 ± 16670	1291220 ± 61190	9
		↓	327390 ± 12870	1316720 ± 46760	8
AUT SAM + dBSA	12	↑	381590 ± 7570	1424330 ± 26170	10
		↓	389230 ± 11060	1455510 ± 37110	8
	7	↑	235920 ± 7100	94800 ± 22650	10
		↓	251720 ± 6740	994360 ± 22930	10
AUT SAM + dBSA (charge neutralized)	12	↑	48230 ± 2200	187390 ± 5200	6
		↓	45320 ± 1590	178110 ± 5800	8
***L*-Peptide SAM (charge neutralized)**	12	↑	20780 ± 1530	87790 ± 4790	9
		↓	20180 ± 1020	90320 ± 4140	10

Table SIII.2. Binding energies of the secondary electron cutoffs (E_B^{max}) and valence band (Fermi) edges (E_B^{min}), spectra widths (W), work functions (ϕ), and ionization energies (I) determined from ultraviolet photoelectron spectra when samples were magnetized up or down (↑ or ↓) and magnetized with ±12 kOe or ±7 kOe applied magnetic fields. The errors represent standard errors of the means. SAM: self-assembled monolayer; AUT: 11-amino-1-undecanethiol; BSA: bovine serum albumin; dBSA; thermally denatured bovine serum albumin.

Condition	Field (kOe)		E_B^{max} (eV)	E_B^{min} (eV)	W (eV)	ϕ (eV)	I (eV)	N
Bare substrates	12	↑	16.68 ± 0.01	0.01 ± 0.01	16.67 ± 0.01	4.52 ± 0.01	-	9
		↓	16.67 ± 0.00	0.01 ± 0.01	16.67 ± 0.01	4.53 ± 0.00	-	8
AUT SAM	12	↑	17.19 ± 0.01	1.24 ± 0.01	15.95 ± 0.01	4.01 ± 0.01	5.25 ± 0.01	9
		↓	17.19 ± 0.01	1.25 ± 0.01	15.94 ± 0.01	4.01 ± 0.01	5.26 ± 0.01	9
***L*- and *D*-Peptide Mixed SAM**	12	↑	17.08 ± 0.01	3.09 ± 0.01	13.99 ± 0.01	4.12 ± 0.01	7.21 ± 0.01	8
		↓	17.07 ± 0.01	3.09 ± 0.01	13.98 ± 0.01	4.13 ±0.01	7.22 ± 0.01	8
***L*-Peptide SAM**	12	↑	17.13 ± 0.02	3.04 ± 0.01	14.09 ± 0.03	4.07 ± 0.02	7.11 ± 0.03	10
		↓	17.12 ± 0.02	3.13 ± 0.02	14.00 ± 0.01	4.08 ± 0.02	7.20 ± 0.01	10
	7	↑	17.20 ± 0.03	3.15 ± 0.02	14.05 ± 0.02	4.00 ± 0.03	7.15 ± 0.02	8
		↓	17.20 ± 0.02	3.15 ± 0.02	14.05 ± 0.02	4.00 ± 0.02	7.15 ± 0.02	8
***D*-Peptide SAM**	12	↑	17.06 ± 0.02	3.03 ± 0.02	14.03 ± 0.02	4.14 ± 0.02	7.17 ± 0.02	10
		↓	17.14 ± 0.04	3.10 ± 0.04	14.04 ± 0.01	4.10 ± 0.02	7.16 ± 0.01	10
	7	↑	17.11 ± 0.06	3.07 ± 0.04	14.04 ± 0.03	4.09 ± 0.06	7.16 ± 0.03	7
		↓	17.11 ± 0.03	3.09 ± 0.01	14.02 ± 0.03	4.09 ± 0.03	7.18 ± 0.03	8
AUT SAM + BSA	12	↑	17.36 ± 0.01	3.55 ± 0.01	13.82 ± 0.00	3.84 ± 0.01	7.38 ± 0.00	10
		↓	17.36 ± 0.01	3.57 ± 0.00	13.79 ± 0.01	3.84 ± 0.01	7.41 ± 0.01	9
	7	↑	17.31 ± 0.02	3.50 ± 0.01	13.81 ± 0.01	3.89 ± 0.02	7.39 ± 0.01	9
		↓	17.31 ± 0.01	3.51 ± 0.02	13.81 ± 0.01	3.89 ± 0.01	7.40 ± 0.01	8
AUT SAM + dBSA	12	↑	17.78 ± 0.01	3.86 ± 0.01	13.92 ± 0.01	3.42 ± 0.01	7.28 ± 0.01	10
		↓	17.82 ± 0.02	3.86 ± 0.01	13.96 ± 0.01	3.38 ± 0.02	7.24 ± 0.01	8
	7	↑	17.64 ± 0.02	3.71 ± 0.02	13.92 ± 0.01	3.57 ± 0.02	7.28 ± 0.01	10
		↓	17.65 ± 0.01	3.72 ± 0.01	13.93 ± 0.01	3.55 ± 0.01	7.27 ± 0.01	10
AUT SAM + dBSA (charge neutralized)	12	↑	17.28 ± 0.01	3.23 ± 0.03	14.05 ± 0.03	3.92 ± 0.01	7.15 ± 0.03	6
		↓	17.27 ± 0.02	3.21 ± 0.02	14.06 ± 0.01	3.93 ± 0.02	7.14 ± 0.01	8
***L*-Peptide SAM (charge neutralized)**	12	↑	17.10 ± 0.02	3.01 ± 0.02	14.09 ± 0.02	4.10 ± 0.02	7.12 ± 0.02	9
		↓	17.02 ± 0.01	2.92 ± 0.03	14.10 ± 0.03	4.18 ± 0.01	7.10 ± 0.03	10

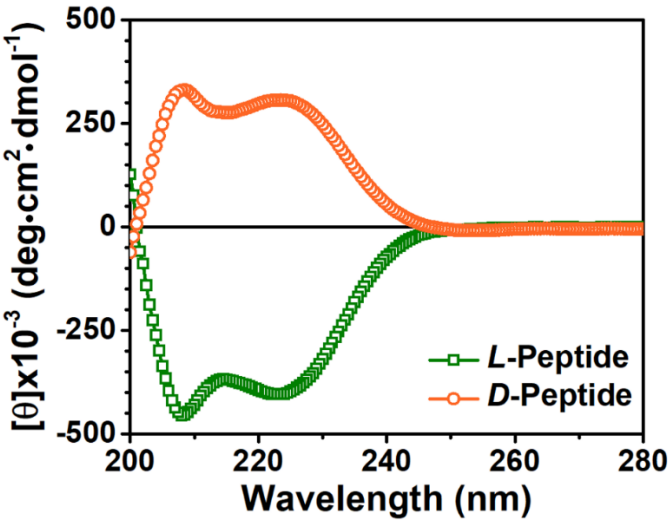

Figure SIII.2. Molar ellipticity (Θ) as a function of wavelength for *L*- and *D*-peptides in ethanol.

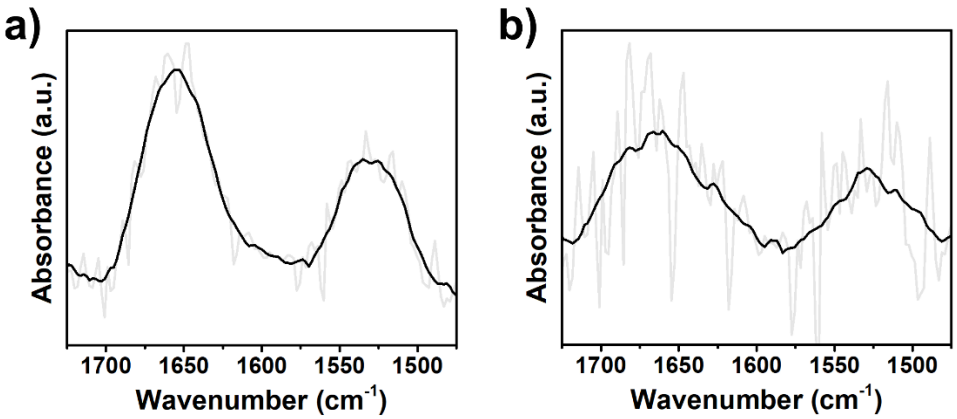

Figure SIII.3. Representative amide I and II band region of infrared reflection-absorption spectra of (**a**) *L*-peptide and (**b**) *D*-peptide self-assembled monolayers on ferromagnetic substrates.

Table SIII.3. Average thicknesses of organic films on ferromagnetic substrates measured by ellipsometry. The errors represent standard errors of the means. SAM: self-assembled monolayer; AUT: 11-amino-1-undecanethiol; BSA: bovine serum albumin; dBSA; thermally denatured bovine serum albumin.

Condition	Film Thickness (nm)	*N*
***L*-Peptide SAM**	3.7 ± 0.5	7
***D*-Peptide SAM**	1.9 ± 0.3	10
***L*- and *D*-Peptide SAM (racemic solution)**	3.1 ± 0.5	6
AUT SAM	1.6 ± 0.1	6
AUT SAM + BSA	7.1 ± 0.4	6
AUT SAM + dBSA	9.4 ± 0.4	6

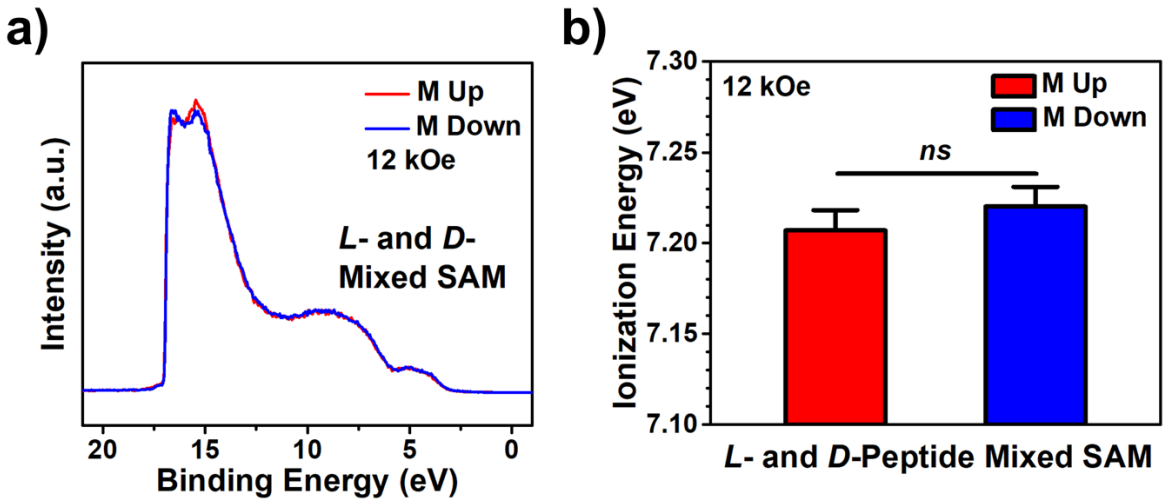

Figure SIII.4. (**a**) Representative ultraviolet photoelectron spectra of self-assembled monolayers (SAMs) of *L*- and *D*-peptides formed from racemic mixtures in solution on ferromagnetic substrates magnetized up (red) or down (blue) at full saturation (magnetized with ±12 kOe magnetic field). (**b**) Ionization energy values of the surfaces magnetized up (red) or down (blue) at full saturation calculated from the ultraviolet photoelectron spectra. Error bars represent standard error of the means; *ns* is not significant ($P > 0.05$).

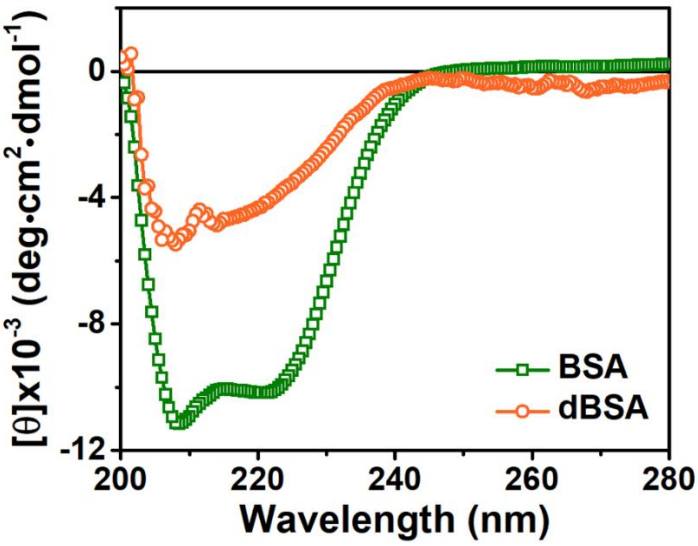

Figure SIII.5. Molar ellipticity (Θ) as a function of wavelength for bovine serum albumin (BSA) and thermally denatured bovine serum albumin (dBSA) in phosphate-buffered saline.

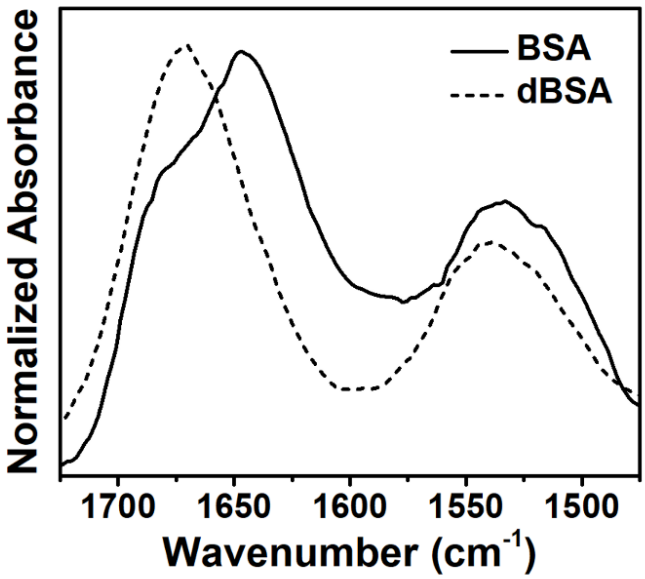

Figure SIII.6. Representative amide I and II band region of infrared reflection-absorption spectra of bovine serum albumin (BSA, solid line) and thermally denatured bovine serum albumin (dBSA, dashed line) films on ferromagnetic substrates.

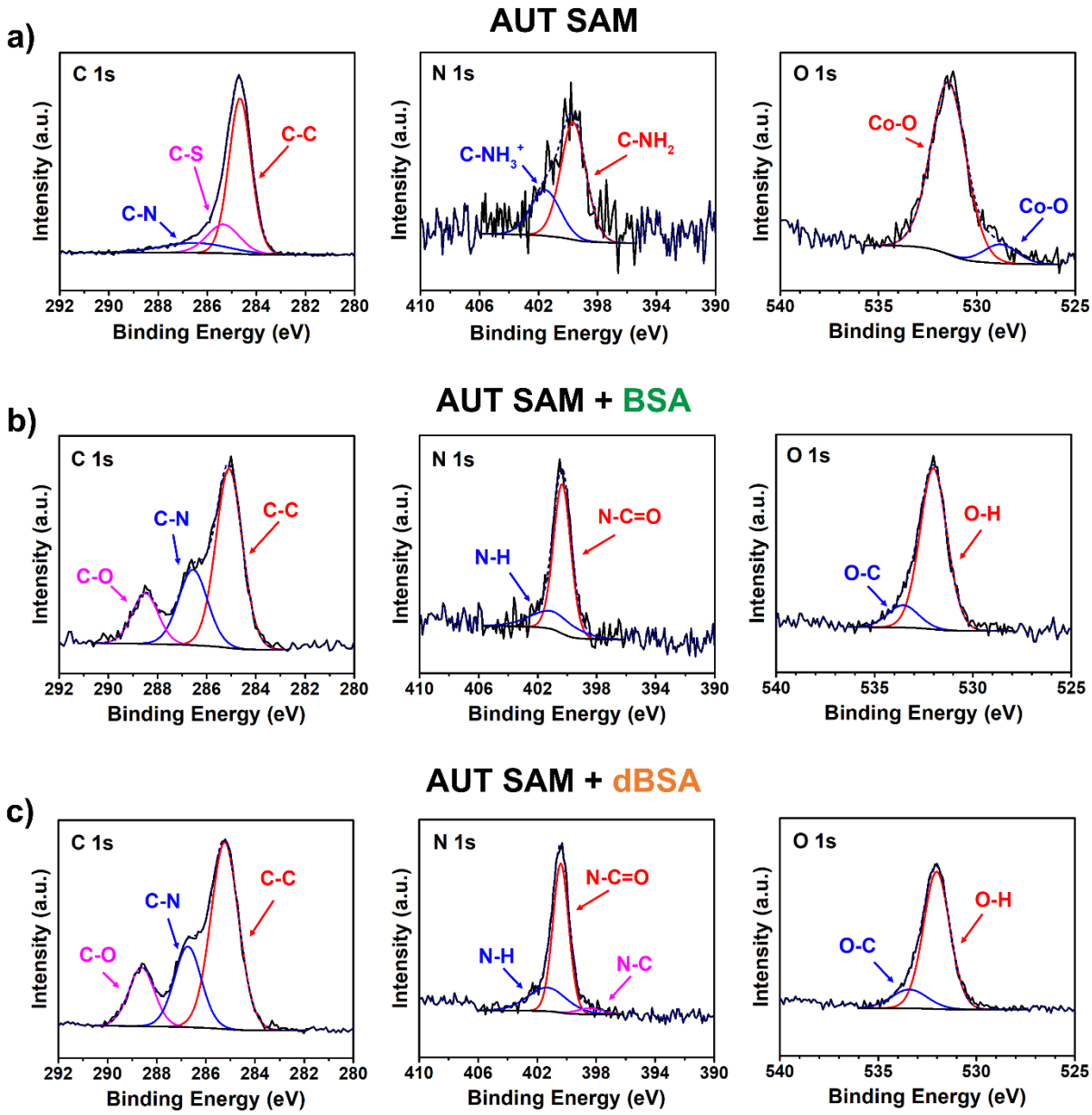

Figure SIII.7. Representative high-resolution X-ray photoelectron spectra showing C 1s, N 1s, and O 1s regions as indicated in each plot for (**a**) ferromagnetic (FM) substrates functionalized with 11-amino-1-undecanethiolate (AUT) self-assembled monolayers (SAMs), (**b**) bovine serum albumin (BSA) films on AUT SAMs on FM substrates, and (**c**) thermally denatured BSA (dBSA) films on AUT SAMs on FM substrates. Chemical states in (**a**),[54-58] and (**b,c**)[59,60] were assigned in agreement with previous reports.

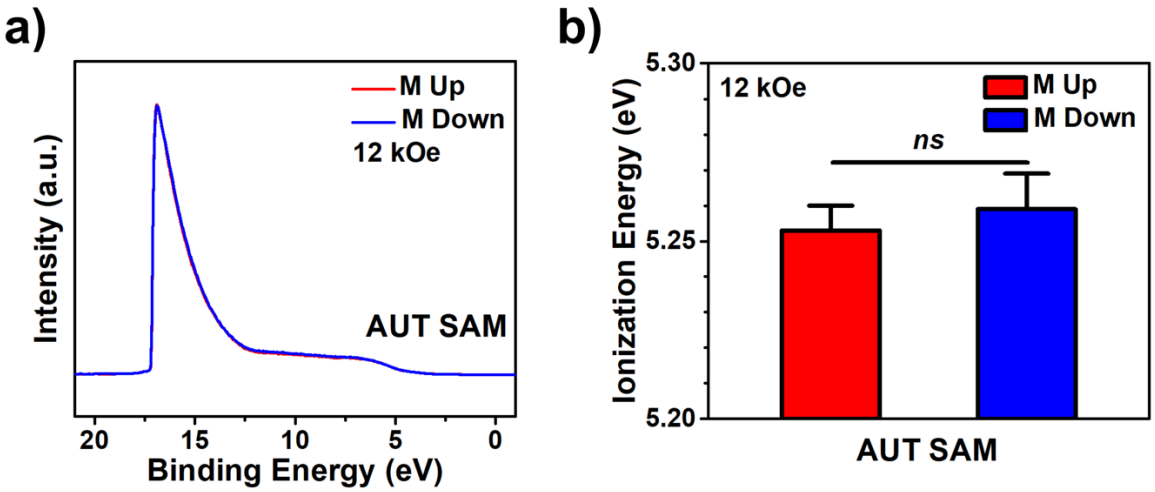

Figure SIII.8. (**a**) Representative ultraviolet photoelectron spectra of ferromagnetic substrates functionalized with *achiral* 11-amino-1-undecanethiolate (AUT) self-assembled monolayers (SAMs) and magnetized up (red) or down (blue) at full saturation (magnetized with ±12 kOe magnetic field). (**b**) Ionization energy values of the surfaces magnetized up (red) or down (blue) at full saturation calculated from the ultraviolet photoelectron spectra. Error bars represent standard error of the means; *ns* is not significant ($P > 0.05$).

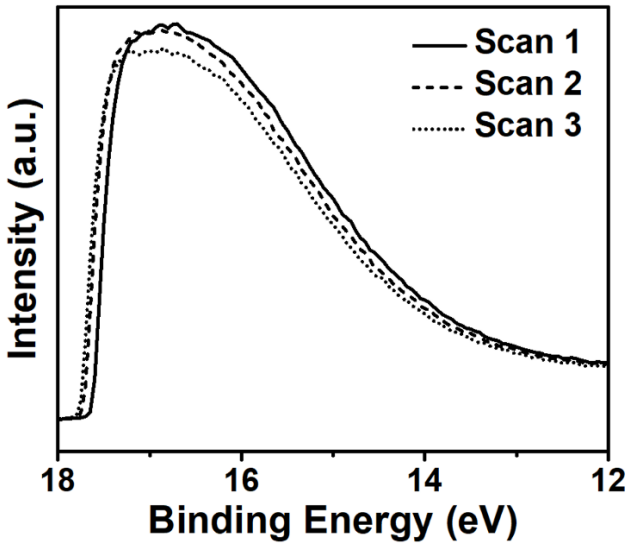

Figure SIII.9. Magnified secondary electron cutoff region of a representative ultraviolet photoelectron spectra of thermally denatured BSA films assembled on 11-amino-1-undecanethiolate self-assembled monolayers on ferromagnetic substrates magnetized up with +12 kOe magnetic field displaying the charging effect (shift to higher binding energies) of sequential scans on the same sample.

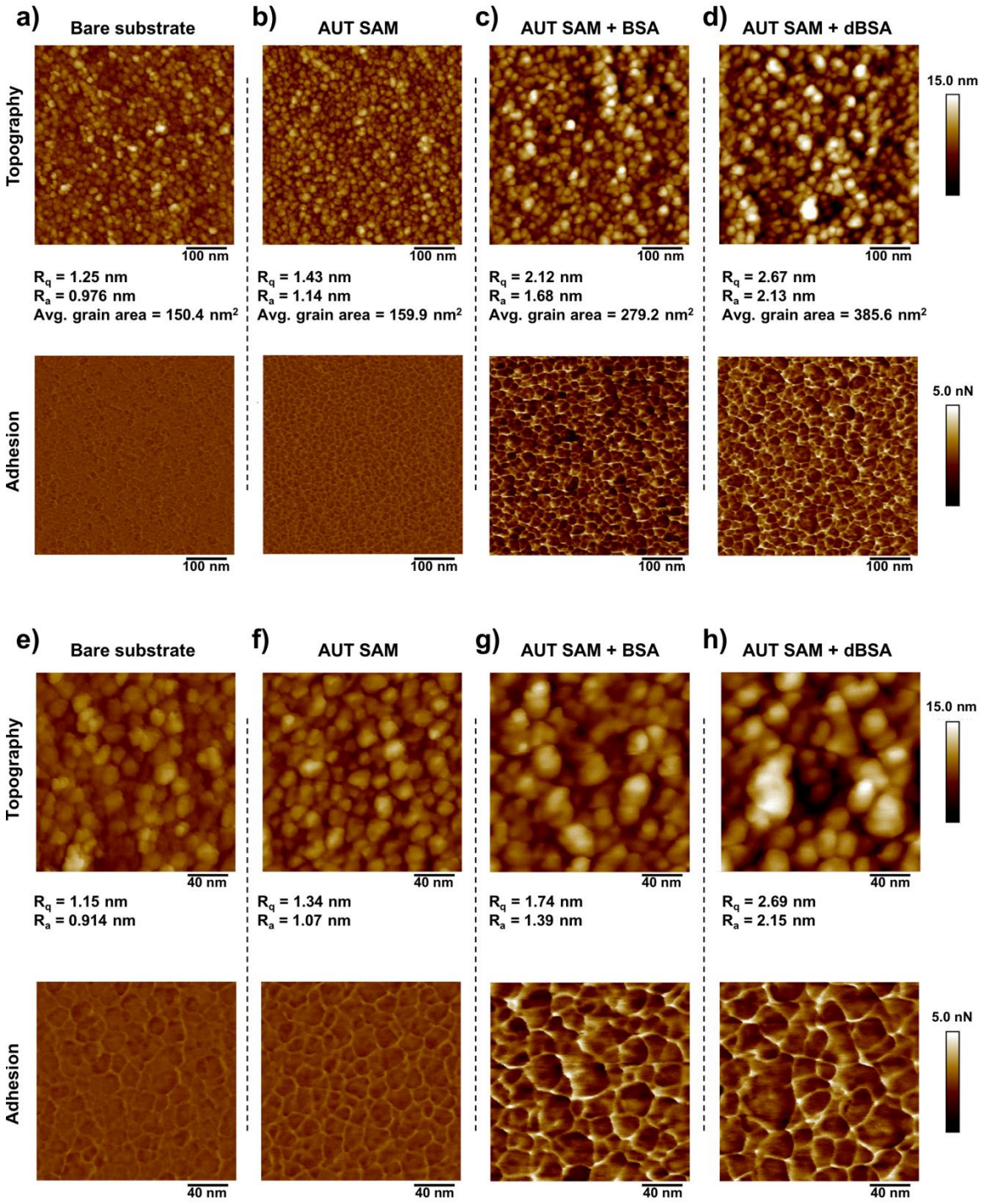

Figure SIII.10. (**a**-**h**) Representative atomic force microscopy topography and adhesion maps for (**a**,**e**) bare ferromagnetic (FM) surfaces, (**b**,**f**) 11-amino-1-undecanethiol (AUT) self-assembled monolayers (SAMs) of FM surfaces, (**c**,**g**) bovine serum albumin (BSA) films on AUT SAM-functionalized FM surfaces, and (**d**,**h**) and denatured bovine serum albumin (dBSA) films on AUT SAM-functionalized FM surfaces. Corresponding root mean square (R_q) and average (R_a) roughnesses are reported for all topography maps(**a-h**), and average grain areas are reported for (**a**-**d**).

Table SIII.4. Results of two-tailed, unpaired *t*-tests to compare secondary electron peak intensities, integrated areas, work functions (ϕ), and ionization energies (I) between sample magnetization orientations (↑ *vs* ↓). SAM: self-assembled monolayer; AUT: 11-amino-1-undecanethiol; BSA: bovine serum albumin; dBSA; thermally denatured bovine serum albumin.

Condition	Secondary Electron Peak Intensity	Integrated Area	ϕ	I
Bare substrates	$P > 0.05$	$P > 0.05$	$P > 0.05$	-
AUT SAM	$P > 0.05$	$P > 0.05$	$P > 0.05$	$P > 0.05$
***L*- and *D*-Peptide Mixed SAM**	$P > 0.05$	$P > 0.05$	$P > 0.05$	$P > 0.05$
***L*-Peptide SAM**	$P > 0.05$	$P > 0.05$	$P > 0.05$	-
***L*-Peptide SAM**	$P > 0.05$	$P > 0.05$	$P > 0.05$	-
***D*-Peptide SAM**	$P > 0.05$	$P > 0.05$	$P > 0.05$	-
***D*-Peptide SAM**	$P > 0.05$	$P > 0.05$	$P > 0.05$	-
AUT SAM + BSA	$P > 0.05$	$P > 0.05$	$P > 0.05$	-
AUT SAM + BSA	$P > 0.05$	$P > 0.05$	$P > 0.05$	-
AUT SAM + dBSA	$P > 0.05$	$P > 0.05$	$P > 0.05$	-
AUT SAM + dBSA	$P > 0.05$	$P > 0.05$	$P > 0.05$	-
AUT SAM + dBSA (charge neutralized)	$P > 0.05$	$P > 0.05$	$P > 0.05$	$P > 0.05$
***L*-Peptide SAM (charge neutralized)**	$P > 0.05$	$P > 0.05$	$P < 0.01$	$P > 0.05$

Table SIII.5. Results of two-way analyses of variance of ionization energy (***I***) with main effects of magnetization orientation (↑ *vs* ↓) and applied magnetization field (±12 kOe or ±7 kOe). SAM: self-assembled monolayer; AUT: 11-amino-1-undecanethiol; BSA: bovine serum albumin; dBSA; thermally denatured bovine serum albumin.

	Interaction Term	**Magnetization Orientation**	**Magnetization Field**
***L*-Peptide SAM (Figure III.3d)**	$F(1,31) = 5.21$ $P < 0.05$	$F(1,31) = 5.49$ $P < 0.05$	$F(1,31) = 0.07$ $P > 0.05$
***D*-Peptide SAM (Figure III.3e)**	$F(1,32) = 0.37$ $P > 0.05$	$F(1,32) = 0.01$ $P > 0.05$	$F(1,32) = 0.03$ $P > 0.05$
AUT SAM + BSA (Figure III.4d)	$F(1,32) = 1.23$ $P > 0.05$	$F(1,32) = 3.00$ $P > 0.05$	$F(1,32) = 0.24$ $P > 0.05$
AUT SAM + dBSA (Figure III.4e)	$F(1,34) = 4.13$ $P < 0.05$	$F(1,34) = 5.35$ $P < 0.05$	$F(1,34) = 1.65$ $P > 0.05$

References

1. Michaeli, K.; Kantor-Uriel, N.; Naaman, R.; Waldeck, D. H. The Electron's Spin and Molecular Chirality – How are They Related and How Do They Affect Life Processes? *Chem. Soc. Rev*. **2016**, 45, 6478–6487.

2. Michaeli, K.; Varade, V.; Naaman, R.; Waldeck, D. H. A New Approach towards Spintronics: Spintronics with No Magnets. *J. Phys.: Condens. Matter* **2017**, 29, 103002.

3. Naaman, R.; Waldeck, D. H. Chiral-Induced Spin Selectivity Effect. *J. Phys. Chem. Lett.* **2012**, 3, 2178–2187.

4. Mondal, P. C.; Fontanesi, C.; Waldeck, D. H.; Naaman, R. Spin-Dependent Transport through Chiral Molecules Studied by Spin-Dependent Electrochemistry. *Acc. Chem. Res.* **2016**, 49, 2560–2568.

5. Fontanesi, C.; Capua, E.; Paltiel, Y.; Waldeck, D. H.; Naaman, R. Spin-Dependent Processes Measured without a Permanent Magnet. *Adv. Mater.* **2018**, DOI: 10.1002/adma.201707390.

6. Göhler, B.; Hamelbeck, V.; Markus, T. Z.; Kettner, M.; Hanne, G. F.; Vager, Z.; Naaman, R.; Zacharias, H. Spin Selectivity in Electron Transmission through Self-Assembled Monolayers of Double-Stranded DNA. *Science* **2011**, 331, 894–897.

7. Mishra, D.; Markus, T. Z.; Naaman, R.; Kettner, M.; Göhler, B.; Zacharias, H.; Friedman, N.; Sheves, M.; Fontanesi, C. Spin-Dependent Electron Transmission through Bacteriorhodopsin Embedded in Purple Membrane. *Proc. Natl. Acad. Sci. U. S. A*. **2013**, 110, 14872–14876.

8. Kettner, M.; Göhler, B.; Zacharias, H.; Mishra, D.; Kiran, V.; Naaman, R.; Fontanesi, C.; Waldeck, D. H.; Sęk, S.; Pawłowski, J.; Juhaniewicz, J. Spin Filtering in Electron Transport through Chiral Oligopeptides. *J. Phys. Chem. C* **2015**, 119, 14542–14547.

9. Kettner, M.; Maslyuk, V. V.; Nürenberg, D.; Seibel, J.; Gutierrez, R.; Cuniberti, G.; Ernst, K. –H.; Zacharias, H. Chirality-Dependent Electron Spin Filtering by Molecular Monolayers of Helicenes. *J. Phys. Chem. Lett.* **2018**, 9, 2025–2030.

10. *Polarized Electrons in Surface Physics*, Vol. 1; Feder, R., Ed.; World Scientific: Singapore, **1985**.

11. Ray, K.; Ananthavel, S. P.; Waldeck, D. H.; Naaman, R. Asymmetric Scattering of Polarized Electrons by Organized Organic Films of Chiral Molecules. *Science* **1999**, 283, 814–816.

12. Schönhense, G. Circular Dichroism and Spin Polarization in Photoemission from

Adsorbates and Non-Magnetic Solids. *Physica Scripta.* **1990**, T31, 255–275.

13. Heizmann, U.; Schönhense, G.; Kessler, J. Polarization of Photoelectrons Ejected by Unpolarized Light from Xenon Atoms. *Phys. Rev. Lett.* **1979**, 42, 1603–1605.

14. Mondal, P. C.; Roy, P.; Kim, D.; Fullerton, E. E.; Cohen, H.; Naaman, R. Photospintronics: Magnetic Field-Controlled Photoemission and Light-Controlled Spin Transport in Hybrid Chiral Oligopeptide-Nanoparticle Structures. *Nano Lett*. **2016**, 16, 2806–2811.

15. Eckshtain-Levi, M.; Capua, E.; Refaely-Abramson, S.; Sarkar, S.; Gavrilov, Y.; Mathew, S. P.; Paltiel, Y.; Levy, Y.; Kronik, L.; Naaman, R. Cold Denaturation Induces Inversion of Dipole and Spin Transfer in Chiral Peptide Monolayers. *Nat. Commun.* **2016**, 7, 10744.

16. Abendroth, J. M.; Nakatsuka, N.; Ye, M.; Kim, D.; Fullerton, E. E.; Andrews, A. M.; Weiss, P. S. Analyzing Spin Selectivity in DNA-Mediated Charge Transfer *via* Fluorescence Microscopy. *ACS Nano* **2017**, 11, 7516–7526.

17. Kim, J.; Rim, Y. S.; Liu, Y.; Serino, A. C.; Thomas, J. C.; Chen, H.; Yang, Y.; Weiss, P. S. Interface Control in Organic Electronics using Mixed Monolayers of Carboranethiol Isomers. *Nano Lett.* **2014**, 14, 2946–2951.

18. Cabarcos, O. M.; Schuster, S.; Hehn, I.; Zhang, P. P.; Maitani, M. M.; Sullivan, N.; Giguère, J. -B.; Morin, J. -F.; Weiss, P. S.; Zojer, E.; Zharnikov, M.; Allara, D. L. Effects of Embedded Dipole Layers on Electrostatic Properties of Alkanethiolate Self-Assembled Monolayers. *J. Phys. Chem. C* **2017**, 121, 15815–15830.

19. Serino, A. C.; Anderson, M. E.; Saleh, L. M. A.; Dziedzic, R. M.; Mills, H.; Heidenreich, L. K.; Spokoyny, A. M.; Weiss, P. S. Work Function Control of Germanium through Carborane-Carboxylic Acid Surface Passivation. *ACS Appl. Mater. Interfaces* **2017**, 9, 34592–34596.

20. Yeganah, S.; Ratner, M. A.; Medina, E.; Mujica, V. Chiral Electron Transport: Scattering through Helical Potentials. *J. Chem. Phys.* **2009**, 131, 014707.

21. Gutierrez R.; Díaz, E.; Naaman, R.; Cuniberti, G. Spin Selective Transport through Helical Molecular Systems. *Phys. Rev. B* **2012**, 85, 081404.

22. Guo, A. M.; Sun, Q. F. Spin-Selective Transport of Electrons in DNA Double Helix. *Phys. Rev. Lett.* **2012**, 108, 218102.

23. Guo, A. M.; Sun, Q. F. Sequence-Dependent Spin-Selective Tunneling along Double-

Stranded DNA. *Phys. Rev. B* **2012**, 86, 115441.

24. Vager, D.; Vager, Z. Spin Order without Magnetism: A New Phase of Spontaneously Broken Symmetry in Condensed Matter. *Phys. Lett. A* **2012**, 376, 1895–1897.

25. Gutierrez, R.; Díaz, E.; Gaul, C.; Brumme, T.; Domínguez-Adame, F.; Cuniberti, G. Modeling Spin Transport in Helical Fields: Derivation of an Effective Low-Dimensional Hamiltonian. *J. Phys. Chem. C* **2013**, 117, 22276–22284.

26. Gersten, J.; Kaasbjerg, K.; Nitzan, A. Induced Spin Filtering in Electron Transmission through Chiral Molecule Layers Adsorbed on Metals with Strong Spin-Orbit Coupling. *J. Chem. Phys.* **2013**, 139, 114111.

27. Eremko, A. A.; Loktev, V. M. Spin Sensitive Electron Transmission through Helical Potentials. *Phys. Rev. B* **2013**, 88, 165409.

28. Rai, D.; Galperin, M. Electrically Driven Spin Currents in DNA. *J. Phys. Chem.* **2013**, 117, 13730–13737.

29. Guo, A. M.; Sun, Q. F. Spin-Dependent Electron Transport in Protein-like Single-Helical Molecules. *Proc. Natl. Acad. Sci. USA* **2014**, 111, 11658–11662.

30. Medina, E.; González-Arraga, L. A.; Finkelstein-Shapiro, D.; Berche, B.; Mujica, V. Continuum Model for Chiral Induced Spin Selectivity in Helical Molecules. *J. Chem. Phys.* **2015**, 142, 194308–194313.

31. Michaeli, K.; Naaman, R. Origin of Spin Dependent Tunneling through Chiral Molecules. arXiv 1512.03435v2, **2016**.

32. Varela, S.; Mujica, V.; Medina, E. Effective Spin-Orbit Couplings in an Analytical Tight-Binding Model of DNA: Spin Filtering and Chiral Spin Transport. *Phys. Rev. B: Condens. Matter Mater. Phys*. **2016**, 93, 155436.

33. Medina, E.; Lopez, F.; Ratner, M. A. Mujica, V. Chiral Molecular Films as Electron Polarizers and Polarization Modulators. *Europhys. Lett.* **2012**, 99, 17006.

34. Kim, J.; Somorjai, G. A. Molecular Packing of Lysozyme, Fibrinogen, and Bovine Serum Albumin on Hydrophilic and Hydrophobic Surfaces Studied by Infrared-Visible Sum Frequency Generation and Fluorescence Microscopy. *J. Am. Chem. Soc.* **2003**, 125, 3150–3158.

35. Jeyachandran, Y. L.; Mielczarski, E.; Rai, B.; Mielczarski, J. A. Quantitative and Qualitative Evaluation of Adsorption/Desorption of Bovine Serum Albumin on Hydrophilic and Hydrophobic Surfaces. *Langmuir* **2009**, 25, 11614–11620.

36. Phan, H. T. M.; Bartelt-Hunt, S.; Rodenhausen, K. B.; Schubert, M.; Bartz, J. C. Investigation of Bovine Serum Albumin (BSA) Attachment onto Self-Assembled Monolayers (SAMs) using Combinatorial Quartz Crystal Microbalance with Dissipation (QCM-D) and Spectroscopic Ellipsometry (SE). *PLoS One* **2015**, 10, 0141282.

37. Norde, W.; Giacomelli, C. E. BSA Structural Changes During Homomolecular Exchange Between the Adsorbed and the Dissolved States. *J. Biotechnol.* **2000**, 79, 259–268.

38. Militello, V.; Casarino, C.; Emanuele, A.; Giostra, A.; Pullara, F.; Leone, M. Aggregation Kinetics of Bovine Serum Albumin Studied by FTIR Spectroscopy and Light Scattering. *Biophys. Chem.* **2004**, 107, 175–187.

39. Moriyama, Y.; Watanabe, E.; Kobayashi, K.; Harano, H.; Inui, E.; Takeda, K. Secondary Structural Change of Bovine Serum Albumin in Thermal Denaturation up to 130 ^{o}C and Protective Effect of Sodium Dodecyl Sulfate on the Change. *J. Phys. Chem. B* **2008**, 112, 16585–16589.

40. Roach, P.; Farrar, D.; Perry, C. C. Interpretation of Protein Adsorption: Surface-Induced Conformational Changes. *J. Am. Chem. Soc.* **2005**, 127, 8168–8173.

41. Aragonès, A. C.; Medina, E.; Ferrer-Huerta, M.; Gimeno, N.; Teixidó, M.; Palma, J. L.; Tao, N.; Ugalde, J. M.; Giralt, E.; Díez-Pérez, I.; Mujica, V. Measuring the Spin-Polarization Power of a Single Chiral Molecule. *Small* **2017**, 13, 1602519.

42. Varade, V.; Markus, T.; Vankayala, K.; Friedman, N.; Sheves, M.; Waldeck, D. H.; Naaman, R. Bacteriorhodopsin-Based Non-Magnetic Spin Filters for Biomolecular Spintronics. *Phys. Chem. Chem. Phys.* **2018**, 20, 1091–1097.

43. Amdursky, N.; Marchak, D.; Sepunaru, L.; Pecht, I.; Sheves, M.; Cahen, D. Electronic Transport *via* Proteins. *Adv. Mater.* **2014**, 26, 7142–7161.

44. Vilan, A.; Aswal, D.; Cahen, D. Large-Area, Ensemble Molecular Electronics: Motivation and Challenges. *Chem. Rev.* **2017**, 117, 4248–4286.

45. Böwering, N.; Lischke, T.; Schmidtke, B.; Müller, N.; Khalil, T.; Heinzmann, U. Asymmetry in Photoelectron Emission from Chiral Molecules Induced by Circularly Polarized Light. *Phys. Rev. Lett.* **2001**, 86, 1187–1190.

46. Turchini, S.; Zema, N.; Contini, G.; Alberti, G.; Alagia, M.; Stranges, S.; Fronzoni, G.; Stener, M.; Decleva, P.; Prosperi, T. Circular Dichroism in Photoelectron

Spectroscopy of Free Chiral Molecules: Experiment and Theory on Methyl-Oxirane. *Phys. Rev. A* **2004**, 70, 014502.

47. Dubs, R. L.; Dixit, S. N.; McKoy, V. Circular Dichroism in Photoelectron Angular Distributions from Oriented Linear Molecules. *Phys. Rev. Lett.* **1985**, 54, 1249–1251.

48. Zwang, T. J.; Hürlimann, S.; Hill, M. G.; Barton, J. K. Helix-Dependent Spin Filtering through the DNA Duplex. *J. Am. Chem. Soc*. **2016**, 138, 15551–15554.

49. Ping, H.; McGahan, W. A.; Woollam, J. A.; Sequeda, F.; McDaniel, T. Magneto-Optical Kerr Effect and Perpendicular Magnetic Anisotropy of Evaporated and Sputtered Co/Pt Multilayer Structures. *J. App. Phys.* **1991**, 69, 4021–4028.

50. Arwin, H. Optical Properties of Thin Layers of Bovine Serum Albumin, γ-Globulin, and Hemoglobin. *Appl. Spectrosc.* **1986**, 40, 313–318.

51. Allara, D. L.; Nuzzo, R. G. Spontaneously Organized Molecular Assemblies. 1. Formation, Dynamics, and Physical Properties of *n*-Alkanoic Acids Adsorbed from Solution on an Oxidized Aluminum Surface. *Langmuir*, **1985**, 1, 45–52.

52. Nečas, D.; Klapetek, P. Gwyddion: An Open-Source Software for SPM Data Analysis. *Cent. Eur. J. Phys.* **2012**, 10, 181–188.

53. Klaptek, P.; Ohlídal, I.; Franta, D.; Montaigne-Ramil, A.; Bonanni, A.; Stifter, D.; Sitter, H. Atomic Force Microscopy Characterization of ZnTe Epitaxial Films. *Acta Physica. Slovaca*. **2003**, 53, 223–230.

54. Dupin, J. –C.; Gonbeau, D.; Vinatier, P.; Levasseur, A. Systematic XPS Studies of Metal Oxides, Hydroxides and Peroxides. *Phys. Chem. Chem. Phys*. **2000**, 2, 1319–1324.

55. Techane, S. D.; Gamble, L. J.; Castner, D. G. X-Ray Photoelectron Spectroscopy Characterization of Gold Nanoparticles Functionalized with Amine-Terminated Alkanethiols. *Biointerphases* **2011**, 6, 98–104.

56. Baio, J. E.; Weidner, T.; Brison, J.; Graham, D. J.; Gamble, L. J.; Castner, D. G. Amine Terminated SAMs: Investigating Why Oxygen is Present in these Films. *J. Electron Spectros. Relat. Phenomena* **2009**, 172, 2–8.

57. Marmisollé, W. A.; Capdevila, D. A.; de la Llave, E.; Williams, F. J.; Murgida, D. H. Self-Assembled Monoalyers of NH_2-Terminated Thiolates: Order, pK_a, and Specific Adsorption. *Langmuir* **2013**, 29, 5351–5359.

58. Schmidt, R.; McNellis, E.; Freyer, W.; Brete, D.; Gießel, T.; Gahl, C.; Reuter, K.; Weinelt, M. Azobenzene-Functionalized Alkanethiols in Self-Assembled Monoalyers on Gold. Appl. Phys. A 2008, 93, 267–275.

59. Roguska, A.; Pisarek, M.; Andrzejczuk, M.; Dolata, M.; Lewandowska, M.; Janik-Czachor, M. Characterization of a Calcium Phosphate-TiO_2 Nanotube Composite Layer for Biomedical Applications. *Mater. Sci. Eng. C* **2011**, 31, 906–914.

60. Belatik, A.; Hotchandani, S.; Carpentier, R.; Tajmir-Riahi, H. –A. Locating the Binding Sites of Pb(II) Ion with Human and Bovine Serum Albumins. *PLoS One* **2012**, 7, e36723.

Chapter IV

Biological Implications and Technological Applications of the Chiral-Induced Spin Selectivity Effect

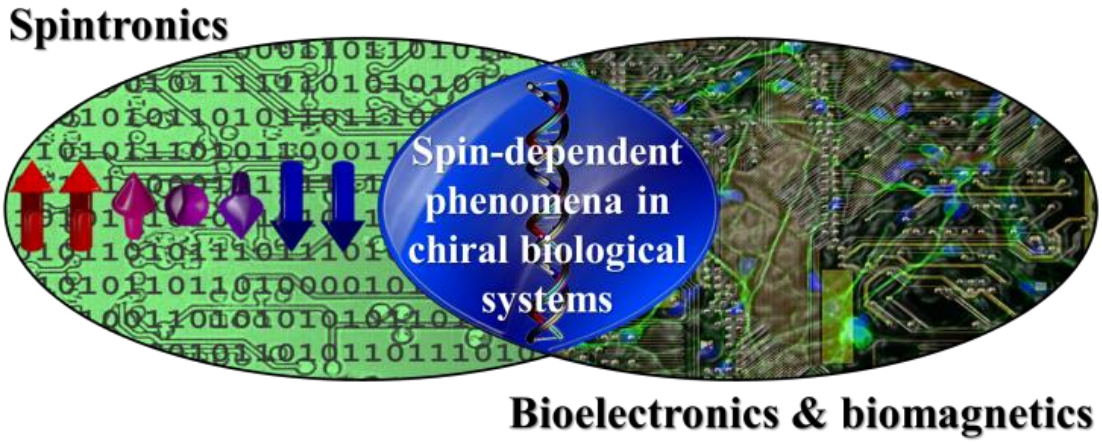

IV.A. Introduction

Due to the prevalence of chirality in Nature, the role of electron spin in biologically relevant chemical reactions that involve electron transfer may be more important than previously considered. Furthermore, potential technological applications that range from information storage and memory technologies to photocatalytic water splitting can benefit from the fundamental understanding of small-molecule chirality and resulting control of electron spin at room temperature.[1] Herein, I summarize the experiments and results that have demonstrated biological precedent of the CISS effect, and the most promising examples of chiral molecule implementation within possible device architectures.

IV.B. Biological Implications

IV.B.1. Homochirality in Nature

With few exceptions,[2,3] nearly all naturally occurring amino acids are of *L*-form, while carbohydrates exist as *D*-form. Supramolecular and hierarchically more complex assemblies of peptides, proteins, and nucleic acids also follow this trend by exhibiting helical secondary and tertiary structures. For example, the most common form of DNA under physiological conditions is the right-handed double helix (B-form). The persistence of not only the structural complexity of chiral molecules and higher-order structures, but also of this homochirality in Nature, has fascinated researchers since the time of Pasteur,[4] yet explanations of its origin remain elusive.[5,6] It is interesting to question whether homochirality was a necessary precondition for the emergence of life, or a predictable result of evolution.

Generally, a stepwise explanation of homochirality is accepted that involves first symmetry-breaking events followed by asymmetric amplification. The amplification of small enantiomeric excess has been experimentally realized,[7] although perhaps not under conditions that represent the primordial Earth. Explanations of the symmetry-breaking step, however, has seen more heated debates.[8-11] While some processes have been proposed that could have led to symmetry breaking on Earth, an extraterrestrial origin is also possible.[12-15] The universe may be racemic, but observations of local enantiomeric excess exist. For example, excess of *L*-amino acids found on the Murchison meteorite have been found, which also supports the extraterrestrial hypothesis.[16] In addition, the first chiral molecules were recently discovered in deep space, 28,000 light years away from our planet and near the center of the Milky Way galaxy, by analyzing radio frequency signals attributed to gaseous propylene oxide collected by radio telescopes.[17] While it has not yet been determined whether the molecules were in enantiomeric excess, the results are nevertheless exciting because the material in this interstellar region is closest to the earliest stages of evolution of a solar system.

Successful demonstration of asymmetric photolysis of chiral molecules due to circular dichroism, or preferential adsorption of circularly polarized light by one enantiomer over another, was reported as early as 1929.[18,19] However, while circularly polarized infrared radiation has been detected in star-forming regions of the Orion nebula,[20] natural circularly polarized radiation in the UV region (necessary for photolysis) of the electromagnetic spectrum has yet to be confirmed, limiting the prospects of this mechanism to lead to enantiomeric excess.[21-23] Other sources of circularly polarized light may have been β-decay, for example of ^{60}Co.[24] As discussed in Chapter I, parity violation in β-decay that leads

to emission of spin-polarized electrons has been hypothesized to contribute to spin-dependent chemical reactions.[25] Our work has demonstrated that photoelectrons emitted from chiral molecular assemblies by sufficiently ionizing (unpolarized) UV radiation leave behind spin-polarized holes (Chapter III), providing another possible source of low-energy spin-polarized electrons that may react selectively or preferentially with enantiomers.[26] While the origins and propagation of homochirality remain elusive, the discovery of the CISS effect, coupled to extensive research conducted in the last 20 years aimed to test spin-dependent and enantioselective interactions between electrons and chiral biomolecules, have contributed new pieces to the puzzle.

IV.B.2. Highly Efficient Charge Transfer *via* Chiral Biomolecules

The influence of magnetic field perturbations on biochemical processes are generally negligible,[27] with few potential exceptions.[28] Thus, the importance of spin in dictating electrochemical reactions in biology is thought to be minor. However, one of the most likely examples of how the CISS effect may be manifested in biological processes is in long-range charge transfer.[29] In saturated organic compounds, electrons are confined within the length scale of a single chemical bonds (*ca.* 1-2 Å), while in conjugated molecules, electrons can be delocalized across multiple atoms. This charge delocalization enables artificial organic conductors or semiconductors with narrow band-gaps (energy gap between HOMO and lowest unoccupied molecular orbital, LUMO) to move electrons and holes over distances up to ten times farther than saturated systems in single reaction "steps".[30] However, in biology, charge transport through chiral systems, which are composed predominately of saturated chemical bonds, is surprisingly efficient.[31,32] Examples include charge transfer processes in

photosynthesis and in respiration. Figure IV.1 compares the conductances of artificial saturated and conjugated molecular systems with proteins as a function of charge transfer distances, and indeed, compared to saturated compounds of comparable size, proteins display more efficient charge transfer.

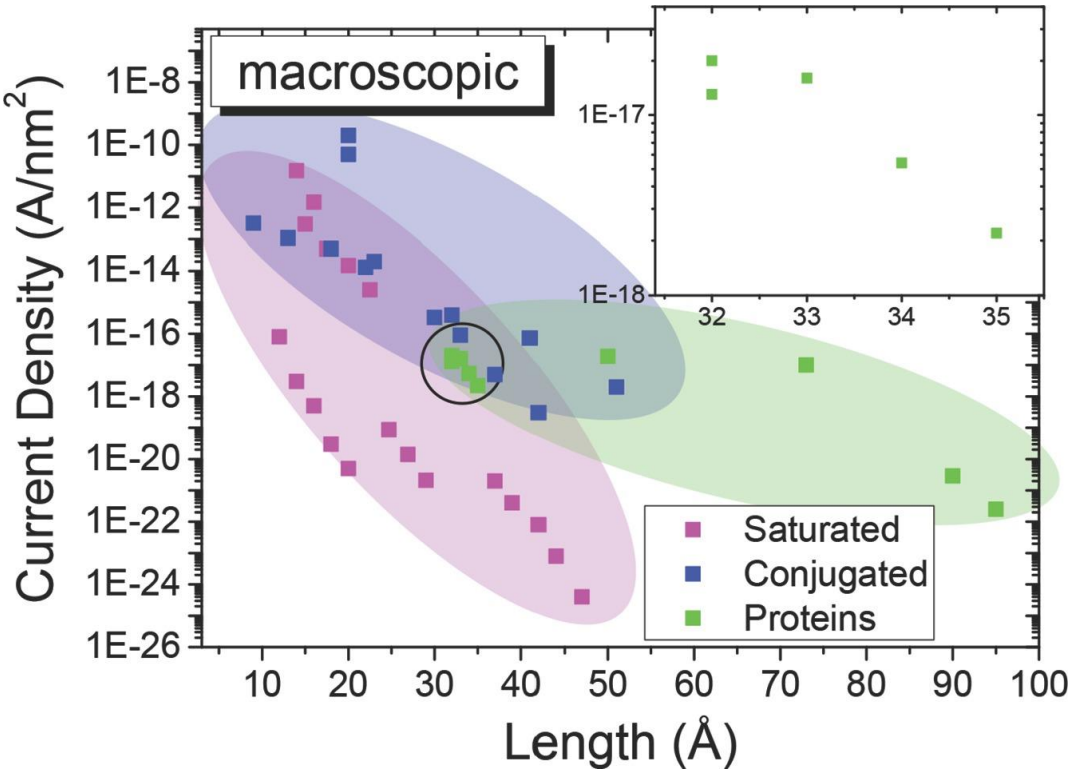

Figure IV.1. Current density as a function of molecule length measured within macroscopic contact molecular junctions for saturated molecules (pink), conjugated molecules (purple) and proteins (green). Inset shows a magnification of the circled group. Reproduced with permission from ref 32. Copyright 2014 WILEY-VCH Verlag GmbH & Co. KGaA, Weinheim.

As described by the CISS effect, the helicity of the transferred electrons and of the electronic states within chiral molecules may provide an explanation to this contradiction. According to current theoretical models, the elastic transport of electrons through chiral molecules requires coupling between the linear momentum of an electron and its spin.[33-35]

The preferred helicity state of an electron should be dictated by the handedness of the helical potential of the molecule. Thus, if an electron is reflected back in the opposite direction due to backscattering, which can be significant in non-rigid biological environments due to thermal fluctuations, the electron would need to also flip its spin. However, due to the weak atomic spin-orbit coupling strengths of the compositional atoms within biomolecules, spin flip probabilities, and thus backscattering, are likely suppressed in chiral molecules compared to achiral analogues.

Experiments on SAMs have revealed that electron transfer through molecular films is sensitive to the composition, connectivity, and geometry of linking moieties.[36,37] Barton and coworkers demonstrated that the electron-transfer rate through dsDNA SAMs adsorbed on Au using thiol-terminated tethers containing different numbers (n) of methylene (-CH_2-) units was limited by charge transport through σ-bonded tethers, showing an exponential increase in electron transfer rate constant with decreasing n.[38] In related work, our group measured the conductance through isolated alkyl molecules within SAMs to understand the contributions of molecular chain length and chemical contact, revealing an exponential dependence of the conductance on molecular length.[39]

The electron transfer rate constant is thus proportional to $exp(-\beta L)$, where L is the length and β is a damping constant. In achiral saturated hydrocarbons, β is typically found to be *ca.* 1.0 $Å^{-1}$.[40,41] However, in chiral α-helical oligopeptides, values of β have been calculated to be as low as 0.1-0.2 $Å^{-1}$.[42,43] Smaller electron transfer damping constants in chiral *vs* achiral molecules may be a direct result of spin polarization of charge carriers through helical electrostatic potentials. However, damping constants as large as 0.9-1.2 $Å^{-1}$ and 1.25-1.6 $Å^{-1}$ within β-sheets and α-helical subunits of proteins, respectively, have been reported.[44] While

low values of β are considered important for efficient molecular wires, high measured values of β do not necessarily correspond to high transconductance under all conditions.[39] Intermolecular interactions including electronic coupling between adjacent molecules and the nature of the electrical contacts may strongly influence the charge transfer efficiency. Further work, and perhaps different experimental designs, are necessary to elucidate how spin polarization may play a role in maximizing charge transfer rates through these systems.

IV.B.3. Spin-Dependent Enantioselectivity in Intermolecular Interactions

Understanding intermolecular interactions between chiral biomolecules is important to understand the stereoselectivity of chemical biological processes. Differences in enantioselective binding in receptor-target interactions play a pivotal role in metabolism, pharmacology, pharmacokinetics, and toxicology.[45,46] However, accurate calculations from first principles of enantioselective noncovalent interactions involved in biorecognition remain elusive. One explanation may be that electron spin-based effects are usually not incorporated within the generation of molecular force fields for calculations.[47,48] Michaeli *et al.* suggested a mechanism to account for the discrepancies between experiment and theory by increasing the interaction strength between molecules with the same handedness over the opposite handedness using the CISS effect (Figure IV.2).[29]

In brief, when two molecules approach one another, charge polarization occurs, for example, due to London dispersion forces. The charge polarization within molecules is accompanied with spin polarization if the molecules are chiral, and the polarization 'current' results in the transient buildup of electrons of a particular spin. If the molecules are close enough such that orbital overlap may occur, electron exchange interactions may be

considered. In regions of high electron density/orbital overlap between the molecules, a favorable singlet-like state (electrons of opposite spin) develops if the molecules have the same chirality. On the other hand, a higher-energy, triplet-like state evolves (electrons with the same spin) if the molecules are of opposite handedness.

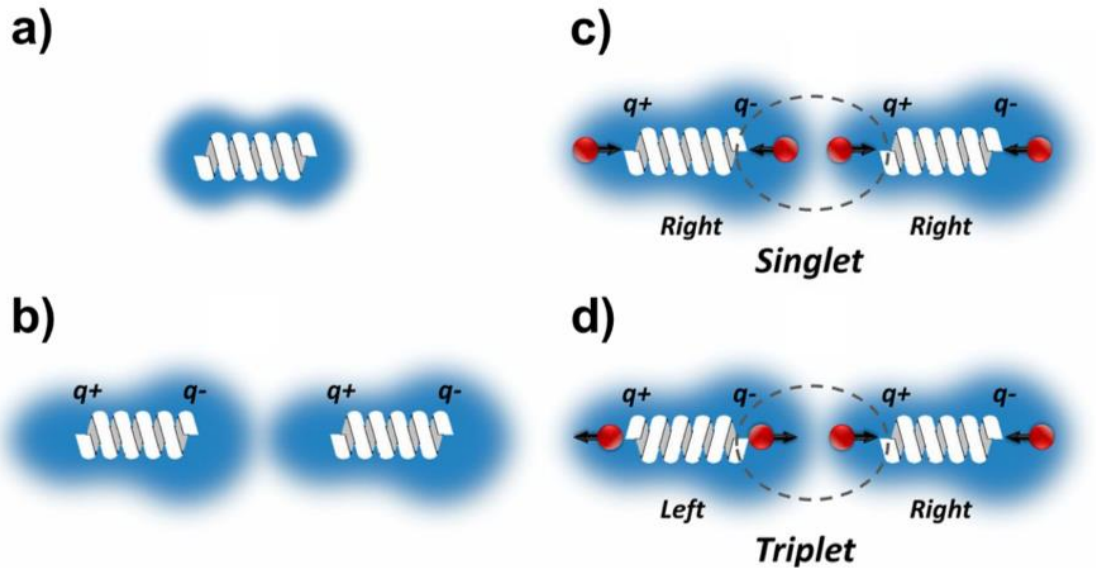

Figure IV.2. Schematic representation of spin polarization that accompanies charge polarization (q+, q-) in induced dipole interactions between chiral molecules. (**a**) A molecule without a dipole moment with a symmetric charge distribution develops an asymmetry *via* dispersive forces when two molecules interact resulting in (**b**) an induced dipole in each molecule. (**c**) When molecules have the same handedness, the spin polarization in each molecule that develops within the region of overlapping electron density between the molecules is opposite, and can be represented as a singlet state. (**d**) If the molecules are of opposite chirality, the same spin polarization of electrons develops in the electron overlap region, represented as an unfavorable triplet state. Reproduced with permission from ref 29. Copyright 2016 The Royal Society of Chemistry.

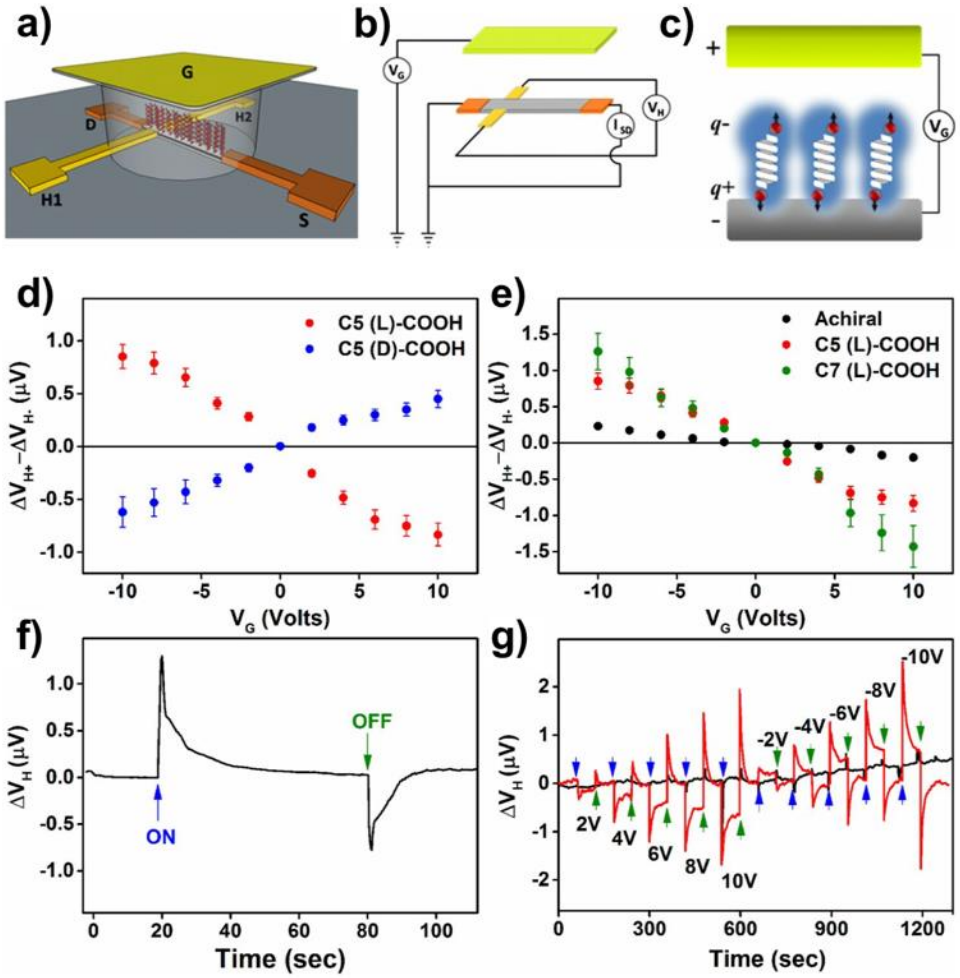

Figure IV.3. (**a-c**) Schematic representation of a solution-exposed chiral molecule-functionalized gallium nitride/aluminum gallium nitride (GaN/AlGaN) Hall bar device (not to scale). Hall voltages (V_H) are measured between H_1 and H_2 while current flowing between source (S) and drain (D) electrodes (I_{SD}) within a two-dimensional free electron gas are subjected to a voltage pulse (V_G) from a gate (G) electrode. Charge polarization within adsorbed chiral molecules from the gate pulses is accompanied by spin polarization. (**d,e**) Hall measurement dependent on gate voltage conducted on devices functionalized with chiral *L*- (red, green) or *D*- (blue) α-helical oligopeptides, or achiral molecules (black). (**f,g**) Time-dependent Hall potential in devices functionalized with *L*-α-helical oligopeptides using a V_G of -10 V to 10 V. Reproduced from ref 49.

Naaman and coworkers subsequently tested the hypothesis that spin polarization occurs with charge polarization for chiral peptides using Hall effect devices composed of gallium nitride (GaN)/aluminum gallium nitride (AlGaN) films grown on sapphire substrates and functionalized with SAMs of organic monolayers (Figure IV.3).[49] The Hall effect

describes the buildup of a voltage perpendicular to the direction of current across a conductor when a magnetic field is applied normal to the surface of the conducting material. The experiments were designed to measure Hall voltages resulting from transient magnetic fields acting on charge carriers within the two-dimensional electron gas at GaN/AlGaN interfaces.[50] The magnetic fields were generated within chiral SAMs upon polarization of the films with an external electrode, and resulting spin polarization. Chiral organic films of opposite handedness produced Hall voltages of opposite signs, implying that transient magnetic fields were generated in opposite directions upon polarization with pulsed electric fields.

Although the spin-related contributions to enantioselective interactions between molecules may only be relevant at short distances, that is, on the order of van der Waals radii (<0.5 nm),[51] the effect may be nevertheless significant. Indeed, substrate-protein interaction distances may often occur over distances of 0.3 nm or less.[52,53] The results of these experiments suggest that quantum mechanical effects in biology resulting from CISS may extend beyond long-range electron transfer and redox reactions to govern intermolecular forces.[54] This effect may be amplified in larger molecules that employ recognition across multiple functional groups, simultaneously.

IV.C. Incorporating Chiral Molecules within Next-Generation Spintronics Devices

IV.C.1. Spin-Valve Device Architectures

Currently, most logic-based solid-state transistors operate on the principle of charging and discharging capacitors to record and to store information.[55] In addition to the charge of electrons, employing spin as an additional degree of freedom to encode information

promises theoretically faster and more energy efficient electronics compared to current technologies because the energy required to manipulate the spin of an electron should in principle require less energy than capacitive charging.[56] Practically, the most efficient and compatible way to incorporate the operating principles of spintronics with existing complementary metal-oxide semiconductor technologies (*i.e.,* silicon-based) would be to combine spin injection, such as from FM layers, into semiconducting materials with small spin-orbit coupling that enable long spin-diffusion lengths.[57,58] However, interfacial (Schottky) barriers yielding resistance mismatches between FM spin injectors and semiconducting materials have limited progress in this direction.[59,60]

Alternatively, device designs that operate on the principles of the giant magnetoresistance[61,62] and tunnel magnetoresistance[63] effects have made their way into commercial hard disks and magnetic memory applications. The operating principle of the prototypical device that take advantage of these effects, the spin valve, is based on high and low resistance states associated with alternating layers of FM and non-ferromagnetic materials (NM, Figure IV.4a). The magnetization orientation of one magnetic layer is fixed, while the other may be changed between parallel (low resistance) and antiparallel (high resistance) magnetic dipole orientations with respect to the reference layer with an external magnetic field.

Still, challenges remain. First, FM materials become superparamagnetic at the nanometer scale when particle sizes approach the dimensions of single magnetic domains. Superparamagnetic materials are susceptible to thermal fluctuations above their characteristic blocking temperature (dictated by the material and its geometry, though typically lower than room temperature). Magnetic dipole orientations, and thus information,

cannot be stored, and restricts miniaturization of FM components. A second challenge is to lock the magnetization of the reference FM layer while enabling the free layer to be switched with an external magnetic field when they are separated by only a few nanometers. While methods exist to stabilize the magnetization of the permanent layer, such as through the use of antiferromagnetic exchange interactions,[64] these approaches are relatively expensive and inter-diffusion from other layers also becomes a concern.

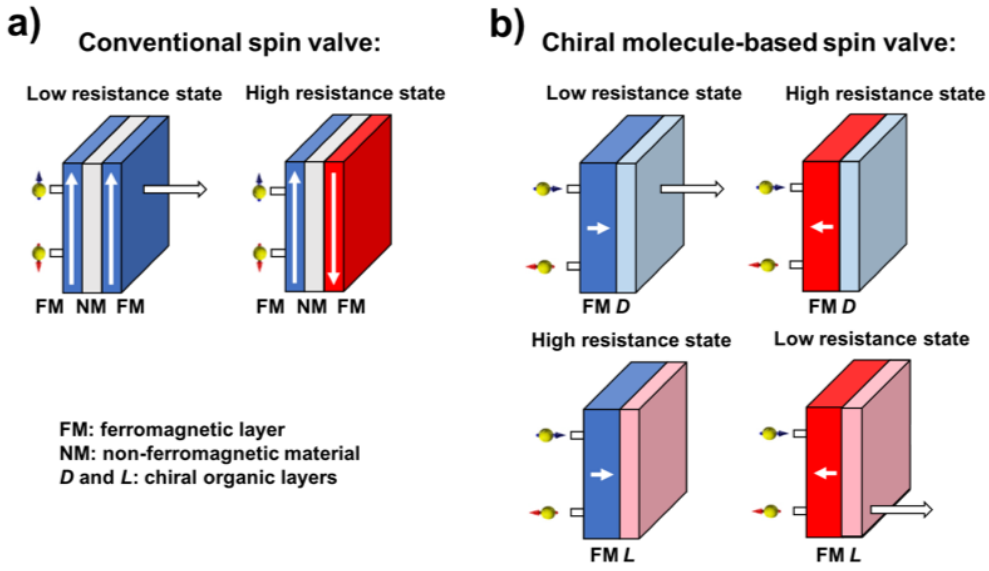

Figure IV.4. (**a**) Operating principles of a conventional spin valve (left) and (**b**) chiral molecule-based spin valve (right) as part of an electrical circuit. In a conventional spin valve, electrons that move from the left ferromagnetic (FM) layer the right FM layer through a non-ferromagnetic material (NM) exhibit low resistance if the magnetic layers are aligned. If the layers are anti-aligned, the electrons face a larger barrier and resistance is higher. In a chiral molecule-based spin valve, only a single ferromagnetic layer is needed, and that material may be functionalized with *D*- or *L*- forms of chiral molecule films to produce analogous low and high resistance states that depend on the FM magnetization orientation and the handedness of the chiral film.

As a result of the CISS effect, chiral molecular assemblies offer solutions to achieve both higher densities of spin-transistors as well as lower costs.[65] The capability of molecular

monolayers with thicknesses on the order of nanometers to generate or to manipulate spin-polarized currents as passive elements at room temperature promises an overall reduction in device size, and is highly compatible with vertically-stacked spintronics device architectures. Thus, spin filters based on chiral SAMs present a paradigm shift in organic spintronics, offering the ability of thin organic films to not only act as tunneling barriers or alleviate the resistance mismatch between inorganic and organic layers, but also to act as a tunable and functional interface.

Compared to conventional spin-valve designs, chiral-molecule-based spin valve architectures may be envisioned that require only a single FM layer functionalized with a chiral film of nanometer-scale thicknesses (Figure IV.4b). Analogous high- or low-resistance states would be dictated by the magnetization orientation of the FM layer (out-of-plane) and the handedness of the organic layer rather than magnetization alignment of multiple FM layers.

Chiral tunneling barriers may be composed of molecules, polymers,[66-68] or chiral-molecule-modified nanoparticles,[69] and numerous examples have been reported in which the current or magnetoresistance is measured as a function of the relative magnetization orientation of FM films or scanning probe tips. Magnetoresistance values that have been measured using CISS-based spin filters have reached as high as 20% at room temperature.[66] Importantly, minimal dependence of magnetoresistance on temperature has been observed. In contrast, with few exceptions, conventional devices utilizing inorganic materials usually display rapid decreases in magnetoresistance approaching room temperature.[63,70]

Yet, while we (Chapter III)[26] and others[31,32,71] have demonstrated the potential of chiral biomolecules such as proteins to serve as components within solid-state electrical

devices, implementation within commercial devices is likely far off. Presentation of data collected on conduction with and without FM analyzers (tips or films) across various systems with standardized procedures will alleviate the difficulties associated with comparing results from different measurement techniques.[72] Additionally, despite early reports of temperature-independent magnetoresistance in chiral molecule films, mechanistic understanding of spin selectivity in tunneling *vs* hopping charge transport regimes through proteins, which are dependent on temperature, will be necessary for device optimization.

IV.C.2. Information Storage and Unconventional Memory Technologies

The magnetization orientation (that may correspond to high or low resistance states) within a FM nanoscale object or film may also be manipulated by spin-polarized currents as a result of spin-transfer torque (STT). This transfer of spin angular momentum to ferromagnetic domains presents a means to read and to write data that is dependent on the direction of charge flow with low power consumption, high density, and enhanced scalability without the need for external magnetic field manipulation such as in conventional spin valves.[73,74] While materials and commercial challenges remain, these spin-transfer torque magnetoresistive random access memory (STT-MRAM) devices represent prime candidates to replace dynamic random access memory (DRAM) due to their potential for scaling below 20 nm as well as for other embedded, non-volatile storage media.[74]

Incorporation of SAMs that have the capability to filter electron spins within perpendicular STT-MRAM device architectures can be accomplished through the marriage of well-established molecular self-assembly techniques and nanofabrication. Hypothetical

device designs separate two NM electrodes from a writable FM thin film *via* SAMs of spin filtering molecules. The direction of charge flow through the molecular monolayers will influence the preferred spin orientation of the charge carriers, thereby facilitating the magnetization (up or down) of the FM layer *via* STT at the interface, and throughout the entire film due to strong exchange coupling. Once the FM has been magnetized, or written, the electrical resistance of the cell can be measured, which is dependent on the direction of current flow (positive or negative bias applied between the two NM electrodes in the cell). A high resistance state would be expected for electrons flowing in the direction of current flow used to write the bit, while a low resistance state would be expected for electrons flowing in the opposite direction. The dual-SAM design allows the FM layer to be magnetized with opposite polarity by reversing the direction of current flow.

Dor *et al*. recently demonstrated a magnetic memory device that utilized SAMs of chiral α-helical *L*-polyalanine as a spin-filtering layer between Au and Ni layers, exemplifying the capacity for spin-dependent SAMs to be utilized as device components for STT.[75] However, in their devices, the Ni layers were magnetized and written with significantly large voltages of -15 V and read with ±2 V. These large voltages were necessary due to the high current densities required for STT, estimated to be of the order of 1×10^{6} A cm^{-2},[76] that is, about 1×10^{25} electrons s^{-1} cm^{-2}. This drawback is a substantial challenge to overcome, and negatively affects the performance and integrity of devices, particularly for designs that incorporate organic materials. In order to prevent degradation of the SAM, significantly lower write-currents must be used. Careful design of the FM thickness or dimensions is likely to result in more efficient read/write cycles by orienting the easy axis of magnetization parallel to the direction of current flow. Although these proof-of-principle results are

preliminary, the high polarization values experimentally observed and theoretically predicted for electron transmission through other chiral species such as dsDNA at room temperature, and further optimization through the mechanistic investigation of molecular and substrate parameters, may enable writing with lower switching-current densities for applications within future STT-MRAM devices.

As an alternative to STT-MRAM technologies, Dor *et al.* reported on magnetization induced by the proximity of chiral molecules as a mechanism by which information can be stored (Figure IV.5).[77] Here, magnetization states within soft, FM thin films with low coercivities could be dictated by the adsorption of chiral molecules, circumventing the need for an external magnetic field or current to flip magnetic domains. Similar observations have been observed on alkanethiol-modified nanoscopic Au that displays paramagnetic properties.[78,79] This result is hypothesized to be due to charge transfer from Au to the S atoms at the Au-S interface, which creates localized 5*d* holes, where the *d*-charge loss is dependent on the dipole orientation and magnitude of the adsorbed molecules. When the substrates are FM, because charge transfer within chiral molecules is spin selective, the underlying magnetic film becomes spin polarized, and thus magnetized in a direction that is dictated by the handedness of nominally vertically oriented α-helical peptides on the surface. Based on this hypothesis, compared to the requirements for STT described above, only *ca.* 1×10^{13} electrons cm^{-2} are necessary to induce magnetization reversal.[77] By patterning surfaces with chiral molecules, or by etching multilayer FM structures selectively, multi-dimensional matrices may be envisioned in which magnetization may be controlled by domain wall motion in magnetic racetrack memory device architectures.[80]

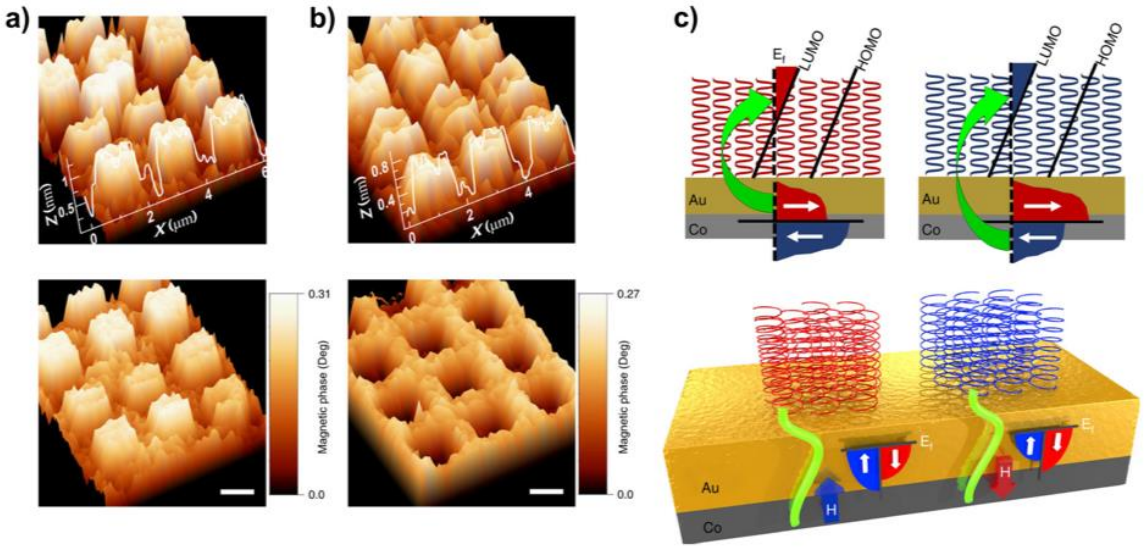

Figure IV.5. (**a**) Representative atomic force microscopy image of the topography (top) and magnetic phase (bottom) of *L*- and (**b**) *D*-α-helical oligopeptides patterned on ferromagnetic substrates that contain perpendicular magnetic anisotropy. (**c**) Schematic representing the experimental concept of magnetism induced by the proximity of chiral molecules. Top: classical picture. Bottom: quantum mechanical picture. Reproduced from ref 77. Copyright 2017 The Author(s).

IV.D. Spin-Polarized Organic Light-Emitting Diodes

Besides memory technologies and the generation and manipulation of spin-polarized currents for faster and more energy-efficient electronics, other technologies can benefit from the use of organic chiral materials to control electron or hole spin states. A bipolar spin-polarized organic light-emitting diode (spin-OLED) was recently developed in which electroluminescence emission intensity is controlled by an external magnetic field with promises of cheaper, brighter, and more environmentally friendly OLEDs.[81] In conventional OLEDs, injected charge carriers with random spin orientation combined to form triplet (S = 1) and singlet (S = 0) excitons in a 3:1 yield. Triplet excitons radiatively decay with low efficiency while singlet excitons radiatively decay with high yield.[82] Alternatively, in the

bipolar spin-OLED device, exciton spin statistics, and therefore light emission, can be actively controlled by the injection of spin-polarized charge carriers through alignment (parallel or antiparallel) of FM electrodes.

Analogously, SAMs of chiral spin-filtering molecules on a non-FM metal surface may be employed in a hypothetical spin-OLED design that utilizes only a single FM electrode, thereby eliminating the need to choose electrodes based on relative coercivities (Figure IV.6). Furthermore, the spin-filtering capacity of chiral SAMs demonstrated at room temperature suggest the possibility of device operation above cryogenic temperatures – a necessary requirement for real-world applications. Figure IV.6 depicts an example of a device architecture that utilizes a dsDNA SAM as a filtering component. A layer of organic semiconductor, such as aluminum *tris*(8-hydroxyquinone) (Alq3), could be thermally evaporated on top of the dsDNA monolayer followed by a thin (<20 nm) FM top-electrode (Ca/Co/Al). The Alq3 serves as the charge transporting and emitting layer. The diamagnetic Au layer serves as the anode that passively injects spin-polarized holes into the HOMO of Alq3 *via* spin-selective conduction through the dsDNA SAM. The thin layer of Ca lowers the work function of the FM Co cathode. Application of an external magnetic field perpendicular to the Co thin film induces out-of-plane polarization and facilitates injection of polarized electrons into the LUMO of Alq3. An Al capping layer would prevent corrosion. The electroluminescence emission may be observed through the thin top electrode.

The spin sense of the injected holes is dictated by (and opposite to) the longitudinal polarization direction for electrons conducted through the chiral DNA monolayer. Alternatively, the spin sense of injected electrons is the same as the polarization of majority-spin electrons in the DM Co cathode, and is determined by the external magnetic field

orientation. When the injected holes and electrons have an antiparallel spin sense, singlet formation can in principle be increased up to 50%. Sweeping the external magnetic field would change the polarization within Co, thereby tuning the emission intensity. The emission intensity could be compared with devices in which the chiral dsDNA monolayer has instead been replaced by a non-chiral SAM of identical thickness. Thus, in the absence of the spin-filtering effect, the spin orientation of injected holes will be random and lower emission intensities would be observed in such a homopolar configuration.

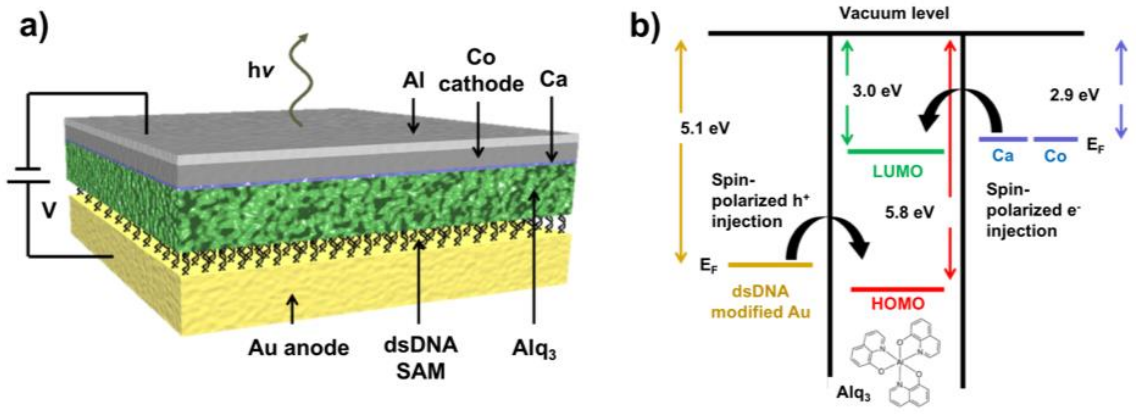

Figure IV.6. (**a**) Schematic of a hypothetical bipolar spin-polarized organic light-emitting diode device utilizing only a single ferromagnetic electrode (not to scale). (**b**) Illustration of energy-level alignment of aluminum *tris*(8-hydroxyquinone) (Alq3) and metal contacts. The double-stranded DNA (dsDNA) self-assembled monolayer- (SAM) modified Au work function is energetically closer to the highest-occupied molecular orbital (HOMO) of Alq3, facilitating hole injection. The Ca insert between Alq3 and Co aligns the work function of the ferromagnetic electrode with the lowest-unoccupied molecular orbital (LUMO) of Alq3 enabling efficient electron injection.

IV.E. Surface Spintronics for Photocatalytic Water Splitting

Hydrogen has long been considered a promising candidate as clean chemical fuel for energy technologies because of its high enthalpy of combustion and because water is its oxidation product.[83] Hydrogen may be produced by water splitting (electrolysis), however this is an unfavorable, uphill reaction that requires 237 kJ/mol or 1.23 eV.[84-86] Practically, (photo)electrochemical water splitting necessitates inexpensive catalysts, electric potentials close to the thermodynamic limits, and high current densities.[87] As such, the goal of sustainable generation of hydrogen at global scales has yet to be reached.[88]

The water-splitting reaction involves four electrons, yielding hydrogen molecules with singlet ground states and oxygen molecules with triplet ground states. Recent theoretical work has suggested that controlling the spin states of hydroxyl radical intermediates may lower the overpotentials required within electrochemical cells to drive electrolysis.[89,90] On one hand, if the unpaired electrons on two hydroxyl radicals are aligned (within the laboratory frame) antiparallel to one another, they may react along a potential energy landscape that yields formation of unfavorable hydrogen peroxide (H_2O_2) byproducts. On the other hand, if the unpaired electrons are aligned parallel, formation of O_2 with a triplet ground state may be favored. Indeed, magnetic electrodes that utilized FM materials or catalysts with heavy metal atoms with large spin-orbit coupling strengths have been used to control electron spin alignment and achieved more efficient O_2 evolution compared to non-magnetic electrodes.[91,92]

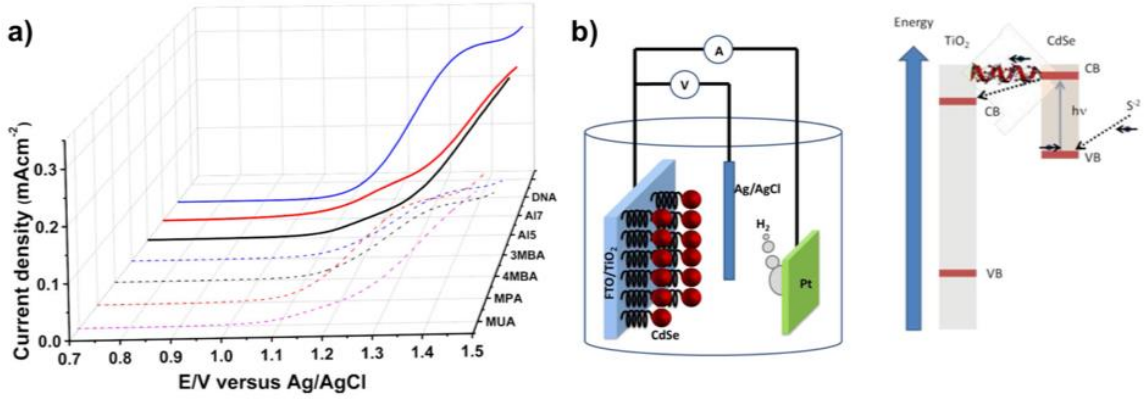

Figure IV.7. (**a**) Current density measured as a function of voltage *vs* a Ag/AgCl reference electrode with fluorine-doped tin oxide (FTO)/titanium dioxide (TiO_2) electrodes functionalized with chiral self-assembled monolayers (SAMs) of DNA, α-helical oligopeptides composed of 5 or 7 amino acid residues (Al5, Al7), or achiral SAMs composed of 3-mercaptobenzoic acid (3MBA), 4-mercaptobenzoic acid (4MBA), 3-mercaptopropionic acid (MPA), or 11-mercapto-undecanoic acid (MUA). (**b**) Schematic representing a photoelectrochemical cell used to investigate water splitting. Cadmium selenide (CdSe) nanoparticles are tethered to FTO/TiO_2 electrodes *via* the tethers listed in (**a**). Photoexcitation of electrons in the CdSe nanoparticles from the valence band (VB) to the conduction band (CB) results in excited electron transfer to the CB of TiO_2 and into the external circuit. At the platinum (Pt) electrode, H^+ ions are reduced to H_2. If the tether is chiral, the electron transfer is spin specific, making the hole in the CdSe VB have a well-defined spin state, which accepts electrons from sacrificial reagents (S^{2-}). Reproduced with permission from ref 93. Copyright 2015 American Chemical Society.

Mtangi *et al*. demonstrated that when titanium dioxide (TiO_2) anodes were functionalized with chiral molecules including dsDNA or oligopeptides, lower overpotentials that are necessary for hydrogen evolution due to water splitting were measured compared to photoanodes coated with achiral molecules (Figure IV.7a).[93] These measurements were performed in the dark. When CdSe nanoparticles were adsorbed on the TiO_2 anodes *via* chiral molecule tethers and excited *via* irradiation, higher photocurrents were measured and corresponding higher yield of hydrogen evolution was determined at low overpotential values (*i.e.,* <0.1 V) (schematic in Figure IV.7b). These results are exciting because practical

implementation of these (photo)electrochemical cells is limited by the need of large overpotentials (*ca.* 0.6 V *vs* the normal hydrogen electrode) to initiate the water-splitting reaction. Further, Mtangi *et al*. reported that formation of the parasitic intermediate, H_2O_2, in photocatalytic water splitting was suppressed when photoanodes were functionalized with chiral molecules.[94] These results were attributed to poor spin alignment at the expense of O_2.

Together, the ability of chiral molecule functionalization to alleviate overpotential barriers and to reduce unwanted oxidation products that may poison photocatalysts show another promising application of chiral organic materials based on phenomena predicted by the CISS effect.[95-99] Complete and detailed understanding of the O_2 evolution reaction remains elusive,[100-102] and while control of the spin state of hydroxyl radicals to promote O_2 formation has been considered in other contexts,[89,103] the suppression of H_2O_2 by spin alignment had not been previously discussed. These results provide additional details to the mechanistic debate and may help to optimize cell stability and lifetime with stringent control of spin-selective chemical kinetics.

IV.F. Enantiomeric Separations

Separating enantiomers from racemic mixtures of products is a necessary step in chemical syntheses, in particular for pharmaceuticals.[104] The widespread stereoselectivity of a particular substrate (molecule) for an enzyme renders therapeutics that are enantiomerically pure more effective. Further, the "inactive" mirror image form may produce unexpected side effects with serious consequences. The importance of obtaining enantiomeric excess in syntheses from basic research to industrial applications was made

evident by the 2001 Nobel Prize in Chemistry awarded to Knowles, Sharpless, and Nyori for their work on chiral-catalyzed chemical syntheses. Still, because of the structural similarity and identical composition, enantiomer separation methods based on chiral chromatography are often tedious, inefficient, and may yield chemically modified byproducts.[105,106]

Enantioselective optical trapping may provide a less-invasive solution to chemical-based separations. Yet, due to the weak nature of the chiroptical forces on nanometer-scale species, these mechanisms have only afforded separation of particles that are substantially larger than biomolecules or drugs of interest.[107-109] While optical tweezers with enhanced electromagnetic fields using plasmonic materials may be used to enhance the optical forces necessary to manipulate molecules at the sub-100-nm scale, enantiomer discrimination remains a challenge.[110-112]

Alternatively, the less well established, possible influence of magnetic fields on enantioselective syntheses and separations has had a long and controversial history.[113] Most recently, Naaman and coworkers showed that enantiomers bind to perpendicularly magnetized surface with appreciable differences (Figure IV.8).[114] However, in this example, the mechanism for enantioselective adsorption is hypothesized to be due not to the magnetic field at the surface, but spin-specific interactions that occur upon adsorption and charge transfer.

Rates of adsorption of one enantiomer *vs* the other on substrates magnetized up *vs* down are expected to be different, even though binding energies are identical. Thus, preferential adsorption of one enantiomer over another was shown to win out only at short time scales. Thermodynamic equilibrium in SAM formation is reached at longer time scales yielding a reduction in enantioselectivity. This is an interesting result considering that if an

initial excess of one enantiomer on the surface exists, one may expect that handedness to be propagated as additional molecules approach and bind to the surface due to steric considerations and domain formation. Additional work needs to be done to determine the efficiencies by which resolution of racemic mixtures can be achieved using this novel technique. Nevertheless, the work may prove to be groundbreaking for the design of new magnetic columns for high-throughput separation strategies.

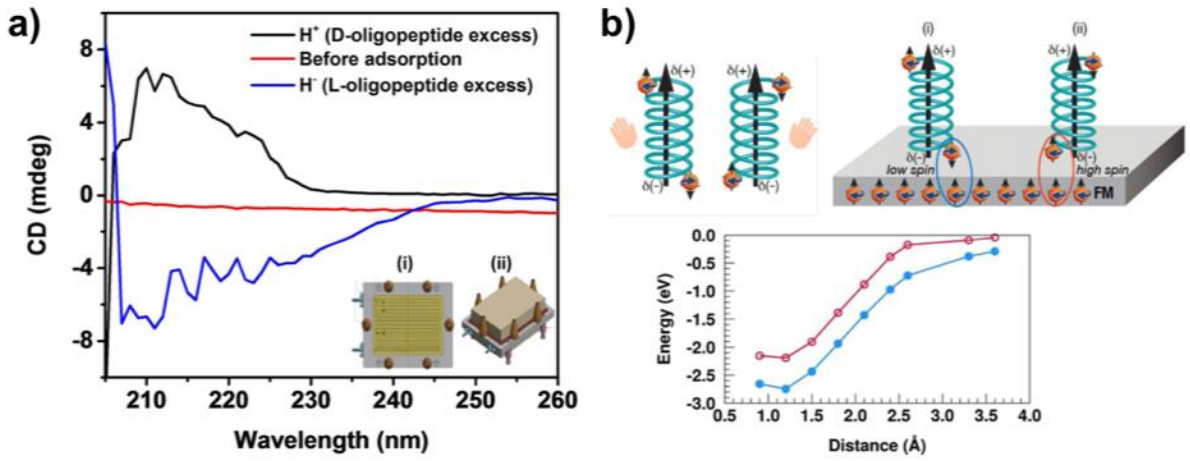

Figure IV.8. Flow-based separation of enantiomers using a magnetic column. (**a**) Circular dichroism spectra of a racemic mixture of an *D*- and *L*-alpha-helical oligopeptide mixture at the inlet (red curve) and at the outlet of a magnetic column with an external magnetic field oriented up *vs* down yielding an excess of *D*-peptides (black curve) or *L*-peptides (blue curve) in the solution, respectively. (**b**) Schematic of spin polarization within a chiral molecule that accompanies electrical polarization upon adsorption to magnetized substrates. The plot shows calculated interaction energies in a model system between a hydrogen atom with electron spin aligned parallel (red) or antiparallel (blue) to the spins with a 2×2×2 cube of nickel atoms. Reproduced with permission from ref 114. Copyright 2018 American Association for the Advancement of Science.

IV.G. Conclusions and Prospects

My thesis work began with the overarching goal of elucidating fundamental and controversial aspects of the chiral-induced spin selectivity effect. I confirmed experimental reports and theoretical predictions that bound electrons with right-handed helicity are selectively transmitted in DNA-mediated charge transfer (Chapter II),[115] and observed spin polarization in previously unexplored photoemission regimes by ionization of chiral molecular films while measuring energy barriers to scattering of unbound, spin-up *vs* spin-down secondary electrons (Chapter III).[26] The results we obtained are relevant for the topics discussed in this chapter: implementation of chiral molecular assemblies as spin-filtering components within devices, and for possible biological implications related to the emergence and propagation of chirality in Nature, respectively.

Moving forward, systematic studies and careful analysis of electron dichroism measurements will be critical to establish the design rules that govern spin-dependent and enantioselective interactions between electrons and chiral molecules. Advanced theoretical accompaniment based on new data will be needed to complement the experimental demonstrations by others and us of room-temperature chiral molecule spin polarization to develop unifying mechanisms. Still, the potential biological significance of these interactions and prospects for next-generation technologies that control electron spin degrees of freedom using chiral molecular assemblies are exciting. Creative experiments carried out during the past two decades have yielded a surge of new observations in a previously divided and inconclusive field. However, while confirming the role of spin in electron interactions with chiral molecules, the results have raised new mechanistic questions. Much remains to be discovered.

References

1. Brandt, J. R.; Salerno, F.; Fuchter, M. J. The Added Value of Small-Molecule Chirality in Technological Applications. *Nat. Rev.* **2017**, 1, 45.

2. Hamase, K.; Morikawa, A.; Zaitsu, K. *D*-Amino Acids in Mammals and their Diagnostic Value. *J. Chromatogr. B* **2002**, 781, 73–91.

3. Radkov, A. D.; Moe, L. A. Bacterial Synthesis of *D*-Amino Acids. *App. Microbiol. Biotechnol.* **2014**, 98, 5363–5374.

4. Pasteur, M. L. Recherches sur les Relations qui Peuvent Exister entre la Forme Crystalline, la Composition Chimique et le Sens de la Polarisation Rotatoire. *Ann. Chim. Phys.* **1848**, 24, 442–459.

5. Bonner, W. A. The Origin and Amplification of Biomolecular Chirality. *Orig. Life Evol. Biosph.* **1991**, 21, 59–111.

6. Podlech, J. Origin of Organic Molecules and Biomolecular Homochirality. *Cell. Mol. Life Sci.* **2001**, 58, 44–60.

7. Girard, C.; Kagan, H. B. Nonlinear Effects in Asymmetric Synthesis and Stereoselective Reactions: Ten Years of Investigations. *Angew. Chem., Int. Ed.* **1998**, 37, 2922–2959.

8. Yamagata, Y. A Hypothesis for the Asymmetric Appearance of Biomolecules on Earth. *J. Theor. Biology* **1966**, 11, 495.

9. Cintas, P. Chirality of Living Systems: A Helping Hand from Crystals and Oligopeptides. *Angew. Chem., Int. Ed.* **2002**, 41, 1139–1145.

10. Wesendrup, R.; Laerdahl, R. J.; Compton, R. N.; Schwerdtfeger, P. Biomolecular Homochirality and Electroweak Interactions. I. The Yamagata Hypothesis. *J. Phys. Chem. A* **2003**, 107, 6668–6673.

11. Lahav, M.; Weissbuch, I.; Shavit, E.; Reiner, C.; Nicholson, G. J.; Schurig, V. Parity Violating Energetic Difference and Enantiomorphous Crystals – Caveats; Reinvestigation of Tyrosine Crystallization. *Orig. Life Evol. Biosph.* **2006**, 36, 151–170.

12. Rubenstein, E.; Bonner, W. A.; Noyes, H. P.; Brown, G. S. Supernovae and Life, *Nature* **1983**, 306, 118.

13. Bonner, W. A.; Rubenstein, E. Supernovae, Neutron Stars, and Biomolecular Chirality. *BioSystems*, **1987**, 20, 99–111.

14. Keszthelyi, L. Origin of the Homochirality of Biomolecules. *Quart. Rev. Biophysics* **1995**, 28, 473–507.

15. Bonner, W. A.; Greenberg, J. M.; Rubenstein, E. The Extraterrestrial Origin of the Homochirality of Biomolecules – Rebuttal to a Critique. *Orig. Life Evol. Biosph.* **1999**, 29, 215–219.

16. Cronin, J. R.; Pizzarello, S. Enantiomeric Excesses in Meteoritic Amino Acids. *Science* **1997**, 275, 951–955.

17. McGuire, B. A.; Carroll, P. B.; Loomis, R. A.; Finneran, I. A.; Jewell, P. R.; Remijan, A. J.; Blake, G. A. Discovery of the Interstellar Chiral Molecule Propylene Oxide (CH_3CHCH_2O). *Science* **2016**, 352, 1449–11452.

18. Kuhn, W.; Braun, E. Photochemische Erzeugung Optisch Aktiver Stoffe. *Naturwissenschaften* **1929**, 17, 227.

19. Buchardt, O. Photochemistry with Circularly Polarized Light. *Angew. Chem., Int. Ed.* **1974**, 13, 179–185.

20. Bailey, J.; Chrysostomou, A.; Hough, J. H.; Gledhill, T. M.; McCall, A.; Clark, S.; Ménard, F.; Tamura, M. Circular Polarization in Star-Forming Regions: Implications for Biomolecular Homochirality. *Science* **1998**, 281, 672–674.

21. Martin, P. G. Interstellar Circular Polarization. *Mon. Not. R. Ast. Soc.* **1972**, 159, 179–190.

22. Cocke, W. J.; Muncaster, G. W.; Gehrels, T. Upper Limit to Circular Polarization of Optical Pulsar NP 0532. *Astrophys. J.* **1971**, 169, L119–L121.

23. Roberts, J. A. Supernovae and Life. *Nature* **1984**, 208, 318.

24. Wu, C. S.; Ambler, E.; Hayward, R. W.; Hoppes, D. D.' Hudson, R. P. Experimental Test of Parity Conservation in Beta Decay. *Phys. Rev.* **1957**, 105, 1413.

25. Garay, A. S. Origin and Role of Optical Isomery in Life. *Nature* **1968**, 219, 338–340.

26. Abendroth, J. M.; Cheung, K. C.; Stemer, D. M.; El Hadri, M. S.; Zhao, C.; Fullerton, E. E.; Weiss, P. S. Spin-Polarized Photoemission by Ionization of Chiral Molecular Films. *In preparation*, *see Chapter III.*

27. Hore, P. J. Are Biochemical Reactions Affected by Weak Magnetic Fields? *Proc. Natl. Acad. Sci. U. S. A.* **2012**, 109, 1357–1358.

28. Zwang, T. J.; Tse, E. C. M.; Zhong, D.; Barton, J. K. A Compass at Weak Magnetic Fields using Thymine Dimer Repair. *ACS Cent. Sci.* **2018**, 4, 405–412.

29. Michaeli, K.; Kantor-Uriel, N.; Naaman, R.; Waldeck, D. H. The Electron's Spin and

Molecular Chirality – How are They Related and How Do They Affect Life Processes? *Chem. Soc. Rev*. **2016**, 45, 6478–6487.

30. Facchetti, A. Semiconductors for Organic Transistors. *Mater. Today* **2007**, 10, 28–37.

31. Ron, I.; Pecht, I.; Sheves, M.; Cahen, D. Proteins as Solid-State Electronic Conductors. *Acc. Chem. Res.* **2010**, 43, 945–953.

32. Amdursky, N.; Marchak, D.; Sepunaru, L.; Pecht, I.; Sheves, M.; Cahen, D. Electronic Transport *via* Proteins. *Adv. Mater.* **2014**, 26, 7142–7161.

33. Medina, E.; González-Arraga, L. A.; Finkelstein-Shapiro, D.; Berche, B.; Mujica, V. Continuum Model for Chiral Induced Spin Selectivity in Helical Molecules. *J. Chem. Phys.* **2015**, 142, 194308–194313.

34. Michaeli, K.; Naaman, R. Origin of Spin Dependent Tunneling through Chiral Molecules. arXiv 1512.03435v2, **2016**.

35. Varela, S.; Mujica, V.; Medina, E. Effective Spin-Orbit Couplings in an Analytical Tight-Binding Model of DNA: Spin Filtering and Chiral Spin Transport. *Phys. Rev. B: Condens. Matter Mater. Phys*. **2016**, 93, 155436.

36. Taft, B. J.; O'Keefe, M.; Fourkas, J. T.; Kelley, S. O. Engineering DNA-Electrode Connectivities: Manipulation of Linker Length and Structure. *Anal. Chim. Acta* **2003**, 496, 81–91.

37. Napper, A. M.; Liu, H.; Waldeck, D. H. The Nature of Electronic Coupling Between Ferrocene and Gold through Alkanethiolate Monolayers on Electrodes: The Importance of Chain Composition, Interchain Coupling, and Quantum Interference. *J. Phys. Chem. B* **2001**, 105, 7699–7707.

38. Drummond, T. G.; Hill, M. G.; Barton, J. K. Electron Transfer Rates in DNA Films as a Function of Tether Length. *J. Am. Chem. Soc.* **2004**, 126, 15010–15011.

39. Bumm, L. A.; Arnold, J. J.; Dunbar, T. D.; Allara, D. L.; Weiss, P. S. Electron Transfer through Organic Molecules. *J. Phys. Chem. B* **1999**, 103, 8122–8127.

40. Smalley, J. F.; Finklea, H. O.; Chidsey, C. E. D.; Linford, M. R.; Creager, S. E.; Ferraris, J. P.; Chalfant, K.; Zawodzinsk, T.; Feldberg, S. W.; Newton, M. D. Heterogeneous Electron-Transfer Kinetics for Ruthenium and Ferrocene Redox Moieties through Alkanethiol Monolayers on Gold. *J. Am. Chem. Soc.* **2003**, 125, 2004–2013.

41. Engelkes, V. B.; Beebe, J. M.; Frisbie, C. D. Length-Dependent Transport in Molecular Junctions Based on SAMs of Alkanethiols and Alkanedithiols: Effect of Metal Work Function and Applied Bias on Tunneling Efficiency and Contact Resistance *J. Am. Chem. Soc.* **2004**, 126, 14287–14296.

42. Sek, S.; Tolak, A.; Misicka, A.; Palys, B.; Bilewicz, R. Asymmetry of Electron Transmission through Monolayers of Polyalanine on Gold Surfaces. *J. Phys. Chem. B* **2005**, 109, 18433–18438.

43. Kai, M.; Takeda, K.; Morita, T.; Kimura, S. Distance Dependence of Long-Range Electron Transfer through Helical Peptides. *J. Pept. Sci.* **2008**, 14, 192–202.

44. Gray, H. B.; Winkler, J. R. Electron Transfer in Proteins. *Ann. Rev. Biochem.* **1996**, 65, 537–561.

45. Williams, D. H.; Stephans, E.; O'Brien, D. P.; Zhou, M. Understanding Noncovalent Interactions: Ligand Binding Energy and Catalytic Efficiency from Ligand-Induced Reductions in Motion within Receptors and Enzymes. *Angew. Chem., Int. Ed.* **2004**, 43, 6596–6616.

46. Wilcheck, M.; Bayer, E. A.; Livnah, O. Essentials of Biorecognition: The (Strept)avidin-Biotin System as a Model for Protein-Protein and Protein-Ligand Interaction. *Immunol. Lett.* **2006**, 103, 27–32.

47. Wagner, J. R.; Lee, C. T.; Durrant, J. D.; Malmstrom, R. D.; Feher, V. A.; Amara, R. E. Emerging Computational Methods for the Rational Discovery of Allosteric Drugs. *Chem. Rev.* **2016**, 116, 6370–6390.

48. Ryde, U.; Söderhjelm, P. Ligand-Binding Affinity Estimates Supported by Quantum-Mechanical Methods. *Chem. Rev.* **2016**, 116, 5520–5566.

49. Kumar, A.; Capua, E.; Kesharwani, M. K.; Martin, J. M. L.; Sitbon, E.; Waldeck, D. H.; Naaman, R. Chirality-Induced Spin Polarization Places Symmetry Constraints on Biomolecular Interactions. *Proc. Natl. Acad. Sci. U. S. A.* **2017**, 114, 2474–2478.

50. Ambacher, O.; Smart, J.; Shealy, J. R.; Weimann, N. G.; Chu, K.; Murphy, M.; Schaff, W. J.; Eastman, L. F.; Dimitrov, R.; Wittmer, L.; Stutzmann, M.; Rieger, W.; Hilsenbeck, J. Two-Dimensional Electron Gases Induced by Spontaneous and Piezoelectric Polarization Charges in N- and Ga-Face AlGaN/GaN Heterostructures. *J. Appl. Phys.* **1999**, 85, 3222.

51. Rowland, R. S.; Taylor, R.; Intermolecular Nonbonded Contact Distances in Organic Crystal Structures: Comparison with Distances Expected from van der Waals Radii. *J. Phys. Chem.* **1996**, 100, 7384–7391.

52. Goulding, C. W.; Bowers, P. M.; Segelke, B.; Lekin, T.; Kim, C. Y.; Terwilliger, T. C.; Eisenberg, D. The Structure and Computational Analysis of Mycobacterium Tuberculosis Protein CitE Suggest a Novel Enzymatic Function. *J. Mol. Biol.* **2007**, 365, 275–283.

53. Hanson, R. M.; Prilusky, J.; Renjian, Z.; Nakane, T.; Sussman, J. L. JSmol and the Next-Generation Web-Based Representation of 3D Molecular Structure as Applied to *Proteopedia*. *Ist. J. Chem.* **2013**, 53, 207–216.

54. London, F. The General Theory of Molecular Forces. *Trans. Faraday. Soc.* **1937**, 33, 8–26.

55. Dickinson, A. G.; Denker, J. S. Adiabatic Dynamic Logic. *IEEE J. Solid-State Circuits* **1995**, 30, 311–315.

56. Bandyopadhyay, S.; Cahay, M. Electron Spin for Classical Information Processing: A Brief Survey of Spin-Based Logic Devices, Gates, and Circuits. *Nanotechnology* **2009**, 20, 412001.

57. Appelbaum, I.; Huang, B.; Monsma, D. J. Electronic Measurement and Control of Spin Transport in Silicon. *Nature* **2007**, 447, 295–298.

58. Dushenko, S.; Koike, M.; Ando, Y.; Shinjo, T.; Myronov, M.; Shiraishi, M Experimental Demonstration of Room-Temperature Spin Transport in *n*-Type Germanium Epilayers. *Phys. Rev. Lett.* **2015**, 114, 196602.

59. Dery, H.; Sham, L. J. Spin Extraction Theory and its Relevance to Spintronics. *Phys. Rev. Lett.* **2007**, 98, 046602.

60. Tran, M.; Jaffrès, H.; Deranlot, C.; George, J. –M.; Fert, A.; Miard, A.; Lemaître, A. Enhancement of the Spin Accumulation at the Interface between a Spin-Polarized Tunnel Junction and a Semiconductor. *Phys. Rev. Lett.* **2009**, 102, 036601.

61. Baibich, M. N.; Broto, J. M.; Fert, A.; Nguyen Van Dau, F.; Petroff, F.; Etienne, P.; Creuzet, G.; Friederich, A.; Chazelas, J. Giant Magnetoresistance of (001)Fe/(001)Cr Magnetic Superlattices. *Phys. Rev. Lett.* **1988**, 61, 2472–2475.

62. Fert, A. Nobel Lecture: Origin, Development, and Future of Spintronics. *Rev. Mod. Phys.* **2008**, 80, 1517.

63. Moodera, J. S.; Kinder, L. R.; Wong, T. M.; Meservey, R. Large Magnetoresistance at Room Temperature in Ferromagnetic Thin Film Tunnel Junctions. *Phys. Rev. Lett.* **1995**, 74, 3273–3276.

64. Nogués, J.; Schuller, I. K. Exchange Bias. *J. Magn. Magn. Mater.* **1999**, 192, 203–232.

65. Michaeli, K.; Varade, V.; Naaman, R.; Waldeck, D. H. A New Approach towards Spintronics: Spintronics with No Magnets. *J. Phys.: Condens. Matter* **2017**, 29, 103002.

66. Mathew, S. P.; Mondal, P. C.; Moshe, H.; Mastai, Y.; Naaman, R. Non-Magnetic Organic/Inorganic Spin Injector at Room Temperature. *Appl. Phys. Lett.* **2014**, 105, 242408.

67. Mondal, P. C.; Kantor-Uriel, N.; Mathew, S. P.; Tassinari, F.; Fontanesi, C.; Naaman, R. Chiral Conductive Polymers as Spin Filters. *Adv. Mater.* **2015**, 27, 1924–1927.

68. Kiran, V.; Mathew, S. P.; Cohen, S. R.; Delgado, I. H.; Lacour, J.; Naaman, R. Helicenes – A New Class of Organic Spin Filter. *Adv. Mater.* **2016**, 28, 1957–1962.

69. Bloom, B. P.; Kiran, V.; Varade, V.; Naaman, R.; Waldeck, D. H. Spin Selective Charge Transport through Cysteine Capped CdSe Quantum Dots. *Nano Lett.* **2016**, 16, 4583–4589.

70. Miyazaki, T.; Tezuka, N. Giant Magnetic Tunneling Effect in Fe/Al_2O_3/Fe Junction. *J. Magn. Magn. Mater.* **1994**, 139, L231–L234.

71. Varade, V.; Markus, T.; Vankayala, K.; Friedman, N.; Sheves, M.; Waldeck, D. H.; Naaman, R. Bacteriorhodopsin-Based Non-Magnetic Spin Filters for Biomolecular Spintronics. *Phys. Chem. Chem. Phys.* **2018**, 20, 1091–1097.

72. Vilan, A.; Aswal, D.; Cahen, D. Large-Area, Ensemble Molecular Electronics: Motivation and Challenges. *Chem. Rev.* **2017**, 117, 4248–4286.

73. Huai, Y.; Spin-Transfer Torque MRAM (STT-MRAM): Challenges and Prospects. *AAPPS Bull.* **2008**, 18, 33–40.

74. Kent, A. D.; Worledge, D. C. A New Spin on Magnetic Memories. *Nat. Nanotechnol.* **2015**, 10, 187–191.

75. Dor, O. B.; Yochelis, S.; Mathew, S. P.; Naaman, R.; Paltiel, Y. A Chiral-Based Magnetic Memory Device without a Permanent Magnet. *Nat. Commun.* **2013**, 4, 2256.

76. Diao, Z.; Li, Z.; Wang, S.; Ding, Y.; Panchula, A.; Chen, E.; Wang, L. –C.; Huai, Y. Spin-Transfer Torque Switching in Magnetic Tunnel Junctions and Spin-Transfer Torque Random Access Memory. *J. Phys.: Condens. Matter* **2007**, 19, 165209.

77. Dor, O. B.; Yochelis, S.; Radko, A.; Vankayala, K.; Capua, E.; Capua, A.; Yang, S. -H.; Baczewski, L. T.; Parkin, S. S. P.; Naaman, R.; Paltiel, Y. Magnetization Switching in Ferromagnets by Adsorbed Chiral Molecules without Current or External Magnetic Field. *Nat. Commun.* **2017**, 8, 14567.

78. Trudel, S. Unexpected Magnetism in Gold Nanostructures: Making Gold Even More Attractive. *Gold Bull.* **2011**, 44, 3–13.

79. Tuboltsev, V.; Savin, A.; Pirojenko, A.; Räisänen, J. Magnetism in Nanocrystalline Gold. *ACS Nano*. **2013**, 7, 6691–6699.

80. Parkin, S. S. P.; Hayashi, M; Thomas, L. Magnetic Domain-Wall Racetrack Memory. *Science* **2008**, 320, 190–194.

81. Nguyen, T. D.; Ehrenfreund, E.; Vardeny, Z. V. Spin-Polarized Light-Emitting Diode Based on an Organic Bipolar Spin Valve. *Science* **2012**, 337, 204–209.

82. Friend, R. H.; Gymer, R. W.; Holmes, A. B.; Burroughes, J. H.; Marks, R. N.; Taliani, C.; Bradley, D. D. C.; Dos Santos, D. A.; Bredas, J. L.; Lögdlund, M.; Salaneck, W. R. Electroluminescence in Conjugated Polymers. *Nature* **1999**, 397, 121–128.

83. Gray, H. B. Powering the Planet with Solar Fuel. *Nat. Chem.* **2009**, 1, 7.

84. Meyer, T. J. Chemical Approaches to Artificial Photosynthesis. *Acc. Chem. Res.* **1989**, 22, 163–170.

85. Bard, A. J.; Fox, M. A. Artificial Photosynthesis: Solar Splitting of Water to Hydrogen and Oxygen. *Acc. Chem. Res.* **1995**, 28, 141–145.

86. Han, Z.; Eisenberg, R. Fuel from Water: The Photochemical Generation of Hydrogen from Water. *Acc. Chem. Res.* **2014**, 47, 2537–2544.

87. Hunter, B. M.; Gray, H. B.; Müller, A. M. Earth-Abundant Heterogeneous Water Oxidation Catalysts. *Chem. Rev.* **2016**, 116, 14120–14136.

88. Ager, J. W.; Shaner, M. R.; Walczak, K. A.; Sharp, I. D.; Ardo, S. Experimental Demonstrations of Spontaneous, Solar-Driven Photoelectrochemical Water Splitting. *Energy Environ. Sci.* **2015**, 8, 2811–2824.

89. Chrétien, S.; Metiu, H. O_2 Evolution on a Clean Partially Reduced Rutile TiO_2(110) Surface and on the Same Surface Precovered with Au_1 and Au_2: The Importance of Spin Conservation. *J. Chem. Phys.* **2008**, 129, 74705

90. Torun, E.; Fang, C. M.; de Wijs, G. a.; de Groot, R. a. Role of Magnetism in Catalysis: RuO_2 (110) Surface. *J. Phys. Chem. C* **2013**, 117, 6353.

91. Zhao, M.; Huang, F.; Lin, H.; Zhou, J.; Xu, J.; Wu, Q.: Wang, Y. $CuGaS_2$-ZnS *p-n* Nanoheterostructures: A Promising Visible Light Photo-Catalyst for Water-Splitting Hydrogen Production. *Nanoscale* **2016**, 8, 16670–16676.

92. Sharpe, R.; Lim, T.; Jiao, Y.; Niemantsverdriet, H.; Gracia, J. Oxygen Evolution Reaction on Perovskite Electrocatalysts with Localized Spins and Orbital Rotation Symmetry. *ChemCatChem.* **2016**, 8, 3762–3768.

93. Mtangi, W.; Kiran, V.; Fontanesi, C.; Naaman, R. Role of the Electron Spin Polarization in Water Splitting. *J. Phys. Chem. Lett.* **2015**, 6, 4916–4922.

94. Mtangi, W.; Tassinari, F.; Vankayala, K.; Jentzsch, A. V.; Adelizzi, B.; Palmans, A. R. A.; Fontanesi, C.; Meijer, E. W.; Naaman, R. Control of Electrons' Spin Eliminates Hydrogen Peroxide Formation during Water Splitting. *J. Am. Chem. Soc.* **2017**, 139, 2794–2798.

95. Jiao, Y.; Sharpe, R.; Lim, T.; Niemantsverdriet, J. W. H.; Gracia, J. Photosystem II Acts as a Spin-Controlled Electron Gate during Oxygen Formation and Evolution. *J. Am. Chem. Soc.* **2017**, 139, 16604–16608.

96. Tassinari, F.; Banerjee-Ghosh, K.; Parenti, F.; Kiran, V.; Mucci, A.; Naaman, R. Enhanced Hydrogen Production with Chiral Conductive Polymer-Based Electrodes. *J. Phys. Chem. C* **2017**, 121, 15777–15783.

97. Zhang, W.; Gao, W.; Zhang, X.; Li, Z.; Lu, G. Surface Spintronics Enhanced Photo-Catalytic Hydrogen Evolution: Mechanisms, Strategies, Challenges, and Future. *Appl. Surf. Sci.* **2018**, 434, 643–668.

98. Wattanakit, C. Chiral Metals as Electrodes. *Curr. Op. Electrochem.* **2018**, 7, 54–60.

99. Mandler, D. Chiral Self-Assembled Monolayers in Electrochemistry. *Curr. Op. Electrochem.* **2018**, 7, 42–47.

100. Siegbahn, P. E. M.; Crabtree, R. H. Manganese Oxyl Radical Intermediates and O-O Bond Formation in Photosynthetic Oxygen Evolution and a Proposed Role for the Calcium Cofactor in Photosystem II. *J. Am. Chem. Soc.* **1999**, 121, 117–127.

101. McEvoy, J. P.; Gascon, J. A.; Batista, V. S.; Brudvig, G. W. The Mechanism of Photosynthetic Water Splitting. *Photochem. Photobiol. Sci.* **2005**, 4, 940–949.

102. Yang, X.; Baik, M. H. The Mechanism of Water Oxidation Catalysis Promoted by $[tpyRu(IV)=O]_2L^{3+}$: A Computational Study. *J. Am. Chem. Soc.* **2008**, 130, 16231–16240.

103. Rivalta, I.; Yang, K. R.; Brudvig, G. W.; Batista, V. S. Triplet Oxygen Evolution Catalyzed by a Biomimetic Oxomanganese Complex: Functional Role of the Carboxylate Buffer. *ACS Catal.* **2015**, 5, 3284–2390.

104. Nguyen, L. A.; He, H.; Pham-Huy, C. Chiral Drugs: An Overview. *Int. J. Biomed. Sci.* **2006**, 2, 85–100.

105. Ward, T. J.; Baker, B. A. Chiral Separations. *Anal. Chem.* **2008**, 80, 4363–4372.

106. Li, B.; Taynie, D. T. In *Encyclopedia of Chemical Processing*, Vol. 1; Lee, S., Ed.; Taylor & Francis: New York, 2005; pp 449–458.

107. Askin, A.; Optical Trapping and Manipulation of Neutral Particles using Lasers. *Proc. Natl. Acad. Sci. U. S. A.* **1997**, 94, 4853–4860.

108. Tkachenko, G.; Brasselet, E. Optofluidic Sorting of Material Chirality by Chiral Light. *Nat. Commun.* **2014**, 5, 4577.

109. Hayat, A.; Balthasar Müller, J. P.; Capasso, F. Lateral Chirality-Sorting Optical Forces. *Proc. Natl. Acad. Sci. U. S. A.* **2015**, 112, 13190–13194.

110. Wheaton, S.; Gordon, R. Molecular Weight Characterization of Single Globular Proteins using Optical Nanotweezers. *Analyst* **2015**, 140, 4799–4803.

111. Saleh, A. A. E.; Dionne, J. A. Toward Efficient Optical Trapping of Sub-10-nm Particles with Coaxial Plasmonic Apertures. *Nano Lett.* **2012**, 12, 5581–5586.

112. Zhao, Y.; Saleh, A. A. E.; Dionne, J. A. Enantioselective Optical Trapping of Chiral Nanoparticles with Plasmonic Tweezers. *ACS Photonics* **2016**, 3, 304–309.

113. Feringa, B. L.; van Delden, R. A. Absolute Asymmetric Synthesis: The Origin, Control, and Amplification of Chirality. *Angew. Chem., Int. Ed.* **1999**, 38, 3418–3438.

114. Banerjee-Ghosh, K.; Dor, O. B.; Tassinari, F.; Capua, E.; Yochelis, S.; Capua, A.; Yang, S. -H.; Parkin, S. S. P.; Sarkar, S.; Kronik, L.; Baczewski, L. T.; Naaman, R.; Paltiel, Y. Separation of Enantiomers by their Enantiospecific Interactions with Achiral Magnetic Substrates. *Science* **2018**, DOI: 10.1126/science.aar4265.

115. Abendroth, J. M.; Nakatsuka, N.; Ye, M.; Kim, D.; Fullerton, E. E.; Andrews, A. M.; Weiss, P. S. Analyzing Spin Selectivity in DNA-Mediated Charge Transfer *via* Fluorescence Microscopy. *ACS Nano* **2017**, 11, 7516–7526.

Appendix

Controlling Motion at the Nanoscale: Rise of the Molecular Machines

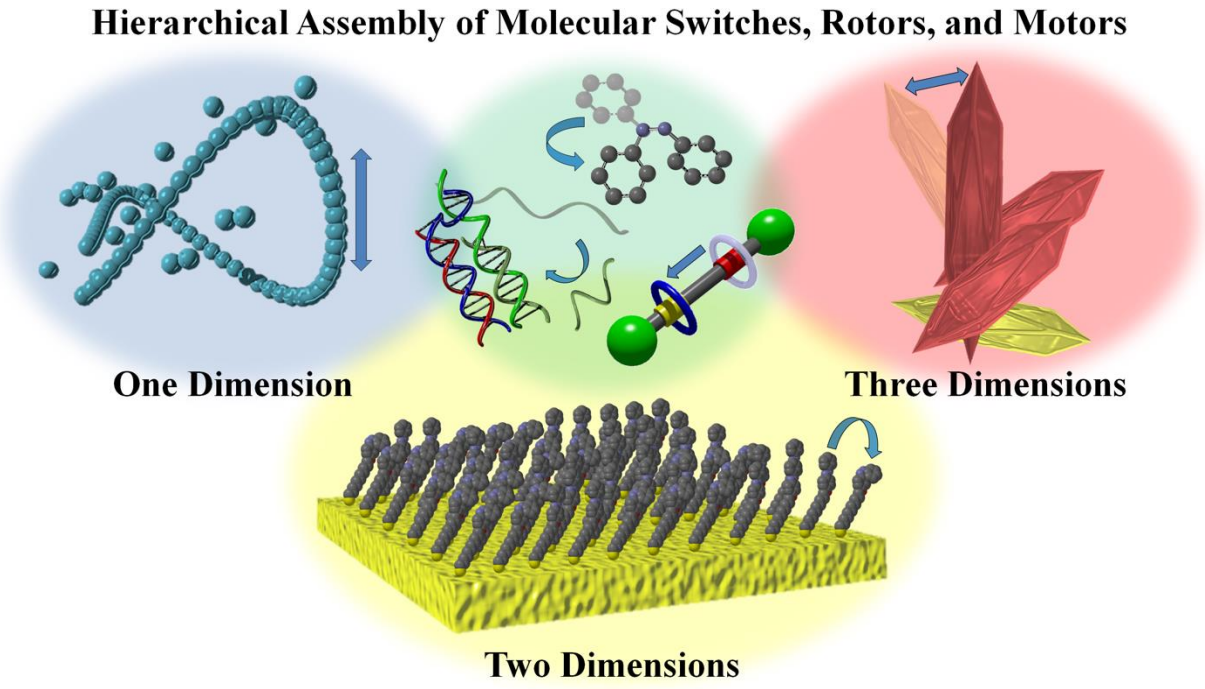

The information in this appendix was published in
ACS Nano 2015, 9, 7746–7768, and is reproduced here.

Authors: John M. Abendroth, Oleksandr S. Bushuyev, Paul S. Weiss, and Christopher J. Barrett

A.A. Introduction

Inspired by the complexity and hierarchical organization of biological machines, the design of artificial molecular machines that exhibit controlled mechanical motion and perform sophisticated tasks is an ultimate pursuit of molecular-scale engineering.[1-7] The design and synthesis of molecules that can undergo reversible structural changes with various stimuli have received considerable attention, but there remain far fewer reports of dynamic molecular systems such as cleverly designed motors and pumps where the mechanistic action of their molecular components has been exploited to do controlled work on their environment. The very definition of a machine has been a fascinating debate since Isaac Asimov began to lay out the early laws of robotics over 70 years ago.[8] In an effort to advance the field, a stringent language has been sought to differentiate simple molecular switches from motors that are capable of driving a system away from equilibrium.[9,10] While the working principles of these molecular devices cannot be compared to macroscopic analogues, a practical acceptance has emerged that a molecular machine can be a multicomponent system with defined energy input that is capable of performing a measurable and useful secondary function either at the nanoscale or, if amplified through collective action, at the macroscale. The system should ideally act in a reversible manner, with the capacity to complete repeated mechanical operations. Spatial control and temporal control over this motion, and work performed, are further hallmarks of successful machines, helping to differentiate deliberate actuated mechanics that leverage Brownian motion from undirected thermal effects, and machines from simple molecules that wiggle or diffuse randomly.[11,12]

In this Review, we draw from this rapidly expanding and diverse field to highlight some of the most exciting recent reports of molecules and assemblies that (a) exemplify practical and advantageous attributes that can be applied to other systems and (b) show the most promise in successfully advancing the development of artificial molecular machines. We first summarize some of the key advances in the development of molecular switches and rotors ranging from simple hydrazone switches to complex deoxyribonucleic acid (DNA)-based nanomechanical walkers. Although these systems in isolation are distinct from scaled-up artificial machines, recent progress in the diversity and complexity of their design has facilitated greater control over mechanical motion at the molecular level. This control has enabled the conversion of simple molecular components into functional tools that can interact with one another or couple to their environment to operate as machines at the nanoscale. We highlight some of the most promising examples of the organization of switches and rotors into linear assemblies, then two-dimensional arrays on surfaces, and finally polymeric networks and dynamic three-dimensional crystals. Ultimately, the precise and robust integration into higher dimensional architectures that take advantage of mechanical action by many components is essential to bridge the gap between actuating molecular motion and performing microscopic, mesoscopic, and macroscopic work. Throughout, we address fundamental obstacles yet to be overcome to advance the field and to convert these molecular systems into functioning machines and offer a glimpse into the untapped potential of these versatile systems in an effort to identify some of the most viable directions toward future molecular machine design and implementation.

A.B. Molecular Switches, Rotors, and Motors

A.B.1. Increasing Sophistication of Molecular Design

Numerous classes of molecules that reversibly isomerize between multiple structural configurations in response to external stimuli fall within the realm of molecular switches. Common examples of photochromic molecular switches are displayed in Figure A.1. Some of the most extensively studied small-molecule motifs include (but are far from limited to) azobenzenes, whose isomerization between *E* and *Z* conformations about a double bond mimics flapping motions;[13,14] diarylethenes and spiropyrans, in which conformational changes are accompanied by ring-opening or ring-closing reactions;[15-18] anthracene and coumarin derivatives that reversibly dimerize with one another;[19-21] and overcrowded alkenes, hydrazones, and imines, which behave as rotors that can revolve about a rigid internal axis.[22-25] Covalent modification of parent switch and rotor molecules provides near infinite opportunities to design alternate isomerization pathways and to tune actuation stimuli.

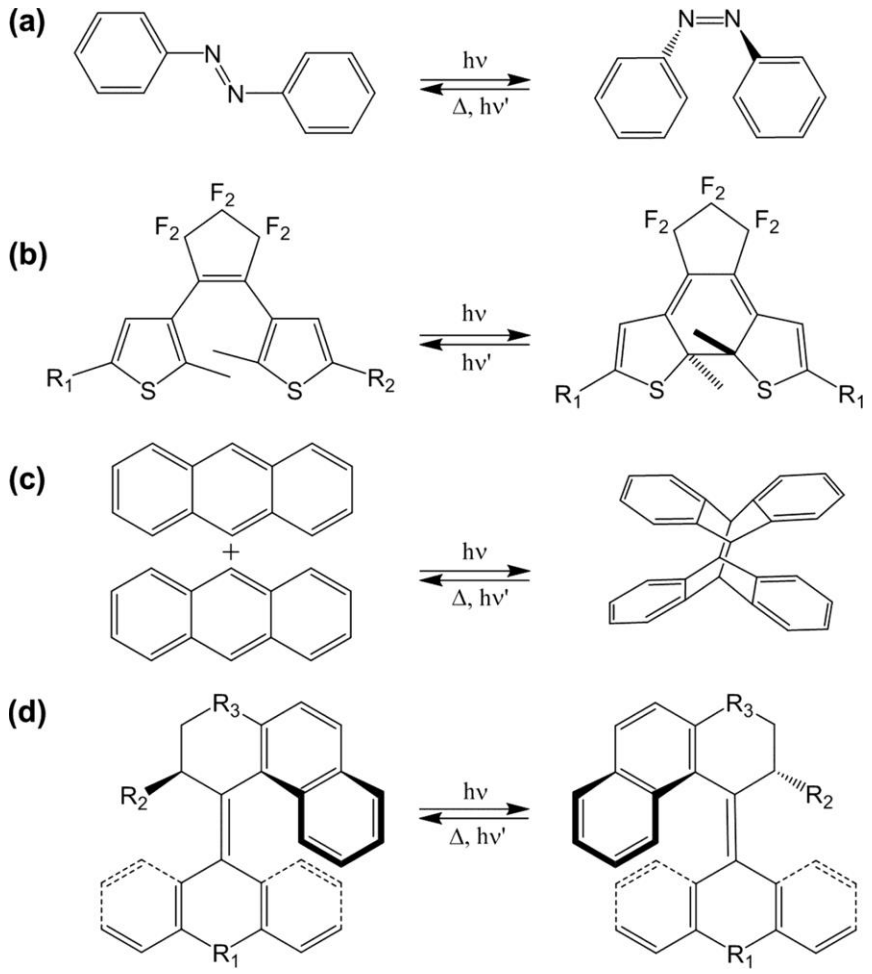

Figure A.1. Examples of common small-molecule switch motifs that undergo various types of chemical bond rearrangements. (**a**) Isomerization of azobenzene between *trans* and *cis* conformations upon irradiation or heating. (**b**) Photoinduced ring-opening and ring-closing reactions of diarylethene derivatives. The closed-ring form is thermally stable and will generally not return to the open-ring configuration under ambient conditions when kept in the dark. (**c**) Formation and disassociation of cyclic dimers of anthracene molecules. (**d**) Rotation about a central double bond in a sterically overcrowded alkene. Numerous structural possibilities exist, but the general form consists of a tricyclic stator (bottom) connected to a heterocyclic rotor (top) by a double bond. The reverse reaction most often proceeds via helix inversion of the tricyclic stator upon heating.

Additionally, noncovalent interactions between molecules such as hydrogen bonding, hydrophobic effects, and π–π stacking enable the construction of dynamic host–guest systems, expanding the versatility of switches *via* supramolecular self-assembly of two or more components.[26] These dynamic molecules represent the smallest building blocks available for a bottom-up approach to synthesize functional mechanical devices that exhibit motion. Increasingly complex mechanically interlocked molecules (MIMs) such as catenanes, rotaxanes, and pseudorotaxanes represent another class of switches and rotors and have regularly been targeted as promising architectures in the design of molecular muscles that facilitate contractile and extensile motions due to their mechanostereochemistry.[27-29] Catenanes are MIMs constructed from two or more interlocked macrocycles in a chain-like architecture that may be designed to adopt distinct and stable conformations with controllable rotary motions (Figure A.2a). Alternatively, rotaxanes, pseudorotaxanes, and their derivatives are molecules composed of a linear rod-like component threaded through a cyclic host; the exact position and orientation (station) of the relative components in the mechanically interlocked compound can be controlled by external stimuli. The macrocycle host may be sterically constrained by bulky end groups on the linear species, as in rotaxanes, or designed to possess sufficient free energy to dethread from the rod-like component, as in pseudorotaxanes (Figure A.2b,c). Finally, nanomechanical switches, rotors, and walkers composed of a few to hundreds of DNA biopolymer strands, whose design and synthesis have developed into a rapidly burgeoning field of its own, offer the capability to extend the dynamic boundaries of individual molecular components to the submicrometer scale.[30-32]

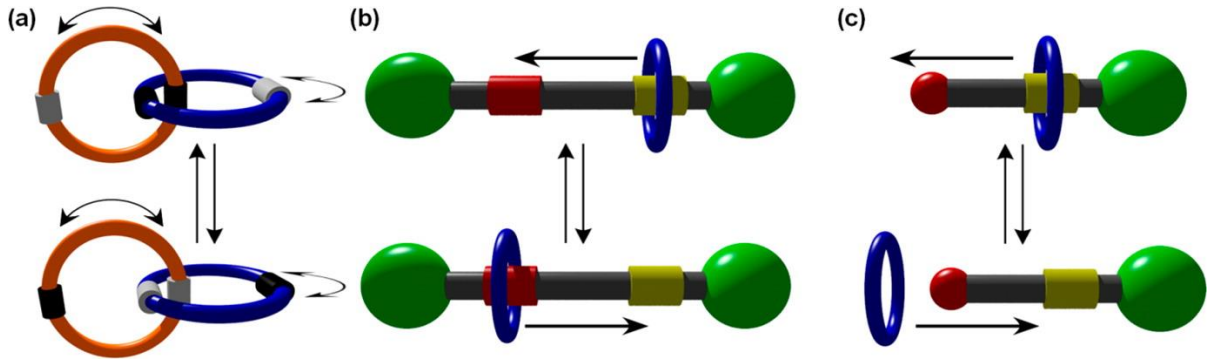

Figure A.2. Example schematics of switchable mechanically interlocked molecules (MIMs). Functional groups incorporated within the molecular architecture that are influenced by various stimuli including light, pH, redox activity, and ions program the switching of stable recognition stations. The actuation stimuli thus facilitate movement of the interlocked components with respect to one another. (**a**) Catenane composed of interlocked macrocycles that are free to rotate and contain multiple thermodynamically stable configurations. (**b**) Shuttling motion of a threaded macrocycle (blue) between two stable states within a rotaxane motif in which sterically bulky end groups (green) on the rod-like component prevent dethreading of the macrocycle. (**c**) Unidirectional dethreading and rethreading of a macrocycle host from the rod in a pseudorotaxane.

While diverse, all of the aforementioned switch and rotor components operate on similar principles.[33] The actuation of switching events, such as the absorption of a photon, electrochemical reduction or oxidation reactions, binding or unbinding of a ligand, or changes in temperature, manipulates the relative energy barrier(s) between two or more possible states. However, intra- or intermolecular rotational, translational, or extensile and contractile movements are ultimately driven by the irrepressible effects of thermal noise. This competing driving force highlights the importance of molecular switch designs to consider the potential energy landscape to facilitate thermodynamically uphill transformations with sufficiently deep new minima and spatiotemporal control over biased switching events. The most remarkable examples of mechanical control employed to overcome the randomizing effect of Brownian motion impart necessary directionality to molecular rotations or translations.[34, 35] Typically, this control is achieved in a variety of

systems by maintaining a judicious balance between molecular flexibility and rigidity and utilizing sterically demanding or asymmetric molecular geometries. Examples include the unidirectional rotation about double bonds in chiral overcrowded alkenes and imines,[36,37] circumrotation in catenanes,[38] preferential threading and dethreading of MIMs,[39,40] and directed walkers and nanocars.[41-43] Recently, Stoddart and co-workers successfully demonstrated the energetically uphill, unidirectional threading of a dumbbell-shaped molecular rod containing a noninteracting oligomethylene chain by tetracationic macrocycle hosts.[44] This redox-driven molecular pump performs work by first confining one macrocycle on the rod and subsequently threading a second ring against a local concentration gradient into an entropically unfavorable configuration on the oligomethylene chain, in close proximity to the first macrocycle. The proposed flashing energy ratchet mechanism for the energetically demanding action of the pump can be described by modulation of the potential energy landscape of the molecule upon redox-switching events.

A significant yet challenging goal in molecular design that has received less attention, however, is the development of switches whose actuation is engineered to trigger cooperative or coordinated action, thus amplifying motion where a switching event directly influences simultaneous or subsequent conformational change in another molecule. Here, the intermolecular coupling of switching events is distinct from collective ensemble motion. The paradigmatic example of cooperativity found in Nature is the uptake of molecular oxygen (O_2) by the metalloprotein, hemoglobin.[45,46] The binding of O_2 by one of four heme groups induces intramolecular conformational changes in the protein that triggers the favorable uptake of three additional O_2 molecules. While examples of cooperativity are abundant in Nature, there has been little success in the field of molecular machine design in

synthesizing and operating switchable moieties whose states are influenced directly by other molecules.

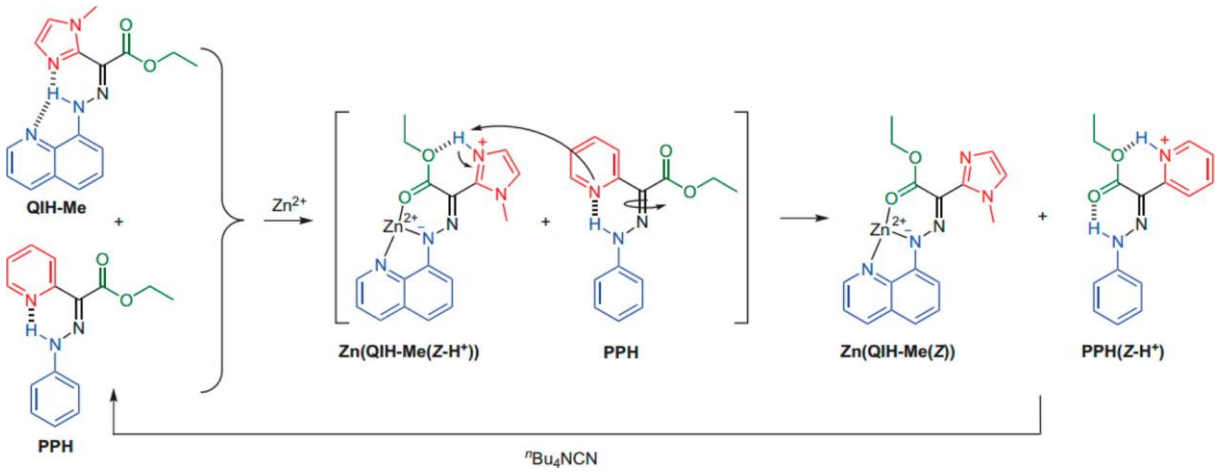

Figure A.3. Cooperative switching events between two distinct molecular switches: an imidazole-containing hydrazone switch (QIH-Me) and pyridine-containing hydrazone switch (PPH). Upon addition of Zn^{2+}, QIH-Me isomerizes to a structure that contains an acidic imidazolium ring (Zn(QIH-Me(Z-H^+))). The PPH switch subsequently isomerizes to PPH(Z-H^+) upon proton transfer from Zn(QIH-Me(Z-H^+)). The addition of tetrabutylammonium cyanide (^{n}Bu$_4$NCN) to the reaction mixture regenerates the original switch configurations. The scheme illustrates coupled switching events between two molecules through proton relay. Reproduced with permission from ref 47. Copyright 2012 Nature Publishing Group.

An early example of an artificial multistep switching cascade was recently reported by Aprahamian and co-workers, in which structurally simple hydrazone-based switches were shown to facilitate cross-talk between molecules, reminiscent of biological proton-relay processes (Figure A.3).[47] The input of Zn^{2+} initiates E/Z isomerization and deprotonation of a hydrazone molecule that contains hydrogen-bond-accepting methylimidazole and quinoline groups to stabilize a metal-ion binding pocket. The subsequent proton transfer to a structurally related hydrazone switch that does not interact strongly with Zn^{2+} results in the isomerization of a second molecule. Capitalizing on the

leveraging of intermolecular interactions to influence switching events represents a paradigm shift in the design of next generation molecular switches, as it exemplifies active and dynamic communication between separate components to work in tandem.[48-50] If analogous approaches toward amplifying molecular motion can be applied to other switching motifs with greater specificity and without the use of sacrificial reagents, substantial increases in the operational yield of isolated or hierarchically assembled systems can be envisioned and may thereby increase their practicality in real-world applications.

A.B.2. Isolated Small Molecule Machines

The rational design of switches and rotors, or even the impressive directional control over walkers and motorized nanocars, is clearly not a final objective (unless, of course, the design is to be entered in a molecular nanocar race).[51,52] It is instead necessary to harness and to amplify the mechanical motion of individual components to drive iterative chemical processes or to complete complex tasks in order to qualify these dynamic systems as functional machines. Some of the most innovative examples of mechanistic function of isolated molecules are switchable catalysts that are capable of raising or lowering the energetic barriers to chemical transformations.[53-55] Molecular machines that control bidirectional enantioselectivity in asymmetric catalysis are particularly exciting, as the preparation of enantiopure catalysts and the separation of racemic mixtures of synthetic products are typically tedious and cumbersome processes. Wang and Feringa demonstrated *in situ* switching with enantiomeric preference of the chiral product of a conjugate addition reaction using a rotary-motor catalyst fueled by light.[56] More recently, Leigh and co-workers described a rotaxane-based asymmetric catalyst that can be switched on and off by revealing

and concealing, respectively, a chiral organo-catalytically active amine built into a mechanically interlocked axle *via* simple protonation or deprotonation of the amine group.[57,58] Temperature may also be used as a means to control product enantioselectivity with a single switchable catalyst, as reported by Storch and Trapp, to direct asymmetric hydrogenation reactions upon catalyst epimerization.[59] The precise spatial control afforded by these dynamic molecular designs facilitates the integration of enzymatic behavior with mechanical motion, thus exemplifying the potential of small-molecule machines to perform useful tasks at the molecular level for applications ranging from catalysis to photopharmacology.[60]

Another ingenious example of leveraging fueled molecular motion for performing useful operations at the molecular scale is the sequence-defined synthesis of oligomer chains. In Nature, the polyribosome has been shown to have roles in both biosynthesis and protein assembly.[61] Utilizing the mechanically interlocked nature of rotaxanes, Leigh and co-workers designed a ribosomal mimic that travels along a molecular strand to assemble amino acids iteratively by native chemical ligation (Figure A.4).[62] Once assembled, the rotaxane-based machine is activated by acidic cleavage of protecting groups on the macrocycle, allowing its movement along the strand bearing amino acid building blocks. A bulky terminal-blocking group on one end of the strand facilitates unidirectional dethreading once all amino acids have been sequentially added to the macrocycle. Although the reaction kinetics remain slow (the formation of each amide bond takes approximately 12 h), the modular desig n and new threading protocol in machine preparation offer the possibility of analogous molecular synthesis from other monomer types and the employment of longer oligo- or polymer tracks.[63]

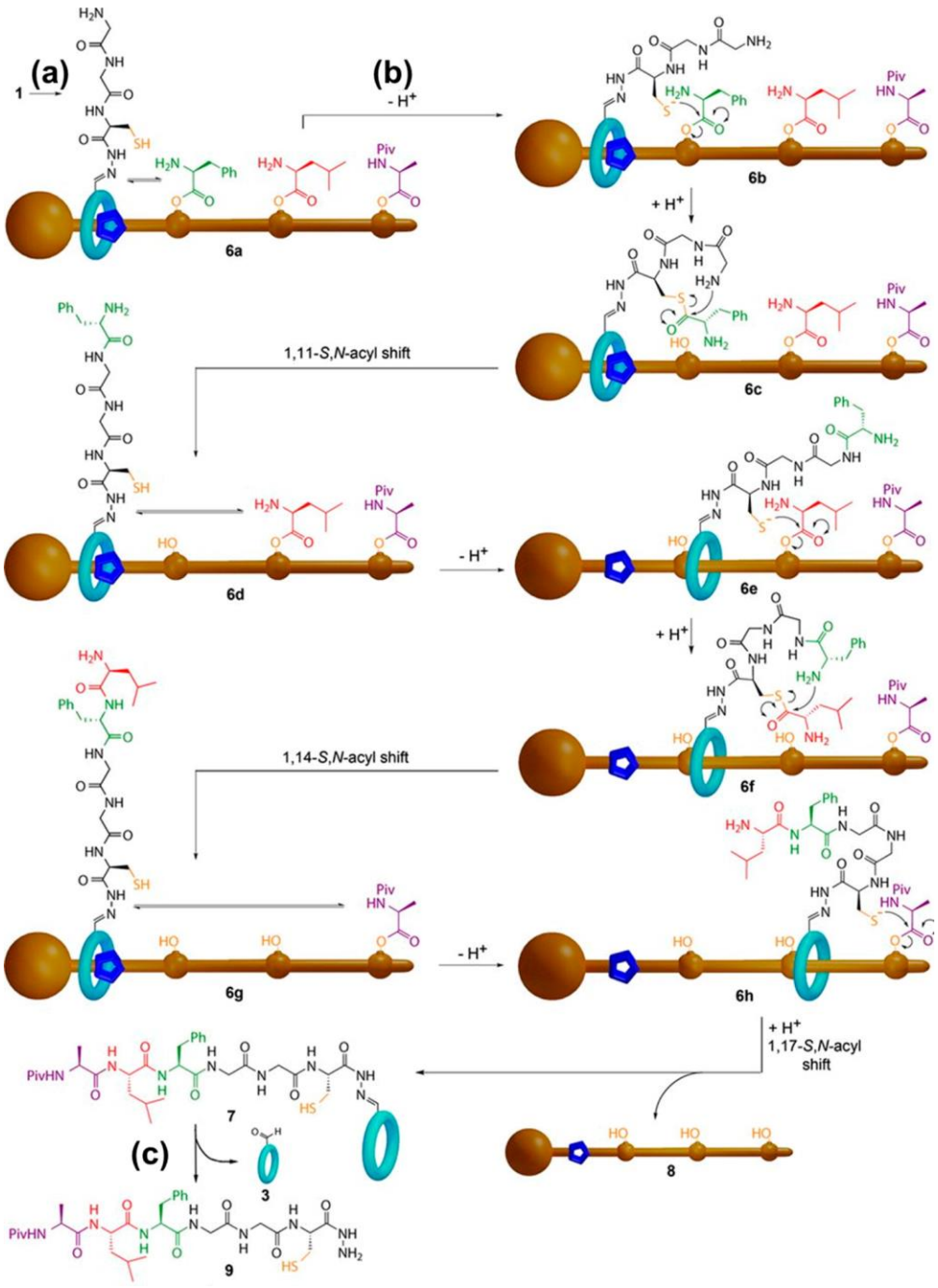

Figure A.4. Scheme depicting the proposed mechanism for sequence-specific oligopeptide synthesis using a rotaxane-based molecular machine. (**a**) Machine is activated upon removal of protective groups from the macrocycle. (**b**) Under basic conditions, the amino acid moieties that are tethered to the rod-like component are sequentially transferred to the macrocycle as it unidirectionally dethreads from the rod. (**c**) Macrocycle can then be subsequently hydrolyzed to obtain the isolated oligopeptide-containing motif. The stimulated, directed motion facilitates small-molecule synthesis by a molecular machine through the intelligent functionalization of the cyclic host and threading strand. Reproduced with permission from ref 62. Copyright 2013 American Association for the Advancement of Science.

A.B.3. DNA-Based Machines and Walkers

DNA-based nanomechanical devices such as tweezers and gears have also shown promise as artificial molecular machines, as demonstrated by the specificity and predictability with which these molecules can be modified.[64,65] Boosted by the advent of DNA origami, the advances in programmability of these devices have enabled rapid strides toward the design and operation of DNA machines.[66] These devices are engineered for a variety of applications including catalysis and the capture and release of targets ranging from single metal ions to large proteins.[67-69] Their motion may be actuated by the targets themselves, sacrificial staple strands or aptamers (synthetically designed DNA/RNA motifs), or light-utilizing oligonucleotide sequences chemically modified with photoswitching molecules such as azobenzene.[70-73] The recognition of targets by DNA or RNA devices that induce sophisticated secondary functions based on Boolean logic-gated mechanisms is particularly impressive, utilizing conjunction (AND), disjunction (OR), or negation (NOT) operations.[74] Logic-gate operations performed by DNA were demonstrated by Adleman and Lipton two decades ago, but DNA-based computing remains underdeveloped due to challenges associated with scale-up and slow reaction kinetics.[75,76] Church and co-workers recently designed a DNA nanorobot composed of over 200 unique oligonucleotides and capable of delivering payloads such as antibody fragments or nanoparticles to cells by incorporating an AND gate based on two locking aptamer-complement duplexes (Figure A.5).[77] Upon simultaneous recognition of their targets, the duplexes dissociate and the nanorobot undergoes a structural rearrangement to expose the sequestered payloads. While the implementation of such complex proof-of-principle nanorobots *in vivo* is not likely in the near future, analogous logic-gated target discrimination may be advantageous in the design of molecular devices for

future biomedical applications such as drug delivery and gene therapy, as well as sensing and computation.[73,78-80]

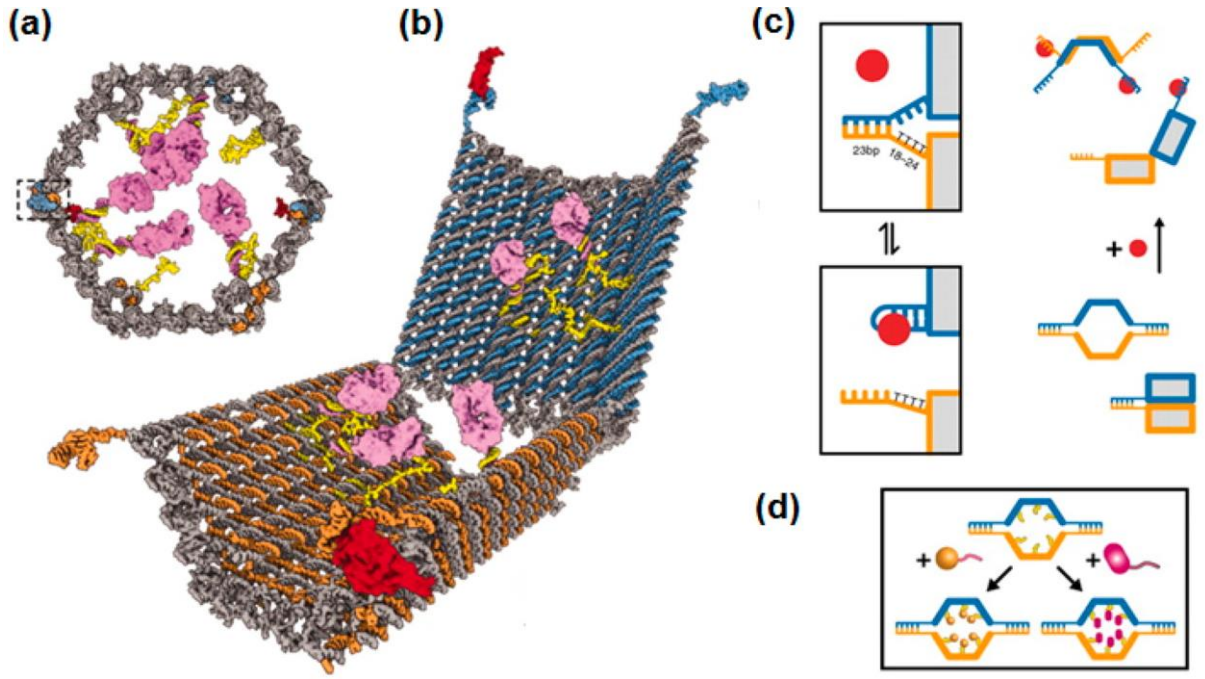

Figure A.5. Design of a logic-gated DNA nanorobot. (**a**) Front and (**b**) perspective view of a DNA nanorobot loaded with a protein payload (pink). The boxed area denotes one of the two aptamer locks that clasp the front of the nanomechanical device. (**c**) Aptamer-based gate is composed of an aptamer (blue) and a partially complementary DNA strand (orange). The "open" configuration can be stabilized by an antigen key (red circle). (**d**) Payloads including gold nanoparticles (gold) or small proteins (magenta) may be tethered inside the nanorobot. The DNA-based nanomechanical device enables the loading and cell-specific delivery of various cargo that utilizes an AND gate: both aptamer-based lock sites must be unlocked with their antigen key for the nanorobot to open. Reproduced with permission from ref 77. Copyright 2012 American Association for the Advancement of Science.

Inspired predominately by biological motor proteins from the kinesin, dynein, and myosin families, clever DNA walkers have been designed to enable progressive movement along prescripted tracks.[81-84] Numerous strategies have been employed to facilitate directional movement including the incorporation of Brownian ratchet and enzymatic

"burnt bridge" mechanisms, asymmetric molecular design, and the use of chemically modified architectures containing azobenzene that initialize walking upon photoisomerization.[85-88] These walkers may behave autonomously or require external intervention; the latter most often enables greater complexity in programmability. Some of the first remarkable reports of functional DNA walkers utilized stepwise mechanics to design systems capable of synthesizing organic molecules or donating cargo.[89,90] In a more recent example, Choi and co-workers described the fueled, autonomous translocation of CdS nanocrystal cargo by a single-stranded RNA-cleaving DNA enzyme over 3 μm along a RNA-decorated carbon nanotube track while demonstrating robust control over stopping and starting the walker (Figure A.6).[91] These proof-of-principle designs for DNA walkers show promise for DNA-based circuits, nanorobotics, and cargo transport, supported by quantitative control over rates for complementary strand displacement reactions.[92,93] Still, these complicated mechanical systems have generally been plagued by slow kinetics and poor overall performance. The operational yields of complementary strand hybridization or displacement reactions that facilitate the progressive and repetitive movement of many DNA walkers are generally lower than the elementary reactions that take place outside the context of complex DNA architectures.[94] Considerable effort has been directed toward improving the operational yield of DNA walkers to improve reliability, motility, and control by targeting various parameters that influence their mechanics.[95,96] For example, Nir and co-workers recently demonstrated a two orders of magnitude increase in the operational yield of a DNA walking device through mechanistic investigation of oligonucleotide strand fuel removal and fuel addition reactions to prevent undesirable trapped states.[97] Nevertheless, further improvements in walking speed, yield, and fuel optimization may be necessary for

efficient and practical transport and assembly of molecular and nanoscale cargo. Maintaining autonomy with increasingly complex programmability in the design of walkers and tracks is a challenging task but will help DNA walkers move beyond the initial steps that have been taken to convert these nanomechanical devices into useful machines.[98,99]

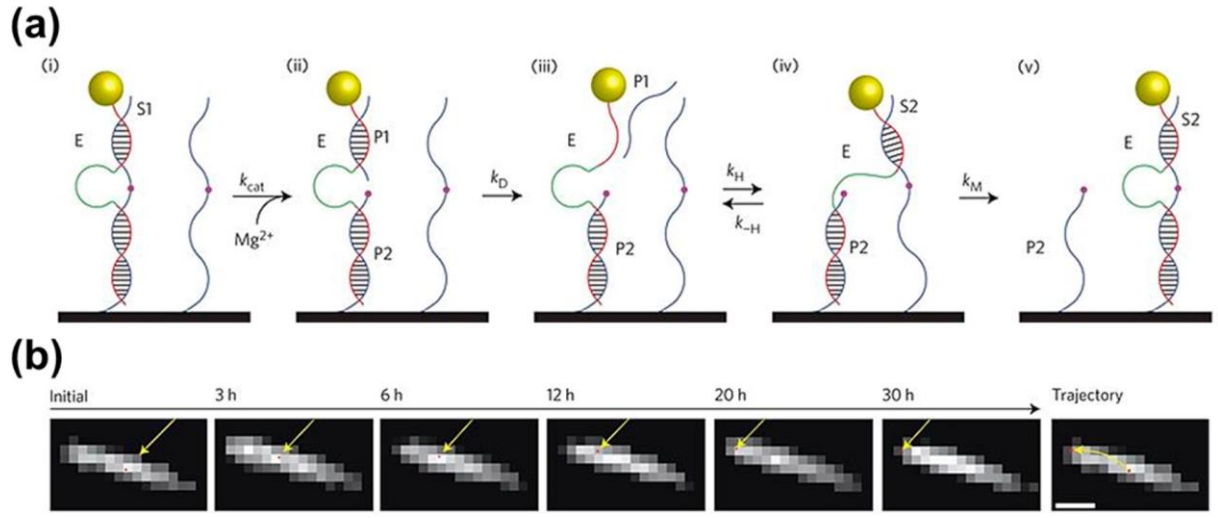

Figure A.6. (**a**) Schematic of a DNA enzyme-based molecular machine that walks autonomously along a RNA-functionalized carbon nanotube track (black) carrying a CdS nanoparticle (yellow). The DNA enzyme (E) here is a synthetic oligonucleotide sequence that contains recognition regions (red) and a catalytically active sequence (green) that cleaves an associated RNA molecule (S1) in the presence of Mg^{2+}. Upon cleaving S1, the DNA enzyme processes through a series of conformational changes to hybridize with another RNA molecule (S2) attached to the carbon nanotube, facilitating its movement along the track as the process is repeated. (**b**) Series of overlaid fluorescence microscopy images (to determine CdS position) and near-infrared nanotube images over 30 h in the presence of Mg^{2+}. Scale bar, 2 μm. The DNA motor is capable of carrying inorganic cargo with a maximum velocity of ca. 0.1 nm s^{-1}. The noninvasive optical measurements used here are ideal for monitoring the real-time, *in situ* motion of cargo-carrying DNA walkers and may be applied to other systems for the characterization of various parameters that influence walker motility. Reproduced with permission from ref 91. Copyright 2014 Nature Publishing Group.

A.B.4. Nanostructure Functionalization

The intelligent functionalization of larger organic or inorganic nanostructures with small molecular switch and rotor components, as well as complex DNA assemblies, further expands the versatility of these dynamic systems for applications such as drug delivery and to tune the chemical and physical properties of the hybrid materials.[100,101] Exemplary demonstrations of artificial molecular machinery that employ functionalized nanostructures are mesoporous nanocrystals modified with molecular nanoimpellers, valves, or gates for the capture and release of cargo with external control.[102] Numerous switch motifs have been utilized as gatekeepers to control payload release from these versatile materials including rotaxanes,[103] pseudorotaxanes,[104,105] DNA molecules,[106,107] coumarins,[108,109] and azobenzenes.[110,111] Besides the necessity for biocompatibility, tissue specificity, and high loading capability, to implement these systems *in vivo* for biomedical applications such as controlled drug release, noninvasive actuation mechanisms are also required because some stimuli may be detrimental to biological environments.[112] In a recent example, a nanoimpeller system developed by Croissant *et al*. utilizes azobenzene photoisomerization as a driving force to release the anticancer drug camptothecin from mesoporous silica nanoparticles (Figure A.7).[113] Contrary to classic designs in which azobenzene *trans* to *cis* isomerization is triggered by ultraviolet (UV) light, which is harmful to living cells, this prototype system is based on two-photon excitation (TPE) of a fluorophore with near-infrared (NIR) light. The use of NIR light facilitates isomerization of the azobenzene moieties through Förster resonance energy transfer (FRET) from a nearby fluorophore. Isomerization of the azobenzene nanoimpellers subsequently kicks out the camptothecin cargo, leading to cancer cell death *in vitro*. Using TPE with NIR light to trigger drug release from mesoporous

nanoparticles has not yet been extensively explored but offers the benefits of deeper tissue penetration in the biological spectral window (700–1000 nm) and lower scattering loss.[114,115] The TPE-based designs illustrate how the actuated mechanics of photoswitches can be tailored by their immediate surroundings by coupling simple switches or rotors to their nanostructured environment, provided that the fluorophores have large two-photon absorption cross sections and sufficient emission quantum yields (>0.5) for FRET.

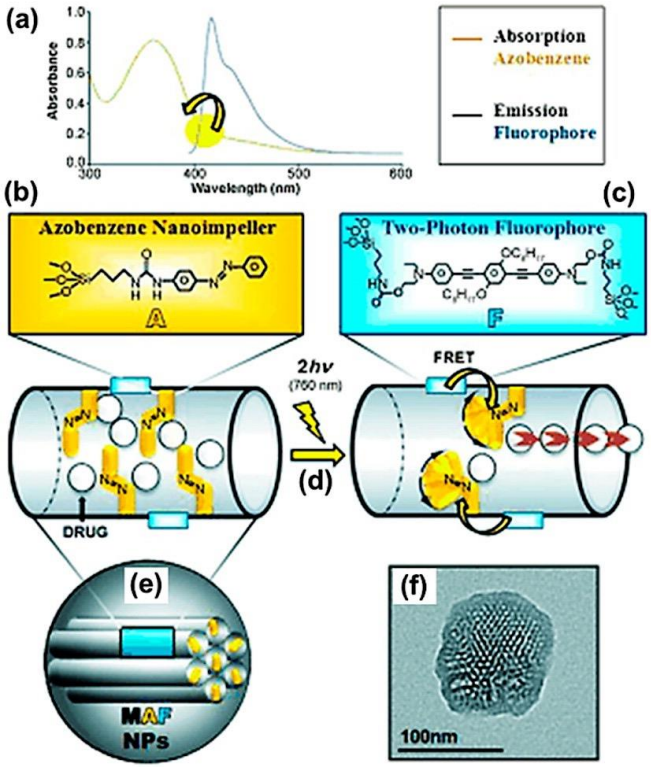

Figure A.7. Two-photon excitation (TPE) of a fluorophore to facilitate Förster resonance energy transfer (FRET) to photoizomerize azobenzene nanoimpellers on mesoporous silica nanocrystals and subsequent cargo release. (**a**) Overlap of the emission spectrum of the fluorophore and absorption spectrum of the azobenzene nanoimpeller enables FRET. (**b**) Structure of the azobenzene moiety. (**c**) Structure of the two-photon fluorophore. (**d**) Photoisomerization of azobenzene using two-photon (760 nm) excitation of the fluorophore. (**e**) Schematic of the mesoporous silica nanocrystal. (**f**) Transmission electron microscopy image of a single nanocrystal. Light-activated nanovalves that utilize near-infrared irradiation such as this TPE-based mechanism show promise for targeted drug delivery applications and should be further explored to extend their scope. Reproduced with permission from ref 113. Copyright 2013 Wiley.

The integration of switchable molecular systems with inorganic nanostructures and nanoparticle assemblies also enables the manipulation of the hybrid material's optical properties *in situ*. Two common methods to direct the optical properties of nanostructured materials are the active tuning of refractive indices at the surface of plasmonic nanoparticles functionalized with switchable molecules[116-118] and physically modulating interparticle distances or orientations.[119-123] Using the latter strategy, Willner and co-workers have designed a myriad of hybrid DNA-based tweezers, catenanes, and rotaxanes functionalized with gold nanoparticles or quantum dots, whose interparticle distances can be directly manipulated with stimuli including pH, metal ions, and oligonucleotide strands.[124] The switchable mechanical control over these hybrid assemblies is accompanied by unique spectroscopic features as a result of plasmonic coupling between gold nanoparticles, chemiluminescence resonance energy transfer between quantum dots, or the photoluminescent properties of attached fluorophores.[125-127] Increasing the modularity and dimensions of DNA-based nanomechanical assemblies in this manner has enabled exceptional function; still, challenges remain as the increases in size and complexity of devices may be accompanied by lower synthetic yield and product heterogeneity.[128,129]

A.C. Increasing Dimensionality and Hierarchical Organization

A.C.1. Linear Assemblies

The actuated inter- or intramolecular motion of small individual switch and rotor components occurs on the Ångström to nanometer scales. In order to perform macroscopic work, it would be useful to harness the synchronized mechanics of ordered ensembles of molecules in which the collective action translates into motion orders of magnitude larger

than that of individuals. This hierarchical organization is exemplified by skeletal muscle tissue. Sarcomeres, the basic repeating units throughout muscle cells, are composed of interdigitated myosin and actin filaments. The sliding of actin along myosin is facilitated by the walking of globular motor proteins attached to cross-bridges between the filaments. This motion generates tension and is responsible for the linear contraction and expansion of each sarcomere.

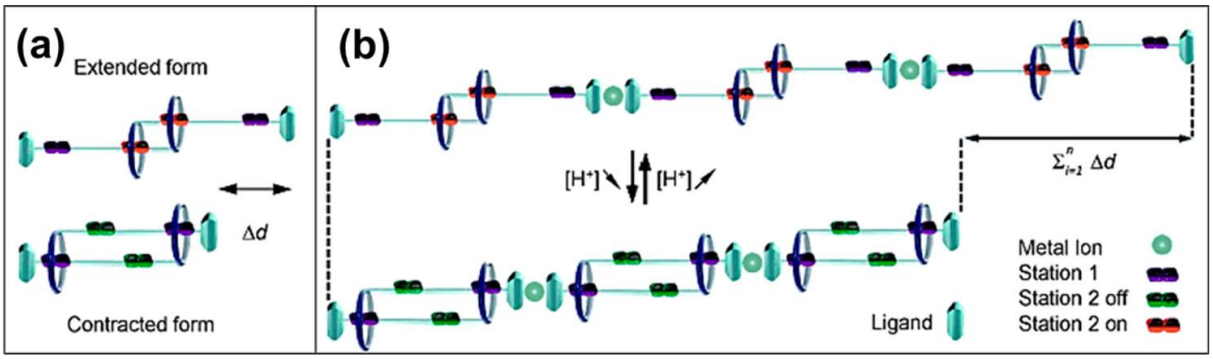

Figure A.8. (**a**) Bistable daisy-chain rotaxane. (**b**) Metallo-supramolecular polymer of multiple pH-switchable daisy-chain rotaxanes. The culmination of contraction or extension by individual monomers results in global changes in large contour length of the polymer on the order of microns. Reproduced with permission from ref 138. Copyright 2012 Wiley.

Analogously, MIMs exhibit practical architectures for the building blocks of synthetic molecular muscles due to their mechanostereochemistry.[130] In particular, bistable daisy-chain rotaxanes, which are composed of two interlocked cyclic dimers, display muscle-like contraction and expansion upon switching (Figure A.8a). Many stimuli may be used to actuate motion in these efficient and versatile switches including pH, redox reactions, light, solvent, and ions.[131-135] Efforts have been made to polymerize daisy-chain rotaxanes into linear assemblies with varying success.[136,137] In one of the most remarkable examples, Giuseppone, Buhler, and co-workers demonstrated a metallo-supramolecular

polymerization process to combine thousands of pH-switchable daisy-chain rotaxanes.[138] The polymers demonstrated global changes of contour length of approximately 6 μm (Figure A.8b). This contraction is on the same order of magnitude as that observed in sarcomeres. Subsequently assembling these chains into ordered fibers and bundles similar to the hierarchical assembly of sarcomeres in myofibrils and their attachment to surfaces will be a significant accomplishment toward enhanced engineering of artificial muscles from small switch components.

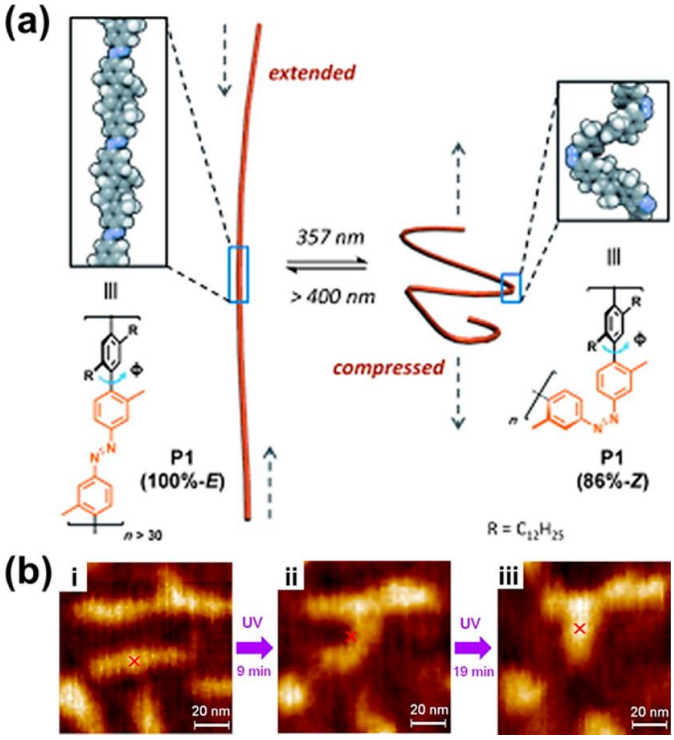

Figure A.9. (**a**) Schematic of a main-chain azobenzene-containing polymer (P1; R = $C_{12}H_{25}$) with a poly(para-phenylene) backbone. Irradiation with UV or visible light facilitates photoisomerization of azobenzene and conversion to the compressed and extended conformations, respectively. Reproduced with permission from ref 141. Copyright 2011 Wiley. (**b**) Scanning force microscopy images of P1 deposited on a modified graphite surface. The polymer crawls along the surface as it contracts upon UV irradiation. Demonstrating control over movement direction, and the functionalization or tethering of the polymer strands to scaffolds may enable the macromolecules to perform work by lifting weights or transporting cargo. Reproduced from ref 142. Copyright 2014 American Chemical Society.

Another molecular switch motif that holds promise for artificial muscles through linear polymerization is the azobenzene chromophore. By incorporating azobenzene within the main chain of a linear assembly, the culmination of modest dimensional changes of merely a few Ångströms for each chromophore can result in dramatic changes in the contour length of the polymer. Utilizing this strategy, Gaub and co-workers demonstrated the capability of individual polyazobenzene peptides to perform mechanical work by tethering one end of the chain to a substrate and the other to a flexible cantilever to measure the force exerted by the contracting polymer upon photoisomerization.[139] The extent of polymer deformation, and thus the usefulness of the molecules for optomechanical applications, depends on both the conformational rigidity of the backbone and minimization of electronic coupling between azobenzene moieties.[140] The synthesis of rigid-rod polymers that include azobenzene within a poly(para-phenylene) backbone is one strategy to maximize photodeformation, enabling accordion-like compression and extension of chains upon cycling with UV and visible light (Figure A.9a).[141] Lee *et al*. demonstrated that these single-chain polymeric assemblies may even exhibit crawling movements when deposited onto an octadecylamine-modified graphite surface and imaged with scanning force microscopy (Figure A.9b).[142] Chemically or physically cross-linked supramolecular assemblies of these linear photomechanical polymers may be envisioned to behave as actuators, to lift weights, and to perform other types of work with greater resistance to deformation fatigue than individual strands.[143] For example, Fang *et al*. reported using a simple melt spinning method to fabricate hydrogen-bonded cross-linked fibers of azobenzene-containing main-chain polymers that were prepared *via* a Michael addition reaction (Figure A.10).[144] The authors also investigated the photoinduced mechanical properties of the fibers, reporting a

maximum stress generated by a single fiber of 240 kPa upon UV irradiation at 35 °C. This force is similar to the maximal tension forces of some chemically cross-linked azobenzene-containing polymer fibers and even human striated muscles (*ca.* 300 kPa).[145]

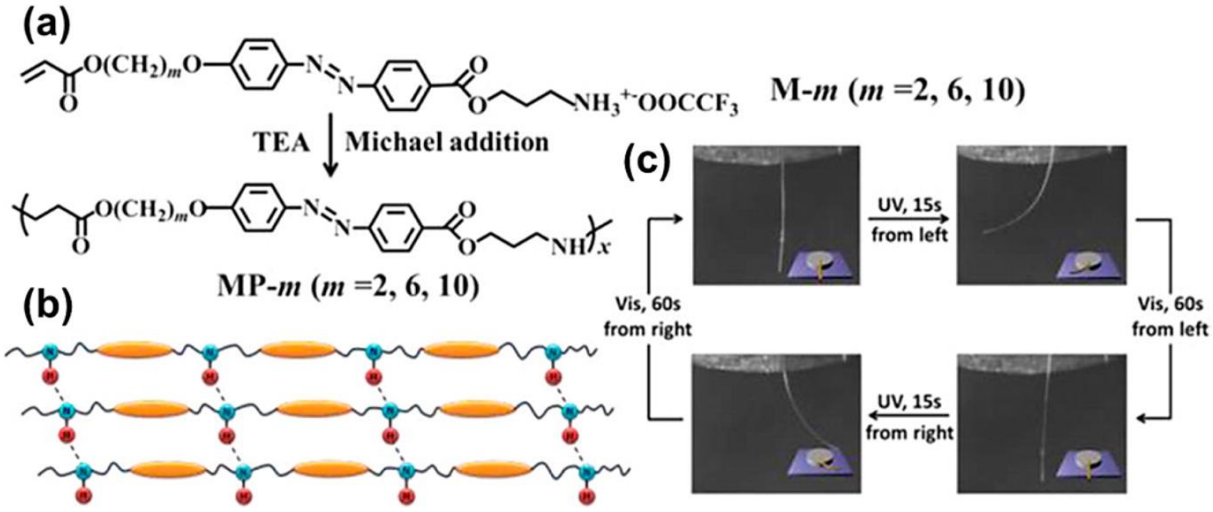

Figure A.10. (**a**) Synthetic route and chemical structures of acrylate-type azobenzene monomers. (**b**) Supramolecular hydrogen-bonding interactions between main-chain polymers to facilitate physical cross-linking. (**c**) Photographs of a polymeric fiber fabricated by simple melt spinning. The fiber reversibly bends upon irradiation with UV and visible light. The fibers demonstrate robust photodeformation fatigue resistance and high thermal stability and show promise for applications as photomechanical actuators. Reproduced from ref 144. Copyright 2013 American Chemical Society.

A.C.2. Two-Dimensional Assemblies and Surface Functionalization

The aforementioned systems describe molecular switches, rotors, and motors in relative isolation. However, without a suitable frame of reference, even the contraction and extension over dramatic micron length scales by polymerized chains of functional rotaxanes is difficult to utilize for practical applications. Complicating matters, to leverage the mechanical motion of ensembles of molecules, some director is mandatory to overcome the chaotic application of force. Similar to Archimedes' need for a place to stand to move the Earth, a surface may be

utilized to instill directionality to harness the power of large numbers of molecular machines. Two-dimensional coverage by molecular switches and rotors on planar surfaces provides advantages over isolated molecules or functionalized nanoparticles by facilitating the manipulation of physical and chemical properties of a material at the micro-, meso-, and macroscales. For example, through the amplification of collective molecular mechanical motion, the integration of small-molecule switches and rotors into ordered arrays has resulted in dynamic control over work function, refractive index, and surface wettability.[146-150] In more obvious demonstrations of performing work, the cumulative nanoscale movements of stimuli-responsive rotaxanes assembled on metal surfaces have been harnessed to move liquid droplets uphill or to bend flexible microcantilever beams.[151-155] Micropumps that are capable of establishing a steady flow of liquid or small particles may also take advantage of surface functionalization by molecular machines for microfluidics or drug delivery.[156] Molecular pumps based on host–guest interactions composed of cyclodextrin and azobenzene designed by Sen and co-workers perform such a function by external stimulation with light.[157] These hybrid systems are organized within gels or adsorbed directly on glass substrates (Figure A.11a,b). Upon UV light absorption, azobenzene molecules isomerize and leave their cyclodextrin hosts. The created cavity is then promptly filled with water molecules. The amplified and collective actions of the multitude of neighboring pumps creates a steady flow of fluid around the surface at the rate of *ca*. 2 μm/s (Figure A.11c,d). The pump can also be activated by chemical stimuli and recharged by visible light irradiation. Despite these impressive examples, there exist few reports of integration of molecular switches and rotors in planar assemblies because of the challenging design rules that accompany surface functionalization, as described below.

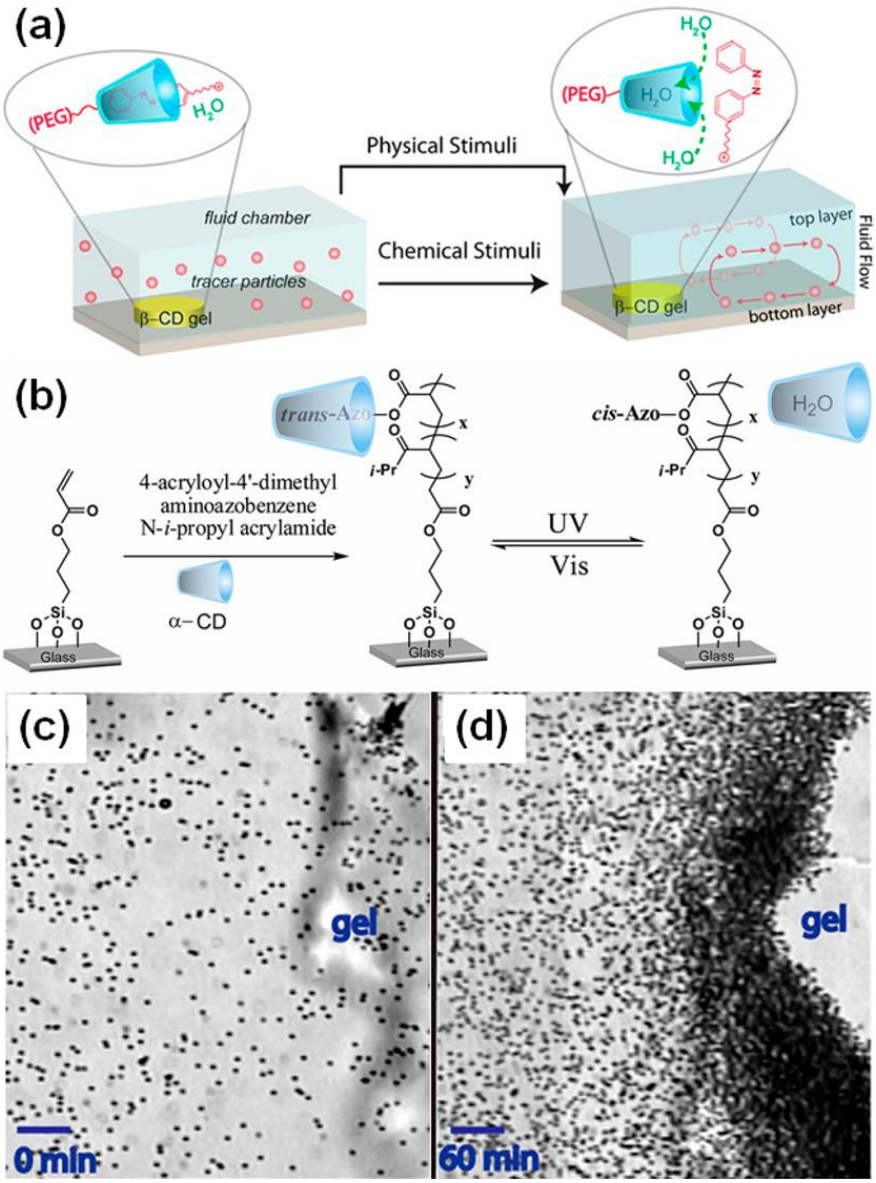

Figure A.11. (**a**) Schematic of a dual-responsive micropump on a glass surface. Light or chemical stimuli may be used to induce fluid flow by a β-cyclodextrin–polyethylene glycol (β-CD-PEG) gel upon isomerization of the azobenzene moiety. (**b**) Schematic of the direct functionalization of glass surfaces by covalently tethering azobenzene-containing molecules. Reversible formation or disassociation of the host/guest complex with α-cyclodextrin results in fluid pumping. (**c**) Optical microscopy image of tracer particles in solution above a β-CD-PEG gel on a glass surface before irradiation. (**d**) Optical microscopy image of tracer particles accumulating at the edge of a β-CD-PEG gel after irradiation with UV light for 1 h. Scale bars, 50 μm. The reversibility of the host/guest interaction makes the design particularly appealing for rechargeable microdevices. Reproduced from ref 157. Copyright 2013 American Chemical Society.

Self-assembled monolayers (SAMs), Langmuir–Blodget (LB) films, and layer-by-layer (LbL) assemblies are all well-understood organic thin-film technologies that can be utilized to fabricate nanoscale functional surfaces.[158-160] Within SAMs, intermolecular distances, molecular orientation, and substrate–molecule interactions strongly influence whether assembled switches and rotors retain their functionality due to the varied chemistries of their interfaces.[161,162]

Physically and electronically decoupling these functional moieties from surfaces or from neighboring molecules is often necessary to avoid steric constraints or quenching of excited states.[163-168] For example, molecular rotors can be tethered such that the axis of rotation is aligned parallel or perpendicular to the surface, in either altitudinal or azimuthal orientations, respectively. Feringa and co-workers reported the tunable and reversible wettability of gold surfaces modified with SAMs of altitudinal rotors based on light-driven overcrowded alkenes bearing perfluorinated alkyl chains (Figure A.12a).[169]

Taking advantage of unhindered rotation enabled by the superior altitudinal orientation of the rotor units dramatically modified the surface energy with resulting water contact angle changes of as much as 8–22° owing to differences in the orientation of the hydrophobic perfluorobutyl group (Figure A.12b). The photoconversion efficiency and rotation speed of these surface-bound rotors are still generally lower than for free molecules in solution, highlighting how proper spatial arrangement and sufficient room to rotate are necessary parameters to optimize for these dynamic molecular motifs to retain their large-scale functionality.[170]

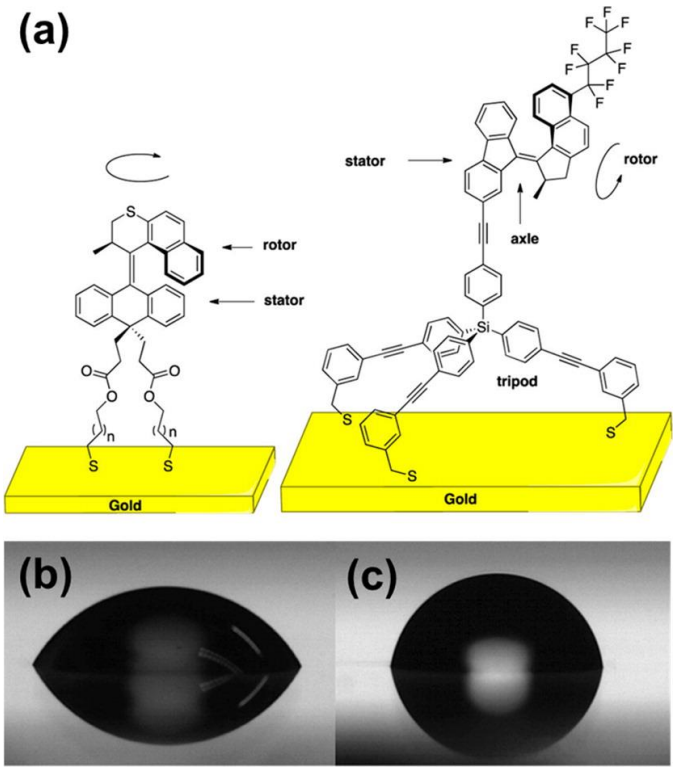

Figure A.12. (**a**) Molecular rotors based on overcrowded alkenes attached to a gold surface in azimuthal (left) and altitudinal (right) orientations. (**b**) Water droplet on a gold surface functionalized with self-assembled monolayers of overcrowded alkenes in the *cis* conformation bearing perfluorinated alkyl chains. The hydrophobic perfluorobutyl group on the rotor is hidden from the interface, resulting in a contact angle of 60 ± 1°. (**c**) In the *trans* conformation, the hydrophobic group is exposed to the interface, resulting in a water contact angle of 82 ± 1°. The altitudinal orientation of the rotor and the tripod tethering unit are advantageous molecular structures that may be applied to other functional surfaces based on self-assembled monolayers of molecular machines. Reproduced from ref 169. Copyright 2014 American Chemical Society.

The design rules to retain functionality and to understand substrate–molecule and intermolecular interactions of MIMs that self-assemble on surfaces are not as well understood. Rotaxanes may be covalently modified with thiol or disulfide tethers to enable binding to noble metal surfaces, providing a platform for potential applications in diverse areas including molecular-scale electronics and nanoelectromechanical systems.[152,154,155,171] However, many rotaxane and pseudorotaxane motifs have poorly defined orientations or conformations when tethered to surfaces due to their flexibility, making it difficult to predict

conditions for reproducible self-assembly.[168] Heinrich *et al*. recently demonstrated that tight packing may be advantageous for the efficient switching of many rotaxane molecules on the surface (Figure A.13a).[172] The authors used angle-resolved near-edge X-ray absorption fine structure (NEXAFS) spectroscopy to study cooperative effects in chemically switchable rotaxanes deposited on gold surfaces by LbL self-assembly. Linear dichroism effects in NEXAFS spectra reflect preferred ensemble molecular orientation, and therefore, the disappearance or enhancement of linear dichroism may be used to monitor conformational changes on surfaces. Densely packed monolayers of rotaxanes exhibited a pronounced increase in linear dichroism upon switching, indicating conversion of one ordered surface structure into another (Figure A.13b). On the other hand, dilute monolayers in which the rotaxanes motifs were less densely packed displayed negligible linear dichroism effects both before and after application of chemical stimuli (Figure A.13c). These results suggest that, in this system, properly designed densely packed rotaxanes can switch in a coupled manner, in contrast to previous reports of interference of proximal, randomly assembled surface-bound rotaxanes.[168] While inducing conformational change in a single rotaxane is unfavorable in the densely packed array, once a small number of molecules have converted to their isomeric forms, it becomes less sterically demanding for neighboring molecules to switch, resulting in rapid growth of newly ordered domains. This cooperative switching scenario is analogous to that observed in densely packed SAMs of molecules containing azobenzene headgroups.[173,174] Applying similar design principles to other assemblies of switch and rotor motifs on surfaces to facilitate cooperative switching mechanisms would be advantageous for faster, more robust, and more energy-efficient molecular machines.

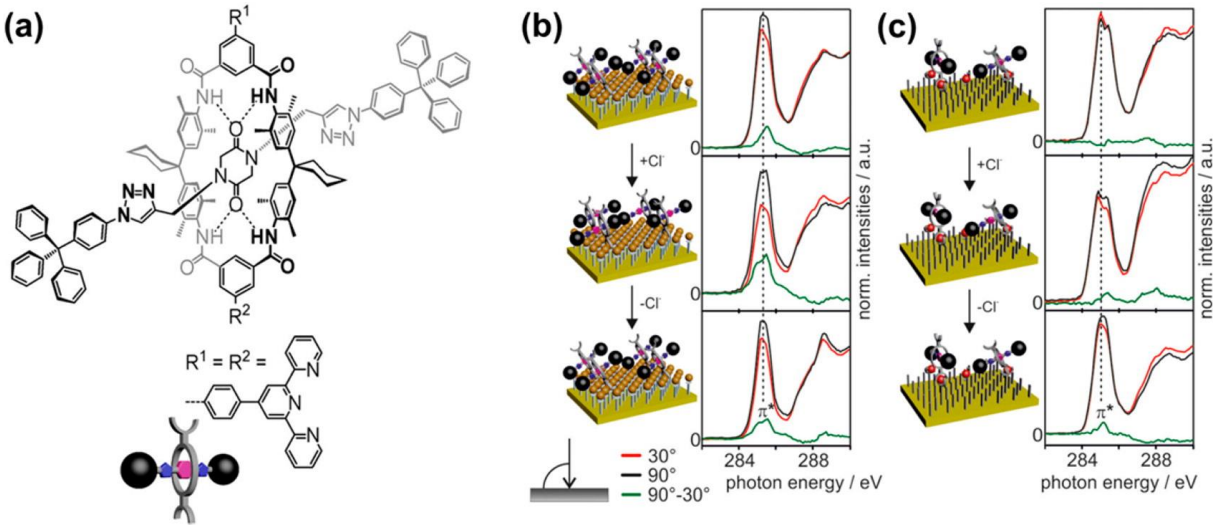

Figure A.13. Molecular structure and angle-resolved near-edge X-ray absorption fine structure (NEXAFS) spectroscopy of layer-by-layer assembled chloride switchable rotaxanes on gold surfaces. (**a**) Rotaxane molecule under investigation containing tritylphenyl stopper groups on the rod and terpyridine side chains attached to a functionalized tetralactam macrocycle. Angle-resolved NEXAFS spectra of (**b**) a densely packed rotaxane monolayer on a rigid pyridine-functionalized self-assembled monolayer (SAM) of (*E*)-4-(pyridin-4-yl)stilbenethiol (PST) and (**c**) a dilute rotaxane monolayer on a terpyridine-terminated dodecanethiol/decanethiol mixed SAM. The NEXAFS results are depicted from top to bottom: before chloride addition, after chloride addition, and after chloride removal. NEXAFS spectra were obtained for the incident synchrotron light beam at 30 and 90° angles (red and black lines). The difference between the two spectra is shown in green. Linear dichroism effects in (**b**) suggest the coupled motion of densely packed rotaxane monolayers, underscoring the advantage of lateral order and molecular alignment for functional surfaces based on large mechanically interlocked molecules. Reproduced from ref 172. Copyright 2015 American Chemical Society.

As described above, the design and fabrication of organic thin films of molecular switches or rotors on surfaces that retain switching yields comparable to those of free molecules in solution remain challenging tasks. Complicating matters, the favored molecular orientations, steric considerations, and intermolecular electronic coupling strengths are different for each system, whether the molecules are chemically adsorbed directly on surfaces or within polymeric assemblies. Nevertheless, the successful demonstrations of predictable surface attachment of molecular machines that give rise to directed and defined stimulus-induced function provide promising examples for applicability in the future. New

directions may take advantage of combining bottom-up molecular assembly techniques with top-down patterning methods to design novel materials with controllable features from sub-100 nm to the centimeter scale.[175-179] Patterning diverse switch and/or rotor components side-by-side with precise two-dimensional control may give rise to new surface functionality with molecular packing density gradients or multiplexed domains with various available actuation mechanisms.

A.C.3. Three-Dimensional Assemblies and Crystals

The integration of dynamic molecular switches and rotors into three-dimensional architectures is a natural and desirable extension of supramolecular assemblies, yielding dynamic materials with controllable properties in all directions. Some of the first three-dimensional molecular machines were fashioned from polymeric materials or photomobile crystalline arrays, such as light-powered walkers, rollers, and belt/pulley motors by Yamada *et al*.[180,181] These examples utilized azobenzene moieties within liquid-crystalline elastomers, in which mechanical strain is strongly correlated with the characteristic orientational order of the mesogens. The incorporation of photoswitching molecules into liquid-crystalline polymer networks enables the amplification of, and greater control over, the reversible photodeformation of actuators. Notable advances in the field of photomechanical polymers include the development of more complex movement patterns, designs that respond to a broader range of stimuli, and better addressability and spatial precision.[182-184] Katsonis and co-workers recently described impressive control over the helical motion of azobenzene-containing liquid-crystalline polymer springs, mimicking the extensile function of plant tendrils.[185] Unlike previous reports of twisting motion within

photomechanical crystalline systems, in which the helical deformations are dictated by the facets that are irradiated with UV or visible light, the handedness and modes of coiling motion can be preprogrammed by including chiral dopants and controlling the relative orientation of the aligned liquid crystals within each spring, respectively.[186]

While polymeric materials offer ease of processing and fabrication, crystalline motifs offer a path to near-perfect three-dimensional arrangements of dynamic molecular building blocks, as well as a facile means to monitor the motion of the crystals using nuclear magnetic resonance (NMR) and X-ray diffraction. Furthermore, energy transduction in crystals is faster, and actuating motion is generally of larger magnitude compared to polymeric assemblies because rigidly packed molecules have to work as an assembly to function, whereas in a less-ordered medium, motion of the same molecular switches may be less directionally biased and ultimately less efficient. Often derided as a "chemical cemetery" after Leopold Ruzicka's famous remark, crystal machines have witnessed a remarkable resurgence in recent years with discoveries of controlled or spontaneous actuation, reversible or irreversible movements, and reactivity.[187-189] Research efforts toward molecular machines fashioned from crystals can be subdivided into two broad classes: one in which movable elements are present in the crystal lattice and the other where the entire crystal becomes a machine.

The former class of crystalline machines is composed of amphidynamic crystals that most often incorporate rotors into a lattice, thereby maintaining macroscopic order. If enough free volume is present, the molecules retain their rotational degrees of freedom and can spin with varying frequencies within the range of hertz to gigahertz. Such rotation demonstrates promise as a new class of mechanical switches, compasses, and

gyroscopes.[190-194] When the rotor units contain an electric dipole, amphidynamic crystals may also provide an avenue for tunable dielectrics.[195-197] Solid-state NMR techniques are useful characterization methods to determine molecular order and the gyroscopic dynamics within amphidynamic crystals when rotors contain atoms that occupy multiple magnetically nonequivalent sites. As a molecule rotates, atoms may exchange positions between these sites, the rate of which is determined by the rotational potential energy barrier and sample temperature.[198] Features in the NMR spectra at different temperatures provide information about ensemble exchange rates and, therefore, rates of rotation of rotors within the crystalline lattice. Spontaneous rotation is common in crystalline rotors with rotational activation energy barriers greater than k_BT (the available thermal energy). Notable studies in this field have reported on engineering coupling between rotors[199-201] and controlling the rate of motion by light or chemical input, similar to the design of synthetic brakes for noncrystalline rotors.[202] Recently, Commins and Garcia-Garibay developed a molecular gyroscope that utilized a photoactive azobenzene unit tethered on either side of a rotatable phenylene center block (Figure A.14).[203] The conformation of the azobenzene switch was shown to exhibit robust control over the rates of phenylene rotation. When the azobenzene brake was in the *trans* conformation, the crystalline assembly rotated 10 times faster than samples containing the *cis* isomer.

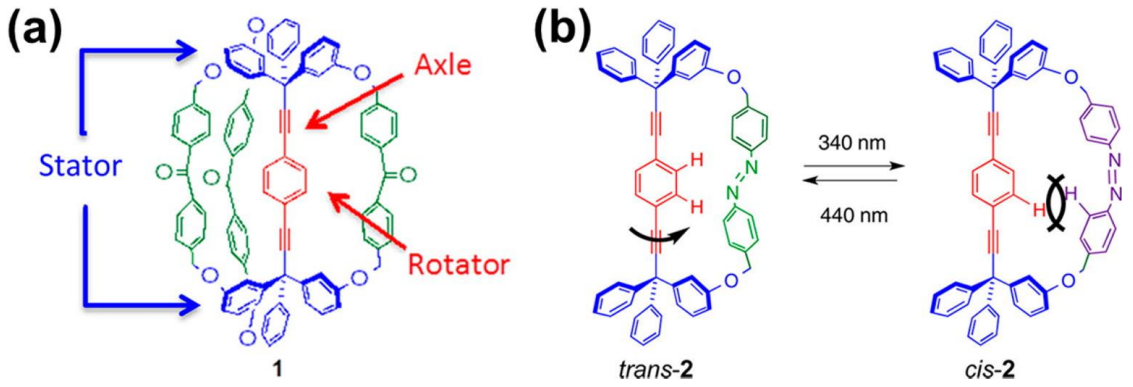

Figure A.14. (**a**) Molecular gyroscope that contains benzophenone motifs (green) that bridge the structure from one stator to the other. (**b**) Azobenzene-bridged molecular gyroscope. In (**a**) and (**b**), the rotation of the central phenylene may be hindered by collapse of the bridge toward the rotor. The use of an azobenzene motif as a bridge enables control over the rate of rotation using UV or visible light to convert the switch, or brake, between *trans* and *cis* conformations. Reproduced from ref 203. Copyright 2014 American Chemical Society.

Sozzani and co-workers demonstrated another sophisticated approach to engineer and to control crystalline rotors using porous molecular crystals.[204] The authors demonstrated that permanently porous crystals that incorporate *p*-phenylene rotors were accessible to small-molecule guests such as CO_2 and I_2 in the vapor phase. In particular, the uptake of I_2 altered the molecular environment of the rotors dramatically: the exchange rate decreased by four orders of magnitude from 108 to 104 Hz (Figure A.15). The same group also proposed using porous organic frameworks as hosts for molecular rotors due to their large surface areas and pore capacities.[205] Comparable to the molecular cocrystals, diffusion of I_2 into the pores resulted in decreased rotation rates by three orders of magnitude at room temperature. Sensing or actuating applications may be envisioned that utilize the resulting influence of small-molecule guests on the rotation rates for the uptake and release of small-molecule guests by these amphidynamic crystals and organic frameworks.

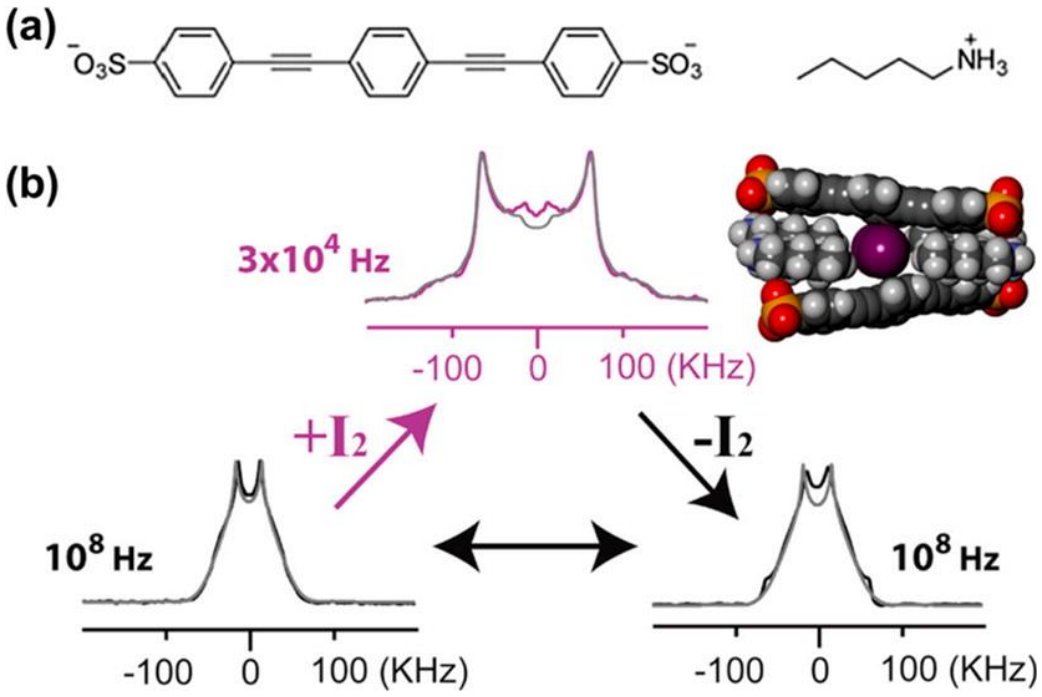

Figure A.15. (**a**) Chemical structures of the components of a porous cocrystal: (left) 4,4′-bis(sulfophenylethynyl)benzene (SPEB) dianion and (right) *n*-pentylammonium (PA) cation. (**b**) Deuterium nuclear magnetic resonance (^{2}H NMR) spectra of porous cocrystals in the absence of molecular iodine, I_2; after exposure to I_2 in the gas phase; and following removal of I_2 from the crystals. Experimental and calculated spectra are displayed in black or violet, and gray, respectively. The exchange rate reversibly decreased by four orders of magnitude upon uptake of the small-molecule guest, suggesting the use of such crystals for gas phase sensing applications. Reproduced from ref 204. Copyright 2014 American Chemical Society.

While the previously described amphidynamic crystals possess sufficient free volume for rotation of essential structural elements, translational motion within a crystal is much less common. By incorporating rotaxane molecules as organic linkers within a metal–organic framework (MOF), Loeb and co-workers recently succeeded in facilitating the reversible translation of a molecular shuttle inside a solid-state material between two stable states.[206] The system contains Zn_4O clusters as the nodes of the MOF and carboxylate struts as structural elements. Individual [24]crown-8 ether macrocycle shuttles could translate between degenerate benzimidazole stations on cross-bar linkers between struts at a rate of

283 Hz at room temperature. Future work to incorporate MIMs within highly dense, crystalline arrays with greater control over the actuation and speed of switching events will provide new potential applications for mechanically bonded host–guest systems with controllable physical and chemical properties in the solid state.

The second approach to fabricate crystalline molecular machines utilizes the entire crystal as an actuator and transfers the external stimulus such as light or heat into mechanical energy, categorized as (a) thermo- and photosalient or (b) photomechanical crystals.[188,184,207] Thermo- and photosalient crystals most often exhibit spontaneous actuation (jumping) upon heating or irradiation. Thermosalient crystals developed by Naumov and co-workers harness the energy of polymorphic transformations that occur upon heating in crystals. The effect is driven by extremely rapid anisotropic expansion and contraction of the unit cell axes upon a phase transition that was found to be 104 times faster than in regular crystal-to-crystal phase transformations.[208] This class of crystalline compounds comprises a diverse range of materials, including brominated organic molecules, terephthalic acid, and organometallic complexes.[209,210] Although there exists little directional control or foresight into which compounds will exhibit the effect, the explosive "popcorn" crystals nonetheless exhibit impressive centimeter-scale jumping movements that greatly exceed the crystal dimensions. Light-activated chemical processes within crystals, such as changes in the coordination sites of small ligands or [2 + 2] cycloaddition reactions, have also been shown to result in "popping" under ultraviolet irradiation.[211,212] Similar to thermosalient materials, little control is possible over "popping" crystals, and thus their utilization as functional molecular machines is difficult to envisage. To circumvent this problem, Sahoo *et al*. developed smart hybrid materials that incorporate thermosalient

microcrystallites on flexible sodium caseinate films to impart directionality to the crystals' movements.[213] The material represents a successful marriage of crystals with biocompatible polymeric films in one system, combining the benefits of the plasticity of soft polymers and the efficient, fast actuation of leaping crystalline solids.

Alternatively, photomechanical materials move, bend, twist, or curl when exposed to light. Some of the most promising photomechanical crystalline systems for converting light into mechanical work have been proposed by Irie and co-workers and are based on diarylethene photoswitches.[214] Light absorption triggers pericyclic ring-opening and ring-closing reactions of this photoswitch throughout the crystal and is responsible for expansion and contraction, respectively, of the unit cell that consequently leads to photomechanical bending of the crystal. Structural studies on crystals of diarylethene derivatives link the initial speed of curvature change to crystal thickness.[215] The bending behavior is also dependent on the crystallographic face that is irradiated, which is be attributed to differences in molecular packing. While the geometric change that occurs during the isomerization of a single diarylethene photoswitch is modest, the collective action of arrays of molecules in the crystal lattice can produce macroscopic motion. Cleverly engineered, such actuating crystals can perform work by pushing or lifting objects many times their weight,[214,216] rotating gears,[217] or acting as an electrical circuit switch (Figure A.16).[218]

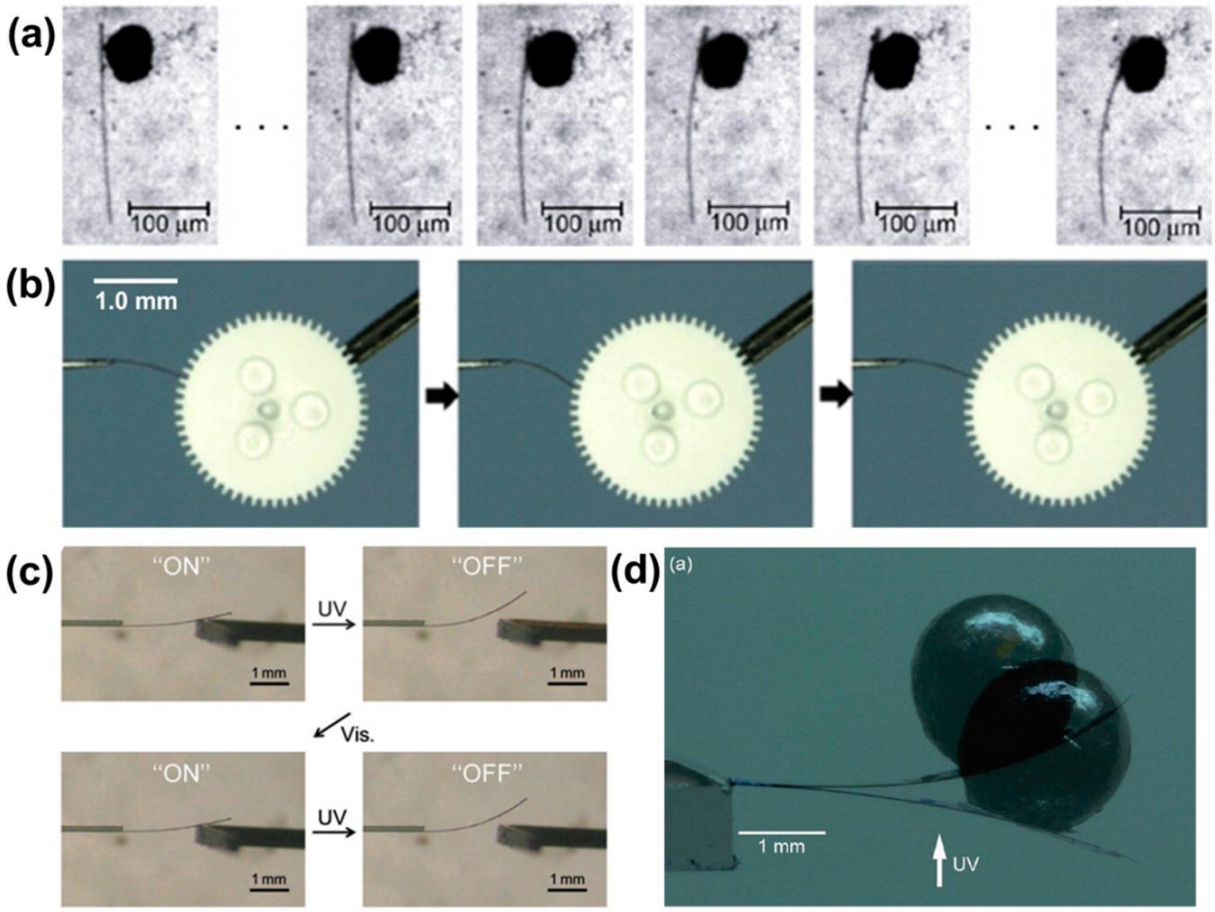

Figure A.16. Photomechanical systems based on diarylethene crystals that convert light into mechanical work. (**a**) Rod-like crystal pushes a gold microparticle that is 90 times heavier than the crystal when irradiated with ultraviolet (UV) light. Bending of the crystal pushes the microparticle up to 30 μm. Reproduced with permission from ref 214. Copyright 2007 Nature Publishing Group. (**b**) Rotation of gears facilitated by the reversible bending of a crystalline actuator upon UV and visible irradiation. Reproduced with permission from ref 217. Copyright 2012 Wiley. (**c**) Irradiation of gold-coated diarylethene crystals with UV and visible light enables the ON/OFF photoreversible current switching of an electric circuit. Reproduced with permission from ref 218. Copyright 2015 Royal Society of Chemistry. (**d**) Superimposed photographs of a crystal cantilever lifting a lead ball with a mass 275 times larger than the crystal upon irradiation with UV light from the underside of the actuator. Reproduced from ref 216. Copyright 2010 American Chemical Society.

Other commonly studied photomechanical crystalline architectures are composed of anthracenes or salicylidenephenylethylamine molecules. Bardeen and co-workers investigated the [4 + 4] dimerization reaction of anthracenes where the photoreaction

results in reversible or irreversible twisting of crystalline microribbons.[219,220] The curling and twisting motion may be attributed to strain between spatially distinct reactant and product domains as a result of differential absorption by different regions of the crystal or intrinsic solid-state reaction kinetics.[221] Another crystalline molecular machine was proposed by Koshima *et al*. based on photomechanical action in platelike crystals of salicylidenephenylethylamine (Figure A.17).[222] These actuators are capable of lifting weights up to 300 times the crystal weight. The motion is linked to geometric changes in the molecules produced upon tautomeric transformation triggered by light absorption and consequent proton migration. Collective reorganization of the molecules within the lattice leads to small uniaxial cell expansion, which in turn results in bending of the crystal.

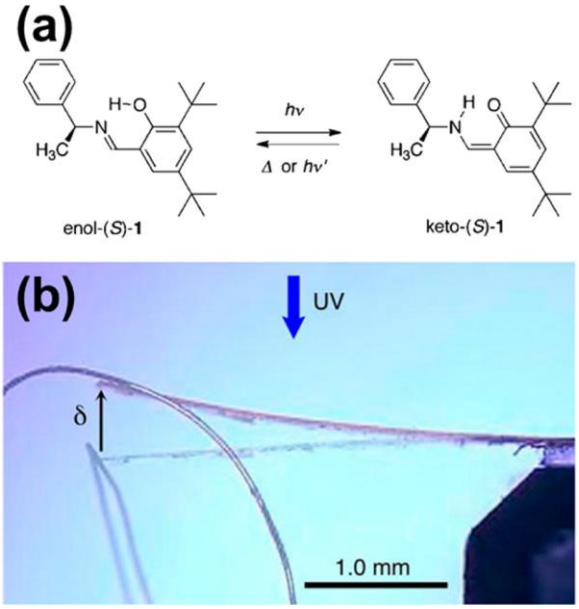

Figure A.17. (**a**) Photoinduced proton transfer in the *S* enantiomers of chiral salicylidenephenylethylamines upon keto–enol tautomerism. (**b**) Superimposed photographs of a chiral enol-(*S*)-1 crystal before and after irradiating the top of the crystal actuator with ultraviolet light. The crystalline cantilever achieved 26 nJ of work by lifting a 4.00 mg metal ring a height, δ, of 0.65 mm. Various photomechanical lifting work was achieved with different enantiomeric compositions within the crystal: the racemic crystal, enol-(*rac*)-1, achieved 59 nJ of work by lifting a weight with mass 300 times larger than the crystal (not shown). Reproduced from ref 222. Copyright 2013 American Chemical Society.

While the workhorse of many photomechanical studies, the azobenzene chromophore, has been extensively probed as isolated molecules, on surfaces, in polymers, and within liquid crystals, it has been far less studied by the crystalline photomechanical community.[223-227] This difference is due, in part, to the sterically demanding *trans* to *cis* isomerization process which may be impeded in a crystal. Surprisingly, Koshima *et al*. demonstrated reversible photomechanical bending of thin *trans*-4-(dimethylamino)azobenzene plates upon ultraviolet irradiation, concluding that isomerization can still occur inside the crystal.[228] That report was followed by a study of thin crystalline plates and needles of pseudostilbenes (azobenzenes with short-lived *cis* states), which were capable of submillisecond bending and relaxation upon irradiation with visible light.[229] Pseudostilbene bending crystals offer the fastest speed of bending–relaxation cycles as the whole event can take less than a second and is the only system that completely circumvents the need for ultraviolet light to induce isomerization. More recent reports have focused on elucidating the mechanistic aspects of azobenzene isomerization in crystals focusing on *in situ* X-ray diffraction studies of irreversible *cis*–*trans* isomerization in crystals[230] and cocrystals[231] of the molecule (Figure A.18). These reports demonstrated that *cis* to *trans* isomerization in crystals is mediated by a transient amorphous state. While the sterically demanding azobenzene isomerization reaction requires considerable free volume to occur and is rarely possible in a single-crystal/single-crystal fashion, an amorphization mechanism enables the photochemical reaction to proceed despite the constraints of the crystal lattice. Amorphous intermediates in the crystal were corroborated by the loss of diffraction spots upon irradiation with visible light at low temperature. Remarkably, isomerization within the crystals of azobenzene represents a topotactic process in which the

orientation of the resultant *trans*-crystal phase is dependent on the initial crystal orientation and effectively represents template crystal growth directed by light.

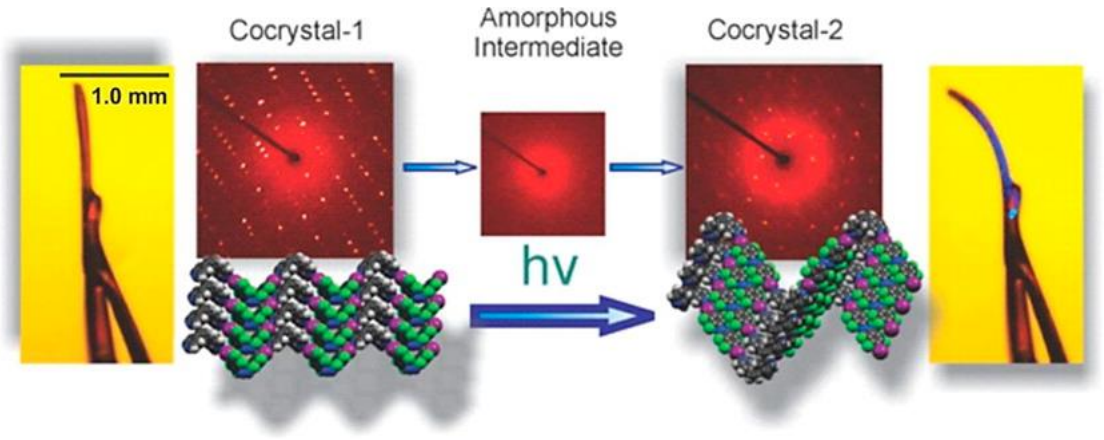

Figure A.18. Amorphous phase-mediated azobenzene isomerization and photomechanical bending in a cocrystal (1.2 mm × 90 μm × 20 μm). The cocrystal contains a 1:1 ratio of a halogen-bond acceptor (*cis*-1,2-bis(4-pyridyl)ethylene) and halogen-bond donor species. Bromine or iodine atoms on perfluorinated azobenzenes act as halogen-bond donors, forming a linear interaction with the pyridine nitrogen atoms on the halogen-bond acceptor. Irradiation of the cocrystals with a 532 nm laser facilitates *cis* to *trans* isomerization of the halogen-bond donors, *via* amorphous intermediates, determined by X-ray diffraction. Reproduced with permission from ref 231. Copyright 2014 Royal Society of Chemistry.

The growing number of investigations on dynamic molecular crystals that can perform as actuators demands new theoretical models. Various models have been reported in the context of polymer films, rods, or plates, such as the analysis by Warner and Mahadevan on photodeformation of nematic elastomers.[232] However, careful structural and kinetic considerations based on the spatial density and uniform orientations of photoactive molecules must be taken into account for these models to be fully applicable to crystalline systems. While the molecular motifs responsible for crystal motions are diverse, an attempt to unify photomechanical processes was done by Nath *et al*., who proposed a mathematical treatment of photomechanical crystal bending by accounting for the gradual profile of the

product in the crystal, irradiation time, direction and power using the azobenzene dye, Disperse Red 1, as a model compound.[233] The model is applicable for any photomechanical crystal system and allows an easier comparison between the different platforms for efficiency, modulus, stress, and other parameters critical for optimization of the process for practical use. Ultimately, with the help of theoretical frameworks and empirical data, the goal of future development of photomechanical systems needs to be directed toward robust and fatigue-resistant designs capable for even faster and reliable actuation over thousands of cycles.

A.D. Conclusions and Outlook

In the quest to synthesize and to assemble genuine molecular machines, the efforts of the scientific community have evolved from mere observation and design of dynamic molecular building blocks to understanding the mechanisms of their function. A necessary advance is the intelligent combination of the available building blocks to prepare useful and functional molecular-driven machines. Thus far, a wide variety of systems have been proposed that perform some kind of action on their environment, and the initial demonstrations of the application are promising. While their size and scope are dramatically different, the underlying mechanisms of action are remarkably similar. Whether linear motion, rotation, bending, or twisting is involved, they are all powered by stimulus-driven reversible chemical reactions. In some cases, like photoactive catalysis, the work is performed at the single-molecule level. However, controllable and measurable macroscopic effects such as changes in surface energy or the bending of crystalline films can be achieved through the collective, amplified motion of many molecules. It should be kept in mind that it is not a simple act of

preparing a binary switch or a bending, expanding, or contracting material that constitutes a machine; the efforts should rather be directed toward the reversible execution of a deliberate function.

In combination with the continued efforts in the design, synthesis, and assembly of novel molecular architectures, the characterization and analysis of stimulus-driven motion by new systems should include an assessment of the efficiency and reproducibility, and thus the viability, of a molecular machine as an invention.[234,235] Molecular machine designs must be highly resistant to degradation over long periods of time and/or numerous actuation cycles, and objectively addressing these requirements is critical for analyzing performance. This robustness is important, for example, for *in vivo* application of DNA-based assemblies that are susceptible to biodegradation by nucleases or repetitive UV irradiation cycles of crystal actuators. Measuring the efficiency at each step of energy transformation, from that of elementary switches and rotors to the entire assemblies, would also be highly beneficial, and results should be disseminated as a normal part of reported research findings. In photoinduced processes, this can be easily determined by calculating quantum yield or photoisomerization cross sections. Quantitative assessment of the forces generated by stimulus-induced motion by individual molecules or hierarchically more complex assemblies is also desirable where applicable.

The most glaring question that remains in the field is in what environments, or at what length scales, molecular machines will find truly impactful applications. While the hierarchical assembly of small switch and rotor components may provide more opportunities for externally controlled motion at greater length scales, will they be able to compete with other materials? For example, the impressive performance of

electrochemically or thermally driven shape-memory polymer fibers and hybrid carbon nanotube bundles may make those materials more viable alternatives for commercial artificial muscles than linear chains of molecular switches.[236,237] Likewise, the combination of mechanical actuators or sensors with integrated circuits based on microelectromechanical systems (MEMS) offers advantages over crystalline molecular machines due to the compatibility of microfabrication processes with complementary metal–oxide semiconductor (CMOS) technology on the scale of 1 μm to millimeters. To find their niche in similar applications, molecular machine designs must take advantage of alternative actuation mechanisms and offer more efficient energy transduction. Ultimately, the candid assessment of the potential applicability for leveraging the stimulated motions of molecules is more important than ascribing the label of a "machine". With this admission in mind, the necessity to demonstrate applications that harness the power of molecular machines to perform work on their environment presents an exciting and unique opportunity for researchers. Understanding the chemistry and physics that govern this motion will be a continuous challenge as designs become increasingly complex. Nevertheless, the future of this field will benefit from the impressive diversity and creativity of individual molecular and assembly motifs that may be used to direct motion from the nano- to the macroscale.

References

1. Duncan, T. M.; Bulygin, V. V.; Zhou, Y.; Hutcheon, M. L.; Cross, R. L. Rotation of Subunits during Catalysis by *Escherichia Coli* F1-ATPase. *Proc. Natl. Acad. Sci. U. S. A*. **1995**, 92, 10964–10968.

2. Yasuda, R.; Noji, H.; Kinosita, K.; Yoshida, M. F1-ATPase is a Highly Efficient Molecular Motor that Rotates with Discrete 120° Steps. *Cell* **1998**, 93, 1117–1124.

3. Berg, H. C.; Anderson, R. A. Bacteria Swim by Rotating Their Flagellar Filaments. *Nature* **1973**, 245, 380–382.

4. Mahadevan, L.; Matsudaira, P. Motility Powered by Supramolecular Springs and Ratchets. *Science* **2000**, 288, 95–99.

5. Kinbara, K.; Aida, T. Toward Intelligent Molecular Machines: Directed Motions of Biological and Artificial Molecules and Assemblies. *Chem. Rev*. **2005**, 105, 1377–1400.

6. Li, D.; Paxton, W. F.; Baughman, R. H.; Huang, T. J.; Stoddart, J. F.; Weiss, P. S. Molecular, Supramolecular, and Macromolecular Motors and Artificial Muscles. *MRS Bull*. **2009**, 34, 671–681.

7. Wang, J. Can Man-Made Nanomachines Compete with Nature Biomotors? *ACS Nano* **2009**, 3, 4–9.

8. Asimov, I. Runaround in Astounding Science Fiction; Street & Smith Publications, Inc.: New York, **1942**; Vol. 1, p 94.

9. Kay, E. R.; Leigh, D. A.; Zerbetto, F. Synthetic Molecular Motors and Mechanical Machines. *Angew. Chem., Int. Ed*. **2007**, 46, 72–191.

10. Coskun, A.; Banaszak, M.; Astumian, R. D.; Stoddart, J. F.; Grzybowski, B. A. Great Expectations: Can Artificial Molecular Machines Deliver on their Promise? *Chem. Soc. Rev*. **2012**, 41, 19–30.

11. Serreli, V.; Lee, C. F.; Kay, E. R.; Leigh, D. A. A Molecular Information Ratchet. *Nature* **2007**, 445, 523–527.

12. Browne, W. R.; Feringa, B. L. Making Molecular Machines Work. *Nat. Nanotechnol*. **2006**, 1, 25–35.

13. Mahimwalla, Z.; Yager, K. G.; Mamiya, J.; Shishido, A.; Priimagi, A.; Barrett, C. J. Azobenzene Photomechanics: Prospects and Potential Applications. *Polym. Bull*. **2012**, 69, 967–1006.

14. Bandara, H. M. D.; Burdette, S. C. Photoisomerization in Different Classes of Azobenzene. *Chem. Soc. Rev*. **2012**, 41, 1809–1825.

15. Wirth, J.; Hatter, N.; Drost, R.; Umbach, T. R.; Barja, S.; Zastrow, M.; Rück-Braun, K.; Pascual, J. I.; Saalfrank, P.; Franke, K. J. Diarylethene Molecules on a Ag(111) Surface: Stability and Electron-Induced Switching. *J. Phys. Chem. C* **2015**, 119, 4874–4883.

16. Irie, M.; Fukaminato, T.; Matsuda, K.; Kobatake, S. Photochromism of Diarylethene Molecules and Crystals: Memories, Switches, and Actuators. *Chem. Rev*. **2014**, 114, 12174–12277.

17. Berkovic, G.; Krongauz, V.; Weiss, V. Spiropyrans and Spirooxazines for Memories and Switches. *Chem. Rev*. **2000**, 100, 1741–1753.

18. Whalley, A. C.; Steigerwald, M. L.; Guo, X.; Nuckolls, C. Reversible Switching in Molecular Electronic Devices. *J. Am. Chem. Soc*. **2007**, 129, 12590–12591.

19. Kim, M.; Hohman, J. N.; Cao, Y.; Houk, K. N.; Ma, H.; Jen, A. K. Y.; Weiss, P. S. Creating Favorable Geometries for Directing Organic Photoreactions in Alkanethiolate Monolayers. *Science* **2011**, 331, 1312–1315.

20. Zheng, Y. B.; Payton, J. L.; Song, T. B.; Pathem, B. K.; Zhao, Y. X.; Ma, H.; Yang, Y.; Jensen, L.; Jen, A. K. Y.; Weiss, P. S. Surface-Enhanced Raman Spectroscopy To Probe Photoreaction Pathways and Kinetics of Isolated Reactants on Surfaces: Flat versus Curved Substrates. *Nano Lett*. **2012**, 12, 5362–5368.

21. Trenor, S. R.; Shultz, A. R.; Love, B. J.; Long, T. E. Coumarins in Polymers: From Light Harvesting to Photo-Cross-Linkable Tissue Scaffolds. *Chem. Rev*. **2004**, 104, 3059–3077.

22. Bauer, J.; Hou, L. L.; Kistemaker, J. C. M.; Feringa, B. L. Tuning the Rotation Rate of Light-Driven Molecular Motors. *J. Org. Chem*. **2014**, 79, 4446–4455.

23. Su, X.; Voskian, S.; Hughes, R. P.; Aprahamian, I. Manipulating Liquid-Crystal Properties Using a pH Activated Hydrazone Switch. *Angew. Chem., Int. Ed*. **2013**, 52, 10734–10739.

24. Belowich, M. E.; Stoddart, J. F. Dynamic Imine Chemistry. *Chem. Soc. Rev*. **2012**, 41, 2003–2024.

25. Tatum, L. A.; Su, X.; Aprahamian, I. Simple Hydrazone Building Blocks for Complicated Functional Materials. *Acc. Chem. Res*. **2014**, 47, 2141–2149.

26. Qu, D.-H.; Wang, Q.-C.; Zhang, Q.-W.; Ma, X.; Tian, H. Photoresponsive Host-Guest Functional Systems. *Chem. Rev*. **2015**, 115, 7543–7588.

27. Grunder, S.; McGrier, P. L.; Whalley, A. C.; Boyle, M. M.; Stern, C.; Stoddart, J. F. A Water-Soluble pH-Triggered Molecular Switch. *J. Am. Chem. Soc*. **2013**, 135, 17691–17694.

28. Bruns, C. J.; Li, J. N.; Frasconi, M.; Schneebeli, S. T.; Iehl, J.; de Rouville, H. P. J.; Stupp, S. I.; Voth, G. A.; Stoddart, J. F. An Electrochemically and Thermally Switchable Donor-Acceptor [c2]Daisy Chain Rotaxane. *Angew. Chem., Int. Ed*. **2014**, 53, 1953–1958.

29. Xue, M.; Yang, Y.; Chi, X.; Yan, X.; Huang, F. Development of Pseudorotaxanes and Rotaxanes: From Synthesis to Stimuli-Responsive Motions to Applications. *Chem. Rev*. **2015**, 115, 7398–7501.

30. Lohmann, F.; Ackermann, D.; Famulok, M. Reversible Light Switch for Macrocycle Mobility in a DNA Rotaxane. *J. Am. Chem. Soc*. **2012**, 134, 11884–11887.

31. Rajendran, A.; Endo, M.; Hidaka, K.; Sugiyama, H. Direct and Real-Time Observation of Rotary Movement of a DNA Nanomechanical Device. *J. Am. Chem. Soc*. **2013**, 135, 1117–1123.

32. Lund, K.; Manzo, A. J.; Dabby, N.; Michelotti, N.; Johnson-Buck, A.; Nangreave, J.; Taylor, S.; Pei, R. J.; Stojanovic, M. N.; Walter, N. G.; Winfree, E.; Yan, H. Molecular Robots Guided by Prescriptive Landscapes. *Nature* **2010**, 465, 206–210.

33. Astumian, R. D. Microscopic Reversibility as the Organizing Principle of Molecular Machines. *Nat. Nanotechnol*. **2012**, 7, 684–688.

34. Hutchison, J. A.; Uji-i, H.; Deres, A.; Vosch, T.; Rocha, S.; Müller, S.; Bastian, A. A.; Enderlein, J.; Nourouzi, H.; Li, C.; Herrmann, A.; Müllen, K.; De Schryver, F.; Hofkens, J. A Surface-Bound Molecule that Undergoes Optically Biased Brownian Rotation. *Nat. Nanotechnol*. **2014**, 9, 131–136.

35. Perera, U. G. E.; Ample, F.; Kersell, H.; Zhang, Y.; Vives, G.; Echeverria, J.; Grisolia, M.; Rapenne, G.; Joachim, C.; Hla, S. W. Controlled Clockwise and Anticlockwise Rotational Switching of a Molecular Motor. *Nat. Nanotechnol*. **2013**, 8, 46–51.

36. Chen, J. W.; Kistemaker, J. C. M.; Robertus, J.; Feringa, B. L. Molecular Stirrers in Action. *J. Am. Chem. Soc*. **2014**, 136, 14924–14932.

37. Greb, L.; Lehn, J. M. Light-Driven Molecular Motors: lmines as Four-Step or Two-Step Unidirectional Rotors. *J. Am. Chem. Soc*. **2014**, 136, 13114–13117.

38. Lu, C. H.; Cecconello, A.; Elbaz, J.; Credi, A.; Willner, I. A Three-Station DNA Catenane Rotary Motor with Controlled Directionality. *Nano Lett*. **2013**, 13, 2303–2308.

39. Arduini, A.; Bussolati, R.; Credi, A.; Secchi, A.; Silvi, S.; Semeraro, M.; Venturi, M. Toward Directionally Controlled Molecular Motions and Kinetic Intra- and Intermolecular Self-Sorting: Threading Processes of Nonsymmetric Wheel and Axle Components. *J. Am. Chem. Soc*. **2013**, 135, 9924–9930.

40. Li, H.; Cheng, C. Y.; McGonigal, P. R.; Fahrenbach, A. C.; Frasconi, M.; Liu, W. G.; Zhu, Z. X.; Zhao, Y. L.; Ke, C. F.; Lei, J. Y.; Young, R. M.; Dyar, S. M.; Co, D. T.; Yang, Y. W.; Botros, Y. Y.; Goddard, W. A.; Wasielewski, M. R.; Astumian, R. D.; Stoddart, J. F. Relative Unidirectional Translation in an Artificial Molecular Assembly Fueled by Light. *J. Am. Chem. Soc*. **2013**, 135, 18609–18620.

41. Yin, P.; Yan, H.; Daniell, X. G.; Turberfield, A. J.; Reif, J. H. A Unidirectional DNA Walker that Moves Autonomously Along a Track. *Angew. Chem., Int. Ed*. **2004**, 43, 4906–4911.

42. You, M. X.; Huang, F. J.; Chen, Z.; Wang, R. W.; Tan, W. H. Building a Nanostructure with Reversible Motions Using Photonic Energy. *ACS Nano* **2012**, 6, 7935–7941.

43. Kudernac, T.; Ruangsupapichat, N.; Parschau, M.; Maciá, B.; Katsonis, N.; Harutyunyan, S. R.; Ernst, K. H.; Feringa, B. L. Electrically Driven Directional Motion of a Four-Wheeled Molecule on a Metal Surface. *Nature* **2011**, 479, 208–211.

44. Cheng, C.; McGonigal, P. R.; Schneebeli, S. T.; Li, H.; Vermeulen, N. A.; Ke, C.; Stoddart, J. F. An Artificial Molecular Pump. *Nat. Nanotechnol*. **2015**, 10, 547–553.

45. Perutz, M. F. Stereochemistry of Cooperative Effects in Haemoglobin. *Nature* **1970**, 228, 726–734.

46. Changeux, J. P.; Edelstein, S. J. Allosteric Mechanisms of Signal Transduction. *Science* **2005**, 308, 1424– 1428.

47. Ray, D.; Foy, J. T.; Hughes, R. P.; Aprahamian, I. A Switching Cascade of Hydrazone-Based Rotary Switches through Coordination-Coupled Proton Relays. *Nat. Chem*. **2012**, 4, 757–762.

48. Foy, J. T.; Ray, D.; Aprahamian, I. Regulating Signal Enhancement with Coordination-Coupled Deprotonation of a Hydrazone Switch. *Chem. Sci*. **2015**, 6, 209–213.

49. Pramanik, S.; De, S. M.; Schmittel, M. Bidirectional Chemical Communication between Nanomechanical Switches. *Angew. Chem., Int. Ed*. **2014**, 53, 4709–4713.

50. Pramanik, S.; De, S.; Schmittel, M. A Trio of Nanoswitches in Redox-Potential Controlled Communication. *Chem. Commun*. **2014**, 50, 13254–13257.

51. Joachim, C.; Rapenne, G. Molecule Concept Nanocars: Chassis, Wheels, and Motors? *ACS Nano* **2013**, 7, 11–14.

52. Weiss, P. S. Nano Races, Prizes, and Awards. *ACS Nano* **2014**, 8, 1–1.

53. Yoon, H. J.; Kuwabara, J.; Kim, J. H.; Mirkin, C. A. Allosteric Supramolecular Triple-Layer Catalysts. *Science* **2010**, 330, 66–69.

54. Stoll, R. S.; Peters, M. V.; Kuhn, A.; Heiles, S.; Goddard, R.; Bühl, M.; Thiele, C. M.; Hecht, S. Photoswitchable Catalysts: Correlating Structure and Conformational Dynamics with Reactivity by a Combined Experimental and Computational Approach. *J. Am. Chem. Soc*. **2009**, 131, 357–367.

55. Göstl, R.; Senf, A.; Hecht, S. Remote-Controlling Chemical Reactions by Light: Towards Chemistry with High Spatio-Temporal Resolution. *Chem. Soc. Rev*. **2014**, 43, 1982–1996.

56. Wang, J. B.; Feringa, B. L. Dynamic Control of Chiral Space in a Catalytic Asymmetric Reaction Using a Molecular Motor. *Science* **2011**, 331, 1429–1432.

57. Blanco, V.; Carlone, A.; Hänni, K. D.; Leigh, D. A.; Lewandowski, B. A Rotaxane-Based Switchable Organocatalyst. *Angew. Chem., Int. Ed*. **2012**, 51, 5166–5169.

58. Blanco, V.; Leigh, D. A.; Marcos, V.; Morales-Serna, J. A.; Nussbaumer, A. L. A Switchable [2]Rotaxane Asymmetric Organocatalyst That Utilizes an Acyclic Chiral Secondary Amine. *J. Am. Chem. Soc*. **2014**, 136, 4905–4908.

59. Storch, G.; Trapp, O. Temperature-Controlled Bidirectional Enantioselectivity in a Dynamic Catalyst for Asymmetric Hydrogenation. *Angew. Chem., Int. Ed*. **2015**, 54, 3580–3586.

60. Velema, W. A.; Szymanski, W.; Feringa, B. L. Photopharmacology: Beyond Proof of Principle. *J. Am. Chem. Soc*. **2014**, 136, 2178–2191.

61. Mrazek, J.; Toso, D.; Ryazantsev, S.; Zhang, X.; Zhou, Z. H.; Fernandez, B. C.; Kickhoefer, V. A.; Rome, L. H. Polyribosomes are Molecular 3D Nanoprinters That Orchestrate the Assembly of Vault Particles. *ACS Nano* **2014**, 8, 11552–11559.

62. Lewandowski, B.; De Bo, G.; Ward, J. W.; Papmeyer, M.; Kuschel, S.; Aldegunde, M. J.; Gramlich, P. M. E.; Heckmann, D.; Goldup, S. M.; D'Souza, D. M.; Fernandes, A. E.; Leigh, D. A. Sequence-Specific Peptide Synthesis by an Artificial Small-Molecule Machine. *Science* **2013**, 339, 189–193.

63. De Bo, G.; Kuschel, S.; Leigh, D. A.; Lewandowski, B.; Papmeyer, M.; Ward, J. W. Efficient Assembly of Threaded Molecular Machines for Sequence-Specific Synthesis. *J. Am. Chem. Soc*. **2014**, 136, 5811–5814.

64. Kuzuya, A.; Ohya, Y. Nanomechanical Molecular Devices Made of DNA Origami. *Acc. Chem.* Res. **2014**, 47, 1742–1749.

65. Jester, S. S.; Famulok, M. Mechanically Interlocked DNA Nanostructures for Functional Devices. *Acc. Chem. Res*. **2014**, 47, 1700–1709.

66. Rothemund, P. W. K. Folding DNA to Create Nanoscale Shapes and Patterns. *Nature* **2006**, 440, 297–302.

67. Yurke, B.; Turberfield, A. J.; Mills, A. P.; Simmel, F. C.; Neumann, J. L. A DNA-Fuelled Molecular Machine Made of DNA. *Nature* **2000**, 406, 605–608.

68. Hu, L. Z.; Lu, C. H.; Willner, I. Switchable Catalytic DNA Catenanes. *Nano Lett*. **2015**, 15, 2099–2103.

69. Idili, A.; Plaxco, K. W.; Vallée-Bélishe, A.; Ricci, F. Thermodynamic Basis for Engineering High-Affinity, High-Specificity Binding-Induced DNA Clamp Nanoswitches. *ACS Nano* **2013**, 7, 10863–10869.

70. Nishioka, H.; Liang, X. G.; Kato, T.; Asanuma, H. A Photon-Fueled DNA Nanodevice that Contains Two Different Photoswitches. *Angew. Chem., Int. Ed*. **2012**, 51, 1165–1168.

71. Endo, M.; Miyazaki, R.; Emura, T.; Hidaka, K.; Sugiyama, H. Transcription Regulation System Mediated by Mechanical Operation of a DNA Nanostructure. *J. Am. Chem. Soc.* **2012**, 134, 2852–2855.

72. Zadegan, R. M.; Jepsen, M. D. E.; Thomsen, K. E.; Okholm, A. H.; Schaffert, D. H.; Andersen, E. S.; Birkedal, V.; Kjems, J. Construction of a 4 Zeptoliters Switchable 3D DNA Box Origami. *ACS Nano* **2012**, 6, 10050–10053.

73. Andersen, E. S.; Dong, M.; Nielsen, M. M.; Jahn, K.; Subramani, R.; Mamdouh, W.; Golas, M. M.; Sander, B.; Stark, H.; Oliveira, C. L. P.; Pedersen, J. S.; Birkedal, V.; Besenbacher, F.; Gothelf, K. V.; Kjems, J. Self-Assembly of a Nanoscale DNA Box with a Controllable Lid. *Nature* **2009**, 459, 73–76.

74. Janssen, B. M. G.; van Rosmalen, M.; van Beek, L.; Merkx, M. Antibody Activation using DNA-Based Logic Gates. *Angew. Chem., Int. Ed*. **2015**, 54, 2530–2533.

75. Adleman, L. M. Molecular Computation of Solutions to Combinatorial Problems. *Science* **1994**, 266, 1021–1024.

76. Lipton, R. J. DNA Solution of Hard Computational Problems. *Science* **1995**, 268, 542–545.

77. Douglas, S. M.; Bachelet, I.; Church, G. M. A Logic-Gated Nanorobot for Targeted Transport of Molecular Payloads. *Science* **2012**, 335, 831–834.

78. Li, T.; Lohmann, F.; Famulok, M. Interlocked DNA Nanostructures Controlled by a Reversible Logic Circuit. *Nat. Commun*. **2014**, 5, 4940.

79. You, M. X.; Zhu, G. Z.; Chen, T.; Donovan, M. J.; Tan, W. H. Programmable and Multiparameter DNA-Based Logic Platform For Cancer Recognition and Targeted Therapy. *J. Am. Chem. Soc*. **2015**, 137, 667–674.

80. Chirieleison, S. M.; Allen, P. B.; Simpson, Z. B.; Ellington, A. D.; Chen, X. Pattern Transformation with DNA Circuits. *Nat. Chem*. **2013**, 5, 1000–1005.

81. Vale, R. D. The Molecular Motor Toolbox for Intracellular Transport. *Cell* **2003**, 112, 467–480.

82. Yildiz, A.; Forkey, J. N.; McKinney, S. A.; Ha, T.; Goldman, Y. E.; Selvin, P. R. Myosin V Walks Hand-Over-Hand: Single Fluorophore Imaging with 1.5-nm Localization. *Science* **2003**, 300, 2061–2065.

83. Yildiz, A.; Tomishige, M.; Vale, R. D.; Selvin, P. R. Kinesin Walks Hand-over-Hand. *Science* **2004**, 303, 676–678.

84. Karagiannis, P.; Ishii, Y.; Yanagida, T. Molecular Machines Like Myosin Use Randomness to Behave Predictably. *Chem. Rev*. **2014**, 114, 3318–3334.

85. Omabegho, T.; Sha, R.; Seeman, N. C. A Bipedal DNA Brownian Motor with Coordinated Legs. *Science* **2009**, 324, 67–71.

86. Shin, J. S.; Pierce, N. A. A Synthetic DNA Walker for Molecular Transport. *J. Am. Chem. Soc.* **2004**, 126, 10834–10835.

87. You, M. X.; Chen, Y.; Zhang, X. B.; Liu, H. P.; Wang, R. W.; Wang, K. L.; Williams, K. R.; Tan, W. H. An Autonomous and Controllable Light-Driven DNA Walking Device. *Angew. Chem., Int. Ed.* **2012**, 51, 2457–2460.

88. Cheng, J.; Sreelatha, S.; Loh, I. Y.; Liu, M. H.; Wang, Z. S. A Bioinspired Design Principle for DNA Nanomotors: Mechanics-Mediated Symmetry Breaking and Experimental Demonstration Methods. **2014**, 67, 227–233.

89. He, Y.; Liu, D. R. Autonomous Multistep Organic Synthesis in a Single Isothermal Solution Mediated by a DNA Walker. *Nat. Nanotechnol*. **2010**, 5, 778–782.

90. Gu, H. Z.; Chao, J.; Xiao, S. J.; Seeman, N. C. A Proximity-Based Programmable DNA Nanoscale Assembly Line. *Nature* **2010**, 465, 202–205.

91. Cha, T. G.; Pan, J.; Chen, H. R.; Salgado, J.; Li, X.; Mao, C. D.; Choi, J. H. A Synthetic DNA Motor that Transports Nanoparticles along Carbon Nanotubes. *Nat. Nanotechnol*. **2014**, 9, 39–43.

92. Zhang, D. Y.; Seelig, G. Dynamic DNA Nanotechnology Using Strand-Displacement Reactions. *Nat. Chem*. **2011**, 3, 103–113.

93. Zhang, D. Y.; Winfree, E. Control of DNA Strand Displacement Kinetics Using Toehold Exchange. *J. Am. Chem. Soc*. **2009**, 131, 17303–17314.

94. Gao, Y.; Wolf, L. K.; Georgiadis, R. M. Secondary Structure Effects on DNA Hybridization Kinetics: A Solution *versus* Surface Comparison. *Nucleic Acids Res*. **2006**, 34, 3370–3377.

95. Wang, C. Y.; Tao, Y.; Song, G. T.; Ren, J. S.; Qu, X. G. Speeding Up a Bidirectional DNA Walking Device. *Langmuir* **2012**, 28, 14829–14837.

96. Loh, I. Y.; Cheng, J.; Tee, S. R.; Efremov, A.; Wang, Z. S. From Bistate Molecular Switches to Self-Directed Track-Walking Nanomotors. *ACS Nano* **2014**, 8, 10293–10304.

97. Tomov, T. E.; Tsukanov, R.; Liber, M.; Masoud, R.; Plavner, N.; Nir, E. Rational Design of DNA Motors: Fuel Optimization through Single-Molecule Fluorescence. *J. Am. Chem. Soc*. **2013**, 135, 11935–11941.

98. Green, S. J.; Bath, J.; Turberfield, A. J. Coordinated Chemomechanical Cycles: A Mechanism for Autonomous Molecular Motion. *Phys. Rev. Lett*. **2008**, 101, 238101.

99. Liu, M. H.; Hou, R. Z.; Cheng, J.; Loh, L. Y.; Sreelatha, S.; Tey, J. N.; Wei, J.; Wang, Z. S. Autonomous Synergic Control of Nanomotors. *ACS Nano* **2014**, 8, 1792–1803.

100. Klajn, R.; Stoddart, J. F.; Grzybowski, B. A. Nanoparticles Functionalised with Reversible Molecular and Supramolecular Switches. *Chem. Soc. Rev*. **2010**, 39, 2203–2237.

101. Swaminathan, S.; Garcia-Amorós, J.; Fraix, A.; Kandoth, N.; Sortino, S.; Raymo, F. M. Photoresponsive Polymer Nanocarriers with Multifunctional Cargo. *Chem. Soc. Rev.* **2014**, 43, 4167–4178.

102. Song, N.; Yang, Y.-W. Molecular and Supramolecular Switches on Mesoporous Silica Nanoparticles. *Chem. Soc. Rev.* **2015**, 44, 3474–3504.

103. Nguyen, T. D.; Tseng, H. R.; Celestre, P. C.; Flood, A. H.; Liu, Y.; Stoddart, J. F.; Zink, J. I. A Reversible Molecular Valve. *Proc. Natl. Acad. Sci. U. S. A*. **2005**, 102, 10029–10034

104. Sun, Y. L.; Yang, Y. W.; Chen, D. X.; Wang, G.; Zhou, Y.; Wang, C. Y.; Stoddart, J. F. Mechanized Silica Nanoparticles Based on Pillar[5]arenes for On-Command Cargo Release. *Small* **2013**, 9, 3224–3229.

105. Chen, T.; Yang, N. W.; Fu, J. J. Controlled Release of Cargo Molecules from Hollow Mesoporous Silica Nanoparticles Based on Acid and Base Dual-Responsive Cucurbit[7]uril Pseudorotaxanes. *Chem. Commun*. **2013**, 49, 6555–6557.

106. Zhang, Z. X.; Balogh, D.; Wang, F. A.; Willner, I. Smart Mesoporous SiO2 Nanoparticles for the DNAzyme-Induced Multiplexed Release of Substrates. *J. Am. Chem. Soc.* **2013**, 135, 1934–1940.

107. Zhang, G. L.; Yang, M. L.; Cai, D. Q.; Zheng, K.; Zhang, X.; Wu, L. F.; Wu, Z. Y. Composite of Functional Mesoporous Silica and DNA: An Enzyme-Responsive Controlled Release Drug Carrier System. *ACS Appl. Mater. Interfaces* **2014**, 6, 8042–8047.

108. Mal, N. K.; Fujiwara, M.; Tanaka, Y. Photocontrolled Reversible Release of Guest Molecules from Coumarin-Modified Mesoporous Silica. *Nature* **2003**, 421, 350–353.

109. Guardado-Alvarez, T. M.; Devi, L. S.; Russell, M. M.; Schwartz, B. J.; Zink, J. I. Activation of Snap-Top Capped Mesoporous Silica Nanocontainers Using Two Near-Infrared Photons. *J. Am. Chem. Soc*. **2013**, 135, 14000–14003.

110. Mei, X.; Yang, S.; Chen, D. Y.; Li, N. J.; Li, H.; Xu, Q. F.; Ge, J. F.; Lu, J. M. Light-Triggered Reversible Assemblies of Azobenzene-Containing Amphiphilic Copolymer with β-Cyclodextrin-Modified Hollow Mesoporous Silica Nanoparticles for Controlled Drug Release. *Chem. Commun.* **2012**, 48, 10010–10012.

111. Li, Q. L.; Wang, L.; Qiu, X. L.; Sun, Y. L.; Wang, P. X.; Liu, Y.; Li, F.; Qi, A. D.; Gao, H.; Yang, Y. W. Stimuli-Responsive Biocompatible Nanovalves Based on β-Cyclodextrin Modified Poly(glycidyl methacrylate). *Polym. Chem*. **2014**, 5, 3389–3395.

112. Yang, Y. W. Towards Biocompatible Nanovalves Based on Mesoporous Silica Nanoparticles. *MedChemComm* **2011**, 2, 1033–1049.

113. Croissant, J.; Maynadier, M.; Gallud, A.; N'Dongo, H. P.; Nyalosaso, J. L.; Derrien, G.; Charnay, C.; Durand, J. O.; Raehm, L.; Serein-Spirau, F.; Cheminet, N.; Jarrosson, T.; Mongin, O.; Blanchard-Desce, M.; Gary-Bobo, M.; Garcia, M.; Lu, J.; Tamanoi, F.; Tarn, D.; Guardado-Alvarez, T. M.; Zink, J. I. Two-Photon-Triggered Drug Delivery in Cancer Cells Using Nanoimpellers. *Angew. Chem., Int. Ed*. **2013**, 52, 13813–13817.

114. Croissant, J.; Chaix, A.; Mongin, O.; Wang, M.; Clément, S.; Raehm, L.; Durand, J. O.; Hugues, V.; Blanchard-Desce, M.; Maynadier, M.; Gallud, A.; Gary-Bobo, M.; Garcia, M.; Lu, J.; Tamanoi, F.; Ferris, D. P.; Tarn, D.; Zink, J. I. Two-Photon-Triggered Drug Delivery via Fluorescent Nanovalves. *Small* **2014**, 10, 1752–1755.

115. Gary-Bobo, M.; Mir, Y.; Rouxel, C.; Brevet, D.; Basile, I.; Maynadier, M.; Vaillant, O.; Mongin, O.; Blanchard-Desce, M.; Morère, A.; Garcia, M.; Durand, J. O.; Raehm, L. Mannose-Functionalized Mesoporous Silica Nanoparticles for Efficient Two-Photon Photodynamic Therapy of Solid Tumors. *Angew. Chem., Int. Ed*. **2011**, 50, 11425–11429.

116. Baudrion, A. L.; Perron, A.; Veltri, A.; Bouhelier, A.; Adam, P. M.; Bachelot, R. Reversible Strong Coupling in Silver Nanoparticle Arrays Using Photochromic Molecules. *Nano Lett*. **2013**, 13, 282–286.

117. Zheng, Y. B.; Kiraly, B.; Cheunkar, S.; Huang, T. J.; Weiss, P. S. Incident-Angle-Modulated Molecular Plasmonic Switches: A Case of Weak Exciton-Plasmon Coupling. *Nano Lett.* **2011**, 11, 2061–2065.

118. Joshi, G. K.; Blodgett, K. N.; Muhoberac, B. B.; Johnson, M. A.; Smith, K. A.; Sardar, R. Ultrasensitive Photoreversible Molecular Sensors of Azobenzene-Functionalized Plasmonic Nanoantennas. *Nano Lett*. **2014**, 14, 532–540.

119. Mirkin, C. A.; Letsinger, R. L.; Mucic, R. C.; Storhoff, J. J. A DNA-Based Method for Rationally Assembling Nanoparticles into Macroscopic Materials. *Nature* **1996**, 382, 607–609.

120. Li, H.; Chen, D. X.; Sun, Y. L.; Zheng, Y. B.; Tan, L. L.; Weiss, P. S.; Yang, Y. W. Viologen-Mediated Assembly of and Sensing with Carboxylatopillar[5]arene-Modified Gold Nanoparticles. *J. Am. Chem. Soc*. **2013**, 135, 1570–1576.

121. Kuzyk, A.; Schreiber, R.; Zhang, H.; Govorov, A. O.; Liedl, T.; Liu, N. Reconfigurable 3D Plasmonic Metamolecules. *Nat. Mater*. **2014**, 13, 862–866.

122. Liu, D. B.; Chen, W. W.; Sun, K.; Deng, K.; Zhang, W.; Wang, Z.; Jiang, X. Y. Resettable, Multi-Readout Logic Gates Based on Controllably Reversible Aggregation of Gold Nanoparticles. *Angew. Chem., Int. Ed*. **2011**, 50, 4103–4107.

123. Lee, J.-W.; Klajn, R. Dual-Responsive Nanoparticles that Aggregate Under the Simultaneous Action of Light and CO_2. *Chem. Commun*. **2015**, 51, 2036–2039.

124. Lu, C. H.; Willner, B.; Willner, I. DNA Nanotechnology: From Sensing and DNA Machines to Drug-Delivery Systems. *ACS Nano* **2013**, 7, 8320–8332.

125. Hu, L. Z.; Liu, X. Q.; Cecconello, A.; Willner, I. Dual Switchable CRET-Induced Luminescence of CdSe/ZnS Quantum Dots (QDs) by the Hemin/G-Quadruplex-Bridged Aggregation and Deaggregation of Two-Sized QDs. *Nano Lett*. **2014**, 14, 6030–6035.

126. Cecconello, A.; Lu, C. H.; Elbaz, J.; Willner, I. Au Nanoparticle/DNA Rotaxane Hybrid Nanostructures Exhibiting Switchable Fluorescence Properties. *Nano Lett*. **2013**, 13, 6275–6280.

127. Shimron, S.; Cecconello, A.; Lu, C. H.; Willner, I. Metal Nanoparticle-Functionalized DNA Tweezers: From Mechanically Programmed Nanostructures to Switchable Fluorescence Properties. *Nano Lett*. **2013**, 13, 3791–3795.

128. Elbaz, J.; Cecconello, A.; Fan, Z. Y.; Govorov, A. O.; Willner, I. Powering the Programmed Nanostructure and Function of Gold Nanoparticles with Catenated DNA Machines. *Nat. Commun*. **2013**, 4, 2000.

129. Hildebrandt, L. L.; Preus, S.; Zhang, Z.; Voigt, N. V.; Gothelf, K. V.; Birkedal, V. Single Molecule FRET Analysis of the 11 Discrete Steps of a DNA Actuator. *J. Am. Chem. Soc*. **2014**, 136, 8957–8962.

130. Bruns, C. J.; Stoddart, J. F. Rotaxane-Based Molecular Muscles. *Acc. Chem. Res*. **2014**, 47, 2186–2199.

131. Wu, J. S.; Leung, K. C. F.; Benítez, D.; Han, J. Y.; Cantrill, S. J.; Fang, L.; Stoddart, J. F. An Acid-Base-Controllable [c2]Daisy Chain. *Angew. Chem., Int. Ed*. **2008**, 47, 7470–7474.

132. Bruns, C. J.; Frasconi, M.; Iehl, J.; Hartlieb, K. J.; Schneebeli, S. T.; Cheng, C. Y.; Stupp, S. I.; Stoddart, J. F. Redox Switchable Daisy Chain Rotaxanes Driven by Radical-Radical Interactions. *J. Am. Chem. Soc*. **2014**, 136, 4714–4723.

133. Tsuda, S.; Aso, Y.; Kaneda, T. Linear Oligomers Composed of a Photochromically Contractible and Extendable Janus [2]Rotaxane. *Chem. Commun*. **2006**, 3072–3074.

134. Zhang, Z. B.; Han, C. Y.; Yu, G. C.; Huang, F. H. A Solvent-Driven Molecular Spring. *Chem. Sci.* **2012**, 3, 3026–3031.

135. Jimenez-Molero, M. C.; Dietrich-Buchecker, C.; Sauvage, J. P. Towards Artificial Muscles at the Nanometric Level. *Chem. Commun*. **2003**, 1613–1616.

136. Clark, P. G.; Day, M. W.; Grubbs, R. H. Switching and Extension of a [c2]Daisy-Chain Dimer Polymer. *J. Am. Chem. Soc*. **2009**, 131, 13631–13633.

137. Hmadeh, M.; Fang, L.; Trabolsi, A.; Elhabiri, M.; Albrecht-Gary, A. M.; Stoddart, J. F. On the Thermodynamic and Kinetic Investigations of a [c2]Daisy Chain Polymer. *J. Mater. Chem*. **2010**, 20, 3422–3430.

138. Du, G. Y.; Moulin, E.; Jouault, N.; Buhler, E.; Giuseppone, N. Muscle-like Supramolecular Polymers: Integrated Motion from Thousands of Molecular Machines. *Angew. Chem., Int. Ed*. **2012**, 51, 12504–12508.

139. Hugel, T.; Holland, N. B.; Cattani, A.; Moroder, L.; Seitz, M.; Gaub, H. E. Single-Molecule Optomechanical Cycle. *Science* **2002**, 296, 1103–1106.

140. Bléger, D.; Dokić, J.; Peters, M. V.; Grubert, L.; Saalfrank, P.; Hecht, S. Electronic Decoupling Approach to Quantitative Photoswitching in Linear Multiazobenzene Architectures. *J. Phys. Chem. B* **2011**, 115, 9930–9940.

141. Bléger, D.; Liebig, T.; Thiermann, R.; Maskos, M.; Rabe, J. P.; Hecht, S. Light-Orchestrated Macromolecular "Accordions": Reversible Photoinduced Shrinking of Rigid-Rod Polymers. *Angew. Chem., Int. Ed*. **2011**, 50, 12559–12563.

142. Lee, C. L.; Liebig, T.; Hecht, S.; Bléger, D.; Rabe, J. P. Light-Induced Contraction and Extension of Single Macromolecules on a Modified Graphite Surface. *ACS Nano* **2014**, 8, 11987–11993.

143. Wie, J. J.; Chatterjee, S.; Wang, D. H.; Tan, L.-S.; Ravi Shankar, M.; White, T. J. Azobenzene-Functionalized Polyimides as Wireless Actuators. *Polymer* **2014**, 55, 5915–5923.

144. Fang, L. J.; Zhang, H. T.; Li, Z. D.; Zhang, Y.; Zhang, Y. Y.; Zhang, H. Q. Synthesis of Reactive Azobenzene Main-Chain Liquid Crystalline Polymers via Michael Addition Polymerization and Photomechanical Effects of Their Supramolecular Hydrogen-Bonded Fibers. *Macromolecules* **2013**, 46, 7650–7660.

145. Yoshino, T.; Kondo, M.; Mamiya, J.; Kinoshita, M.; Yu, Y. L.; Ikeda, T. Three-Dimensional Photomobility of Crosslinked Azobenzene Liquid-Crystalline Polymer Fibers. *Adv. Mater*. **2010**, 22, 1361–1363.

146. Crivillers, N.; Osella, S.; Van Dyck, C.; Lazzerini, G. M.; Cornil, D.; Liscio, A.; Di Stasio, F.; Mian, S.; Fenwick, O.; Reinders, F.; Neuburger, M.; Treossi, E.; Mayor, M.; Palermo, V.; Cacialli, F.; Cornil, J.; Samorì, P. Large Work Function Shift of Gold Induced by a Novel Perfluorinated Azobenzene-Based Self-Assembled Monolayer. *Adv. Mater*. **2013**, 25, 432–436.

147. Zheng, Y. B.; Yang, Y. W.; Jensen, L.; Fang, L.; Juluri, B. K.; Flood, A. H.; Weiss, P. S.; Stoddart, J. F.; Huang, T. J. Active Molecular Plasmonics: Controlling Plasmon Resonances with Molecular Switches. *Nano Lett*. **2009**, 9, 819–825.

148. Chen, M.; Besenbacher, F. Light-Driven Wettability Changes on a Photoresponsive Electrospun Mat. *ACS Nano* **2011**, 5, 1549–1555.

149. Ahmad, N. M.; Lu, X. Y.; Barrett, C. J. Stable Photo-Reversible Surface Energy Switching with Azobenzene Polyelectrolyte Multilayers. *J. Mater. Chem*. **2010**, 20, 244–247.

150. Feng, C. L.; Zhang, Y. J.; Jin, J.; Song, Y. L.; Xie, L. Y.; Qu, G. R.; Jiang, L.; Zhu, D. B. Reversible Wettability of Photoresponsive Fluorine-Containing Azobenzene Polymer in Langmuir-Blodgett Films. *Langmuir* **2001**, 17, 4593–4597.

151. Ichimura, K.; Oh, S. K.; Nakagawa, M. Light-Driven Motion of Liquids on a Photoresponsive Surface. *Science* **2000**, 288, 1624–1626.

152. Berná, J.; Leigh, D. A.; Lubomska, M.; Mendoza, S. M.; Pérez, E. M.; Rudolf, P.; Teobaldi, G.; Zerbetto, F. Macroscopic Transport by Synthetic Molecular Machines. *Nat. Mater.* **2005**, 4, 704–710.

153. Shu, W. M.; Liu, D. S.; Watari, M.; Riener, C. K.; Strunz, T.; Welland, M. E.; Balasubramanian, S.; McKendry, R. A. DNA Molecular Motor Driven Micromechanical Cantilever Arrays. *J. Am. Chem. Soc*. **2005**, 127, 17054–17060.

154. Liu, Y.; Flood, A. H.; Bonvallet, P. A.; Vignon, S. A.; Northrop, B. H.; Tseng, H. R.; Jeppesen, J. O.; Huang, T. J.; Brough, B.; Baller, M.; Magonov, S.; Solares, S. D.; Goddard, W. A.; Ho, C. M.; Stoddart, J. F. Linear Artificial Molecular Muscles. *J. Am. Chem. Soc.* **2005**, 127, 9745–9759.

155. Juluri, B. K.; Kumar, A. S.; Liu, Y.; Ye, T.; Yang, Y. W.; Flood, A. H.; Fang, L.; Stoddart, J. F.; Weiss, P. S.; Huang, T. J. A Mechanical Actuator Driven Electrochemically by Artificial Molecular Muscles. *ACS Nano* **2009**, 3, 291–300.

156. Sengupta, S.; Spiering, M. M.; Dey, K. K.; Duan, W. T.; Patra, D.; Butler, P. J.; Astumian, R. D.; Benkovic, S. J.; Sen, A. DNA Polymerase as a Molecular Motor and Pump. *ACS* Nano **2014**, 8, 2410–2418.

157. Patra, D.; Zhang, H.; Sengupta, S.; Sen, A. Dual Stimuli-Responsive, Rechargeable Micropumps via "Host-Guest" Interactions. *ACS Nano* **2013**, 7, 7674–7679.

158. Love, J. C.; Estroff, L. A.; Kriebel, J. K.; Nuzzo, R. G.; Whitesides, G. M. Self-Assembled Monolayers of Thiolates on Metals as a Form of Nanotechnology. *Chem. Rev*. **2005**, 105, 1103–1169.

159. Zasadzinski, J. A.; Viswanathan, R.; Madsen, L.; Garnaes, J.; Schwartz, D. K. Langmuir-Blodgett-Films. *Science* **1994**, 263, 1726–1733.

160. Rubinstein, I.; Vaskevich, A. Self-Assembly of Nanostructures on Surfaces Using Metal-Organic Coordination. *Isr. J. Chem*. **2010**, 50, 333–346.

161. Pathem, B. K.; Claridge, S. A.; Zheng, Y. B.; Weiss, P. S. Molecular Switches and Motors on Surfaces. *Annu. Rev. Phys. Chem*. **2013**, 64, 605–630.

162. Bellisario, D. O.; Baber, A. E.; Tierney, H. L.; Sykes, E. C. H. Engineering Dislocation Networks for the Directed Assembly of Two-Dimensional Rotor Arrays. *J. Phys. Chem.* C **2009**, 113, 5895–5898.

163. Mielke, J.; Leyssner, F.; Koch, M.; Meyer, S.; Luo, Y.; Selvanathan, S.; Haag, R.; Tegeder, P.; Grill, L. Imine Derivatives on Au(111): Evidence for ″Inverted″ Thermal Isomerization. *ACS Nano* **2011**, 5, 2090–2097.

164. Tegeder, P. Optically and Thermally Induced Molecular Switching Processes at Metal Surfaces. *J. Phys.: Condens. Matter* **2012**, 24, 394001.

165. Pathem, B. K.; Zheng, Y. B.; Payton, J. L.; Song, T. B.; Yu, B. C.; Tour, J. M.; Yang, Y.; Jensen, L.; Weiss, P. S. Effect of Tether Conductivity on the Efficiency of Photoisomerization of Azobenzene-Functionalized Molecules on Au{111}. *J. Phys. Chem. Lett.* **2012**, 3, 2388–2394.

166. Benassi, E.; Granucci, G.; Persico, M.; Corni, S. Can Azobenzene Photoisomerize When Chemisorbed on a Gold Surface? An Analysis of Steric Effects Based on Nonadiabatic Dynamics Simulations. *J. Phys. Chem. C* **2015**, 119, 5962–5974.

167. Klajn, R. Immobilized Azobenzenes for the Construction of Photoresponsive Materials. *Pure Appl. Chem*. **2010**, 82, 2247–2279.

168. Ye, T.; Kumar, A. S.; Saha, S.; Takami, T.; Huang, T. J.; Stoddart, J. F.; Weiss, P. S. Changing Stations in Single Bistable Rotaxane Molecules under Electrochemical Control. *ACS Nano* **2010**, 4, 3697–3701.

169. Chen, K. Y.; Ivashenko, O.; Carroll, G. T.; Robertus, J.; Kistemaker, J. C. M.; London, G.; Browne, W. R.; Rudolf, P.; Feringa, B. L. Control of Surface Wettability Using Tripodal Light-Activated Molecular Motors. *J. Am. Chem. Soc*. **2014**, 136, 3219–3224.

170. London, G.; Chen, K. Y.; Carroll, G. T.; Feringa, B. L. Towards Dynamic Control of Wettability by Using Functionalized Altitudinal Molecular Motors on Solid Surfaces. *Chem. - Eur. J*. **2013**, 19, 10690–10697.

171. Lussis, P.; Svaldo-Lanero, T.; Bertocco, A.; Fustin, C. A.; Leigh, D. A.; Duwez, A. S. A Single Synthetic Small Molecule that Generates Force Against a Load. *Nat. Nanotechnol*. **2011**, 6, 553–557.

172. Heinrich, T.; Traulsen, C. H.-H.; Holzweber, M.; Richter, S.; Kunz, V.; Kastner, S. K.; Krabbenborg, S. O.; Huskens, J.; Unger, W. E. S.; Schalley, C. A. Coupled Molecular Switching Processes in Ordered Mono- and Multilayers of Stimulus-Responsive Rotaxanes on Gold Surfaces. *J. Am. Chem. Soc*. **2015**, 137, 4382–4390.

173. Pace, G.; Ferri, V.; Grave, C.; Elbing, M.; von Hänisch, C.; Zharnikov, M.; Mayor, M.; Rampi, M. A.; Samorì, P. Cooperative Light-Induced Molecular Movements of Highly

Ordered Azobenzene Self-Assembled Monolayers. *Proc. Natl. Acad. Sci. U. S. A*. **2007**, 104, 9937–9942.

174. Moldt, T.; Brete, D.; Przyrembel, D.; Das, S.; Goldman, J. R.; Kundu, P. K.; Gahl, C.; Klajn, R.; Weinelt, M. Tailoring the Properties of Surface-Immobilized Azobenzenes by Monolayer Dilution and Surface Curvature. *Langmuir* **2015**, 31, 1048–1057.

175. Qin, D.; Xia, Y. N.; Whitesides, G. M. Soft Lithography for Micro- and Nanoscale Patterning. *Nat. Protoc*. **2010**, 5, 491–502.

176. Eichelsdoerfer, D. J.; Liao, X.; Cabezas, M. D.; Morris, W.; Radha, B.; Brown, K. A.; Giam, L. R.; Braunschweig, A. B.; Mirkin, C. A. Large-Area Molecular Patterning with Polymer Pen Lithography. *Nat. Protoc*. **2013**, 8, 2548–2560.

177. Liao, W. S.; Cheunkar, S.; Cao, H. H.; Bednar, H. R.; Weiss, P. S.; Andrews, A. M. Subtractive Patterning via Chemical Lift-Off Lithography. *Science* **2012**, 337, 1517–1521.

178. Claridge, S. A.; Liao, W. S.; Thomas, J. C.; Zhao, Y. X.; Cao, H. H.; Cheunkar, S.; Serino, A. C.; Andrews, A. M.; Weiss, P. S. From the Bottom Up: Dimensional Control and Characterization in Molecular Monolayers. *Chem. Soc. Rev*. **2013**, 42, 2725–2745.

179. Saavedra, H.; Mullen, T. J.; Zhang, P.; Dewey, D. C.; Claridge, S. A.; Weiss, P. S. Hybrid Strategies in Nanolithography. *Rep. Prog. Phys*. **2010**, 73, 036501.

180. Yamada, M.; Kondo, M.; Mamiya, J. I.; Yu, Y. L.; Kinoshita, M.; Barrett, C. J.; Ikeda, T. Photomobile Polymer Materials: Towards Light-Driven Plastic Motors. *Angew. Chem., Int. Ed.* **2008**, 47, 4986–4988.

181. Yamada, M.; Kondo, M.; Miyasato, R.; Naka, Y.; Mamiya, J.; Kinoshita, M.; Shishido, A.; Yu, Y. L.; Barrett, C. J.; Ikeda, T. Photomobile Polymer Materials-Various Three-Dimensional Movements. *J. Mater. Chem*. **2009**, 19, 60–62.

182. Ionov, L. Polymeric Actuators. *Langmuir* **2015**, 31, 5015–5024.

183. Ware, T. H.; McConney, M. E.; Wie, J. J.; Tondiglia, V. P.; White, T. J. Voxelated Liquid Crystal Elastomers. *Science* **2015**, 347, 982–984.

184. Ikeda, T.; Mamiya, J.-i.; Yu, Y. Photomechanics of Liquid-Crystalline Elastomers and Other Polymers. *Angew. Chem., Int. Ed*. **2007**, 46, 506–528.

185. Iamsaard, S.; Aßhoff, S. J.; Matt, B.; Kudernac, T.; Cornelissen, J. J. L. M.; Fletcher, S. P.; Katsonis, N. Conversion of Light into Macroscopic Helical Motion. *Nat. Chem*. **2014**, 6, 229–235.

186. Kitagawa, D.; Nishi, H.; Kobatake, S. Photoinduced Twisting of a Photochromic Diarylethene Crystal. *Angew. Chem., Int. Ed*. **2013**, 52, 9320–9322.

187. Dunitz, J. D.; Schomaker, V.; Trueblood, K. N. Interpretation of Atomic Displacement Parameters from Diffraction Studies of Crystals. *J. Phys. Chem*. **1988**, 92, 856–867.

188. Nath, N. K.; Panda, M. K.; Sahoo, S. C.; Naumov, P. Thermally Induced and Photoinduced Mechanical Effects in Molecular Single Crystals – A Revival. *CrystEngComm* **2014**, 16, 1850–1858.

189. Lange, C. W.; Foldeaki, M.; Nevodchikov, V. I.; Cherkasov, K.; Abakumov, G. A.; Pierpont, C. G. Photomechanical Properties of Rhodium(I)-Semiquinone Complexes. The Structure, Spectroscopy, and Magnetism of (3,6-di-tert-butyl-1,2-semiquinonato)dicarbonylrhodium(I). *J. Am. Chem. Soc*. **1992**, 114, 4220–4222.

190. Jiang, X.; Rodríguez-Molina, B.; Nazarian, N.; Garcia-Garibay, M. A. Rotation of a Bulky Triptycene in the Solid State: Toward Engineered Nanoscale Artificial Molecular Machines. *J. Am. Chem. Soc.* **2014**, 136, 8871–8874.

191. Lemouchi, C.; Mézière, C.; Zorina, L.; Simonov, S.; Rodríguez-Fortea, A.; Canadell, E.; Wzietek, P.; Auban-Senzier, P.; Pasquier, C.; Giamarchi, T.; Garcia-Garibay, M. A.; Batail, P. Design and Evaluation of a Crystalline Hybrid of Molecular Conductors and Molecular Rotors. *J. Am. Chem. Soc*. **2012**, 134, 7880–7891.

192. Setaka, W.; Yamaguchi, K. Thermal Modulation of Birefringence Observed in a Crystalline Molecular Gyrotop. *Proc. Natl. Acad. Sci. U. S. A*. **2012**, 109, 9271–9275.

193. Setaka, W.; Yamaguchi, K. A Molecular Balloon: Expansion of a Molecular Gyrotop Cage Due to Rotation of the Phenylene Rotor. *J. Am. Chem. Soc*. **2012**, 134, 12458–12461.

194. Setaka, W.; Yamaguchi, K. Order-Disorder Transition of Dipolar Rotor in a Crystalline Molecular Gyrotop and Its Optical Change. *J. Am. Chem. Soc*. **2013**, 135, 14560–14563.

195. Kobr, L.; Zhao, K.; Shen, Y. Q.; Polívková, K.; Shoemaker, R. K.; Clark, N. A.; Price, J. C.; Rogers, C. T.; Michl, J. Inclusion Compound Based Approach to Arrays of Artificial Dipolar Molecular Rotors: Bulk Inclusions. *J. Org. Chem*. **2013**, 78, 1768–1777.

196. Kobr, L.; Zhao, K.; Shen, Y. Q.; Shoemaker, R. K.; Rogers, C. T.; Michl, J. Tris-o-phenylenedioxycyclotriphosphazene (TPP) Inclusion Compounds Containing a Dipolar Molecular Rotor. *Cryst. Growth Des*. **2014**, 14, 559–568.

197. Zhang, W.; Ye, H. Y.; Graf, R.; Spiess, H. W.; Yao, Y. F.; Zhu, R. Q.; Xiong, R. G. Tunable and Switchable Dielectric Constant in an Amphidynamic Crystal. *J. Am. Chem. Soc*. **2013**, 135, 5230–5233.

198. Karlen, S. D.; Garcia-Garibay, M. A. Amphidynamic Crystals: Structural Blueprints for Molecular Machines. *Top. Curr. Chem*. **2005**, 37, 179–227.

199. Rodríguez-Molina, B.; Farfán, N.; Romero, M.; Méndez-Stivalet, J. M.; Santillan, R.; Garcia-Garibay, M. A. Anisochronous Dynamics in a Crystalline Array of Steroidal Molecular Rotors: Evidence of Correlated Motion within 1D Helical Domains. *J. Am. Chem. Soc*. **2011**, 133, 7280–7283.

200. Sylvester, S. O.; Cole, J. M. Solar-Powered Nanomechanical Transduction from Crystalline Molecular Rotors. *Adv. Mater*. **2013**, 25, 3324–3328.

201. Lemouchi, C.; Iliopoulos, K.; Zorina, L.; Simonov, S.; Wzietek, P.; Cauchy, T.; Rodríguez-Fortea, A.; Canadell, E.; Kaleta, J.; Michl, J.; Gindre, D.; Chrysos, M.; Batail, P. Crystalline Arrays of Pairs of Molecular Rotors: Correlated Motion, Rotational Barriers, and Space-Inversion Symmetry Breaking Due to Conformational Mutations. *J. Am. Chem. Soc*. **2013**, 135, 9366–9376.

202. Kelly, T. R.; Bowyer, M. C.; Bhaskar, K. V.; Bebbington, D.; Garcia, A.; Lang, F. R.; Kim, M. H.; Jette, M. P. A Molecular Brake. *J. Am. Chem. Soc*. **1994**, 116, 3657–3658.

203. Commins, P.; Garcia-Garibay, M. A. Photochromic Molecular Gyroscope with Solid State Rotational States Determined by an Azobenzene Bridge. *J. Org. Chem*. **2014**, 79, 1611–1619.

204. Comotti, A.; Bracco, S.; Yamamoto, A.; Beretta, M.; Hirukawa, T.; Tohnai, N.; Miyata, M.; Sozzani, P. Engineering Switchable Rotors in Molecular Crystals with Open Porosity. *J. Am. Chem. Soc*. **2014**, 136, 618–621.

205. Comotti, A.; Bracco, S.; Ben, T.; Qiu, S. L.; Sozzani, P. Molecular Rotors in Porous Organic Frameworks. *Angew. Chem., Int. Ed.* **2014**, 53, 1043–1047.

206. Zhu, K.; O'Keefe, C. A.; Vukotic, V. N.; Schurko, R. W.; Loeb, S. J. A Molecular Shuttle that Operates Inside a Metal–Organic Framework. *Nat. Chem*. **2015**, 7, 514–519.

207. Kim, T.; Zhu, L.; Al-Kaysi, R. O.; Bardeen, C. J. Organic Photomechanical Materials. *ChemPhysChem* **2014**, 15, 400–414.

208. Panda, M. K.; Runčevsk, T.; Sahoo, S. C.; Belik, A. A.; Nath, N. K.; Dinnebier, R. E.; Naumov, P. Colossal Positive and Negative Thermal Expansion and Thermosalient Effect in a Pentamorphic Organometallic Martensite. *Nat. Commun*. **2014**, 5, 4811.

209. Sahoo, S. C.; Panda, M. K.; Nath, N. K.; Naumov, P. Biomimetic Crystalline Actuators: Structure-Kinematic Aspects of the Self-Actuation and Motility of Thermosalient Crystals. *J. Am. Chem. Soc*. **2013**, 135, 12241–12251.

210. Sahoo, S. C.; Sinha, S. B.; Kiran, M. S. R. N.; Ramamurty, U.; Dericioglu, A. F.; Reddy, C. M.; Naumov, P. Kinematic and Mechanical Profile of the Self-Actuation of Thermosalient Crystal Twins of 1,2,4,5-Tetrabromobenzene: A Molecular Crystalline Analogue of a Bimetallic Strip. *J. Am. Chem. Soc*. **2013**, 135, 13843–13850.

211. Naumov, P.; Sahoo, S. C.; Zakharov, B. A.; Boldyreva, E. V. Dynamic Single Crystals: Kinematic Analysis of Photoinduced Crystal Jumping (The Photosalient Effect). *Angew. Chem., Int. Ed*. **2013**, 52, 9990–9995.

212. Medishetty, R.; Husain, A.; Bai, Z. Z.; Runčevsk, T.; Dinnebier, R. E.; Naumov, P.; Vittal, J. J. Single Crystals Popping Under UV Light: A Photosalient Effect Triggered by a [2 + 2] Cycloaddition Reaction. *Angew. Chem., Int. Ed*. **2014**, 53, 5907–5911.

213. Sahoo, S. C.; Nath, N. K.; Zhang, L. D.; Semreen, M. H.; Al-Tel, T. H.; Naumov, P. Actuation Based on Thermo/Photosalient Effect: A Biogenic Smart Hybrid Driven by Light and Heat. *RSC Adv*. **2014**, 4, 7640–7647.

214. Kobatake, S.; Takami, S.; Muto, H.; Ishikawa, T.; Irie, M. Rapid and Reversible Shape Changes of Molecular Crystals on Photoirradiation. *Nature* **2007**, 446, 778–781.

215. Kitagawa, D.; Kobatake, S. Crystal Thickness Dependence of the Photoinduced Crystal Bending of 1-(5-methyl-2-(4-(*p*-vinylbenzoyloxymethyl)phenyl)-4-thiazolyl)-2-(5-methyl-2-phenyl-4-thiazolyl)perfluorocyclopentene. *Photochem. Photobiol. Sci.* **2014**, 13, 764–769.

216. Morimoto, M.; Irie, M. A Diarylethene Cocrystal that Converts Light into Mechanical Work. *J. Am. Chem. Soc*. **2010**, 132, 14172–14178.

217. Terao, F.; Morimoto, M.; Irie, M. Light-Driven Molecular-Crystal Actuators: Rapid and Reversible Bending of Rodlike Mixed Crystals of Diarylethene Derivatives. *Angew. Chem., Int. Ed*. **2012**, 51, 901–904.

218. Kitagawa, D.; Kobatake, S. Photoreversible Current ON/OFF Switching by the Photoinduced Bending of Gold-Coated Diarylethene Crystals. *Chem. Commun*. **2015**, 51, 4421–4424.

219. Zhu, L. Y.; Al-Kaysi, R. O.; Bardeen, C. J. Reversible Photoinduced Twisting of Molecular Crystal Microribbons. *J. Am. Chem. Soc*. **2011**, 133, 12569–12575.

220. Kim, T.; Al-Muhanna, M. K.; Al-Suwaidan, S. D.; Al-Kaysi, R. O.; Bardeen, C. J. Photoinduced Curling of Organic Molecular Crystal Nanowires. *Angew. Chem., Int. Ed*. **2013**, 52, 6889–6893.

221. Kim, T.; Zhu, L. C.; Mueller, L. J.; Bardeen, C. J. Mechanism of Photoinduced Bending and Twisting in Crystalline Microneedles and Microribbons Composed of 9-Methylanthracene. *J. Am. Chem. Soc*. **2014**, 136, 6617–6625.

222. Koshima, H.; Matsuo, R.; Matsudomi, M.; Uemura, Y.; Shiro, M. Light-Driven Bending Crystals of Salicylidenephenylethylamines in Enantiomeric and Racemate Forms. *Cryst. Growth Des*. **2013**, 13, 4330–4337.

223. Kumar, A. S.; Ye, T.; Takami, T.; Yu, B. C.; Flatt, A. K.; Tour, J. M.; Weiss, P. S. Reversible Photo-Switching of Single Azobenzene Molecules in Controlled Nanoscale Environments. *Nano Lett*. **2008**, 8, 1644–1648.

224. Zheng, Y. B.; Payton, J. L.; Chung, C. H.; Liu, R.; Cheunkar, S.; Pathem, B. K.; Yang, Y.; Jensen, L.; Weiss, P. S. Surface-Enhanced Raman Spectroscopy to Probe Reversibly Photoswitchable Azobenzene in Controlled Nanoscale Environments. *Nano Lett*. **2011**, 11, 3447–3452.

225. Vapaavuori, J.; Goulet-Hanssens, A.; Heikkinen, I. T. S.; Barrett, C. J.; Priimagi, A. Are Two Azo Groups Better than One? Investigating the Photoresponse of Polymer-Bisazobenzene Complexes. *Chem. Mater*. **2014**, 26, 5089–5096.

226. Goulet-Hanssens, A.; Barrett, C. J. Photo-Control of Biological Systems with Azobenzene Polymers. *J. Polym. Sci., Part A: Polym. Chem.* **2013**, 51, 3058–3070.

227. Ikeda, T.; Tsutsumi, O. Optical Switching and Image Storage by Means of Azobenzene Liquid-Crystal Films. *Science* **1995**, 268, 1873–1875.

228. Koshima, H.; Ojima, N.; Uchimoto, H. Mechanical Motion of Azobenzene Crystals upon Photoirradiation. *J. Am. Chem. Soc*. **2009**, 131, 6890–6891.

229. Bushuyev, O. S.; Singleton, T. A.; Barrett, C. J. Fast, Reversible, and General Photomechanical Motion in Single Crystals of Various Azo Compounds Using Visible Light. *Adv. Mater.* **2013**, 25, 1796–1800.

230. Bushuyev, O. S.; Tomberg, A.; Friščić, T.; Barrett, C. J. Shaping Crystals with Light: Crystal-to-Crystal Isomerization and Photomechanical Effect in Fluorinated Azobenzenes. *J. Am. Chem. Soc.* **2013**, 135, 12556–12559.

231. Bushuyev, O. S.; Corkery, T. C.; Barrett, C. J.; Friščić, T. Photo-Mechanical Azobenzene Cocrystals and *in situ* X-Ray Diffraction Monitoring of their Optically-Induced Crystal-to-Crystal Isomerisation. *Chem. Sci*. **2014**, 5, 3158–3164.

232. Warner, M.; Mahadevan, L. Photoinduced Deformations of Beams, Plates, and Films. *Phys. Rev. Lett*. **2004**, 92, 134302.

233. Nath, N. K.; Pejov, L.; Nichols, S. M.; Hu, C. H.; Saleh, N.; Kahr, B.; Naumov, P. Model for Photoinduced Bending of Slender Molecular Crystals. *J. Am. Chem. Soc.* **2014**, 136, 2757–2766.

234. Luber, E. J.; Buriak, J. M. Reporting Performance in Organic Photovoltaic Devices. *ACS Nano* **2013**, 7, 4708–4714.

235. Gogotsi, Y. What Nano Can Do for Energy Storage. *ACS Nano* **2014**, 8, 5369–5371.

236. Haines, C. S.; Lima, M. D.; Li, N.; Spinks, G. M.; Foroughi, J.; Madden, J. D. W.; Kim, S. H.; Fang, S.; Jung de Andrade, M.; Göktepe, F.; Göktepe, Ö.; Mirvakili, S. M.; Naficy, S.; Lepró, X.; Oh, J.; Kozlov, M. E.; Kim, S. J.; Xu, X.; Swedlove, B. J.; Wallace, G. G.; Baughman, R. H. Artificial Muscles from Fishing Line and Sewing Thread. *Science* **2014**, 343, 868–872.

237. Lee, J. A.; Kim, Y. T.; Spinks, G. M.; Suh, D.; Lepró, X.; Lima, M. D.; Baughman, R. H.; Kim, S. J. All-Solid-State Carbon Nanotube Torsional and Tensile Artificial Muscles. *Nano Lett.* **2014**, 14, 2664–2669.